

May 2022

Triboinformatic Approaches for Surface Characterization: Tribological and Wetting Properties

Md Syam Hasan
University of Wisconsin-Milwaukee

Follow this and additional works at: <https://dc.uwm.edu/etd>



Part of the [Mechanical Engineering Commons](#)

Recommended Citation

Hasan, Md Syam, "Triboinformatic Approaches for Surface Characterization: Tribological and Wetting Properties" (2022). *Theses and Dissertations*. 2896.
<https://dc.uwm.edu/etd/2896>

This Dissertation is brought to you for free and open access by UWM Digital Commons. It has been accepted for inclusion in Theses and Dissertations by an authorized administrator of UWM Digital Commons. For more information, please contact scholarlycommunicationteam-group@uwm.edu.

TRIBOINFORMATIC APPROACHES FOR SURFACE CHARACTERIZATION:
TRIBOLOGICAL AND WETTING PROPERTIES

by

Md Syam Hasan

A Dissertation Submitted in

Partial Fulfillment of the

Requirements for the Degree of

Doctor of Philosophy

in Engineering

at

The University of Wisconsin-Milwaukee

May 2022

ABSTRACT

TRIBOINFORMATIC APPROACHES FOR SURFACE CHARACTERIZATION: TRIBOLOGICAL AND WETTING PROPERTIES

by

Md Syam Hasan

The University of Wisconsin-Milwaukee, 2022
Under the Supervision of Professor Michael Nosonovsky

Tribology is the study of surface roughness, adhesion, friction, wear, and lubrication of interacting solid surfaces in relative motion. In addition, wetting properties are very important for surface characterization. The combination of Tribology with Machine Learning (ML) and other data-centric methods is often called *Triboinformatics*. In this dissertation, triboinformatic methods are applied to the study of Aluminum (Al) composites, antimicrobial, and water-repellent metallic surfaces, and organic coatings.

Al and its alloys are often preferred materials for aerospace and automotive applications due to their lightweight, high strength, corrosion resistance, and other desired material properties. However, Al exhibits high friction and wear rates along with a tendency to seize under dry sliding or poor lubricating conditions. Graphite and graphene particle-reinforced Al metal matrix composites (MMCs) exhibit self-lubricating properties and they can be potential alternatives for Al alloys in dry or starved lubrication conditions.

In this dissertation, artificial neural network (ANN), k -nearest neighbor (KNN), support vector machine (SVM), random forest (RF), gradient boosting machine (GBM), and hybrid ensemble algorithm-based ML models have been developed to correlate the dry friction and wear

of aluminum alloys, Al-graphite, and Al-graphene MMCs with material properties, the composition of alloys and MMCs, and tribological parameters. ML analysis reveals that the hardness, sliding distance, and tensile strength of the alloys influences the COF most significantly. On the other hand, the normal load, sliding speed, and hardness were the most influential parameters in predicting wear rate.

The graphite content is the most significant parameter for friction and wear prediction in Al-graphite MMCs. For Al-graphene MMCs, the normal load, graphene content, and hardness are identified as the most influential parameters for COF prediction, while the graphene content, load, and hardness have the greatest influence on the wear rate.

The ANN, KNN, SVM, RF, and GBM, as well as hybrid regression models (RF-GBM), with the principal component analysis (PCA) descriptors for COF and wear rate were also developed for Al-graphite MMCs in liquid-lubricated conditions. The hybrid RF-GBM models have exhibited the best predictive performance for COF and wear rate. Lubrication condition, lubricant viscosity, and applied load are identified as the most important variables for predicting wear rate and COF, and the transition from dry to lubricated friction and wear is studied.

The micro- and nanoscale roughness of zinc (Zn) oxide-coated stainless steel and sonochemically treated brass (Cu Zn alloy) samples are studied using the atomic force microscopy (AFM) images to obtain the roughness parameters (standard deviation of the profile height, correlation length, the extreme point location, persistence diagrams, and barcodes). A new method of the calculation of roughness parameters involving correlation lengths, extremum point distribution, persistence diagrams, and barcodes are developed for studying the roughness patterns and anisotropic distributions inherent in coated surfaces. The analysis of the 3×3 , 4×4 , and 5×5 sub-matrices or patches has revealed the anisotropic nature of the roughness profile at

the nanoscale. The scale dependency of the roughness features is explained by the persistence diagrams and barcodes.

Solid surfaces with water-repellent, antimicrobial, and anticorrosive properties are desired for many practical applications. TiO_2/ZnO phosphate and Polymethyl Hydrogen Siloxane (PMHS) based 2-layer antimicrobial and anticorrosive coatings are synthesized and applied to steel, ceramic, and concrete substrates. Surfaces with these coatings possess complex topographies and roughness patterns, which cannot be characterized completely by the traditional analysis. Correlations between surface roughness, coefficient of friction (COF), and water contact angle for these surfaces are obtained. The hydrophobic modification in anticorrosive coatings does not make the coated surfaces slippery and retained adequate friction for transportation application.

The dissertation demonstrates that Triboinformatic approaches can be successfully implemented in surface science, and tribology and they can generate novel insights into structure-property relationships in various classes of materials.

© Copyright by Md Syam Hasan, 2022
All Rights Reserved

To
my parents

TABLE OF CONTENTS

ABSTRACT	ii
TABLE OF CONTENTS	vii
LIST OF FIGURES	xiii
LIST OF TABLES	xvii
LIST OF ABBREVIATIONS	xix
ACKNOWLEDGEMENTS	xx
CHAPTER 1: INTRODUCTION	1
1.1. The object of study and methodology	1
1.2. Objective of the dissertation	6
1.3. Organization of the dissertation	8
1.4. References	10
CHAPTER 2: BASIC CONCEPTS OF SURFACE SCIENCE, WETTING, TRIBOLOGY, AND A REVIEW ON TRIBOINFORMATICS	12
2.1. Surface Science and Tribology	12
2.1.1. Surface Roughness	13
2.1.2. Adhesion	13
2.1.3. Friction and friction mechanisms	13
2.1.4. Wear and wear mechanisms	16
2.1.5. Lubrication and lubrication regimes	18
2.2. Wetting	20
2.2.1. Wettability, Contact Angle, and surface types	20
2.2.2. Models of wetting and wetting mechanisms	21
2.3. Triboinformatics approaches	23

2.3.1. Machine learning analysis	23
2.3.1.1. Artificial Neural Network (ANN)	25
2.3.1.2. K-Nearest neighbor (KNN)	27
2.3.1.3. Support vector machine (SVM)	28
2.3.1.4. Random Forest (RF)	28
2.3.1.5. Gradient boosting machine (GBM)	29
2.3.1.6. Principal component analysis (PCA)	30
2.3.1.7. Hybrid and ensemble models	30
2.3.2. Triboinformatics studies of metals and composites	31
2.3.2.1. Typical variables affecting friction, wear, and surface Properties	31
2.3.2.2. Tribological and surface property prediction for metals and metallic composites	32
2.3.3. Topological data analysis (TDA)	36
2.3.3.1. Data topology of visual images	38
2.3.3.2. Data topology for surface characterization	40
2.4. Conclusion	41
2.5. References	41

**CHAPTER 3: FRICTION AND WEAR PREDICTION OF ALUMINUM ALLOYS USING
TRIBOINFORMATICS APPROACHES** 48

3.1. Introduction	48
3.2. Variables influencing tribological behavior of aluminum alloys	51
3.2.1. Material variables	51
3.2.1.1. Effect of alloy composition	51
3.2.1.2. Effect of microstructural properties and material processing	52
3.2.1.3. Effect of mechanical properties on tribological behavior	56
3.2.2. Tribological test variables	58
3.2.2.1. Effect of sliding speed	59
3.2.2.2. Effect of sliding distance	60

3.2.2.3. Effect of normal load	61
3.3. Materials and methods	62
3.3.1. Data collection	62
3.3.2. Input and output parameters	63
3.3.3. Machine learning algorithms	63
3.3.4. Data preprocessing	63
3.3.5. Parameter optimization of ML models	64
3.4. Result and discussion	65
3.4.1. Model performance evaluation	66
3.4.2. Importance of different independent variables	70
3.5. Conclusion	72
3.6. References	73
CHAPTER 4: FRICTION AND WEAR MODELING OF GRAPHITE AND GRAPHENE REINFORCED ALUMINUM METAL MATRIX COMPOSITES USING TRIBOINFORMATICS APPROACHES	81
4.1. Introduction	81
4.2. Friction mechanisms in aluminum-graphite and aluminum-graphene MMCs	86
4.3. Wear mechanisms in aluminum-graphite and aluminum-graphene MMCs	88
4.4. Variables influencing friction and wear	91
4.4.1. Material variables	91
4.4.1.1. Effect of graphite content	91
4.4.1.2. Influence of graphene content	94
4.4.1.2.1. Graphene as a solid lubricant	94
4.4.1.2.2. Graphene addition and mechanical properties	96
4.4.1.3. Effect of matrix material	98
4.4.1.4. Effect of the manufacturing process and heat treatment	101
4.4.1.5. Effect of hardness	103
4.4.2. Tribological variables	104
4.4.2.1. Effect of normal load	104
4.4.2.2. Influence of sliding distance	106

4.4.2.3. Influence of sliding speed	107
4.5. Friction and wear performance of aluminum-graphite and aluminum-graphene composites	108
4.6. Materials and methods	109
4.6.1. Data collection and input-output parameters	110
4.6.2. Machine learning algorithms	111
4.6.3. Data preprocessing and standardization	111
4.6.4. Optimization of the ML models	112
4.7. Result and discussion	114
4.7.1. Evaluation of model performance	114
4.7.2. Result for COF prediction	115
4.7.3. Influence of input variables in COF prediction	117
4.7.4. Wear rate prediction	120
4.7.5. Influence of the input variables on wear rate prediction	124
4.7.6. Prediction performance comparison	127
4.8. Conclusion	128
4.9. References	130
CHAPTER 5: TRIBOINFORMATICS MODELING OF THE TRANSITION FROM SOLID TO LIQUID LUBRICATED FRICTION AND WEAR IN ALUMINUM-GRAPHITE COMPOSITES	141
5.1. Introduction	141
5.2. Liquid and solid lubricated wear and friction of aluminum-graphite	144
5.2.1. Friction behavior of Al/Gr MMCs in dry condition	145
5.2.2. Friction behavior of Al/Gr MMCs in liquid lubrication	146
5.2.3. Friction behavior of Al/Gr MMCs in the transition from liquid to dry condition	147
5.2.4. Wear behavior of Al/Gr MMCs in dry	150
5.2.5. Wear mechanism of Al/Gr composites in liquid Lubrication	152
5.3. Materials and methods	153

5.3.1. Data collection	153
5.3.2. Machine Learning models	155
5.3.3. Data preprocessing	155
5.3.4. Optimization of parameters for regression models	156
5.4. Result and discussion	157
5.4.1. Friction and wear patterns through dimensionality reduction using PCA	157
5.4.2. ML regression model performance analysis	159
5.4.2.1. Model performance for COF prediction	160
5.4.2.2. Feature importance for COF prediction	163
5.4.2.3. Model performance in wear rate prediction	164
5.4.2.4. Feature importance for predicting wear rate	166
5.4.3. Selection of ML models in tribological behavior prediction	167
5.5. Conclusion	169
5.6. References	170
CHAPTER 6: DATA TOPOLOGY APPROACHES FOR ROUGHNESS CHARACTERIZATION AND FRICTION MODELING	175
6.1. Introduction	175
6.2. Persistence analysis of data topology	183
6.3. Experimental procedure	184
6.4. Data analysis for roughness characterization	187
6.5. Contact parameters for friction	196
6.6. Contact of rough surfaces	199
6.6.1. Static contact	199
6.6.2. Stick-slip	199
6.7. Conclusion	201
6.8. References	201

CHAPTER 7: ROUGHNESS, WETTING, AND TRIBOLOGICAL ANALYSIS OF ANTIMICROBIAL AND ANTICORROSIVE COATINGS USING TRADITIONAL AND DATA TOPOLOGY APPROACHES	208
7.1. Introduction	208
7.2. Materials and procedures	213
7.2.1. Surface roughness characterization	213
7.2.2. Tribological test procedure	214
7.2.3. Wetting test procedure	215
7.3. Result and discussion	216
7.3.1. Surface roughness characterization	216
7.3.2. Topological data analysis and surface characterization	217
7.3.3. Wetting test	224
7.3.4. Tribological tests	226
7.4. Conclusion	232
7.5. References	233
CHAPTER 8: CONCLUSIONS	239
CURRICULUM VITAE	243

LIST OF FIGURES

Figure 2.1. Lubrication regimes in Stribeck curve.....	19
Figure 2.2. (a) hydrophilic surface ($CA < 90^\circ$) (b) hydrophobic surface ($90^\circ < CA < 150^\circ$) (c) superhydrophobic surface ($CA > 150^\circ$).....	21
Figure 2.3. Machine learning algorithm types.....	24
Figure 2.4. The architecture of a feed-forward multilayer perception of an ANN model.....	27
Figure 2.5. (a) The primary circle and two mutually nonintersecting secondary circles corresponding to isotropic contrast gradients and vertical and horizontal features, respectively, in 3×3 patches in the R^8 space for natural images. Each secondary circle intersects twice with the primary circle. (b) The Klein bottle surface that fits that such configuration topologically. (c) The roughness profile image of a ceramic tile surface received from confocal microscopy, and (d) isotropy and anisotropy in surface roughness distribution.....	39
Figure 3.1. Average (a) COF [12-19, 31-32], (b) wear rate [12-14, 16-20, 32] of different aluminum base alloys under dry conditions against a steel counterface.....	52
Figure 3.2.(a) COF vs average grain size, (b) wear rate vs average grain size, (Al 7075 = $60 \mu m$, Al 6061 = $28 \mu m$, A356 = $50 \mu m$, A356.2 = $73 \mu m$, A359 = $35 \mu m$, Al 6101 = 110 , Al 2024 = 40) [12-15,17-19] under dry conditions against a steel counterface.....	53
Figure 3.3. Optical microstructures of (a) Al 7075 [33], (b) Al 6061 [34], (c) A356 [14], (d) A356.2 [35], (e) Al 2024 [19], (f) A359 [17].....	55
Figure 3.4.(a) COF vs Brinell hardness (b) wear rate vs Brinell hardness of aluminum base alloys (Al 7075 = 86 BHN, Al 6061 = 95 BHN, A356 = 75 BHN, A356.2 = 70 BHN, A359 = 87.5 BHN, Al 6101 = 71 BHN, Al 2024 = 120 BHN, Al 2014 = 135 BHN) [12-15,17-19] under dry conditions against a steel counterface.....	57
Figure 3.5. (a) COF vs sliding speed for A359 alloy [17], (b) wear rate vs sliding speed for Al 2219 alloy [43], (c) COF vs sliding distance for Al 2024 alloy [44], (d) wear rate vs sliding distance for Al 6061 alloy [45], (e) COF vs normal load for Al 2024 alloy [19], (f) wear rate vs normal load for Al 2024 alloy [44] under dry conditions against a steel counterface.....	59
Figure 3.6. Predicted vs actual COF and wear rate for aluminum base alloys using RF model.....	69
Figure 3.7. Feature importance for predicting (a) COF and (b) wear rate of aluminum base alloys.....	71
Figure 4.1. Dependencies on the graphite content of (a) the COF (Al 6061/ Gr) [10], and (b) wear rate, Al 6061/Gr [70], (c) Al 6061/Gr and Al 6061/30% SiC/Gr [22], (b) Al 6061/7% Gr composites [71] for sliding against steel.....	93

Figure 4.2. Effect of graphene content on (a) wear rate [41,44,48] (b) COF [38,41,44] of aluminum-graphene MMCs.....	95
Figure 4.3. Effect of graphene content on (a) hardness [38,39,44] and (b) tensile strength [74,75,76] of aluminum-graphene MMCs.....	97
Figure 4.4. Comparison of (a) the COF [9,10,13,14,23,77-79] and (b) wear rate [9,10,12,14,23,78,79] between different Al base alloys and their graphite (Gr) MMCs (5 wt.% Gr).....	99
Figure 4.5. (a) wear rate and [32, 36, 37, 40, 44, 80] (b) coefficient of friction [32, 37, 40, 44, 45] of different aluminum base alloys and their corresponding aluminum-graphene (Gr) composites.....	100
Figure 4.6. Effect of normal load on (a) wear rate [37, 44, 23], (b) coefficient of friction [36, 40, 72].....	105
Figure 4.7. Effect of sliding distance on (a) wear rate [32, 47, 23], (b) coefficient of friction [31, 47, 72].....	106
Figure 4.8. Effect of sliding speed on (a) wear rate [40, 41, 71], (b) coefficient of friction [36, 78].....	107
Figure 4.9. The comparison of the actual (experimentally measured) COF and the anticipated COF by GBM regression model for aluminum-graphene MMCs.....	117
Figure 4.10. Relative significance of material and tribological test variables identified by the RF model for predicting the COF of aluminum-graphite MMCs.....	119
Figure 4.11. The relative importance of input variables for predicting the COF (feature importance).....	120
Figure 4.12. The comparison of the actual (experimentally measured) and the anticipated wear rate by GBM regression model.....	123
Figure 4.13. The relative importance of input variables for predicting the wear rate of aluminum-graphite MMCs.....	125
Figure 4.14. The relative importance of input variables for predicting the wear rate of aluminum-graphene MMCs.....	127
Figure 5.1. Schematic of sliding surfaces and lubricating film, lubrication regimes in Stribeck curve for standard alloys and graphite MMCs, dimensionality reduction technique in ML, and the schematic of a typical wear map.....	144
Figure 5.2. (a) COF vs sliding distance in dry and fully lubricated conditions, (b) in situ COF data with time for Al-16Si-5Ni-5Graphite MMC in different lubrication conditions (Reprinted by permission from Springer, Ref. [24], Copyright (2016)), (c) Mean of COF vs Gr content plot from the Linear Contrast Analysis, (d) wear and seizure behavior of LM13 alloy and LM13/3% Gr MMC under different normal load at the same sling speed.....	148
Figure 5.3. Cumulative explained variance and PCA plot for wear rate.....	158

Figure 5.4. Cumulative explained variance and PCA plot for COF.....	159
Figure 5.5. Plot of predicted vs. actual COF using GBM, feature importance chart for predicting COF.....	162
Figure 5.6. Plot of actual vs. predicted COF and wear rate using RF-GBM hybrid model.....	163
Figure 5.7. Plot of predicted vs. actual wear rate using RF, feature importance chart for predicting wear rate.....	166
Figure 6.1 (a) Statistics of 3×3 pixel patches from natural images involves the primary circle (due to isotropic brightness gradients) and two secondary circles due to the prevalence of vertical and horizontal over inclined features in the images. Each secondary circle intersects twice with the primary circle. (b) Such configuration topologically fits the Klein bottle surface.....	177
Figure 6.2. Schematics of the persistence barcodes concept. With increasing the proximity radius (horizontal axis), connected structures (red bars) are formed and disappear, as well as 1D voids (holes, blue).....	180
Figure 6.3. AFM surface roughness profiles of the (a) 5×5 μm and (b)10×10 μm untreated brass samples and roughened samples sonicated at amplitudes of (c) 30%, (d) 50%, (e) 70%, and (f) 90% of the maximum power.....	185
Figure 6.4. ACFs for the roughness profile extracted from the AFM images (a) untreated 5×5 μm surface, (b) untreated 10×10 μm surface, and treated surfaces sonicated at amplitudes (c) 30%, (d) 50%, (e) 70% and (f) 90% of the maximum power.....	189
Figure 6.5. Position of the min and max values for 3×3, 4×4, and 5×5 pixel sub-matrices for (a, c, e) Dataset 1 (5×5 μm), (b, d, f) Dataset 2 (10×10 μm).....	192
Figure 6.6. Position of the min and max v in 3×3 pixel sub matrices subject to NaOH sonicated at amplitudes (a) 30%, (b) 50%, (c) 70% and (d) 90% of the maximum power.....	193
Figure 6.7. Persistence diagram and barcodes showing topological invariants for untreated sample (a-b) 5×5 μm surface, (c-d) 10×10 μm surface.....	194
Figure 6.8. Persistence barcodes showing topological invariants for 3×3 patches subject to NaOH solution sonicated at amplitudes corresponding to (a) 30%, (b) 50%, (c) 70% and (d) 90% of the maximum power.....	195
Figure 6.9. (a) 3D plot for state-and-rate model, (b) the dependency of the real area of contact with sliding velocity, (c) the increase of the real area of contact with the age of contact, (d) the plots of the number of slips vs. slip size for different threshold heights, h_T	198
Figure 7.1. Schematic diagram of different coating layers on the base material surface.....	212
Figure 7.2. Measurement of contact angles in Rame-Hart goniometer.....	216
Figure 7.3. Persistence diagram and persistence barcodes for the surface roughness of (a-b) CS BM, (c-d) CS BM-PMHS, (e-f) S1 CS, and (g-h) 2-layer S1 CS-PMHS samples.....	220

Figure 7.4. Position of the maximum and minimum values in 3×3 sub-matrices and corresponding autocorrelation function for surface profile data for (a-b) CS BM, (c-d) CS BM-PMHS, (e-f) S1 CS (BM-ZP), (g-h) S1 CS-PMHS.....	224
Figure 7.5. Contact angle vs. average roughness plot of hydrophobic samples coated with antimicrobial and anticorrosive coatings.....	225
Figure 7.6. COF vs. average roughness plot for uncoated steel BMs and BMs coated with TP/ZP+PMHS and comparison with COF vs average roughness for ceramic tile samples coated with TP and TP+PMHS.....	228
Figure 7.7. COF vs CA plot for the coated hydrophobic samples.....	230
Figure 7.8. Confocal microscope images of the coated tile surfaces with the (a) R2 and (b) optimal (O2) anticorrosive hydrophobic coatings observed after the tribological test.	231

LIST OF TABLES

Table 2.1. Overview of the application of ML approaches in friction, wear, and roughness prediction of metal, alloys, and composites.....	34
Table 3.1. Parameter optimization for COF.....	65
Table 3.2. Parameter optimization for wear rate.....	65
Table 3.3. Performance of the ML methods for COF.....	66
Table 3.4. Performance of the ML methods for wear rate.....	67
Table 4.1. Parameter optimization for COF of aluminum-graphite MMCs.....	112
Table 4.2. Parameter optimization for wear rate of aluminum-graphite MMCs.....	113
Table 4.3. Optimization of COF models for aluminum-graphene MMCs.....	113
Table 4.4. Optimization of wear rate models for aluminum-graphene MMCs.....	114
Table 4.5. Performance of the ML methods for COF.....	115
Table 4.6. Performance of the ML models for wear rate prediction.....	120
Table 5.1. Lubricant types, grades, and dynamic viscosities at room temperature.....	154
Table 5.2. Optimized parameters for COF prediction.....	156
Table 5.3. Optimized parameters for wear rate prediction.....	157
Table 5.4. Prediction performance metrics for COF.....	160
Table 5.5. Prediction performance metrics for wear rate.....	164

Table 6.1. Surface roughness properties of the samples..... 190

Table 7.1. Properties of base materials before and after hydrophobic treatment (antimicrobial coatings)..... 226

Table 7.2. Properties of the coated hydrophilic and hydrophobic samples (antimicrobial).. 227

Table 7.3. The properties of anticorrosive TiO₂-phosphate coated (hydrophilic) and TiO₂-phosphate + PMHS coated (hydrophobic) samples..... 229

LIST OF ABBREVIATIONS

AFM – Atomic Force Microscopy

AI – Artificial Intelligence

ANN – Artificial Neural Network

CA – Contact Angle

CAH – Contact Angle Hysteresis

CLSM - Confocal Laser Scanning Microscopy

COF – Coefficient of Friction

GBM – Gradient Boosting Machine

KNN – *K*-Nearest Neighbor

ML – Machine Learning

PCA - Principal Component Analysis

PESHO - Polyethyl Hydrogen Siloxane

PMHS - Polymethyl Hydrogen Siloxane

PTFE – Polytetrafluoroethylene

PVA - Polyvinyl Alcohol

UMT - Universal Mechanical Tester

HSM – High Speed Mixer

RF – Random Forest

SEM – Scanning Electron Microscope

SVM – Support Vector Machine

TDA – Topological Data Analysis

XRD - X-ray powder diffraction

ACKNOWLEDGEMENTS

I would like to offer my sincere thanks and gratitude to my Ph.D. advisor Dr. Michael Nosonovsky for his outstanding supervision and support during my graduate study. His passionate mentoring, guidance, and motivation have helped me to grow as a researcher and enabled me to overcome the challenges of graduate study and research. I would also like to thank my Ph.D. thesis committee members Dr. Konstantin Sobolev, Dr. Benjamin C. Church, Dr. H. Rahman, and Dr. Yongjin Sung for their valuable time, guidance, support, and constructive comments to improve my thesis.

I want to thank Dr. Konstantin Sobolev and his group members for the collaborative research. I want to especially thank Filip Zemajtis for the samples coated with ZnO/TiO₂ based coatings which I used for further characterization in my research. I am also grateful to Dr. Pradeep K. Rohatgi for his guidance and support and to his group for the collaboration in the research on data-driven tribology.

Additionally, I want to offer my sincere gratitude to all administrative staff members of the department of Mechanical Engineering, Graduate School, and UWM Center for International Education for their sincere support during my graduate study.

Finally, I want to thank my family for the unconditional love and support which were my biggest motivation in this difficult path. I do not have enough words to thank my parents for all the sacrifices they made to ensure a quality education for me. I want to thank my dear wife, Nabila for always being there for me throughout the journey of the graduate study. Her comforting and support as a friend, her counsel as a fellow graduate student, and her sacrifices as a partner have helped me in overcoming the challenges of my Ph.D. journey. I also want to thank all my friends and well-wishers for the mental support and the best wishes.

CHAPTER 1: INTRODUCTION

1.1. The object of study and methodology

The selection of objects of study of this dissertation is motivated by their importance for practical applications, such as light-weight and self-lubricating materials for industry and antimicrobial and anticorrosive coatings. Aluminum and its alloys have many desired material properties including low density, high stiffness, high strength, corrosion resistance, and good thermal conductivity [1]. Further improved material and tribological performance can be achieved using graphite and graphene reinforced self-lubricating aluminum metal matrix composites (MMCs). Consequently, aluminum alloys and its MMCs are promising materials for weight-critical automotive and aerospace engineering.

Certain metals, such as Copper (Cu) and Zinc (Zn), have anti-bacterial properties. Additionally, surface coatings can be synthesized to confer antimicrobial, water repellent, and anticorrosive properties to metals, ceramics, concrete, and other substrates. Titanium dioxide/ Zinc oxide (TiO_2/ZnO)-phosphate (TP/ZP) and polymethyl hydrogen siloxane (PMHS) based 2-layer hydrophobic antimicrobial coatings are tuned for application on steel which can resist the settling of pathogens. Similarly, TiO_2 -phosphate and PMHS based 2-layer water-repellent anticorrosive coatings are developed for ceramics concrete, ceramic, and asphalt surfaces to increase durability and to decrease water and ice-induced damages in roads and pavements.

The methods used in this study involve tribological and wetting characterization of solid surfaces as well as Machine Learning (ML) methods. Tribology is the study of the surface roughness, adhesion, friction, wear, and lubrication of interacting solid surfaces in relative motion. Friction and wear are very common and even ubiquitous. For example, dry friction between two

surfaces occurs with all types of materials (e.g., metals, polymers, ceramics, composites, soft materials, and biomaterials) and in a broad range of conditions, such as loads ranging from nano-newtons in nanotribology to billions of tons in seismology and geophysics. However, despite being very common, there is no general theory of dry friction explaining it from the first principles of physics or chemistry. Since the term “Tribology” was introduced by Peter H. Jost in 1966, the field has evolved and yielded new areas such as nanotribology, biotribology, ecotribology (sometimes called “Green Tribology”), biomimetic tribology, and many others [2].

The tribological characterization of a surface includes measuring the coefficient of friction (COF), wear rate, and surface roughness parameters. COF or μ is a dimensionless scalar quantity used to quantify friction. COF is the ratio of the friction force (F_f) and normal load (N) pressing the sliding surfaces together, $\mu = \frac{F_f}{N}$. Wear rate quantifies the progressive removal of materials during sliding interactions and is often presented in mm^3/m unit. Amplitude parameters and spacing parameters are the most used roughness parameters. Amplitude parameters characterize the vertical deviation of the surface profile relative to the mean line [2]. The most common amplitude parameter is the average roughness, R_a , defined as the arithmetic average of the absolute values of the profile height deviations from the mean line of the roughness profile. Mathematically, for a 2D roughness profile $z(x)$, R_a is given by $R_a = \frac{1}{L} \int_0^L |z - m| dx$. Here, L is the sampling length of the profile and $m = \frac{1}{L} \int_0^L z dx$ is the mean value of $z(x)$. Spacing parameters are related to the shape of the asperities of the surface profile. Mean peak spacing, S_m is a commonly used spacing parameter defined as the mean spacing between peaks at the centerline along the sampling length of the profile and given by the formula, $S_m = \frac{1}{n} \sum_{i=1}^n S_i$. Here, n is the total number of profile peaks and S_i is the individual peak spacing [2].

One of the main challenges in tribological studies is that while there is an abundance of data about the frictional, wear, and surface properties of various materials, systems, and engineering components, this interdisciplinary area is highly empirical. While many attempts have been made to formulate various laws or rules in tribology, the study of friction and surface properties still lacks derivation from physical or chemical first principles. Consequently, tribology remains a data-driven scientific discipline, especially for complex multi-phase materials, whose surface characteristics change with time. Due to the emergence and rapid development of new methods of “Big Data” analysis including ML, artificial intelligence (AI), topological data analysis (TDA), and others, it became possible to obtain and study new correlations in data-driven areas of science. In particular, recently, the area of so-called Triboinformatics (sometimes called “Intelligent Tribology) has been suggested [3]. Triboinformatics can be defined as an application of ML, TDA, and other data-centric methods of data analysis to tribological problems, such as establishing relationships between material and surface structure and properties and the tribological performance.

Besides dry friction, which characterizes interaction of two solid surfaces, the interaction of rough surfaces with liquid (wetting) is also very important. The conventional parameter of quantitating the wettability of a surface by a liquid is the contact angle (CA) between the liquid and the solid surface. Surfaces are called hydrophilic ($0^\circ \leq CA \leq 90^\circ$), hydrophobic ($90^\circ \leq CA \leq 120^\circ$), “over-hydrophobic” ($120^\circ \leq CA < 150^\circ$) [4], and superhydrophobic ($150^\circ \leq CA \leq 180^\circ$) depending upon the CA. In many cases, the measured value of the CA depends on whether liquid advances or recedes. The advancing CA (θ_{Adv}) is usually higher than the receding CA (θ_{Rec}) corresponding to the maximum and the minimum values of the CA on a solid substrate when a liquid droplet is placed on it. CA hysteresis (CAH) which is the difference between the advancing

and the receding CAs is another important parameter in wetting characterization. The CA and CAH are two quantitative measures of adhesion between a liquid and a solid surface. Water repellent surfaces, such as superhydrophobic surfaces, generally have both a high CA and low CAH.

The extreme water repellence observed in the lotus leaf is an inspiration for developing artificial water repellent surfaces for engineering applications. A unique hierarchical roughness profile along with the presence of a low surface energy epicuticular wax crystalloids in the lotus leaf is responsible for the water repellence commonly known as the “lotus effect” [5]. Advancements in micro/nanotechnology have made it possible to synthesize water repellent superhydrophobic and self-cleaning surfaces mimicking the lotus effect. Biomimetic superhydrophobic surfaces are synthesized, for example, by introducing particle or fiber induced micro/nano-level roughness along with a low surface energy coating like polydimethylsiloxane (PDMS), polymethyl hydrogen siloxane (PMHS), polyethyl hydrogen siloxane (PESHO) or polytetrafluoroethylene (PTFE) [4]. Such techniques have been used recently also for synthesizing water repellent anticorrosive coatings for concrete, ceramic, and asphalt surfaces to increase durability and to decrease water and ice-induced damages in roads and pavements. These techniques have been further used to develop antimicrobial coating materials for a wide range of surfaces which can resist the settling of pathogens [6].

The CA depends on the surface free energy of a solid surface. For a low surface energy surface, the contact area and adhesion between the solid surface and a water droplet are small, which results in a high contact angle. As the low surface energy coating materials used for hydrophobic/superhydrophobic surfaces can reduce adhesion between the interacting surfaces and they can potentially affect the frictional behavior. Consequently, the application of “non-sticky”

coating materials, such as PTFE, PESH0, PMHS, and similar, would reduce the COF of the surfaces. For example, the COF between the tire and the concrete surface may be reduced due to the application of the water repellent anticorrosive coating materials. This is why, the question arises whether the application of hydrophobic/superhydrophobic anticorrosive coating materials to roads and pavements makes them slippery and unsafe for vehicles. This example suggests that any modifications of wetting properties can potentially alter the frictional behavior. However, a well-defined correlation between the wetting and frictional properties of hydrophobic/superhydrophobic surfaces is yet to be developed. A combined tribological and wetting characterization can help to develop such a comprehensive correlation. Additionally, such characterization can provide comprehensive information about a surface, for example, how the surface will interact with water and other liquids and how will be the friction and wear behavior, corrosion resistance, and durability in different engineering applications. Such characterization is also helpful in modifying a surface or synthesizing and optimizing novel surface coating materials for different applications.

Rough surfaces possess complex topography, which cannot be characterized completely by a single parameter. The selection of appropriate roughness parameters depends on a particular application. The traditional surface analysis often comes short in characterizing complex surface properties and their interrelations. Recent advancements in data science have opened the door of successfully applying data-driven approaches like Machine Learning and Topological Data Analysis (TDA) in surface characterization. These datacentric analysis approaches can reveal novel insights into the roughness patterns, functional designs, and anisotropic distributions inherent in the complex surfaces not identifiable in traditional analysis. In this dissertation, a methodology of data-driven surface roughness analysis is developed consisting of calculating

roughness parameters, correlation length, extremum point distribution, persistence diagrams, and barcodes and applied for the 2-layer antimicrobial coatings, brass (Cu Zn alloy) samples roughened by a sonochemical treatment, and zinc oxide-coated stainless steel samples.

In this dissertation, the friction and wear mechanisms of these alloys and MMCs will be studied using traditional 2-parameter analysis and data-driven ML models. Supervised standalone ML regression models: artificial neural network (ANN), k nearest neighbor (KNN), support vector machine (SVM), random forest (RF), and gradient boosting machine (GBM), and hybrid ensemble RF-GBM regression ML models will be developed to predict the COF and wear rate of these alloys and MMCs from the material properties and tribological test variables in dry and liquid lubricated conditions.

The surface roughness, wetting, and friction properties of TiO₂/ZnO-phosphate (TP/ZP) and polymethyl hydrogen siloxane (PMHS) based 2-layer hydrophobic antimicrobial and anticorrosive coatings tuned for application on steel and ceramics will be studied. Confocal laser scanning microscope (CLSM- Olympus LEXT OSL 4100 model), atomic force microscope (AFM), and scanning electron microscope (SEM- JEOL JSM-6460L model) will be used to characterize the surface roughness. The water contact angles will be measured using the Rame-Hart 250 goniometer. The universal mechanical tester (CETR UMT 2) will be used to measure the COF of the coated samples under dry conditions.

1.2. Objectives of the dissertation

In this dissertation, data-driven Triboinformatic approaches will be applied to surface characterization, wetting, and tribological behavior prediction. The objectives are the following.

First, the development of artificial neural network, k -nearest neighbor, support vector machine, gradient boosting machine, and random forest algorithm-based ML regression models geared towards establishing correlations in structure and tribological properties of aluminum alloys and particle reinforced aluminum MMCs (aluminum-graphite and aluminum-graphene) in dry conditions by employing a Python language-based computational procedure.

Second, to analyze structure-property relationships between the material properties, composition of the alloys and MMCs, test conditions, and tribological properties of aluminum alloys and aluminum-based MMCs and identify the most influential material properties and tribological parameters in predicting the friction and wear behavior of these alloys and MMCs.

Third, the development of principal component analysis based unsupervised ML models and random forest and gradient boosting machine algorithm-based hybrid ensemble ML models for dimensionality reduction in structure-property relationships data and predicting the friction and wear behavior of aluminum-graphite MMCs in during the transition of lubrication regimes by employing a Python language-based computational method.

Fourth, the development of a new method of data-driven surface roughness analysis consisting of the calculation of roughness parameters, correlation lengths, extremum point distribution, persistence diagrams, and barcodes for studying the roughness patterns, functional designs, and anisotropic distributions inherent in steel substrates coated with TiO_2/ZnO phosphate and PMHS based 2-layer antimicrobial coating materials and brass (Cu Zn alloy) samples roughened by a sonochemical treatment.

Fifth, to establish comprehensive correlations between surface roughness, COF, and water contact angle for steel substrates coated with TiO_2/ZnO phosphate and PMHS based antimicrobial

and ceramic substrates coated with TiO₂ phosphate and PMHS based anticorrosive coating materials.

1.3. Organization of the dissertation

In chapter 2, first the concepts of surface science and tribology including wetting, surface roughness, adhesion, friction, and wear will be introduced. Then, the basics of different ML algorithms commonly used in developing prediction models will be discussed. The strengths and weaknesses of these ML algorithms, their applicability for different types of data, and techniques of their optimization for problem solving will also be discussed. Additionally, topological data analysis (TDA), persistence homology, and other data centric methods which can be potentially applied in surface characterization will be discussed. Finally, a review of data-driven and Triboinformatics approaches of problem-solving in tribology, wetting, and surface characterization will be presented.

In chapter 3, traditional and Triboinformatics approaches will be presented for analyzing the friction and wear behavior of aluminum alloys. Tribological behavior prediction of these alloys are important for their application in automotive and aerospace applications. For friction and wear behavior prediction of aluminum alloys, five supervised ML regression models: ANN, KNN, SVM, RF, and GBM will be developed and optimized. Moreover, performance of these ML algorithms will be analyzed and a comparative analysis of different material and tribological test parameters influencing the friction and wear of these alloys will be presented.

In chapter 4, friction and wear mechanisms of aluminum-graphite and aluminum-graphene metal matrix composites will be studied using traditional and Triboinformatics approaches. Graphite and graphene reinforced aluminum MMCs are often preferred over the base alloys in

many engineering applications due to their improved tribological and material properties. Five supervised ML regression models: ANN, KNN, SVM, RF, and GBM will be developed using tribological data reported in the literature to predict the tribological behaviors of these MMCs and to find patterns in their tribological behavior. Also, the study will focus on identifying the most influential material variables for friction and wear rate prediction for these MMCs in dry conditions.

In chapter 5, friction and wear behavior of aluminum-graphite MMCs in liquid lubricated conditions and in the transition from lubricated to unlubricated conditions will be analyzed using traditional and Triboinformatics approaches. Analyzing the tribological and self-lubricating behavior in the presence of liquid lubrication and the transition from lubricated to unlubricated state as a result of drainage in lubricating liquid are of importance in situations where such sudden loss of lubricant can lead to instant seizures and catastrophic failures. Unsupervised principal component analysis (PCA) model, five supervised standalone ML regression models: ANN, KNN, SVM, RF, and GBM, and hybrid ensemble RF-GBM regression model will be developed for tribological behavior prediction and finding wear and friction patterns in the transition of lubrication conditions.

In chapter 6, data topology approaches will be applied to analyze the surface roughness of zinc oxide-coated stainless steel samples and sonochemically treated brass (Cu Zn alloy) samples. Surface roughness data for these samples will be obtained from CLSM and AFM analysis. Microscale and nanoscale roughness of these metallic samples will be studied applying different approaches to the evaluation of roughness parameters including the standard deviation of the rough profile height, correlation length, analyzing the extreme point location, persistence diagrams, and barcodes in the surface roughness data space. Additionally, a data-driven analysis of asperity

contact and stick-slip motion using AFM data over the Robin Hood landscape for friction modeling will be discussed.

In chapter 7, roughness patterns, wetting, and frictional behavior of TiO₂/ZnO phosphate and PMHS based novel antimicrobial coatings and TiO₂ phosphate and PMHS based anticorrosive coatings will be characterized using the traditional and data topology approaches. For many application, water-repellant and antimicrobial properties of the substrate materials are desired without a notable change in the friction behavior compared to the uncoated state. A proper understanding of the correlations between surface roughness, wetting, and friction parameters of the substrates is necessary to develop and optimize the performance of these novel coating materials for different applications. In this chapter, such correlations will be investigated.

In chapter 8, the conclusions of the dissertation are summarized.

1.4. References

1. Macke, Anthony, B. F. Schultz, and Pradeep Rohatgi. "Metal matrix composites." *Adv. Mater. Processes* 170, no. 3 (2012): 19-23.
2. Menezes, Pradeep L., Michael Nosonovsky, Sudeep Prabhakar Ingole, Satish Vasu Kailas, and Michael R. Lovell, eds. *Tribology for scientists and engineers*. New York: Springer, 2013.
3. Kordijazi, Amir, Hathibelagal M. Roshan, Arushi Dhingra, Marco Povolo, Pradeep K. Rohatgi, and Michael Nosonovsky. "Machine-learning methods to predict the wetting properties of iron-based composites." *Surface Innovations* 9, no. 2–3 (2020): 111-119.
4. Lanka, Sridhar, Evgeniya Alexandrova, Marina Kozhukhova, Md Syam Hasan, Michael Nosonovsky, and Konstantin Sobolev. "Tribological and wetting properties of TiO₂ based hydrophobic coatings for ceramics." *Journal of Tribology* 141, no. 10 (2019).

5. Hasan, Md Syam, and Michael Nosonovsky. "Lotus effect and friction: does nonsticky mean slippery?." *Biomimetics* 5, no. 2 (2020): 28.
6. Hasan, Md Syam, Konstantin Sobolev, and Michael Nosonovsky. "Evaporation of droplets capable of bearing viruses airborne and on hydrophobic surfaces." *Journal of Applied Physics* 129, no. 2 (2021): 024703.

CHAPTER 2: BASIC CONCEPTS OF SURFACE SCIENCE, WETTING, TRIBOLOGY, AND A REVIEW ON TRIBOINFORMATICS

In this chapter, the basic concepts of surface science, wetting, and tribology will be introduced. Basics of data-driven approaches, for example, ML algorithms and topological data analysis (TDA) that will be used extensively in the consequent chapters will be discussed. Finally, a comprehensive review of the Triboinformatic approaches to tribology, wetting, and surface science will be presented.

2.1. Surface Science and Tribology

Surface science is the scientific study of different physical and chemical phenomena that take place at the interfaces of two different phases. Solid-liquid, solid-gas, solid-vacuum, liquid-gas interfaces all are covered in the study of surface science. Surface physics, surface chemistry, and surface engineering at the macro-, micro-, and nano-levels are the branches of surface science. *Surface chemistry* is the study of chemical reactions at the interfaces while surface physics is the study of physical interactions at the interfaces. *Surface engineering* focuses on the modification of the chemical composition of the surfaces by controlled incorporation of selected materials and functional groups to enhance certain properties of the surfaces. Surface diffusion, adhesion, roughness, surface reconstruction all are the important topics of surface science.

Tribology is a section of surface science which deals with the study of interacting solid surfaces in their relative motion. Due to its complex and multidisciplinary aspects, tribology has established itself as interdisciplinary and draws the attention of researchers from versatile fields

like physics, chemistry, material science, engineering and so on. Surface roughness, adhesion, friction, wear, and lubrication are the most important topics of tribology.

2.1.1. Surface Roughness

Surface roughness is defined as the irregularities observed as repetitive or random deviations from the nominal surface forming the three-dimensional topography. According to the texture scale, roughness can be classified into two different types: macroroughness (roughness at the centimeter or millimeter level) and micro/nanoroughness (roughness at the micrometer/nanometer level). Waviness in the surface texture resulting from machine or workpiece deflection, vibration, chatter or heat treatment is the example of the macroroughness. Nano/microroughness is formed by short wavelengths fluctuations of the surface of, characterized by hills and valleys of varying amplitude and spacing [1]. Irregularities due to nano- and microroughness are inherent in surface treatment process. There are several methods to quantify roughness. Most commonly surface roughness is quantified by variations in the height of the surface relative to a reference plane. It is measured along a single line profile or along a set of parallel line profiles (surface maps).

Surface roughness has notable effects on tribological and wetting properties and the interaction with the environment. With an increase in surface roughness, the coefficient of friction (COF) also usually increases. Surface roughness may also affect adhesion. Rough surfaces tend to wear quicker than smooth surfaces. An increase in roughness value promotes the corrosion as the irregularities in surface texture may form nucleation sites for crack and corrosion.

2.1.2. Adhesion

Adhesion is the phenomenon that occurs when dissimilar particles or solid surfaces are brought into contact. Surface roughness governs the contact at discrete contact spots, and interfacial adhesion takes place. A finite normal force, which is known as adhesive force, is required for adhesion or bonding across the interface. Adhesion is different from cohesion. Atomic bonding forces associated within the same material is known as cohesion. On the other hand, adhesive bonds resulting from bringing two dissimilar (or even the same) materials into solid state contact with an interface is referred to as adhesion. Adhesion occurs in solid-solid contacts with or without the presence of a liquid (i.e. lubricated surfaces). Generally, the presence of thin films of lubricants and contaminants reduces the adhesion between the solid surfaces; however, in some cases the opposite may happen.

Depending upon the engineering application, adhesion can be either desirable or undesirable. Machineries involving sliding and rotational mechanism, adhesion is undesirable as adhesion results in friction and wear. In some application like transportation system, controlled adhesion is required.

2.1.3. Friction and friction mechanisms

Friction is an important phenomenon in physics and engineering with a great practical significance [2]. Friction is the resistance to motion, which is experienced in relative motion of solid surfaces, liquid layers, or material elements in contact. The resistive tangential force is the friction force. Dry friction, as the name implies, describes the friction between two solid surfaces. The quantitative properties of friction between solid surfaces are generally subject to Amontons-Coulomb's laws of friction (sometimes called "Coulomb's laws"). The first law states that the friction force between the surface of two bodies is directly proportional to the normal load with which the two bodies are pressed together. The proportionality constant is the COF. The COF

between two sliding surfaces is defined as the ratio of the frictional force (F_f) between them and the normal force, N (the force pressing them together), $COF = \frac{F_f}{N}$.

According to the second law, the friction force and the COF do not depend on the apparent (or nominal) area of contact between the contacting bodies. This is because the contact occurs only on the tops of the asperities, and the real area of contact is only a small fraction of the apparent area of contact. The third law governs the kinetic friction, and it states that the friction force is independent of the sliding velocity. Amontons-Coulomb's laws of friction are just empirical approximations and are not theoretically justified propositions. In many cases, especially at the micro- and nanoscale, Coulomb's laws of friction are not valid. In particular, the friction force and the COF are not always independent of the apparent area of contact [3]. Several experimental results have also established that the COF is dependent on the size (macroscale vs. micro/nanoscale), load, and sliding velocity [4-5].

Friction is a complex phenomenon, with several mechanisms contributing to it. Adhesion and deformation have the most significant contributions to the overall friction force. The widely accepted theory of friction mechanisms was proposed by Bowen and Tabor [6]. They proposed that for sliding contacts, friction mechanisms have two components: interfacial adhesion between asperities and asperity deformation (ploughing) at the real areas of contact between the surfaces (known as asperity contacts). There is negligible interaction between the adhesion component (F_a) and the deformation component (F_d) of friction and the total friction force (F) can be presented as the sum of these two friction components, $F = F_a + F_d$.

Adhesion occurs when dissimilar particles or solid surfaces are brought into contact under a certain normal loading condition or a combination of normal and shear loads. The molecular

forces between the surfaces cause adhesion between them. The interaction force between the solids due to adhesion can be caused by the covalent, ionic, metallic, or van der Waals bonds. When two surfaces are placed in contact under load, the tip of the asperities of the two mating surfaces form the real area of contact. The physical and chemical interactions between the asperities result in adhesion at the interface [1]. The adhesion component F_a of the friction force is proportional to the real area of contact (A_r) and to the shear strength (τ_a) of the material. The friction force for a dry contact due to adhesion is defined as $F_a = A_r \tau_a$.

The deformation component of friction is caused by both microscopic and macroscopic deformation. At the microscopic level, the displacements of the interlocked surfaces occur through the plastic deformation of the asperities. Asperities of the harder material plow grooves in the softer material. Surface roughness and relative hardness of the two surfaces greatly influence the deformation component of friction. Reducing surface roughness reduces F_d . To maintain motion in the deformation process, the lateral force equal or exceeding F_d is required. For perfectly smooth surfaces, no groove is produced through the deformation of the contacting bodies in sliding. In case of plowing, the shear strength of the material is proportional to the average value of the surface slope [7]. During plowing, wear particles of various sizes are generated.

Depending upon the application, friction can be desirable or undesirable. For automobile tires on roadways, in vehicle clutch and braking systems and in frictional transmission of power (i.e., v belt drives), friction is desired. However, in most other machine assembly, where rotating, rolling and sliding contacts are expected, friction is undesired (i.e., bearings and seals). Loss of energy and wear the common consequence of friction in these cases.

2.1.4. Wear and wear mechanisms

The surface damage or removal of material from one or both sliding surfaces due to friction is known as wear. The wear mechanism governs the progressive removal of material from the surfaces sliding against one other taking place under different loading conditions. Adhesive, abrasive, delamination, and fatigue wear are the most common wear mechanisms. The wear mechanisms in monolithic materials can be significantly different from those of composites and multi-phase materials.

Adhesive wear is caused due to the adhesion between the mating surfaces during sliding contact. As the atoms from different surfaces come in contact due to the applied load, short-range forces (covalent bonding forces) act among them. Consequently, adhesive junctions are formed at the spots of the real area of contact. These adhesive junctions are sheared when sliding is initiated. Due to the fracture and plastic deformation during extensive shearing, material transfer from the softer to the harder surface takes place. In this form of wear, extended sliding produces loose wear debris.

In delamination wear, the accumulation of dislocations causes subsurface cracking at a certain depth under the tribosurface as the surface is deformed. Frictional and material properties, and tribological parameters govern the crack initiation and propagation at the subsurface region. Under repeated loading, an unstable propagation of a crack takes place once it exceeds a critical length, and a thin laminate of the softer material is generated as wear debris. Besides these two forms of wear, abrasive wear is observed in materials while sliding against a much harder counterface. Several forms of plastic deformation: cutting, plowing, and wedge formation of the asperities of the softer surface take place in abrasive wear.

Archard and Hirst suggested that there are two mechanisms of sliding wear, and they depend upon the normal load [8]. When the normal load is below a critical value, the wear regime

is known as mild. The mild wear mechanism is steady and involves oxidation of material during sliding contact. For a normal load above the critical value, the wear mechanism is considered severe. This wear mechanism involves adhesive wear and delamination as significant material removal and surface failure take place. The critical load at which the transition from mild to severe wear occurs is known as the transition point which is characterized by a sudden increase in wear rate. A higher transition point is preferred for MMCs in engineering applications.

Wear regimes of various materials are often characterized by so-called wear maps, where a particular mechanism of wear is typically presented as a function of two variables: the normal pressure and sliding velocity. They provide an instantaneous and convenient approximation of general wear pattern in a wide range of tribological interactions.

2.1.5. Lubrication and lubrication regimes

Lubrication is an important concept of tribology. For the contact of fluid-lubricated surfaces, different lubrication regimes define the frictional behavior. The effect of liquid lubrication on friction is usually analyzed with the so-called Stribeck curve (**Figure 2.1**) which summarizes different fluid lubrication regimes. Typically, the coefficient of friction (COF) is plotted against the Hersey number [9], a dimensionless lubrication parameter, which is the product of absolute viscosity, η , and sliding speed, V , divided by the normal load, P . Large values of the Hersey number correspond to hydrodynamic lubrication regime, when liquid viscosity is the main factor supporting the load. Small values of the Hersey number correspond to the boundary lubrication with a nanoscale or molecular layer of the lubricant exists. The plot presents the COF between the two fluid-lubricated surfaces as a function of a dimensionless Hersey number [9].

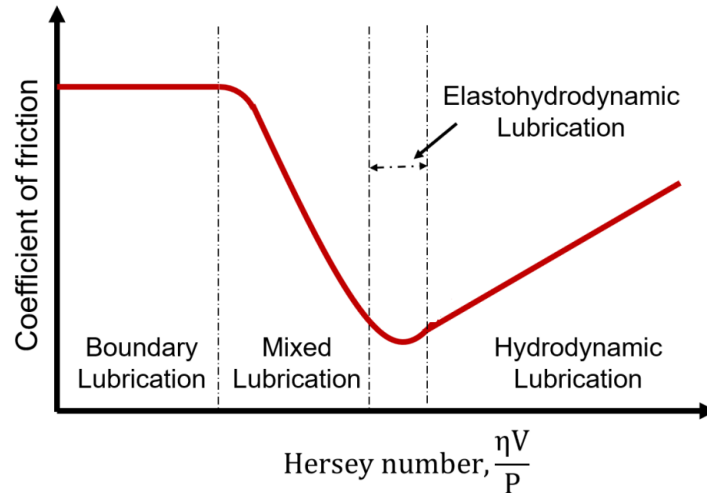


Figure 2.1. Lubrication regimes in Stribeck curve

Four distinct lubrication regimes are shown in the Stribeck plot: the hydrodynamic, elastohydrodynamic (EHD), mixed, and boundary lubrication. These regimes are characterized by different friction and wear behavior. For the hydrodynamic lubrication regime, the lubricating films between sliding surfaces are stable and thicker than the height of the asperities or irregularities. No direct contact among the asperities of the mating surfaces occurs in this regime, which is often considered as the ideal lubricating condition in sliding applications. Since the lubricating film supports almost the entire normal load, friction and wear are low. However, adhesive wear is noticed at the initiation and at the ending of sliding.

The elastohydrodynamic lubrication regime is found for heavily loaded contacts where elastic deformation of the mating surfaces shapes the HDL process [1]. Deformation changes the geometry of the contacting surface which affects the film formation and overall lubrication process. Like HDL, the normal load is supported almost entirely by the lubricating film although the film thickness is notably thinner in EHD. Adhesive wear at the beginning and ending of sliding, corrosion, and fatigue are some common forms of wear mechanism noticed in EDL regime.

The mixed lubrication regime occurs at a low sliding speed and higher load or temperature where the lubricant viscosity is notably reduced. With further increased normal load combined with lower sliding speed and reduced viscosity of the lubricant, the boundary lubrication regime is observed. Due to the absence of any stable lubricating film between the sliding surfaces, the normal load is entirely supported by extensive asperity contact. Consequently, this lubrication regime is characterized by a high COF and wear rate. For composites and self-lubricating materials, such as the Al/Gr MMC, the Stribeck curve can be significantly different, because in the limit of moderate and absent lubrication, the solid lubrication prevails over other mechanisms.

2.2. Wetting

Wetting can be defined as the ability of liquids to form interfaces with solid or liquid surfaces. This section will focus on the basic concepts of wetting, for example, wettability, contact angle, contact angle hysteresis, and wetting states.

2.2.1. Wettability, Contact Angle, and surface types

The conventional way of quantitating the wettability of the surface by the liquid is the contact angle (CA) between a liquid and a solid surface. When there exists an interface between a liquid and a solid, the angle measured through the liquid where the liquid-vapor interface meets the solid is known as the contact angle. The smaller the contact angle, the greater the degree of wetting. When the contact angle is 0° , maximum wetting occurs and is known as spreading. Contact angle between 0° to 90° , the solid is wettable and above 90° it is not wettable.

A surface that is wetted by water (CA less than 90°) is known as a hydrophilic surface. Contact angle more than 90° refers to a hydrophobic surface which is characterized by a reduced contact area between the solid surface and a water droplet. CAs higher than 150° are for superhydrophobic

surfaces (**Figure 2.2**), which have further reduced contact area between the solid surface and the liquid droplet.

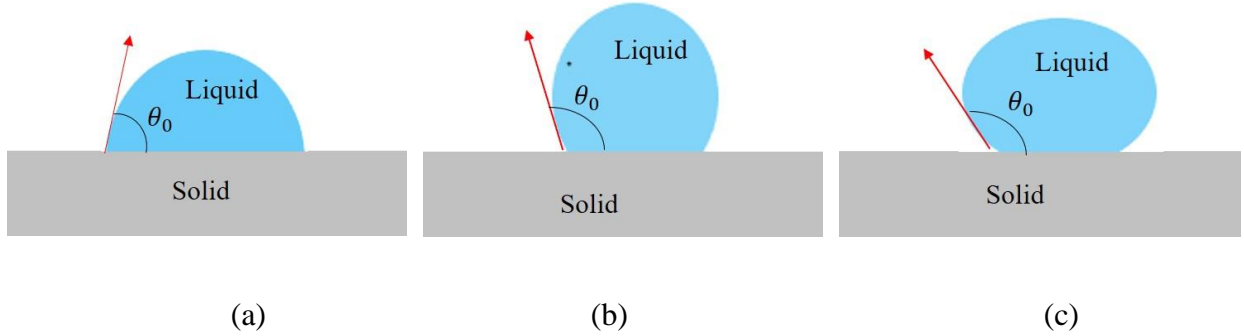


Fig.2.2. (a) hydrophilic surface ($CA < 90^\circ$) (b) hydrophobic surface ($90^\circ < CA < 150^\circ$) (c) superhydrophobic surface ($CA > 150^\circ$)

2.2.2. Models of wetting and wetting mechanisms

In the ideal situation, for a perfectly smooth and homogeneous surface, the wetting mechanism can be described by the Young equation. According to Young, the equilibrium value of the most stable contact angle (CA), θ_0 is expressed by the following equation [9].

$$\cos\theta_0 = \frac{\gamma_{sv} - \gamma_{sl}}{\gamma_{lv}} \quad (1)$$

where γ_{sv} , γ_{lv} , and γ_{sl} are the surface tension forces (or interfacial energies) of the solid-vapor, the liquid-vapor and the solid-liquid interfaces respectively acting on the contact line.

However, Young equation cannot explain the wetting mechanism of rough, chemically heterogeneous solid surfaces properly. The observed contact angles for such surfaces are much different from θ_0 , [10] predicted by Young equation. Two wetting states: the Wenzel [11] state and Cassie-Baxter [12] state explain the effect of surface roughness and chemical heterogeneity on contact angle. Wenzel proposed the equation for finding the apparent contact angle on a rough

but chemically homogeneous surface. According to the Wenzel, the apparent contact angle θ_w which incorporates with the stable equilibrium state of a rough surface is given by

$$\cos\theta_w = r\cos\theta_0 \quad (2)$$

Here, r is termed as the roughness factor which is the ratio of the “actual surface” to the superficial or “geometric surface”. The “actual surface” is the total solid surface area and the “geometric surface” is the surface area measured in the plane of the interface. For a smooth surface $r = 1$ and for rough surfaces $r > 1$. From equation (2), it is observed that roughening the surface (increasing value of roughness factor, r) yields dissimilar effects for hydrophobic and hydrophilic surfaces. Roughening a hydrophobic surface makes it more hydrophobic (i.e., an increase in contact angle) and roughening a hydrophilic surface makes it more hydrophilic (i.e., a reduction in contact angle). The Wenzel wetting state is known as complete homogeneous wetting as the surface below the droplet is completely wetted by the liquid and thus creates a homogeneous solid liquid interface. The Cassie-Baxter state extends Wenzel’s analysis and explains the wetting mechanism of heterogeneous surfaces (i.e., composite material surfaces). According to this model, interfacial heterogeneities affect wetting as the apparent contact angle changes when composite materials are involved. According to Cassie-Baxter state, the apparent contact angle, θ_c for a smooth but chemically heterogeneous surface consisting of N components is expressed by the following equation

$$\cos\theta_c = \sum_{i=1}^N f_i \cos\theta_i \quad (3)$$

Where, f_i is the fraction of the solid surface area wetted by the liquid and θ_i is the equilibrium contact angle. When tiny air pockets are trapped between the solid surface and the liquid droplets,

the interface formed by the solid, liquid and air pockets becomes non-homogeneous. In the Cassie-Baxter state, the apparent contact angle (θ_c) is measured using the following equation.

$$\cos\theta_c = r_f f_{SL} \cos\theta_0 - 1 + f_{SL} \quad (4)$$

Here, r_f is the roughness factor which is the ratio of the total solid-liquid surface area to the projected solid-liquid surface area, f_{SL} is the fractional solid-liquid interfacial area and θ_0 is the equilibrium contact angle. f_{SL} ranges between $0 \leq f_{SL} \leq 1$ and the equation is valid when air pockets are formed and liquid penetration into the air pockets doesn't take place. [13]. If the air cavities on the surface are filled by the liquid (known as "impregnating" Cassie wetting regime), the apparent contact angle is given by

$$\cos\theta_c = 1 + f_{SL}(\cos\theta_0 - 1) \quad (5)$$

2.3. Triboinformatic approaches

Triboinformatics can be defined as an application of ML and other data-centric methods of data analysis to tribological problems, such as establishing relationships between material and surface structure and properties and the tribological performance.

2.3.1. Machine learning analysis

ML is a data-driven analysis, which utilizes the idea that a model can learn from newly acquired data, similar to how humans learn from experience. ML algorithms use the learning experience to recognize patterns, establish correlations, and make decisions without extended programming and human intervention.

ML approaches are particularly effective for solving problems where there are numerous potential answers, but no fully satisfactory models are available to label the correct answers. In

such cases, ML models can be trained with the available data to establish correlations among variables, refine the model from the learning experience, and find correct answers. ML has been successfully implemented in solving complex real-world problems in diverse areas ranging from trade and commerce to medical sciences, to face and pattern recognition, to materials behavior prediction, and in many other areas.

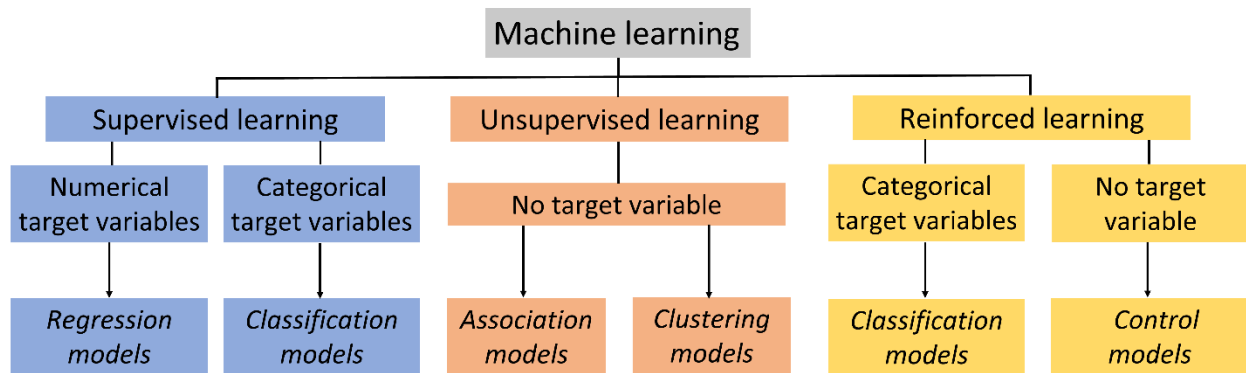


Figure 2.3. Machine learning algorithm types

ML algorithms are roughly classified into three general categories: *supervised* learning, *unsupervised* learning, and *reinforced* learning (**Figure 2.3**). Supervised learning algorithms which are often considered the most successful ML algorithms can automate the decision-making process through learning from training examples. For example, the coefficient of friction and wear rate could be the outputs and the material variables are the inputs. In supervised learning, first, the model is trained with examples where the output is known for a particular set of input variables. From these training examples, the model effectively learns about the input-output relation and develops a prediction scheme for any new set of input variables. Such supervised algorithms can be used in developing *regression* and *classification* models. Regression models are used to predict numerical or continuous outputs, for example, predicting the wear rate of a material from material

variables. Classification models are used to predict categorical or discrete outputs, for example, predicting the wear mechanism.

On the contrary, in *unsupervised* learning, the algorithms are provided with only input data with no known output data or target variables. The algorithms exhibit self-organization and learn to identify patterns using data that are neither known nor labeled. Consequently, the unsupervised ML algorithms are more complex to visualize and evaluate in problem-solving. Mapping and clustering wear zones depending on the sliding speed and load during sliding interactions are an example of unsupervised learning problems.

In reinforcement learning, the model is trained to make a sequence of decisions through trial and error. For example, reinforcement learning is used to train a self-driving car. In the training process, the ML model selects different options to perform a task and receives feedback. The feedback is provided through predefined award and punishment functions. If a selected option is beneficial to achieve the goal, a reward is assigned and vice versa. The model thus learns through its own actions and corresponding feedback and optimizes its actions for minimizing punishments and maximizing rewards. Reinforcement learning can be applied in experimental modeling, manufacturing process modeling, and optimization.

The selection of the ML algorithms and the development of ML models depend on the problem to be solved, the goal of the problem-solving, and the available data. In this section, we present a brief description of different types of ML models successfully implemented in problem-solving involving tribological structure-property relationships in metals and composites.

2.3.1.1. Artificial Neural Network (ANN)

ANN is by far the most popular ML algorithm used in tribological studies [14-16]. ANN is an advanced ML algorithm that can mimic the learning process of a human brain and can be used in supervised, unsupervised, and reinforced learning. Through billions of neurons and synapses, the human brain forms a complex network that can process information, learn from past experiences, and generate meaningful decisions from these processes. ANN uses a similar data processing technique having a large number of interconnected processing units (**Figure 2.4**). With the processing network, ANN models map the input-output relation from the training examples and use that to predict outputs for new input variables.

Generally, the structure of an ANN model consists of an input layer, multiple hidden layers, and an output layer. A large number of neurons or intermodal units in the hidden layer between the input and the output layers convert the data of the previous layer using a predefined activation function and pass it to the next layer. Backpropagation or feed-forward networks are selected for the multilayer perceptron (MLP) to develop the ANN model. Optimized performance of ANN models is generally ensured by adjusting the regularization parameter, activation function, number of hidden layers, and the number of neurons in each layer. ANN is an efficient algorithm for handling complex non-linear relationships with a big-data framework. Though several studies have shown that it can be satisfactorily adjusted for a small dataset [17], still its predictive performance for small datasets is often considered as its limitation.

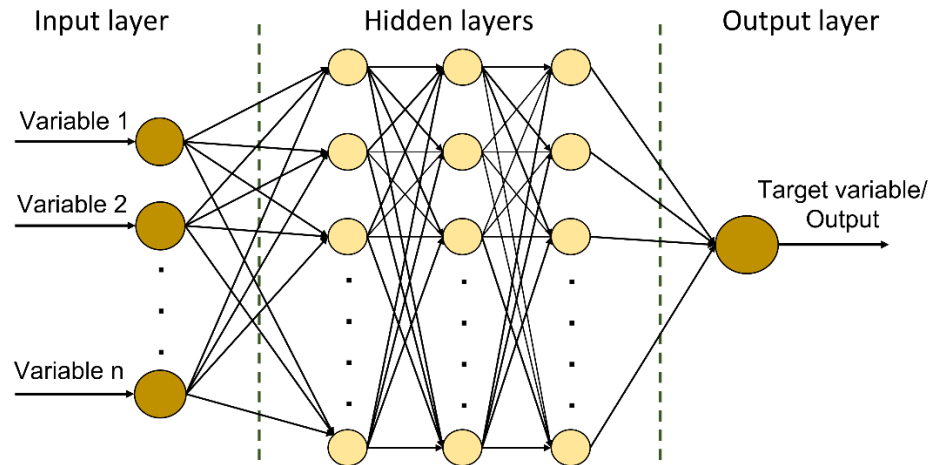


Figure 2.4. The architecture of a feed-forward multilayer perception of an ANN model

2.3.1.2. *K-Nearest neighbor (KNN)*

KNN is a popular supervised ML algorithm used for both classification and regression analysis. This comparatively simple ML algorithm utilizes a non-parametric statistical method to develop a prediction model. The prediction for a new data point is based on a distance function and KNN predicts the output based on the closest data points (neighbor) in training data. Distance-based weights can be assigned for each neighboring point to make sure that the nearest points are contributing more than the distant points in the overall prediction. The number of nearest data points ($n_neighbors$) that are considered for deciding the result for a new point is an important parameter in developing a KNN model. A poor generalization behavior for a new data point due to overfitting is observed for a small “ $n_neighbors$ ”. On the contrary, the model may fail to address the sensitivity of a new data point due to underfitting for a large “ $n_neighbors$ ”. The proper adjustment of “ $n_neighbors$ ” ensures the optimized model performance for KNN models. The “weight” of the distance function is another important optimization parameter for KNN models. Some strengths of the algorithm include easier understanding, simpler modeling, and reasonable performance with minimum parameter adjustments. The inability of handling many features, weak

performance in depicting complex correlations, and a slow processing speed for a large dataset are some of the limitations associated with this algorithm.

2.3.1.3. Support vector machine (SVM)

SVM is a popular supervised learning algorithm known for its excellent performance for a small dataset with a large number of input variables. Though SVM is more common in solving classification problems, it also performs satisfactorily in regression problems. Arranging data in the hyperplanes are performed through different kernel functions including the linear kernel, polynomial kernel, sigmoid kernel, and radial basis function (RBF) kernel. The ability to define hyperplanes in high-dimensional input space allows the kernelized SVM to solve non-linear complex problems effectively. RBF kernel is popular in developing SVM models for both classification and regression. Kernel coefficient (γ) and the regularization parameter (C) are the two highly correlated parameters that regulate the complexity of these models and are adjusted concomitantly to ensure optimized model performance. However, SVM often underperforms in handling a large dataset, especially with the presence of noise and outliers in the data.

2.3.1.4. Random Forest (RF)

RF is a powerful ensemble algorithm that combines the prediction capacities of multiple prediction or decision-making units known as decision trees. A decision tree is a decision-making or prediction unit that employs a tree-like structure. As the name suggests, RF uses a collection of decision trees to develop the prediction model. Each decision tree is unique and works on a small portion of the data. The individual trees make effective prediction results with that small portion of the data. However, developing decision trees with a small portion of the data can cause the overfitting

problem in the presence of outliers and noise in the data. Overfitting is a situation when a prediction model fits precisely against a small number of training data and hence fails to provide accurate prediction for new data due to poor generalization capacity.

The overfitting problem associated with a single tree is overcome in RF using the “bagging mechanism” in which the results of all decision trees are averaged to generate the final result. Unlike the GBM algorithm, RF incorporates randomness in the decision tree-building process that retains the uniqueness of the decision trees. The model complexity largely depends on the number of decision trees or `n_estimators` and the number of features in splitting or `max_features`. Feature scaling is optional, and RF performs satisfactorily even without a proper parameter optimization. RF is a popular choice in both regression and classification problems in all fields and can handle large datasets with outliers and many input variables efficiently [18]. Weak prediction performance for very complex, high dimensional, and sparse data is considered a limitation of the RF algorithm.

2.3.1.5. Gradient boosting machine (GBM)

GBM is a powerful ensemble algorithm that uses decision trees as the building block. This is a popular algorithm for both classification and regression problems and it often exhibits better performance than other ML algorithms with the same data. In this tree-based algorithm, each tree works on a small portion of the data and the optimization of the arbitrary loss function are done for each of them which is popularly known as the “boosting mechanism”. In different stages of tree-building in GBM regression algorithms, decision trees are adjusted to the negative gradient of the loss functions [18]. In an iterative process, collectively, the decision trees of GBM models, provide strong predictive performance. Unlike the RF algorithm, decision trees are not randomized in GBM, instead, they are pre-pruned in a serial manner. In this way, mistakes in the tree-building

of previous steps are corrected in the next tree. This feature along with the “boosting mechanism” enables the GBM algorithm to adapt with higher-order complex correlations existing in the data. For GBM, the number of boosting stages (`n_estimators`) and the learning rate are the most important optimization parameters to optimize the model complexity. Feature scaling is considered optional for GBM although feature scaling makes the model more sensitive to parameter tuning. Its ability to use very shallow decision trees to develop the prediction model makes it efficient in terms of memory utilization and speed. However, the sensitivity of this algorithm towards outliers present in the data is considered a limitation of GBM.

2.3.1.6. Principal component analysis (PCA)

PCA is an unsupervised learning algorithm popularly used in the visualization of higher-dimensional data. It is well known for dimensionality reduction where numerous variables are transformed into a small number of uncorrelated variables preserving almost the entire information of the data. In this algorithm, the new variables or the features possess no statistical correlation as the actual dataset is rotated accordingly. The first principal component is a linear combination of variables presenting the maximum variance in the data. Similarly, the second principal component presents the maximum possible remaining variance while having no correlation with the first principal component. Using these two components, a dimensionally reduced visual representation of the high dimensional dataset is possible. The accuracy of the PCA models can be adjusted to a permissible level but the loss of information during the dimensionality reduction is considered as a limitation. However, PCA offers the extraction of the relevant features from a large multivariable dataset. The extracted features can also be used as inputs for other supervised ML algorithms in solving complex problems.

2.3.1.7. Hybrid and ensemble models

Hybrid and ensemble models are developed through the integration of multiple ML algorithms by soft computing and following certain optimization techniques [19]. The goal is to enhance the predictive performance by overcoming the limitations of a standalone algorithm while utilizing its strength. In the hybridization process of two standalone algorithms, often one unit develops the input-output prediction frame, and the other unit is responsible for its optimization for achieving superior accuracy in output prediction. Though organizing the standalone algorithms properly and optimizing the hyperparameters can be more complex in hybrid and ensemble models, they often yield better predictive performance for complex datasets.

2.3.2. Triboinformatic studies of metals and composites

This section discusses different variables affecting friction, wear, and surface properties of metals alloys, and MMCs and present studies where ML models have been used to predict these properties.

2.3.2.1. Typical variables affecting friction, wear, and surface properties

In traditional tribological studies, friction, wear, and surface properties are often presented as functions of a single variable considering several others as constant [20,21]. This approach is useful for simple and prompt visualization of the effect of a single variable on the output. However, this approach is too simplistic to get an accurate prediction of the tribological and surface properties. Friction, wear, and surface properties of metals, alloys, and metal matrix composites depend on numerous variables and factors. Intrinsic properties of a material, for example, density, hardness, or tensile strength, are closely related to the manufacturing process, for example, material processing techniques and heat treatment can be recognized as material variables. Sliding

speed, sliding distance, normal load, counterface, lubrication condition, and tribological testing methods are considered tribological variables.

Friction and wear have complex mechanisms and share complex, higher-order relationships with material variables and tribological test conditions. The friction and wear mechanisms for metals and monolithic alloys can also be significantly different from those of multi-phase MMCs [1,6,8]. For example, unlike the base aluminum alloys, in the graphite reinforced aluminum MMCs, the formation of a self-lubricating graphite film from the smeared graphite particles dictates the friction and wear mechanisms [22].

Kumar et al. [23] used surface methodology response (RSM) and ANN models to analyze the surface roughness properties of Al 7075 hybrid composites. They reported that multiple variables of the machining process including feed rate, speed, and approach angle have a significant impact on the average surface roughness of these composites. Radhika and co-workers [24] used pattern recognition-based RF models to predict the surface roughness of hybrid aluminum MMCs. They considered multiple variables of the turning process including feed, speed, depth of cut, and flank wear to successfully predict the average roughness of the hybrid MMCs.

These studies suggest the importance of multivariate analysis for a reliable prediction of friction, wear, and surface properties. Data-driven, multivariate, ML models incorporating strong prediction algorithms can not only predict the tribological and surface properties with a satisfactory accuracy but are also capable of generating novel perceptions about them.

2.3.2.2. Tribological and surface property prediction for metals and metallic composites

The study by Jones et al. [25] was one of the first applications of an ML algorithm in wear volume prediction for metal and alloys. They collected experimental tribological data for rub shoe,

pin-on-disk, and four-ball test methods for various materials including different grades of steel and polymers from different sources to develop ANN models to predict the wear volume. They used load, speed, sliding distance, temperature, friction coefficient, and kinematic viscosity as the input variables. Despite having some limitations, such as a small dataset (55 datapoints) and fewer variables as the inputs, this preliminary study reported promising results and inspired future studies of ML in tribological behavior prediction.

Zhang and co-workers [26] developed ANN prediction models for the specific wear rate and the coefficient of friction for short fiber reinforced polyamide composites. They used matrix volume, fiber volume, PTFE volume, compression modulus, compression strength, hardness, fracture toughness, temperature, normal force, and wear speed as the input variables in a 3-layer feed-forward ANN model with a tan-sigmoid transfer function. Despite using a small dataset of 103 datapoints of experimental wear measurements, these models could predict the output satisfactorily ($R^2 > 0.9$).

Genel et al. [27] developed ANN models to predict the specific wear rate and friction coefficient of alumina fiber reinforced zinc-aluminum matrix composites. They considered applied load, fiber volume fraction, and orientation of fiber as the input variables for the multilayer feed-forward ANN models. They determined the mean relative errors (MRE) for the prediction models and reported the accuracy of 94.2% and 99.4% in specific wear rate and friction coefficient prediction. However, they used only 44 experimental data as the dataset and only three variables as input. Rahimipour et al. [28] developed an optimization model with ANN to optimize the manufacturing process of boron carbide reinforced aluminum-copper MMCs to achieve a high wear resistance. They considered the cooling rate, temperature gradient, volume percentage, and average particle size of boron carbide as the optimization parameters for the output of porosity and

wear loss. They reported 10 C/Sec, 100,000 C/m, and 20.1% as the optimized cooling rate, temperature gradient, volume percentage of boron carbide, respectively, from the model.

Besides the above-mentioned studies, several others also pursued ML and Triboinformatic approaches in surface and tribological behavior prediction and optimization of metals, alloys, and composites [29-35]. **Table 2.1** presents a list of such studies in which ML models have been implemented.

Table 2.1: Overview of the application of ML approaches in friction, wear, and roughness prediction of metal, alloys, and composites

Material	Dataset details	Input variables	Outputs	ML models	Prediction performance Metrics	References
Steel, polymers, and other metals	A collected dataset of 55 wear volume measurements (training set: 43, test set: 12)	load, speed, sliding distance, temperature, friction coefficient, and kinematic viscosity	wear volume	ANN regression (backpropagation, dampened recurrent, and jump connections)	Coefficient of determination (R^2) $0.63 < R^2 < 0.97$	Jones et al. [25]
PA46 (Nylon 46) reinforced with glass or carbon fibers, PTFE and/or Graphite	A dataset of 72 wear volume measurements (training set: 62, test set: 10)	compressive strength, compression modulus, contraction to failure, tensile strength, strain to failure, impact strength, testing temperature, starting load, average load, average velocity	wear volume	ANN regression model (3-layer feed forward neural network)	Coefficient of determination (R^2) $0.6 < R^2 < 0.8$	Velten et al. [16]

Short fiber reinforced polyamide 4.6 (PA4.6) composites	A dataset of 103 wear measurements (training set: 88, test set: 15)	matrix volume, fiber volume, PTFE volume, compression modulus, compression strength, hardness, fracture toughness, temperature, normal force, and wear speed	Specific wear rate, COF	3-layer feed forward ANN regression model with tan-sigmoid transfer function	Coefficient of determination (R^2), $R^2 < 0.9$	Zhang et al. [26]
Alumina fiber reinforced zinc–aluminum composites	Separate datasets of 44 wear and friction measurements (training set: 32, test set: 12)	Applied load, fiber volume fraction, and orientation of fiber	Specific wear rate and friction coefficient	multiple-layer feed-forward ANN regression	Mean relative error (MRE), MRE = 5.8% for wear rate, MRE = 0.6% for COF	Genel et al. [27]
Boron carbide-reinforced aluminum-copper composites	Optimization problem to select the input variables	Cooling rate, temperature gradient, volume percentage, and average particle size of B4C	Porosity, wear loss	3-layer back propagation ANN optimization model	Root mean squared error (RMSE), Optimized RMSE = 0.09	Rahimipour et al. [28]
Tungsten reinforced copper composites	Experimental dataset of 180 datapoints, training: 126, validation: 27, test: 27	W wt.%, sintering temperature, sliding distance, and load	Specific wear rate and COF	ANN regression model (RBFNN)	Correlation coefficient (R), R= 0.976452 (wear rate), R= 0.96571 (COF)	Leema et al. [29]
SiC reinforced Al 2219 composites	81 datapoints, training set: 49, validation set: 16, test set: 16.	Weight percent of SiC, sintering temperature, normal load, and speed	Wear, friction force, temperature rise of pin	ANN regression model (feed forward back propagation)	Correlation coefficient (R) and MSE, wear (MSE=0.0017, R=0.7149), friction force (MSE=2.68218, R=0.8175), temperature rise of pin (MSE=2.97357, R=0.9138)	Radhakrishnan et al. [30]

Hybrid copper composites	27 experimental datapoints (training: 24, validation: 3)	Volume percentage, load, sliding velocity, sliding speed	Wear rate	ANN regression (feed forward back propagation)	Mean absolute error (MAE), MAE < 3.41%	Thankachan et al. [31]
SiC reinforced aluminum composites	27 experimental datapoints (training: 19, validation: 4, test: 4)	applied load, experiment time, and SiC wt %	Wear (%)	ANN regression (Back propagation)	Mean squared error (MSE), MSE = 2.0×10^{-4}	Idrisi and Mourad [32]
Al ₂ O ₃ reinforced Al7075 MMCs	1080 datapoints (training set: 898, test set: 182)	Density, Al ₂ O ₃ wt.%, load, and sliding distance	Wear height loss	ANN regression (Back propagation)	Mean squared error (MSE) = 4.6563, Correlation coefficient (R) = 0.99908	Pramod et al. [33]
Al/SiC/Gr hybrid composites	27 experimental datapoints (training: 70%, validation: 15%, test: 15%)	sliding speed, normal load, and graphite addition (wt.%)	Wear rate, COF	ANN regression (feed forward back propagation)	Regression coefficient (R) = 0.98905	Stojanović et al. [34]
SiC reinforced Al 7075 composites	Experimental dataset of 160 datapoints, training set: 120, validation set: 20, test set: 20	feed rate, speed, and approach angle	Surface roughness	surface methodology response (RSM) and ANN (feed forward back propagation)	Regression coefficient (R), Mean squared error (MSE), R = 0.9972 (RSM), R = 0.99571 (ANN), MSE = 0.0022678 (ANN)	Kumar and Chauhan [23]
9SMnPb28k (DIN) machining steel	Experimental dataset of 30 datapoints, training set: 27, validation set: 3	feed rate, cutting speed and depth of cut	average roughness (Ra) and maximum peak to valley height (Rt)	ANN regression (back propagation)	Mean absolute error (MAE), MAE < 28.29% (Ra), MAE < 8.91% (Rt)	Davim et al. [35]

2.3.3. Topological data analysis (TDA)

Topological data analysis (TDA) is another method that belongs to the Big Data paradigm which has been applied for surface roughness analysis. TDA is an approach to the analysis of multi-dimensional datasets using techniques from topology, an area of geometry concerned with the properties of objects that are preserved under continuous deformations. The traditional analysis of surfaces involves their characterization of a single or a limited number of parameters. Such analysis often comes short in characterizing surfaces with complex topographies.

From the physics point of view, dry friction is a collective phenomenon characterized by a dramatic reduction of the number of degrees of freedom (e.g., corresponding to individual asperity contacts) to a small number of macroscale degrees of freedom. However, traditional approaches, such as thermodynamic methods, do not always explain friction because it is a thermodynamically non-equilibrium process. In this situation, computational methods of reduction of degrees of freedom (e.g., principal component analysis) may be useful. TDA is one of such methods, which has been successfully applied to the analysis of visual images.

A rough surface is a complex object, and it is often difficult to completely characterize surface roughness with one or several parameters. Such parameters may be different for different applications. Thus, the traditional tribological surface roughness parameter, R_a , or the mean deviation of the rough profile is not applicable to the studies of wetting of rough surfaces and superhydrophobicity, where other parameters, such as the Wenzel roughness factor, R_f , are used [36]. Moreover, different surfaces may need different parameters even for the same application; thus, the same value of R_a , which only characterizes the height of surface asperities, may correspond to surfaces with very different horizontal surface roughness features. In general, a rough surface is characterized by an infinite number of parameters that can be represented as belonging to certain high-dimensional data space. TDA is used for dimensionality reduction of

complex higher-dimensional surface property data and inferring relevant features and properties of the underlying surfaces [37]. The difference between the PCA and TDA methods is that the latter concentrate on topological features (such, for example, as multidimensional holes) rather than on finding principal components.

2.3.3.1. Data topology of visual images

The TDA analysis of 2D surface roughness profiles is based on the analogy with visual images consisting of pixels of various brightness, which corresponds to the height of the rough profile. Natural images captured by a digital camera are represented as vectors of pixels in a very high dimensional vector space with each dimension corresponding to one pixel [38]. Lee et al. [39] suggested that images can be effectively processed by breaking them down into small pixel patches and extracting useful information through dimensionality reduction. They worked on the database of black and white images collected by Van Hateren et al. [40] and considered 3×3 pixel patches within the images. Each patch was represented by one value of contrast, and the 3×3 patches were viewed as arrays of pixels in a 9D dataspace. Through the normalization of the data, the probability distribution of the contrast gradient could be identified from the gradual change in contrast in the high and low contrast patches.

The distribution of patches in the dataspace was not random. It turned out, that patches with either sharp (i) horizontal or (ii) vertical features dominated over those inclined under an arbitrary angle, while (iii) gradual change of brightness (in any direction) dominated over random features. Depending on the directionality in the isotropic contrast gradients, data points tended to organize in parametrically specified nonintersecting primary and secondary circles (one primary circle corresponding to a gradual change of brightness in any direction and two secondary circles corresponding to the horizontal and vertical features) in the 9D or 8D data space (**Figure 2.5**).

Carlsson et al. [38] further reported that the organization of data in primary and secondary circles in the study of Lee et al. [39] can be considered topologically equivalent to the Klein bottle formation.

Singh et al [41] studied the cell arrangement architecture in breast cancer histology images using TDA and proposed a framework of using this approach in extracting the geometric features inherent in tumor cell arrangements. They developed classifiers where they employed Betti numbers as means to extract relevant features from the images and differentiate various subtypes of cancer. They reported an accuracy of 69.86% of their TDA based classifier which was impressive compared to other alternative methods. Dey et al. [42] also used topological persistence analysis to develop models to improve image classification techniques. Vandaele and co-workers [43] further developed TDA based methods for Topological Image Processing (TIP) and Topological Image Modification (TIM) to detect objects. They presented a case study using skin lesion images to demonstrate the effectiveness of their TDA based model.

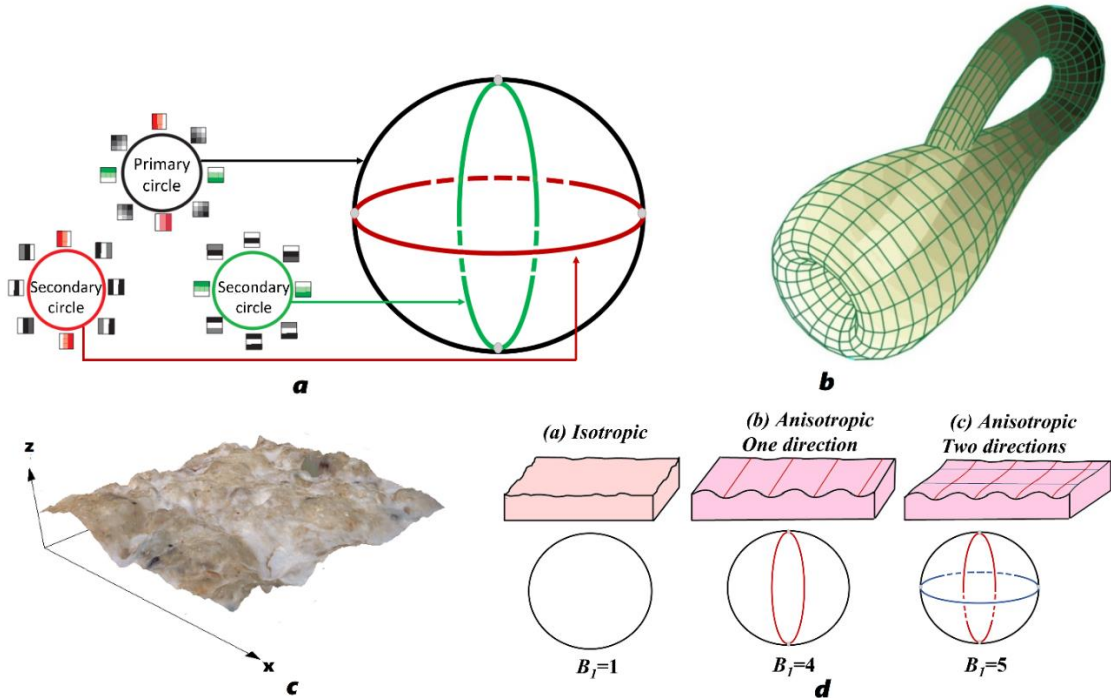


Figure 2.5. (a) The primary circle and two mutually nonintersecting secondary circles corresponding to isotropic contrast gradients and vertical and horizontal features, respectively, in 3×3 patches in the \mathbb{R}^8 space for natural images. Each secondary circle intersects twice with the primary circle. (b) The Klein bottle surface that fits that such configuration topologically. (c) The roughness profile image of a ceramic tile surface received from confocal microscopy, and (d) isotropy and anisotropy in surface roughness distribution

2.3.3.2. *Data topology for surface characterization*

In tribological applications, surface roughness and topography are crucial aspects in characterizing friction, wear, and damage [44]. Rough surfaces possess complex topography, which cannot be characterized by a single parameter. The selection of appropriate roughness parameters depends on a particular application. Large datasets representing surface topography possess orderliness, which can be expressed in terms of topological features in high-dimensional dataspace reflecting such properties as anisotropy and number of lay directions. The features are scale dependent because both sampling length and resolution affects them. In traditional analysis, often macroscale measurements are devised for surface roughness and irregularities which are sometimes nanoscale in nature. Such approaches may come short in characterizing the true nature of the underlying surface. The study of correlation length, extremum point distribution, persistence diagrams, and barcodes using data-driven analysis can provide valuable information such as scale dependency and anisotropic behavior besides the traditional analysis. However, there are only a few examples of TDA based study in surface characterization.

Yesilli and Khasawneh [45] employed a TDA-based approach to study persistent homology for extracting information about the surface. They used persistence images, Carlsson coordinates, and template functions to acquire feature matrices for each surface or profile. They

considered both areal images and profiles of synthetic surfaces in their study and proposed a TDA-based approach to classifying the roughness level. They also argued that the TDA-based approach can be utilized to fully automate the process of adaptive feature extraction, unlike the traditional surface analysis tools. Besides the above-mentioned study, several others also pursued TDA based approaches in analyzing surface properties [46-48].

2.4. Conclusion

The basic concepts of surface science, tribology, and wetting are discussed in this chapter. Triboinformatics approaches, different ML algorithms and TDA approaches have been discussed. These concepts have been extensively used in next chapters of the dissertation where tribological, wetting and surface properties have been studied. Also, a review on Triboinformatic approaches in surface science have been presented.

2.5. References

1. Bhushan, Bharat. *Introduction to tribology*. John Wiley & Sons, 2013.
2. Persson, Bo NJ. *Sliding friction: physical principles and applications*. Springer Science & Business Media, 2013.
3. Nosonovsky, Michael. "Modelling size, load and velocity effect on friction at micro/nanoscale." *International Journal of Surface Science and Engineering* 1, no. 1 (2007): 22-37.
4. Bhushan, Bharat, and Michael Nosonovsky. "Scale effects in friction using strain gradient plasticity and dislocation-assisted sliding (microslip)." *Acta materialia* 51, no. 14 (2003): 4331-4345.

5. Carpinteri, Alberto, and Marco Paggi. "Size-scale effects on the friction coefficient." *International Journal of Solids and Structures* 42, no. 9-10 (2005): 2901-2910.
6. Bowden, Frank Philip, Frank Philip Bowden, and David Tabor. *The friction and lubrication of solids*. Vol. 1. Oxford university press, 2001.
7. Nosonovsky, Michael. "Model for solid-liquid and solid-solid friction of rough surfaces with adhesion hysteresis." *The Journal of chemical physics* 126, no. 22 (2007): 224701.
8. Archard, John Frederick, and Wallace Hirst. "The wear of metals under unlubricated conditions." *Proceedings of the Royal Society of London. Series A. Mathematical and Physical Sciences* 236, no. 1206 (1956): 397-410.
9. Hasan, Md Syam, and Michael Nosonovsky. "Lotus effect and friction: does nonsticky mean slippery?." *Biomimetics* 5, no. 2 (2020): 28.
10. Marmur, Abraham. "Wetting on hydrophobic rough surfaces: to be heterogeneous or not to be?." *Langmuir* 19, no. 20 (2003): 8343-8348.
11. Wenzel, Robert N. "Resistance of solid surfaces to wetting by water." *Industrial & Engineering Chemistry* 28, no. 8 (1936): 988-994.
12. Cassie, A. B. D., and S.J. Toth F.S. Baxter. "Wettability of porous surfaces." *Transactions of the Faraday society* 40 (1944): 546-551.
13. Milne, A. J. B., and A. Amirfazli. "The Cassie equation: How it is meant to be used." *Advances in colloid and interface science* 170, no. 1-2 (2012): 48-55.
14. Zhang, Z., and K. Friedrich. "Artificial neural networks applied to polymer composites: a review." *Composites Science and technology* 63, no. 14 (2003): 2029-2044.

15. El Kadi, Hany. "Modeling the mechanical behavior of fiber-reinforced polymeric composite materials using artificial neural networks—A review." *Composite structures* 73, no. 1 (2006): 1-23.
16. Velten, K., R. Reinicke, and K. Friedrich. "Wear volume prediction with artificial neural networks." *Tribology International* 33, no. 10 (2000): 731-736.
17. Pasini, Antonello. "Artificial neural networks for small dataset analysis." *Journal of thoracic disease* 7, no. 5 (2015): 953.
18. Hasan, Md Syam, Amir Kordijazi, Pradeep K. Rohatgi, and Michael Nosonovsky. "Triboinformatics Approach for friction and wear prediction of al-graphite composites using machine learning methods." *Journal of Tribology* 144, no. 1 (2022).
19. Ardabili, Sina, Amir Mosavi, and Annamária R. Várkonyi-Kóczy. "Advances in machine learning modeling reviewing hybrid and ensemble methods." In *International Conference on Global Research and Education*, pp. 215-227. Springer, Cham, 2019.
20. Akhlaghi, F., and A. Zare-Bidaki. "Influence of graphite content on the dry sliding and oil impregnated sliding wear behavior of Al 2024–graphite composites produced by in situ powder metallurgy method." *Wear* 266, no. 1-2 (2009): 37-45.
21. Lanka, Sridhar, Evgeniya Alexandrova, Marina Kozhukhova, Md Syam Hasan, Michael Nosonovsky, and Konstantin Sobolev. "Tribological and wetting properties of TiO₂ based hydrophobic coatings for ceramics." *Journal of Tribology* 141, no. 10 (2019).
22. Rohatgi, P. K., S. Ray, and Yun Liu. "Tribological properties of metal matrix-graphite particle composites." *International materials reviews* 37, no. 1 (1992): 129-152.

23. Kumar, Ravinder, and Santram Chauhan. "Study on surface roughness measurement for turning of Al 7075/10/SiCp and Al 7075 hybrid composites by using response surface methodology (RSM) and artificial neural networking (ANN)." *Measurement* 65 (2015): 166-180.
24. 30. Radhika N, Senapathi SB, Subramaniam R, Subramany R and Vishnu KN "Pattern recognition based surface roughness prediction in turning hybrid metal matrix composite using random forest algorithm." *Industrial Lubrication and Tribology* 65, no. 5 (2013): 311-319.
25. Jones, Steven P., Ralph Jansen, and Robert L. Fusaro. "Preliminary investigation of neural network techniques to predict tribological properties." *Tribology Transactions* 40, no. 2 (1997): 312-320.
26. Zhang, Z., K. Friedrich, and K. Velten. "Prediction on tribological properties of short fibre composites using artificial neural networks." *Wear* 252, no. 7-8 (2002): 668-675.
27. Genel, Kenan, Süleyman Can Kurnaz, and Mehmet Durman. "Modeling of tribological properties of alumina fiber reinforced zinc–aluminum composites using artificial neural network." *Materials Science and Engineering: A* 363, no. 1-2 (2003): 203-210.
28. Rahimipour, Mohammad Reza, Ali Asghar Tofigh, Ali Mazahery, and Mohsen Ostad Shabani. "Strategic developments to improve the optimization performance with efficient optimum solution and produce high wear resistance aluminum–copper alloy matrix composites." *Neural Computing and Applications* 24, no. 7 (2014): 1531-1538.
29. Leema, N., P. Radha, S. C. Vettivel, and H. Khanna Nehemiah. "Characterization, pore size measurement and wear model of a sintered Cu–W nano composite using radial basis functional neural network." *Materials & Design* 68 (2015): 195-206.

30. Radhakrishnan, Ganesh, Chandrasekaran Kesavan, Vignesh Ramesh, and Tamilarasan Anandan. "Application of artificial neural network (ANN) for predicting the wear behaviour of Al 2219-SiCp composite." In *Applied Mechanics and Materials*, vol. 852, pp. 397-401. Trans Tech Publications Ltd, 2016.
31. Thankachan, Titus, K. Soorya Prakash, and Mujiburrahman Kamarthin. "Optimizing the tribological behavior of hybrid copper surface composites using statistical and machine learning techniques." *Journal of Tribology* 140, no. 3 (2018).
32. Idrisi, Amir Hussain, and Abdel Hamid Ismail Mourad. "Wear performance analysis of Aluminum matrix composites using Artificial neural network." In *2019 Advances in Science and Engineering Technology International Conferences (ASET)*, pp. 1-5. IEEE, 2019.
33. Pramod, R., GB Veeresh Kumar, PS Shivakumar Gouda, and Arun Tom Mathew. "A study on the Al₂O₃ reinforced Al7075 metal matrix composites wear behavior using artificial neural networks." *Materials Today: Proceedings* 5, no. 5 (2018): 11376-11385.
34. Stojanović, Blaža, Aleksandar Vencl, Ilija Bobić, Slavica Miladinović, and Jasmina Skerlić. "Experimental optimisation of the tribological behaviour of Al/SiC/Gr hybrid composites based on Taguchi's method and artificial neural network." *Journal of the Brazilian Society of Mechanical Sciences and Engineering* 40, no. 6 (2018): 1-14.
35. Davim, J. Paulo, V. N. Gaitonde, and S. R. Karnik. "Investigations into the effect of cutting conditions on surface roughness in turning of free machining steel by ANN models." *Journal of materials processing technology* 205, no. 1-3 (2008): 16-23.
36. Nosonovsky, Michael, and Bharat Bhushan. "Biologically inspired surfaces: broadening the scope of roughness." *Advanced Functional Materials* 18, no. 6 (2008): 843-855.

37. Chazal, Frédéric, and Bertrand Michel. "An introduction to topological data analysis: fundamental and practical aspects for data scientists." *Frontiers in Artificial Intelligence* 4 (2021).
38. Carlsson, Gunnar. "Topology and data." *Bulletin of the American Mathematical Society* 46, no. 2 (2009): 255-308.
39. Lee, Ann B., Kim S. Pedersen, and David Mumford. "The nonlinear statistics of high-contrast patches in natural images." *International Journal of Computer Vision* 54, no. 1 (2003): 83-103.
40. Van Hateren, J. Hans, and Arjen van der Schaaf. "Independent component filters of natural images compared with simple cells in primary visual cortex." *Proceedings of the Royal Society of London. Series B: Biological Sciences* 265, no. 1394 (1998): 359-366.
41. Singh, Nikhil, Heather D. Couture, J. S. Marron, Charles Perou, and Marc Niethammer. "Topological descriptors of histology images." In *International Workshop on Machine Learning in Medical Imaging*, pp. 231-239. Springer, Cham, 2014.
42. Dey, Tamal, Sayan Mandal, and William Varcho. "Improved image classification using topological persistence." In *Proceedings of the conference on Vision, Modeling and Visualization*, pp. 161-168. 2017.
43. Vandaele, Robin, Guillaume Adrien Nervo, and Olivier Gevaert. "Topological image modification for object detection and topological image processing of skin lesions." *Scientific Reports* 10, no. 1 (2020): 1-15.
44. Suh, Allison Y., Andreas A. Polycarpou, and Thomas F. Conry. "Detailed surface roughness characterization of engineering surfaces undergoing tribological testing leading to scuffing." *Wear* 255, no. 1-6 (2003): 556-568.

45. Yesilli, Melih C., and Firas A. Khasawneh. "Data-driven and Automatic Surface Texture Analysis Using Persistent Homology." In 2021 20th IEEE International Conference on Machine Learning and Applications (ICMLA), pp. 1350-1356. IEEE, 2021.
46. Suzuki, Anna, M. Miyazawa, Atsushi Okamoto, Hiroyuki Shimizu, Ippei Obayashi, Yasuaki Hiraoka, Takeshi Tsuji, Patricia K. Kang, and Takatoshi Ito. "Inferring fracture forming processes by characterizing fracture network patterns with persistent homology." *Computers & Geosciences* 143 (2020): 104550.
47. Khasawneh, Firas A., Elizabeth Munch, and Jose A. Perea. "Chatter classification in turning using machine learning and topological data analysis." *IFAC-PapersOnLine* 51, no. 14 (2018): 195-200.
48. Kurtz, S. M., C. L. Muhlstein, and A. A. Edidin. "Surface morphology and wear mechanisms of four clinically relevant biomaterials after hip simulator testing." *Journal of Biomedical Materials Research: An Official Journal of The Society for Biomaterials, The Japanese Society for Biomaterials, and The Australian Society for Biomaterials and the Korean Society for Biomaterials* 52, no. 3 (2000): 447-459.

CHAPTER 3: FRICTION AND WEAR PREDICTION OF ALUMINUM ALLOYS USING TRIBOINFORMATIC APPROACHES

In the previous chapter, the basic concepts of surface science, wetting, and tribology along with a review of Triboinformatics approaches had been presented. In this chapter, Correlations of friction and wear of aluminum (Al) base alloys with their material properties, processing procedure, and tribological test variables are studied using traditional and Triboinformatics approaches. Data-driven approaches, for example, ML algorithms can yield a better understanding of how tribological and material properties correlate. Five ML regression models are developed to predict the friction and wear behavior of these alloys and to find the most important parameters influencing these behaviors.

3.1. Introduction

Monolithic aluminum and its alloys receive widespread attention in industrial applications due to their unique material properties. About 75% of the total aluminum metal ever processed is still in the application for high durability and excellent recyclability of aluminum while retaining desirable properties [1]. Corrosion resistance, high specific strength and stiffness, and high conductivity are some of the desired mechanical properties that make aluminum and its alloys promising materials in weight-critical aerospace and automotive applications [2-3]. Due to superior mechanical properties and commercial aspects, they have been extensively investigated for their potential use in tribological applications [4-7]. Modest wear rate, less friction, limited material removal, and less temperature raise during sliding contacts are some of the requirements in such applications. However, a high wear rate and friction, tendency to seize, and extensive plastic deformation [8-9] are some limitations in the tribological performance of aluminum alloys

that prevent their widespread tribological applications in dry sliding and under poor lubrication. To improve the tribological performances of aluminum alloys while retaining their desired mechanical properties, the incorporation of graphite particles as solid lubricants into the aluminum matrix for manufacturing self-lubricating aluminum metal matrix composites (MMC) has been explored extensively in recent years [10-18]. However, understanding the tribological behavior and the effect of different material and tribological variables on tribological performance remains the key aspect for such tribological performance enhancement of aluminum alloys.

The coefficient of friction (COF) is a dimensionless scalar quantity used to quantify friction [19]. COF is the ratio of the friction force (F_f) and normal load (N) pressing the sliding surfaces together.

$$\mu = \frac{F_f}{N} \quad (1)$$

Bowden and Tabor theorized two independent components of friction for sliding contacts: adhesion (F_a) and deformation / plowing (F_d) [20]. Although the assumption that these components are independent is a simplification, the total friction force (F_f), and the COF is often presented as a sum

$$\mu = \frac{F_f}{N} = \frac{F_a + F_d}{N} = \frac{F_a}{N} + \frac{F_d}{N} = \mu_a + \mu_d \quad (2)$$

Where the COF due to adhesion and deformation are μ_a and μ_d , respectively. Physical and chemical interactions due to molecular forces at the real area of contact between the asperities of the surfaces under different loading conditions cause adhesion [21]. The deformation component of friction is caused by deformations (both elastic and plastic) of asperities of the mating surfaces

at both microscopic and macroscopic levels. It depends upon several mechanical properties, for example, yield strength and hardness of the aluminum alloys.

Oxidation-dominated wear, adhesive wear, delamination wear, and melt lubrication wear are the most dominant wear mechanisms found in aluminum alloys [9]. The frictional heat generated during sliding promotes the oxidation of aluminum and form a thin, chemically inert oxide layer on the surface. With increasing loads, adhesion between the surfaces initiates adhesive wear where the adhesive junctions are deformed plastically and material removal from the aluminum surface takes place including the oxide layer. In delamination wear, plastic shearing of metal in the sliding direction takes place. The laminate wear debris is generated through subsurface cracking taking place at certain depths under the surface.

Though several fields of science including chemistry, medical science, and biology have already accommodated AI and data-driven ML algorithms as reliable tools, they are comparatively newer addition in material science [22]. Recent successes in integrating ML in material and tribological property prediction [23-25] have opened new prospects in material science and tribology. Traditional analysis focusing on isolated experimental observations often comes short in generating a universal understanding of tribological behavior due to the complexity associated with numerous parameters characterizing friction and wear. ML algorithms can be trained with experimental tribological data to predict the tribological behavior for different combinations of material and tribological variables. Complex ML algorithms like support vector machine (SVM) and artificial neural network (ANN) can identify the variability in the data and adjust their learning process to predict an accurate outcome which can provide a broader understanding of tribological behavior.

In this chapter, first, a traditional analysis of the friction and wear behavior of aluminum alloys is presented in terms of material and tribological test variables. Then, using tribological data of these alloys reported in the literature, ML models are developed to predict the COF and wear rate. Finally, the performance of different ML algorithms in predicting the tribological behavior is analyzed and a comparative analysis of different material and tribological test parameters influencing the tribological behavior of aluminum alloys is presented.

3.2. Variables influencing tribological behavior of aluminum alloys

Variables influencing the tribological behavior of aluminum alloys can be classified into two general classes: material variables and tribological test variables. In this section, a traditional analysis of the effect of these variables on the tribological behavior of aluminum alloys will be discussed.

3.2.1. Material variables

Quantitative material or microstructural properties, and parameters related to the processing procedure are the material variables. Alloying composition, average grain size, hardness, yield strength, ductility, processing procedure, and heat treatment are some of the material variables affecting the tribological behavior of aluminum alloys.

3.2.1.1. Effect of alloy composition

Alloying composition is a primary reason of the variation in tribological behavior among aluminum alloys. Copper, silicon, manganese, magnesium, iron, zinc, chromium, nickel, and titanium are some of the typical alloying elements combined with pure aluminum in different weight percentages to form various industrial-grade aluminum alloys with unique physical and

mechanical properties [7-9]. Alloying enhances wear resistance, strength, modulus, material hardening [8, 26], and the critical load for mild to severe wear transition [4, 27-28].

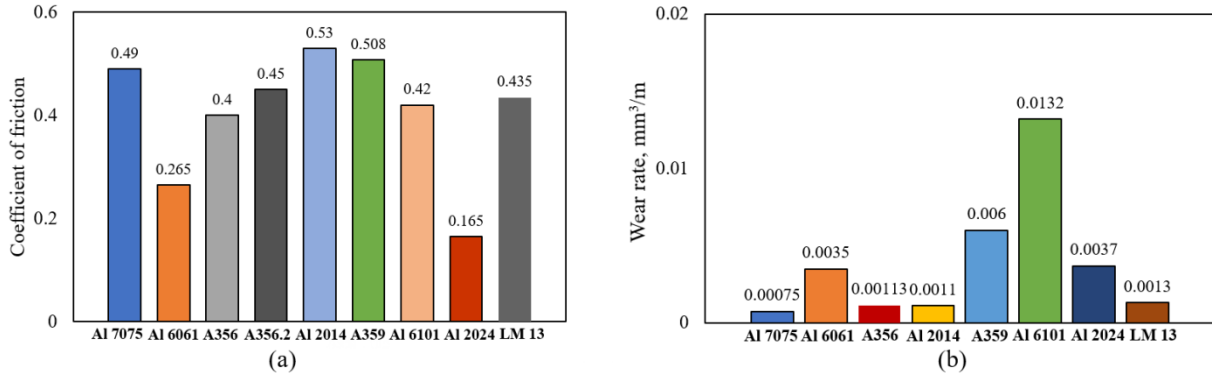


Figure 3.1. Average (a) COF [10-17, 29-30], (b) wear rate [10-12, 14-18, 30] of different aluminum base alloys under dry conditions against a steel counterface

Comparisons of average COF and average wear rate among some common aluminum alloys under dry conditions against steel counterfaces in pin-on-disc testing methods are presented in **Figure 3.1(a)** and **Figure 3.1(b)**, respectively. The average COF of aluminum alloys varied significantly with alloy composition ranging from 0.165 to 0.53. Al 2024 alloy exhibited the lowest average COF while the maximum was reported for Al 2014 alloy. The average wear rate also varied notably with alloy composition ranging between 0.00075 mm³/m to 0.0132 mm³/m. The lowest average wear rate was reported for Al 7075 alloy, and the maximum was reported for Al 6101.

3.2.1.2. Effect of microstructural properties and material processing

Microstructural properties such as degrees of grain refinement, nature of the grain boundary, distribution and size of grains, distribution of second phases, dislocation density, presence of nano and microscale cracks in microstructure influence tribological behavior of aluminum alloys.

Grain refinement is a microstructural recrystallization process that ensures uniform distribution of second phases in the primary aluminum phase, reduces casting defects such as porosity, improves fatigue life, and enhances mechanical performance. Improved friction and wear performance in aluminum alloys can be attributed to grain refinement of alloy microstructure generally performed through classical thermo-mechanical treatments and severe plastic deformation methods [31]. The average grain size of the microstructure is a measurable representation of grain refinement. The COF and wear rate of different aluminum base alloys are plotted against the average grain size in **Figure 3.2(a)** and **Figure 3.2(b)**, respectively.

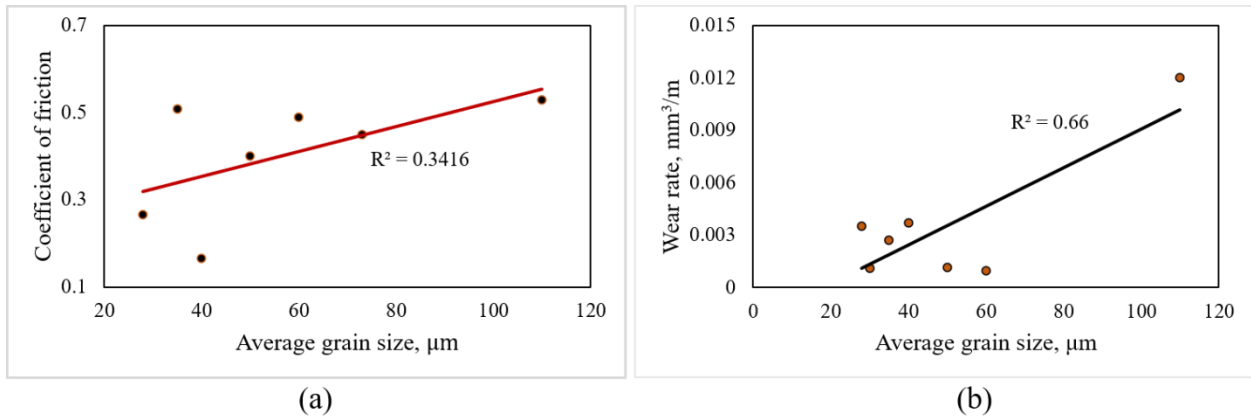


Figure 3.2.(a) COF vs average grain size, (b) wear rate vs average grain size, (Al 7075 = 60 μm , Al 6061 = 28 μm , A356 = 50 μm , A356.2 = 73 μm , A359 = 35 μm , Al 6101 = 110, Al 2024 = 40) [10-13,15-17] under dry conditions against a steel counterface

For wear rate, an overall linear relationship can be observed in **Figure 3.2(b)**, and wear rate decreases with decreasing grain size of aluminum alloys. An R^2 value of 0.66 indicates that the linear approximation between wear rate and average grain size is statistically significant. In contrast, a small R^2 value of 0.3416 in **Figure 3.2(a)** indicates that there exists no statistically significant linear relationship between COF and grain size. However, an overall improvement of

tribological behavior is observed with grain refinement as both COF and wear rate decreased with decreasing grain size.

Figure 3.3. presents the optical microstructures of several aluminum alloys considered in previous sections for traditional tribological analysis. In the microstructure of Al 2024 (**Figure 3.3e**) that exhibited the minimum COF among the alloys in the previous section, a homogeneous crystalline distribution of grains is observed, and the grain boundaries are not well-defined. Extensive grain refinement, homogeneous distribution of grains, and the absence of well-defined grain boundaries are some probable reasons that contributed to the low COF.

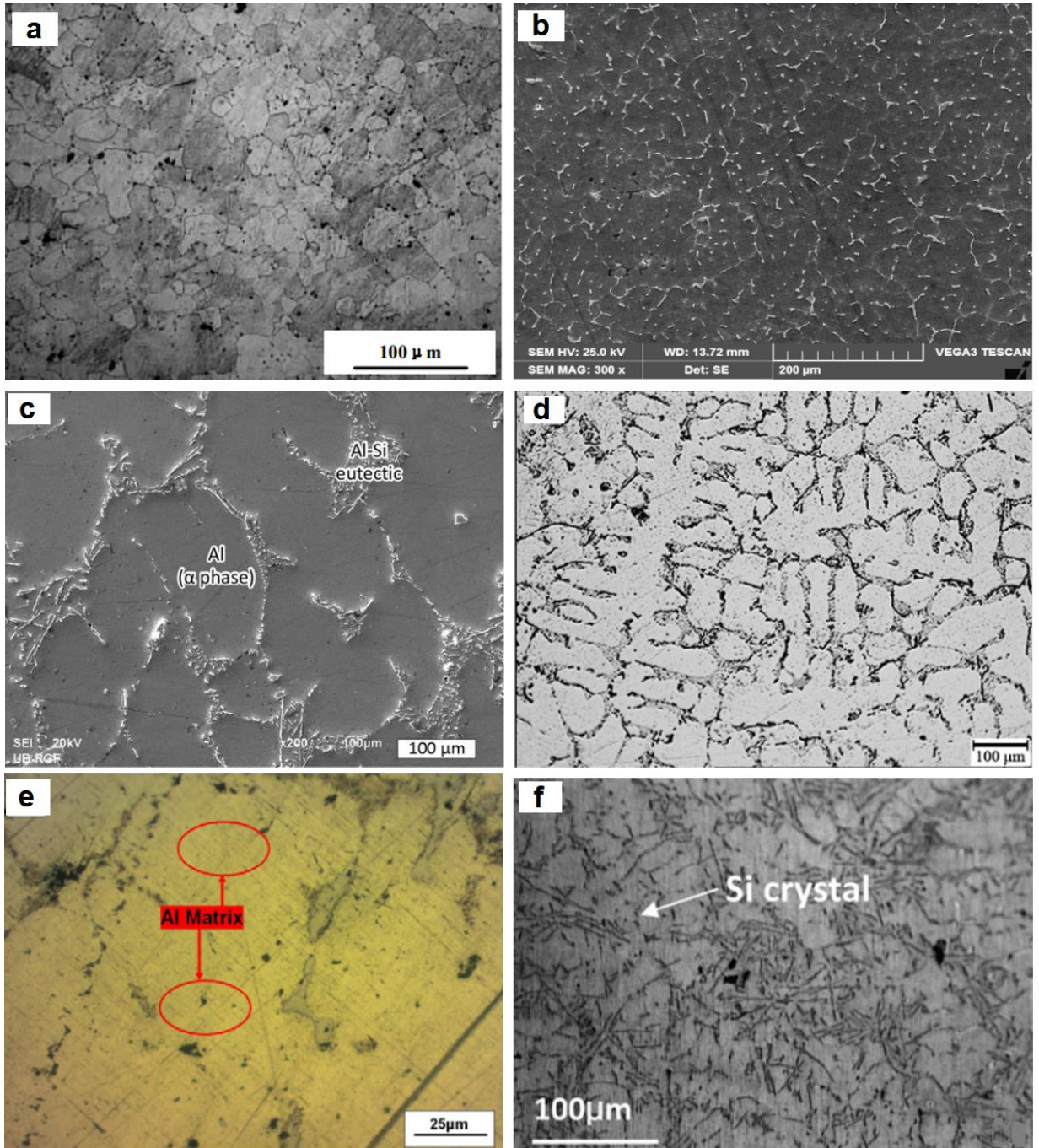


Figure 3.3. Optical microstructures of (a) Al 7075 [31], (b) Al 6061 [32], (c) A356 [12], (d) A356.2 [33], (e) Al 2024 [17], (f) A359 [15].

In Al 7075 microstructure (**Figure 3.3a**) that exhibited the minimum wear rate, isometric crystals and many undissolved large-phase particles of secondary phases are observed [10].

Moreover, precipitation hardening of the base alloy contributed to the excellent wear performance during tribological tests.

Casting, powder metallurgy, mechanical alloying, hot extrusion, cold extrusion, rolling, and forging are some common processing procedures for aluminum alloys. Mechanical and physical properties like tensile strength, yield strength, density, residual stress, and ductility and microstructural properties like distribution and size of the grains are greatly influenced by material processing procedures. Heat treatment is an essential process additive to processing procedures that enhances mechanical properties by increasing ductility, fatigue resistance, modulus, strength, and hardness. All these improvements in microstructural and mechanical properties directly affect tribological behavior. Some of the most common heat treatment processes of aluminum alloys are annealing, homogenization, solution treatment, and T6 heat treatment which is a two-phase process consists of the solution treatment followed by an age hardening.

3.2.1.3. Effect of mechanical properties on tribological behavior

Hardness, yield strength, tensile strength, and ductility are some of the mechanical properties influencing the tribological behavior of aluminum alloys. Hardness is often considered as the most important mechanical property in the traditional tribological analysis [34]. During surface interactions, alloys having high hardness exhibit higher cohesion and lower adhesion with another material than a softer alloy. The deformation component of friction is also low for harder alloys due to low plastic deformability. Having both adhesion and deformation components of friction low, harder alloys are expected to have low overall COF. The COF vs Brinell hardness plot (**Figure 3.4a**) for different aluminum base alloys shows that COF decreases linearly with the increasing hardness of the alloys. However, such a simple traditional approach of correlating COF

and hardness can produce flawed results as there exists no straightforward relation between COF and hardness.

Unlike COF, in the wear rate vs Brinell hardness plot for aluminum alloys (**Figure 3.4b**), a nonlinear trend was observed. Generally, the wear rate of harder materials during sliding contact is low due to low adhesive wear, plastic deformation, and material removal. Gore and Gates reported that the general trend of wear rate reduction with increasing hardness is observed for single-phase materials [35]. They found no such general trend for multiphase materials and suggested that micro-fracture wear mechanisms in multi-phase materials could be a possible reason for this. However, Gopi et al. reported that the wear rate reduced consistently with increasing hardness for multi-phase materials and alloys [36]. The inconsistencies in different findings of traditional analysis indicate that the relation between hardness and tribological behavior is not straightforward either.

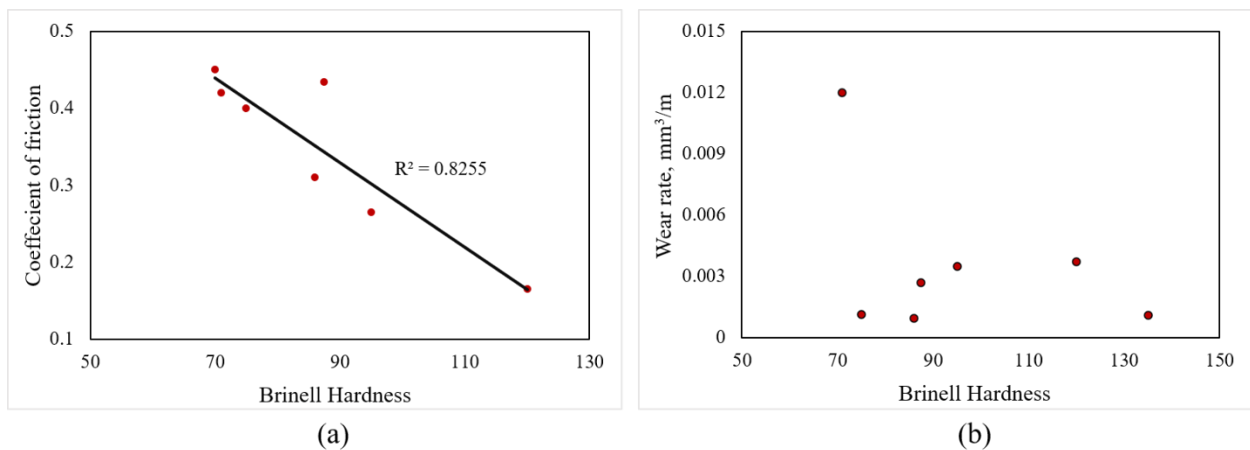


Figure 3.4(a) COF vs Brinell hardness (b) wear rate vs Brinell hardness of aluminum base alloys (Al 7075 = 86 BHN, Al 6061 = 95 BHN, A356 = 75 BHN, A356.2 = 70 BHN, A359 = 87.5 BHN, Al 6101 = 71 BHN, Al 2024 = 120 BHN, Al 2014 = 135 BHN) [10-13,15-17] under dry conditions against a steel counterface

The contact region of tribo-surfaces made from ductile metals like aluminum, iron, copper, nickel, and their alloys undergoes extensive plastic deformation and wear in sliding contact. Reducing ductility of these materials within a certain range (not turning brittle) by incorporating a reinforcement phase (e.g., SiC or graphite particles) at a certain volume percentage reduces the wear rate. Brittle materials tend to have a brittle fracture at tribo-surface during sliding contacts and are not recommended for many tribological applications. Thus, ductility plays an important role in the tribological behavior and can be an important material variable in the tribological study. Tensile and yield strength are other mechanical properties that affect the tribological behavior. Dhokey et al. reported that there is a reasonable correlation between wear behavior and tensile strength [37]. After statistical factorial analysis, Aly and El-Koussy reported an inverse relation between wear rate and yield strength [38]. In another study, Bellemare et al. reported that the effect of yield strength on COF for elastoplastic materials is significant while COF is independent of yield strength for completely plastic materials [39].

3.2.2. Tribological test variables

Variables that are related to the tribological tests are sliding speed, sliding distance, and normal load. The effect of these variables on the tribological behavior of aluminum alloys will be discussed in this section.

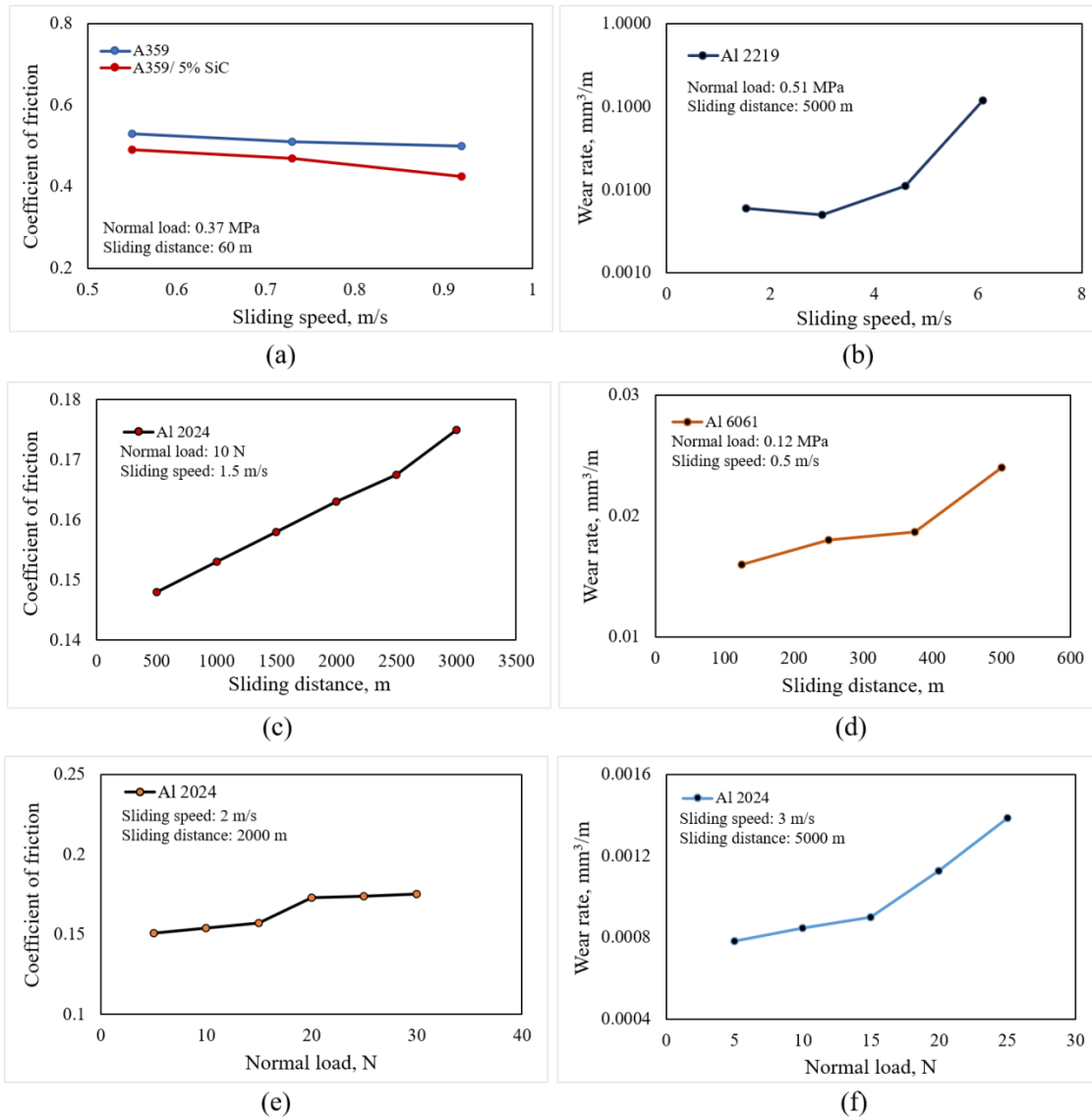


Figure 3.5. (a) COF vs sliding speed for A359 alloy [15], (b) wear rate vs sliding distance for Al 2219 alloy [41], (c) COF vs sliding distance for Al 2024 alloy [42], (d) wear rate vs sliding distance for Al 6061 alloy [43], (e) COF vs normal load for Al 2024 alloy [17], (f) wear rate vs normal load for Al 2024 alloy [42] under dry conditions against a steel counterface

3.2.2.1. Effect of sliding speed

The empirical third law of friction (Coulomb's law) identifies friction to be independent of sliding speed. However, in practice, COF is reported to be a function of sliding speed throughout

the sliding contact [40]. Predicting frictional behavior depending on sliding speed can be challenging due to two contrasting factors. The frictional heat due to high sliding speed promotes the formation of thin molten layers and oxide layers on metallic surfaces that results in low friction. In contrast, the resulting frictional heat from high sliding speed softens the metallic surface and induces increased plastic deformation and plowing that generates high friction. Generally, for a constant normal load, COF decreases with increasing sliding speed. In the COF vs sliding speed plot for A359 alloy, a reduction in COF is observed with increasing sliding speed (**Figure 3.5a**).

Unlike COF, as a general trend, wear rate increases when sliding speed increases. Microthermal softening of the tribo-surface, flow stress reduction, dissolution of precipitates, and oxide formation are some are the consequences of the interfacial temperature increase caused by frictional heat due to increasing sliding speed that contribute to increased wear rate. In the wear rate vs sliding speed plot for Al 2219 alloy, an increase in wear rate with increasing sliding speed is observed (**Figure 3.5b**).

3.2.2.2. Effect of sliding distance

Sliding distance and COF do not have a straightforward relationship. It depends upon the nature of sliding surfaces, sliding arrangements, and the wear mechanism that causes material removal during sliding. However, for most tribo-pairs, a steady increase or decrease in COF is observed before reaching an asymptotic value. No specific trend incorporating random increase and decrease in COF with increasing sliding distance is also found for different materials. In COF vs sliding distance plot for Al 2024 alloy, a steady increase in COF has been observed with increasing sliding distance (**Figure 3.5c**) [42].

Generally, the wear rate increases when the sliding distance is increased. Frictional heat generated at the interface due to extensive sliding softens the metallic surface. This microthermal softening of the tribo-surface induces increased plastic deformation and plowing that result in extensive material removal at a higher rate. In the wear rate vs sliding distance plot for Al 6061 alloy, an increase in wear rate is observed with increasing sliding distance (**Figure 3.5d**).

3.2.2.3. Effect of normal load

The normal load is an important tribological parameter, especially for metals and alloys. Due to a high oxygen affinity, when exposed to air, aluminum and its alloys are oxidized, and a thin, chemically inert, hard, and whitish-colored oxide layer is formed on the surface. This thin oxide layer separates the metal surfaces during sliding and reduces the COF. The effect of normal load on COF largely depends on the durability of this layer. At low loads, the oxide layer remains intact and causes a low COF. When the load is high enough to breakdown the layer, a higher COF is observed due to extensive metal-metal contact. When the normal load is increased, the micro and nano-level asperity contacts between the sliding surfaces also increase which contributes to an increased COF. COF as a function of normal load for Al 2024 alloy is presented in **Figure 3.5(e)** where an increase in COF with normal load is observed.

During sliding contact, metal and alloys exhibit two forms of wear: mild and severe depending on normal load [44]. The mild form is observed at small loads where oxidation of material takes place, and a steady increase in wear rate is observed with the increasing load during sliding. In contrast, the severe form of wear takes place at higher loads where delamination and adhesive wear cause extensive material removal at a high rate. The transition between mild to severe form takes place at the critical load when an abrupt increase in wear rate is observed. In the

wear rate vs normal load plot for Al 2024 alloy, the wear rate increases with the normal load (**Figure 3.5f**).

In preceding sections, a traditional analysis of the effect of material and tribological test variables on tribological behavior of aluminum alloys has been presented. Though the 2-parameter traditional analysis is a simple and useful approach to understand tribological relationships, it often comes short in addressing the complexity associated with those relationships. Data-driven ML analysis can potentially be a useful tool in understanding the tribological behavior of aluminum alloys more efficiently.

3.3. Materials and methods

ML algorithms were formulated to predict the tribological behavior of aluminum alloys under dry conditions. In this section, we will discuss data collection, data preprocessing, parameter optimization, and performance-enhancing techniques used for the ML algorithms.

3.3.1. Data collection

Data collection is a crucial step to develop an efficient data-driven ML algorithm. When a large, relevant dataset is used to train an ML algorithm, a better predictive performance is observed. Performing tribological experiments to generate adequate data for an ML analysis is an expensive and time-consuming task. Moreover, experimental data from a single experimental setup may pass undesired trends and biases in the training process of an ML model. This can severely hamper the predictive performance of the ML model for new datasets of other sources. Considering these issues, we have collected friction and wear rate data of aluminum alloys under dry condition against a steel counterpart from different sources reported in the literature [10-

18,29,41-43,45-59]. For wear rate and COF prediction, tribological data sets of 612 and 463 sample data points were used, respectively.

3.3.2. Input and output parameters

Seven material variables: hardness, tensile strength, yield strength, ductility, heat treatment, processing procedure, silicon carbide content, and three tribological test variables: sliding speed, sliding distance, and normal load were the input parameters for the ML algorithms. Among the input parameters, heat treatment and processing procedure were defined as categorical data for the ML algorithms while the rest of them were numerical. COF and wear rate were the target or output parameters.

3.3.3. Machine learning algorithms

Regression analysis of supervised ML is used to find the correlation between the input and output parameters and get numerical outputs. For this study, we have trained five ML algorithms: K Nearest Neighbor (KNN), Support Vector Machine (SVM), Artificial Neural Network (ANN), Random Forest (RF), and Gradient Boosting Machine (GBM) with tribological data of aluminum alloys to find correlations between the input and output parameters and predict the tribological behavior. The ML analyses were performed using Python and its built-in “scikit-learn” toolkit. A detailed description of the ML algorithms used in this study is presented in **Chapter 2** of this dissertation.

3.3.4. Data preprocessing

Data preprocessing or data cleaning is important for developing an efficient ML model. Correction for unusual and missing values, data splitting for training and test sets, and data normalization (feature scaling) are some important data preprocessing techniques. We looked for

any missing or unusual values in the dataset and corrected them accordingly. Data shuffling was done to prevent the passing of any bias or undesired trend in the dataset (associated with data collection) to the ML models. Then using python, the entire data was split into two mutually exclusive sets: training set and test set. ML model building and validation were done using the training set while the performance of the models on new data was evaluated using the test set. Standard data splitting strategy was chosen: 75% for the training and 25% for the test set. Again, 75% of the training set data was used for training and the rest 25% was used for model validation. ML algorithms incorporated 344, 115, and 153 data points (total 612 data points) in the training, validation, and test set respectively for wear rate prediction. For COF prediction all ML algorithms used a total of 463 data points (260 in the training, 87 in the validation, and 116 in the test set).

Data normalization or data standardization is the next data cleaning step. It is also known as feature scaling where all the features are brought in the same scale for a better predictive performance of the ML algorithms. “RobustScaler” of the Scikit-learn toolkit was used for feature scaling of the training, validation, and test sets as it can handle outliers in the dataset more efficiently.

3.3.5. Parameter optimization of ML models

Parameter optimization is a process of performance optimization of ML algorithms. We used the grid search method to find the optimal parameters (including the activation function of the ANN algorithms) for ML models that are reported in **Table 3.1** and **Table 3.2**. Python codes were written to run the grid search method which is an optimization technique additive to the ML algorithms. Ranges of different parameters were set, and the grid search method took different combinations of these parameters and executes numerous ML analysis. Comparing the model performance for different parameter combinations, the grid search method suggests the parameters

that produce the best performance. The parameter optimization of ML algorithms for COF and wear rate predictions are presented in **Table 3.1** and **Table 3.2**.

Table 3.1. Parameter optimization for COF

ML model	Parameter optimization
Artificial Neural Network	Hidden layer sizes = (5,5,5), alpha = 0.035, activation function: tanh
K-Nearest Neighbor	n=3, weight = “uniform”
Random Forest	n_estimators= 70, max_features = 7
Support Vector Machine	kernel = "rbf", C = 50, gamma = “scale”
Gradient boosting	n_estimator =100, learning rate = 0.3

Table 3.2. Parameter optimization for wear rate

ML model	Parameter optimization
Artificial Neural Network	Hidden layer sizes = (10,10,10), alpha = 0.01, activation function: “relu”
K-Nearest Neighbor	n=3, weight = “uniform”
Random Forest	n_estimators= 90, max_features = 5
Support Vector Machine	kernel = "rbf", C = 20, gamma = 0.9
Gradient boosting	n_estimator = 50, learning rate = 0.4

3.4. Result and discussion

In this section, we will present the results of ML analysis for COF and wear rate prediction of aluminum base alloys and interpret them based on established concepts of material science. We

will also analyze the performance of each ML model and discuss the feature importance in COF and wear rate prediction.

3.4.1. Model performance evaluation

Performance metrics present a numerical estimation of ML models fitting with actual data. For a supervised learning regression problem, the coefficient of determination (R^2 value) is the most important performance metric. The percentage of variation in data explained by the model is indicated by the R^2 value. This value ranges from 0 to 1. $R^2 = 0$ indicates no correlation, and the model cannot explain the variation in data. $R^2 < 0.5$ indicates a small correlation, and the ML model is considered inadequate in predicting the output. R^2 value ranging between 0.70 to 0.9 indicates satisfactory performance and a value over 0.9 refers to a very satisfactory model execution. $R^2 = 1$ indicates perfect fitting, and the model can accurately explain the variation in data without any error which is unlikely for experimental data.

Mean absolute error (MAE), mean squared error (MSE), and root mean squared error (RMSE) are three other important metrics used to evaluate model performance. MAE presents the average value of the absolute difference between the predicted and actual values. MSE is the average of the squared differences between the actual and predicted values of the data points while RMSE is the square root of MSE. These error terms provide important information about the model performance. Small values of these error terms indicate the high accuracy of the prediction performance of the ML models.

Table 3.3. Performance of the ML methods for COF

ML Model	Mean squared error (MSE)	Root mean squared error (RMSE)	Mean absolute error (MAE)	R-squared value
Artificial Neural Network	0.0055	0.0744	0.0487	0.76
K Nearest Neighbor	0.0028	0.0536	0.0345	0.82
Random Forest	0.0028	0.0529	0.0324	0.83
Support Vector Machine	0.0034	0.0583	0.0340	0.79
Gradient Boosting	0.0030	0.0551	0.0331	0.81

Table 3.4. Performance of the ML methods for wear rate

ML Model	Mean squared error (MSE)	Root mean squared error (RMSE)	Mean absolute error (MAE)	R-squared value on test
Artificial Neural Network	0.0009	0.0294	0.0084	0.71
K Nearest Neighbor	0.0008	0.0281	0.0053	0.73
Random Forest	0.00001	0.0037	0.0015	0.81
Support Vector Machine	0.0007	0.0273	0.0063	0.75

Gradient Boosting	0.00002	0.0041	0.0022	0.76
-------------------	---------	--------	--------	------

Table 3.3. presents the performance metrics of ML models in COF prediction. For different ML models, R^2 values on test sets ranged from 0.76 to 0.83. MAE ranged between 0.0331 to 0.0487, MSE ranged between 0.0028 to 0.0055 and RMSE varied between 0.0529 to 0.0744 for the ML models which are significantly low. These statistical performance metrics indicate that the developed ML models can predict the COF of aluminum alloys from the material and tribological variables at a satisfactory level.

The decision tree-based RF model exhibited the maximum R^2 value of 0.83 that can be considered satisfactory. This model could predict the COF of aluminum alloys from the material and tribological test variables with an accuracy of 83%. MSE, RMSE, and MAE values of this model were 0.002, 0.0529, and 0.0324 respectively which are significantly low and indicated high prediction accuracy. The predicted vs actual COF plot for the RF model is presented in **Figure 3.6**. The figure indicates that there is an acceptable agreement between the predicted and actual results. KNN and decision tree-based RF and GBM models also performed satisfactorily almost had identical performance metrics as RF. ANN and SVM models also performed reasonably well in predicting the COF of aluminum base alloys.

Table 3.4. presents the performance metrics of ML models for the wear rate prediction of aluminum base alloys. The R^2 values on test sets ranged from 0.71 to 0.81 for the ML models. MAE ranged between 0.0015 to 0.0084, MSE ranged between 0.00001 to 0.0009 and RMSE varied between 0.0037 to 0.0294 which are significantly low. The values of these statistical performance metrics indicate that the developed ML models can predict the wear rate satisfactorily from the material and tribological variables for aluminum alloys. Decision tree-based RF outperformed the

other ML models and generated the maximum R^2 value of 0.81. This indicates that the model can predict the wear rate of aluminum alloys from the material and tribological variables with an accuracy of 81%. Moreover, MSE, RMSE, and MAE values of this model were notably low (0.00001, 0.0037, and 0.0015 respectively). **Figure 3.6** presents the predicted vs the actual wear rate plot of the RF model. The actual experimental wear rate data varied in a wide range. The figure shows that the RF model could satisfactorily predict the wear rate and address the variability inherent in the wear rate data of the aluminum base alloys.

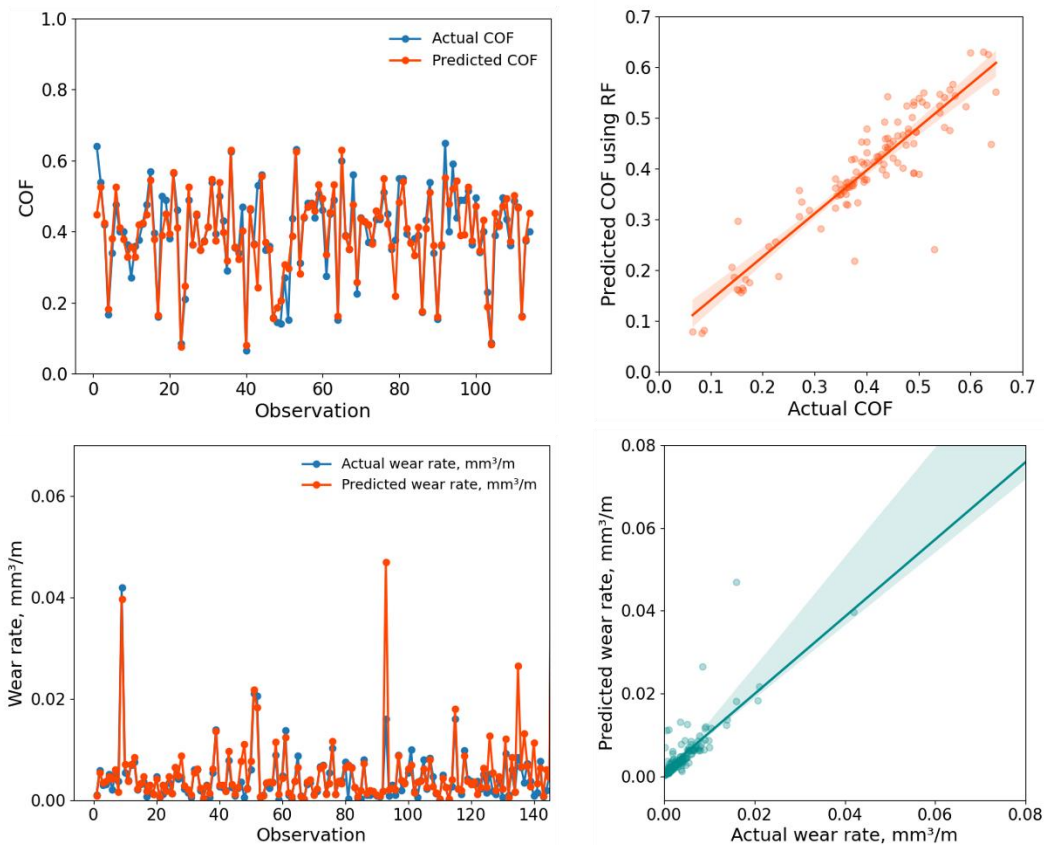


Figure 3.6. Predicted vs actual COF and wear rate for aluminum base alloys using RF model

The ML models developed in our study successfully predicted the wear rate and COF of aluminum base alloys at a satisfactory level from different material and tribological variables.

3.4.2. Importance of different independent variables

The “feature importance” attribute of RF models allows us to analyze the relative importance of different independent variables or features in predicting the output. Scores ranging from 0 to 1 are assigned to the features where the sum of the scores equals 1. A high score indicates the high importance of a feature in output prediction. **Figure 3.7(a)** presents the feature importance chart for COF prediction of aluminum alloys.

All the considered independent variables had nonzero scores and contributed to COF prediction. The hardness of the aluminum alloys had the highest score and thus the highest contribution in COF prediction. Aluminum alloys having high hardness exhibit higher cohesion at the molecular level and lower adhesion with another material than a softer alloy. Consequently, a low adhesion component of friction is observed. The deformation component of friction is also low for harder alloys due to low plastic deformability in sliding contact. Having both adhesion and deformation components of friction low, harder alloys generally exhibit low overall COF during sliding contact.

The sliding distance was identified as the second most important feature in COF prediction. Frictional heat generated at the interface due to extensive sliding softens the metallic surface. This microthermal softening of the tribo-surface causes increased plastic deformation and plowing that affect the COF. A steady increase or decrease in COF is observed before reaching an asymptotic value with increasing sliding distance for most tribo-pairs. Among other variables, tensile strength, load, sliding speed, and yield strength of the base alloys have notable effects on COF prediction. Heat treatment and processing procedure were found to have a negligible impact in predicting the COF of aluminum alloys.

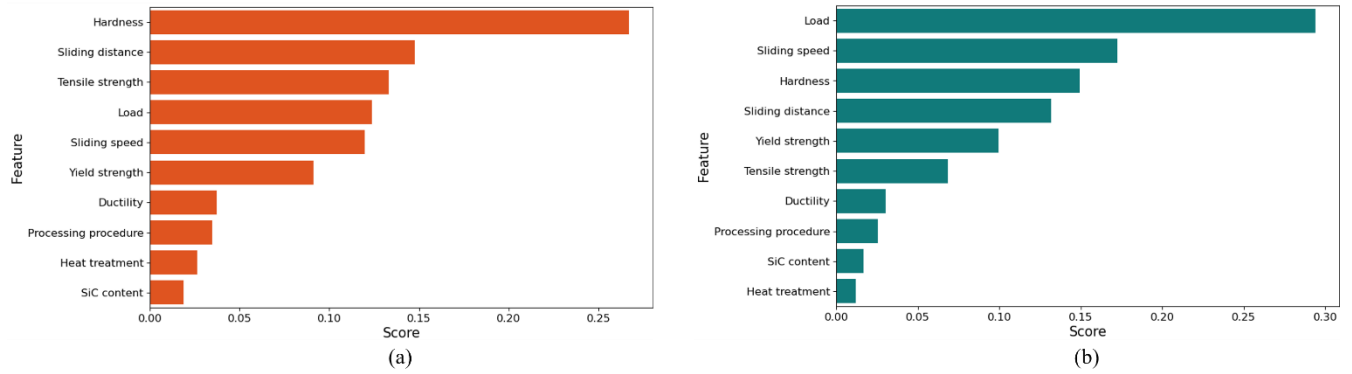


Figure 3.7. Feature importance for predicting (a) COF and (b) wear rate of aluminum base alloys

Figure 3.7(b) presents the feature importance chart for wear rate prediction of aluminum alloys. All the independent variables contributed fairly (nonzero score) in wear rate prediction. Normal load, an important tribological variable had the highest score and the maximum contribution in wear rate prediction. The transition between the mild to severe form of wear of aluminum base alloys depends on the load. At a lower load, mild wear takes place when a low wear rate is observed due to the intact oxide layer on the tribosurface. In contrast, the severe form of wear takes place at higher loads when delamination and adhesive wear cause extensive material removal at a high rate during sliding contact. Therefore, the normal load was identified as the most important parameter in wear rate prediction.

Sliding speed was identified as the second most important variable in wear rate prediction. Interfacial temperature increase caused by frictional heat during sliding depends on the sliding speed. Oxide layer formation, microthermal softening of the tribo-surface, flow stress reduction, and dissolution of precipitates are some are the consequences of the interfacial temperature increase. Consequently, the sliding speed becomes an important variable in wear rate prediction of aluminum alloys. Hardness was identified as the most important material variable in wear rate

prediction. The extent of plastic deformation, adhesive wear, and material removal during sliding contact depends on hardness. Generally, harder materials tend to have low wear rates. Stronger molecular bonds at the surface of harder materials cause a higher resistance to adhesive wear. Therefore, for aluminum base alloys, the difference in hardness was found as a key parameter in wear rate prediction.

Data-driven ML analysis provides novel insights analyzing the tribological data that are often unattainable with traditional analysis. For example, the feature importance attribute provides a broader understanding of the impact of different parameters on friction and wear behavior. This information can be further utilized in tribological behavior modification of aluminum alloys in different applications.

3.5. Conclusion

The tribological behavior of aluminum base alloys and their dependency on material and tribological test variables were studied through traditional and data-driven analysis. Using tribological data of these alloys reported in the literature, five different ML models were developed to predict COF and wear rate. Through performance analysis, it was demonstrated that the ML models can satisfactorily predict the friction and wear behavior of aluminum alloys. In absence of any form of lubrication (liquid and solid), the transition from mild to severe wear is more abrupt during extended sliding. Consequently, more fluctuations and outliers are prevalent in COF and wear rate data of aluminum base alloys. The performance metrics (R^2 values and error terms) of the ML algorithms greatly depend on the uniformity of the dataset. Decision tree-based RF outperformed other ML models in both COF prediction (R^2 value = 0.83, MSE = .0028, RMSE = 0.0529, MAE = 0.0324) and wear rate prediction (R^2 value = 0.81, MSE= 0.00001, RMSE =

0.0037, MAE = 0.0015). This can be attributed to the bagging mechanism employed by the RF algorithms in the tree building process which is more efficient in handling large fluctuations or inherent variability present in the tribological dataset. Feature importance analysis further revealed that normal load, sliding speed, and hardness have the maximum influence in predicting wear rate of aluminum base alloys. The variation in hardness, sliding distance, and tensile strength of the aluminum alloys influenced the COF prediction the most. Such findings from ML analysis can be used in material designing for specialized tribological applications.

3.6. References

1. Martínez, Susana Silva, Wendy López Benítez, Alberto A. Álvarez Gallegos, and P. J. Sebastián. "Recycling of aluminum to produce green energy." *Solar energy materials and solar cells* 88, no. 2 (2005): 237-243.
2. Macke, Anthony, B. F. Schultz, and Pradeep Rohatgi. "Metal matrix composites." *Adv. Mater. Processes* 170, no. 3 (2012): 19-23.
3. Molina, J-M., Martin Rhême, Julien Carron, and Ludger Weber. "Thermal conductivity of aluminum matrix composites reinforced with mixtures of diamond and SiC particles." *Scripta Materialia* 58, no. 5 (2008): 393-396.
4. Dwivedi, Dheerendra Kumar. "Wear behaviour of cast hypereutectic aluminium silicon alloys." *Materials & design* 27, no. 7 (2006): 610-616.
5. Ruiz-Andrés, M., A. Conde, J. De Damborenea, and Ignacio García. "Wear behavior of aluminum alloys at slow sliding speeds." *Tribology Transactions* 58, no. 5 (2015): 955-962.
6. Zhang, J., and A. T. Alpas. "Transition between mild and severe wear in aluminium alloys." *Acta materialia* 45, no. 2 (1997): 513-528.

7. Kuo, S. M., and D. A. Rigney. "Sliding behavior of aluminum." *Materials Science and Engineering: A* 157, no. 2 (1992): 131-143.
8. Chen, M., T. Perry, and A. T. Alpas. "Ultra-mild wear in eutectic Al–Si alloys." *Wear* 263, no. 1-6 (2007): 552-561.
9. Liu, Y., R. Asthana, and P. Rohatgi. "A map for wear mechanisms in aluminium alloys." *Journal of materials science* 26, no. 1 (1991): 99-102.
10. Deaquino-Lara, R., N. Soltani, A. Bahrami, E. Gutiérrez-Castañeda, E. García-Sánchez, and M. A. L. Hernandez-Rodríguez. "Tribological characterization of Al7075–graphite composites fabricated by mechanical alloying and hot extrusion." *Materials & Design* 67 (2015): 224-231.
11. Chu, Hsu-Shen, Kuo-Shung Liu, and Jien-Wei Yeh. "An in situ composite of Al (graphite, Al₄C₃) produced by reciprocating extrusion." *Materials Science and Engineering: A* 277, no. 1-2 (2000): 25-32.
12. Vencl, Aleksandar, Filip Vučetić, Biljana Bobić, Ján Pitel, and Ilija Bobić. "Tribological characterisation in dry sliding conditions of compocasted hybrid A356/SiCp/Grp composites with graphite macroparticles." *The International Journal of Advanced Manufacturing Technology* 100, no. 9 (2019): 2135-2146.
13. Yang, J. B., C. B. Lin, T. C. Wang, and H. Y. Chu. "The tribological characteristics of A356. 2Al alloy/Gr (p) composites." *Wear* 257, no. 9-10 (2004): 941-952.
14. Liu, Y. B., S. C. Lim, S. Ray, and P. K. Rohatgi. "Friction and wear of aluminium-graphite composites: the smearing process of graphite during sliding." *Wear* 159, no. 2 (1992): 201-205.

15. Lin, C. B., T. C. Wang, Z. C. Chang, and H. Y. Chu. "Tribological analysis of copper-coated graphite particle-reinforced A359 Al/5 wt.% SiC composites." *Journal of materials engineering and performance* 22, no. 1 (2013): 94-103.
16. Sharma, Pardeep, Krishan Paliwal, Ramesh Kumar Garg, Satpal Sharma, and Dinesh Khanduja. "A study on wear behaviour of Al/6101/graphite composites." *Journal of Asian ceramic societies* 5, no. 1 (2017): 42-48.
17. Ravindran, P., K. Manisekar, P. Rathika, and P. Narayanasamy. "Tribological properties of powder metallurgy–Processed aluminium self lubricating hybrid composites with SiC additions." *Materials & design* 45 (2013): 561-570.
18. Biswas, S. K., and BN Pramila Bai. "Dry wear of Al-graphite particle composites." *Wear* 68, no. 3 (1981): 347-358.
19. Lanka, Sridhar, Evgeniya Alexandrova, Marina Kozhukhova, Md Syam Hasan, Michael Nosonovsky, and Konstantin Sobolev. "Tribological and wetting properties of TiO₂ based hydrophobic coatings for ceramics." *Journal of Tribology* 141, no. 10 (2019).
20. Bowden, Frank Philip, Frank Philip Bowden, and David Tabor. *The friction and lubrication of solids*. Vol. 1. Oxford university press, 2001.
21. Hasan, Md Syam, and Michael Nosonovsky. "Lotus effect and friction: does nonsticky mean slippery?." *Biomimetics* 5, no. 2 (2020): 28.
22. Schmidt, Jonathan, Mário RG Marques, Silvana Botti, and Miguel AL Marques. "Recent advances and applications of machine learning in solid-state materials science." *npj Computational Materials* 5, no. 1 (2019): 1-36.

23. Gyurova, Lada A., and Klaus Friedrich. "Artificial neural networks for predicting sliding friction and wear properties of polyphenylene sulfide composites." *Tribology International* 44, no. 5 (2011): 603-609.
24. Graser, Jake, Steven K. Kauwe, and Taylor D. Sparks. "Machine learning and energy minimization approaches for crystal structure predictions: a review and new horizons." *Chemistry of Materials* 30, no. 11 (2018): 3601-3612.
25. Hasan, Md Syam, Amir Kordijazi, Pradeep K. Rohatgi, and Michael Nosonovsky. "Triboinformatics Approach for friction and wear prediction of al-graphite composites using machine learning methods." *Journal of Tribology* 144, no. 1 (2022).
26. Vencl, Aleksandar, Ilija Bobić, and Z. Mišković. "Effect of thixocasting and heat treatment on the tribological properties of hypoeutectic Al–Si alloy." *Wear* 264, no. 7-8 (2008): 616-623.
27. Rao, AK Prasada, K. Das, B. S. Murty, and M. Chakraborty. "Microstructural and wear behavior of hypoeutectic Al–Si alloy (LM25) grain refined and modified with Al–Ti–C–Sr master alloy." *Wear* 261, no. 2 (2006): 133-139.
28. Omrani, Emad, Afsaneh Dorri Moghadam, Pradeep L. Menezes, and Pradeep K. Rohatgi. "Influences of graphite reinforcement on the tribological properties of self-lubricating aluminum matrix composites for green tribology, sustainability, and energy efficiency—a review." *The International Journal of Advanced Manufacturing Technology* 83, no. 1 (2016): 325-346.
29. Chen, C. M., C. C. Yang, and C. G. Chao. "Dry sliding wear behaviors of Al–25Si–2.5 Cu–1Mg alloys prepared by powder thixocasting." *Materials Science and Engineering: A* 397, no. 1-2 (2005): 178-189.

30. Baradeswaran, A., and A. Elaya Perumal. "Wear and mechanical characteristics of Al 7075/graphite composites." *Composites Part B: Engineering* 56 (2014): 472-476.
31. Liu, Chi, Yilun Liu, Liyong Ma, and Jiuhuo Yi. "Effects of solution treatment on microstructure and high-cycle fatigue properties of 7075 aluminum alloy." *Metals* 7, no. 6 (2017): 193.
32. Nagaral, Madeva, V. Auradi, K. I. Parashivamurthy, B. K. Shivananda, and S. A. Kori. "Dry sliding wear behaviour of aluminium 6061-SiC-graphite particulates reinforced hybrid composites." In *IOP Conference Series: Materials Science and Engineering*, vol. 310, no. 1, p. 012156. IOP Publishing, 2018.
33. Yan, Guanhai, Shengdun Zhao, Shengqiang Ma, and Hongtao Shou. "Microstructural evolution of A356. 2 alloy prepared by the SIMA process." *Materials Characterization* 69 (2012): 45-51.
34. Albright, D. L., and David J. Dunn. "Wear behavior of iron and steel castings for the mining industry." *JoM* 35, no. 11 (1983): 23-29.
35. Gore, G. J., and J. D. Gates. "Effect of hardness on three very different forms of wear." *Wear* 203 (1997): 544-563.
36. Gopi, Vivek, R. Sellamuthu, and Sanjivi Arul. "Measurement of hardness, wear rate and coefficient of friction of surface refined Al-Cu alloy." *Procedia Engineering* 97 (2014): 1355-1360.
37. Dhokey, N. B., and K. K. Rane. "Wear behavior and its correlation with mechanical properties of TiB₂ reinforced aluminium-based composites." *Advances in Tribology 2011* (2011).
38. Aly, N. A. A., and M. R. El-Koussy. "Relationship between ductility and wear resistance of high Mn-steels." In *Surface Engineering*, pp. 640-651. Springer, Dordrecht, 1990.

39. Bellemare, S. C., M. Dao, and S. Suresh. "Effects of mechanical properties and surface friction on elasto-plastic sliding contact." *Mechanics of Materials* 40, no. 4-5 (2008): 206-219.
40. Rabinowicz, Ernest, and R. I. Tanner. "Friction and wear of materials." *Journal of Applied Mechanics* 33, no. 2 (1966): 479.
41. Basavarajappa, S., G. Chandramohan, K. Mukund, M. Ashwin, and M. Prabu. "Dry sliding wear behavior of Al 2219/SiCp-Gr hybrid metal matrix composites." *Journal of Materials Engineering and Performance* 15, no. 6 (2006): 668-674.
42. Ravindran, P., K. Manisekar, R. Narayanasamy, and P. Narayanasamy. "Tribological behaviour of powder metallurgy-processed aluminium hybrid composites with the addition of graphite solid lubricant." *Ceramics International* 39, no. 2 (2013): 1169-1182.
43. Jha, A. K., S. V. Prasad, and G. S. Upadhyaya. "Dry sliding wear of sintered 6061 aluminium alloy—graphite particle composites." *Tribology international* 22, no. 5 (1989): 321-327.
44. Archard, John Frederick, and Wallace Hirst. "The wear of metals under unlubricated conditions." *Proceedings of the Royal Society of London. Series A. Mathematical and Physical Sciences* 236, no. 1206 (1956): 397-410.
45. Akhlaghi, F., and A. Zare-Bidaki. "Influence of graphite content on the dry sliding and oil impregnated sliding wear behavior of Al 2024—graphite composites produced by in situ powder metallurgy method." *Wear* 266, no. 1-2 (2009): 37-45.
46. Mahdavi, S., and F. Akhlaghi. "Effect of the graphite content on the tribological behavior of Al/Gr and Al/30SiC/Gr composites processed by in situ powder metallurgy (IPM) method." *Tribology Letters* 44, no. 1 (2011): 1-12.

47. Guo, ML Ted, and C-YA Tsao. "Tribological behavior of self-lubricating aluminium/SiC/graphite hybrid composites synthesized by the semi-solid powder-densification method." *Composites science and technology* 60, no. 1 (2000): 65-74.
48. Baradeswaran, A., and A. Elayaperumal. "Effect of graphite content on tribological behaviour of aluminium alloy-graphite composite." *European Journal of Scientific Research* 53, no. 2 (2011): 163-170.
49. Gibson, P. R., A. J. Clegg, and A. A. Das. "Wear of cast Al-Si alloys containing graphite." *Wear* 95, no. 2 (1984): 193-198.
50. Basavarajappa, S., G. Chandramohan, K. Mukund, M. Ashwin, and M. Prabu. "Dry sliding wear behavior of Al 2219/SiCp-Gr hybrid metal matrix composites." *Journal of Materials Engineering and Performance* 15, no. 6 (2006): 668-674.
51. Dwivedi, Dheerendra Kumar. "Wear behaviour of cast hypereutectic aluminium silicon alloys." *Materials & design* 27, no. 7 (2006): 610-616.
52. Kaiser, Mohammad Salim, Sakib Hasan Sabbir, Mohammad Syfullah Kabir, Mashiur Rahman Soummo, and Maglub Al Nur. "Study of mechanical and wear behaviour of hyper-eutectic Al-Si automotive alloy through Fe, Ni and Cr addition." *Materials Research* 21 (2018).
53. Kumar, Parveen, and M. F. Wani. "Friction and wear behaviour of hypereutectic Al-Si alloy/steel tribopair under dry and lubricated conditions." *Jurnal Tribologi* 15 (2017): 21-49.
54. Liu, Gang, Guodong Li, Anhui Cai, and Zhaoke Chen. "The influence of Strontium addition on wear properties of Al-20 wt% Si alloys under dry reciprocating sliding condition." *Materials & Design* 32, no. 1 (2011): 121-126.
55. Sarkar, A. D., and J. Clarke. "Friction and wear of aluminium-silicon alloys." *Wear* 61, no. 1 (1980): 157-167.

56. Torabian, Hamid, J. P. Pathak, and S. N. Tiwari. "Wear characteristics of Al-Si alloys." *Wear* 172, no. 1 (1994): 49-58.
57. Singh, Kalyan Kumar, Saurabh Singh, and Anil Kumar Shrivastava. "Comparison of wear and friction behavior of aluminum matrix alloy (Al 7075) and silicon carbide based aluminum metal matrix composite under dry condition at different sliding distance." *Materials Today: Proceedings* 4, no. 8 (2017): 8960-8970.
58. Hekmat-Ardakan, Alireza, Xichun Liu, Frank Ajersch, and X-Grant Chen. "Wear behaviour of hypereutectic Al–Si–Cu–Mg casting alloys with variable Mg contents." *Wear* 269, no. 9-10 (2010): 684-692.
59. Ul Haq, Mir Irfan, and Ankush Anand. "Friction and wear behavior of AA 7075-Si₃N₄ composites under dry conditions: effect of sliding speed." *Silicon* 11, no. 2 (2019): 1047-1053.

CHAPTER 4: FRICTION AND WEAR MODELING OF GRAPHITE AND GRAPHENE REINFORCED ALUMINUM METAL MATRIX COMPOSITES USING TRIBOINFORMATICS APPROACHES

In the previous chapter, correlations of friction and wear of aluminum alloys with their material properties, processing procedure, and tribological test variables had been studied using traditional and Triboinformatics approaches. The friction and wear mechanisms in aluminum-graphite and aluminum-graphene metal matrix composites (MMC) are significantly different than those of aluminum base alloys. Graphite and graphene embedded in the aluminum matrix act as a solid lubricant during sliding interaction that affect the friction and wear behavior in these MMCs. In this chapter, ML models have been developed to predict the friction and wear behavior of these MMCs in dry conditions and to establish correlations between material properties, tribological test conditions, and tribological properties.

4.1. Introduction

Metal matrix composites (MMCs) are often preferred over the base alloys in many engineering applications due to their improved material properties. For example, aluminum MMCs are more attractive than monolithic aluminum alloys for weight critical aerospace and automobile industry and for tribological applications [1-2]. Though aluminum alloys are known for their high stiffness, strength, and corrosion resistance, they exhibit poor tribological performance and suffer a seizure in dry sliding or with insufficient lubrication [3-4]. Suitable particles, for example, ceramic, graphite, graphene, or fiber-reinforced aluminum MMCs can be attractive alternatives having superior mechanical and tribological properties. Aluminum composites reinforced with ceramic particles have been considered by many researchers for improved strength and tribological

performance [5-6]. Powder metallurgy, stir casting, centrifugal casting, and conventional casting are some of the processing routes of these MMCs. However, poor dispersion of ceramic particles in the aluminum matrix, increasing brittleness, and inferior machinability are some of the undesired properties associated with these composites.

Self-lubricating Al/Graphite particles composites are the promising low-cost materials to reduce friction, wear, and the tendency of seizing. Graphite has a hexagonal structure where the carbon atoms are arranged in layers. The atoms in the plane of a layer share strong covalent bonds, while the layers are bonded by weak van der Waals bonds which allows them to shear past each other easily. The layered structure in graphite makes it strong in compression but weak in shear. This is the reason for the inherent quality of lubricity in graphite [7]. In aluminum MMCs, graphite acts as a solid lubricant and improves the tribological properties. In graphite reinforced aluminum (Al/Gr) MMCs, the continuous supply of the solid lubricant between the two sliding surfaces is ensured by incorporating graphite particles into the aluminum matrix. Rohatgi et al. reported that the friction and wear of the Al/Gr MMCs are characterized by the transient process followed by the steady state [1,2]. At first, the graphite particles of the MMCs are squeezed out from the embedded state and smeared on the surface reducing surface to surface contact and forming a lubricating film. The graphite film is continuously replenished since newly exposed graphite particles due to wear contribute to the lubricating film. Embedding solid lubricating graphite particles in the matrix has an advantage over self-lubricating graphite coatings, which wear off after short periods.

Tribological behavior of self-lubricating Al/Gr MMCs has been studied since the synthesis of low-cost cast aluminum graphite composites around 1965. Low friction and wear properties of these materials have been documented by several researchers [8-15]. Low thermal expansion,

improved antiseizure properties [16-17], high damping behavior [18], and reduced temperature rise at the contact surface [6,19] are some other attractive features of these composites. On the other hand, mechanical properties including ductility, hardness, and fracture toughness of the MMCs can decrease with the addition of large graphite particles to the metal matrix [20-22]. Several other studies reported the optimization of mechanical and tribological properties by controlling graphite content and other variables [20, 23]. The friction and wear of Al/Gr MMCs are influenced by material variables such as matrix characteristics, graphite content, size and shape of the graphite particles, and material processing procedure [24-25]. Tribological test variables like the normal load, sliding velocity, and sliding distance are also important factors. However, since such a large number of variables influence the mechanical and tribological properties of Al/Gr composites, the effects of multiple-parameter variations have not been quantified, despite considerable investigation of two-parameter relationships. The multi-parameter study requires data-driven approaches.

Though the self-lubricating aluminum-graphite MMCs possess improved thermal, tribological, and antiseizure properties, mechanical properties including tensile strength, hardness, ductility, and fracture toughness can deteriorate with the incorporation of large graphite particles [20,22]. However, recent studies on self-lubricating aluminum-graphene MMCs have revealed that superior tribological and mechanical properties can be achieved at the same time using graphene as the reinforcement material [26].

Graphene has a two-dimensional honeycomb lattice structure with compactly packed single atomic carbon sheets [24]. The unique friction and wear properties of graphene separate it from conventional materials. Being ultrathin in both single and multilayers with atomically smooth surfaces, graphene can be used in nanoscale and microscale applications. The extremely high

mechanical strength of graphene is one of the reasons behind its excellent wear resistance [27]. Using the nanoindentation technique in atomic force microscopy (AFM) for monolayer graphene membranes, Lee and coworkers [28] identified graphene as the strongest material ever quantified. They reported the tensile strength and the Young's modulus (E) of defect-free monolayer graphene as 130 GPa, and 1 TPa, respectively. In a separate study, Lee et al. [29] measured the tensile strengths of bi and trilayer graphene as 126 and 101 GPa, and the Young's moduli as 1.04 and 0.98 TPa, respectively. MMCs possess mechanical and material properties which are a combination of those of the matrix and the reinforcement materials. For example, MMCs often obtain similar toughness and ductile nature of the matrix material and strength and moduli of the reinforcement material. Moreover, due to the plate shape, the dispersion of graphene in the matrix phase is more convenient than other carbon-based reinforcements like graphite or carbon nanotubes (CNTs) [30]. With superior mechanical properties besides easy shear capability, excellent electrical, optical, and thermal properties, graphene can be an ideal material as the reinforcement phase in self-lubricating MMCs.

Manufacturing processes and the corresponding mechanical properties of graphene reinforced aluminum MMCs have been reported in many recent research publications [24, 28-31]. The mechanical strength of these MMCs relies on the dispersion of the graphene as a reinforcement in the metal matrix. A nonuniform dispersion due to the agglomeration of particles may adversely affect the strengths. For example, Wang and co-workers [18] reported an increase in the tensile strength of the aluminum-graphene MMC compared to the aluminum base alloy by 62% using 0.3 wt% of graphene nano-sheets as the reinforcement phase. El-Ghazaly and co-worker [31] reported a 20.4% and 21.6% increase in tensile strength and a 104% and 127% increase in yield strength for 3 and 5 wt% of graphene, respectively, in the aluminum AA2124 matrix. Alipour et al. [32]

also reported similar increases in the tensile strength for 0.1-1 wt% of graphene nanoplatelets addition in aluminum AA7068 matrix. On the contrary, several researchers including Bartolucci and co-workers [33] reported a decrease in tensile strength in aluminum-graphene MMCs due to graphene addition. However, graphene nanoparticle reinforced aluminum MMCs are reported to have higher hardness compared to base alloys, macroparticle reinforced (graphite) MMCs or even CNT reinforced MMCs [34].

A number of recent studies have reported the tribological behavior of aluminum-graphene MMCs to date [24, 31, 32, 34-56]. During sliding application, after a brief running-in period, the tribosurface of the aluminum-graphene MMC is covered with soft lubricating films of graphene. With further sliding, due to extensive smearing of graphene, a continuously replenishable, stable graphene-rich solid-lubricating film is formed at the interface [31, 36, 46]. Similar to self-lubricating aluminum-graphite MMCs, the graphene lubricant film separates the sliding surfaces, inhibits metal-on-metal contact, and lowers the friction and wear. However, with superior mechanical strength and hardness, graphene nanoparticle reinforced aluminum MMCs are expected to exhibit superior tribological performance as compared to graphite macroparticle reinforced MMCs [24]. Tribological behavior, which is a system response rather than a material property, is of paramount importance for designing and synthesizing machine elements involving sliding, rotating, and oscillating contacts. Friction and wear of aluminum-graphene MMCs follow complex mechanisms, and a proper understanding and characterization of these behaviors may help in designing efficient systems for tribological applications. However, this is a challenging task as the complex friction and wear behavior of such two-phase materials depend on numerous material, mechanical, and tribological variables. Most of the traditional studies on aluminum-graphene MMCs have tried to characterize the friction and wear behavior using isolated

experiments and studying 2-parameter relationships. In such an analysis, the coefficient of friction (COF) or wear rate is presented as a function of a single variable with a few experimental data considering other parameters as constants. Such a simple approach of presenting complex tribological correlations is often inadequate, and not efficient to generate a comprehensive understanding. However, a data-driven approach incorporating the effect of multiple variables simultaneously in a wider range can overcome the shortcomings of the 2-parameter analysis.

As seen from the above, the absence of mathematical derivations from the first principles of physics and chemistry is a major challenge in the tribological study [57]. However, a data-driven approach in tribological studies, popularly known as “Triboinformatics” has been successfully applied to anticipate the wear and friction characteristics of aluminum alloys and aluminum-graphite MMCs from tribological test conditions and mechanical and material properties [58-60]. Hasan and co-workers [61] further used standalone and hybrid models to understand the wear and friction of aluminum-graphite MMCs during the progression between lubrication conditions. Such a data-driven approach can reveal novel insights and present a broader understanding of the friction and wear phenomena observed in aluminum-graphene MMCs.

In this chapter, friction and wear mechanisms of aluminum-graphite and aluminum-graphene MMCs and the effect of different material and tribological test variables on their tribological behaviors will be systematically studied. Finally, ML models will be developed using tribological data reported in the literature to predict the tribological behaviors of these aluminum MMCs and to find patterns in their tribological characteristics.

4.2. Friction mechanisms in aluminum-graphite and aluminum-graphene MMCs

Friction and wear are behind the processes of material deterioration and energy dissipation of dynamic systems and are the central aspects of tribological studies. For multi-phase metal matrix composite materials like aluminum-graphite and aluminum-graphene, the proper characterization of the friction and wear mechanisms is a challenging task. In this section, we present the mechanisms of friction and wear observed in these MMCs.

Friction is the resistance of motion between interacting surfaces and is often quantified by the dimensionless coefficient of friction (COF) or μ [62, 63]. The following equation involving the friction force (F_f) and the normal load (N) quantifies the COF between the surfaces.

$$\mu = \frac{F_f}{N} = \frac{F_a + F_d}{N} = \frac{F_a}{N} + \frac{F_d}{N} = \mu_a + \mu_d \quad (1)$$

μ_a , the COF due to the adhesion between the sliding surface is caused by the molecular forces acting in covalent, ionic, metallic, and van der Waals bonds [64]. μ_d is the COF due to the microscopic and macroscopic deformation of asperities of the tribosurface and is influenced by mechanical and material properties like hardness, strength, and modulus. The real area of the asperity contact between the sliding surfaces controls the adhesion component of friction.

. The F_a and μ_a are strongly influenced by the microstructure including the presence of second phase particles like graphite, lubricants, surface films, and contaminants. They prevent the direct contacts between the mating surfaces and impede strong adhesion. When a graphite reinforced MMC slides against another surface, a thin film of graphite solid lubricant covers the interface reducing F_a and μ_a . The COF of the two-phase material containing graphite depends on the extent of graphite film formation on the tribosurface [1]. According to the rule of mixture, the COF can be expressed by the following equation.

$$\mu = (1 - A_g)\mu_m + A_g\mu_g \quad (2)$$

where μ_m and μ_g are the COFs of the matrix material and the tribosurface covered by the graphite film respectively, and A_g is the fraction of the tribosurface covered by the graphite film. The COF of the matrix is the sum of the adhesion and deformation components

$$\mu_m = \mu_{ma} + \mu_{md} \quad (3)$$

Microscopic and macroscopic deformations of the asperities of the interlocked surfaces facilitate the deformation component of friction. The latter is highly dependent on material properties such as hardness, yield strength, and elastic properties. The hardness, yield strength, and deformation behavior of Al alloys are influenced by the incorporation of graphite particles in the matrix, and therefore the friction and wear are influenced by the presence of graphite particles in the matrix.

For aluminum-graphene MMCs, after a brief running-in period, due to smearing of graphene the tribosurface is covered with soft graphene tribofilms [31, 36, 46]. With further sliding, a stable solid-lubricating graphene film is formed at the interface that reduces the real area of the asperity contact between the MMC and the counterface. With the diminution of the real area of the asperity contact and reduced metal-on-metal contact, the adhesive component of the COF reduces significantly. Moreover, mechanical and material properties like hardness, tensile strength, and ductility undergo significant improvement due to the graphene additions to an aluminum matrix. As a result, a decrease in the deformation component or the plowing component of friction occurs against the same harder counterface material like steel. As, both the adhesive and deformation components of the COF are reduced, a low overall COF is expected for aluminum-graphene MMCs.

4.3. Wear mechanisms in aluminum-graphite and aluminum-graphene MMCs

The wear mechanism governs the progressive removal of material from the surfaces sliding against one another taking place under different loading conditions. Analysis of the worn surface can reveal the dominant wear mechanisms for a material pair. In the tribological application of aluminum MMCs, the dominant wear mechanisms involve adhesive, abrasive, and delamination wear [65].

Adhesive wear is caused by the adhesion between the sliding surfaces. At spots of asperity contacts, strong interatomic adhesive junctions are formed due to intermolecular forces and cold welding. A relative motion between the mating surfaces results in shear at the adhesive junctions. Plastic deformation and surface fracture at asperity level cause detachment and transfer of materials from one surface to another.

Subsurface cracking at a certain depth under the surface due to the accumulation of dislocations generate the laminate wear debris. Crack initiation and propagation at the subsurface are dependent on tribological variables, material properties, and friction properties of the surface. When the crack exceeds a critical length, it propagates unstably and generates a thin laminate of the softer material as wear debris.

In aluminum-graphite MMCs, the wear behavior depends upon the wear of the matrix and graphite originally present in the composites and the formation of the graphite film over the tribological interface. At the starting of the sliding or when graphite content is low, the interface is only partially covered by the graphite film. At this point, due to a direct metal to metal contact, a high wear rate is observed. With increasing graphite content, the tribosurface is extensively covered by the graphite film and a superior wear behavior is observed. When a stable graphite film has been established and its thickness has exceeded a critical value, the delamination wear mechanism becomes dominant for these composites. Subsurface cracking occurs as the softer

asperities of the graphite film is deformed by the counterface. Under repeated loading, as the crack exceeds the critical length, the material between the surface, and the subsurface-crack shears. Finally, delamination wear occurs.

The wear mechanisms in aluminum-graphite MMCs are highly dependent on material properties and tribological test parameters. Wear resulting from adhesion, abrasion, and delamination are also related to hardness, applied normal load, and the sliding distance. While various attempts to create comprehensive models of friction and wear have been made [1,65,66], it is still extremely difficult to take into account all complex interactions involved. This is why looking for data correlations may be more helpful.

For aluminum-graphene MMCs, the graphene film provides lubrication at the tribosurface and limits the cold welding and adhesive junctions between asperities during the sliding contact [31, 46]. Consequently, an overall smaller wear rate compared to aluminum alloys is observed. Several tribological studies on aluminum-graphene have reported adhesive wear as the dominant wear mechanism [31, 35].

Besides material properties, the operating condition plays a vital role in defining the dominant wear mechanism. According to Archard and Hirst [67], the wear during sliding interaction can be either mild or severe based on the normal load. These two wear regimes cause distinct wear behavior, and the transition between these two occurs at a critical load. A similar change in the wear pattern is observed for the sliding speed as well. The mild wear regime is characterized by a smaller wear rate where abrasion often becomes the dominant wear mechanism. Smoother worn surface and the presence of fine grooves in the sliding direction indicate abrasive wear in aluminum-graphene MMCs. In mild wear, the graphene film remains operational and contributes to limiting the wear [31,68,69].

The transition between mild to severe wear is indicated by a sudden increase in wear rate that occurs at a higher load or sliding speed (beyond the critical values). The lubricating film is often destroyed or is no longer able to protect against severe wear. Delamination is often reported as the prevalent wear mechanism in severe wear [24]. Accumulation of dislocations, initiation of crack at a subsurface level, and poor mechanical properties due to an ununiform mixing of the matrix and reinforcement phases are some of the prerequisites of the delamination wear. Delamination wear is characterized by the removal of thin laminates as wear debris due to unstable crack propagation at the subsurface level of the tribosurface. Comparing the worn surfaces, El-Ghazaly and co-workers [31] reported that the delamination, craters, and scratches on aluminum-graphene MMCs are notably less than those of base aluminum alloys.

4.4. Variables influencing friction and wear

Tribological variables and material variables are two distinct types of variables influencing the wear and friction of aluminum-graphite and aluminum-graphene MMCs. Here, the effect of these variables on friction and wear of these MMCs will be discussed using traditional analysis.

4.4.1. Material variables

Material variables are quantitative material or microstructural properties, or parameters directly related to the processing procedure, which affect the tribological behaviors. For analyzing the friction and wear of aluminum graphite and aluminum-graphene MMCs, manufacturing process, heat treatment, graphite content, graphene content, type of graphene, aluminum content, density, the composition of the matrix, and mechanical properties such as tensile strength, ductility, and hardness are some of the crucial material variables.

4.4.1.1. Effect of graphite content

The friction and wear of the aluminum-graphite MMCs depend on the volume fraction, size, and shape of graphite particles, matrix microstructure, matrix-reinforcement bonding and the graphite film formation on the tribosurface. Besides that, tribological behavior depends upon two contrasting factors [21]. First, addition of graphite particles reinforcement above certain sizes often negatively affects mechanical properties including ductility, hardness, and fracture toughness of the MMC. Particle agglomeration and weak bonding between the Al matrix and graphite particles may also lead to crack propagation during sliding contact. Increasing graphite content leads to crack propagation and delamination of the reinforcement phase due to its weaker bonding with the matrix. These factors can potentially increase wear of aluminum-graphite composites. On the other hand, during sliding, once the metallic layer masking the graphite layer wears away, the graphite particles are squeezed out from the matrix under normal and shear stresses, and they spread over the surface forming an in situ tribofilm of graphite solid lubricant, which reduces friction [1]. Using Auger spectroscopy, Rohatgi et al. found that on the tribosurface of Al/10% vol.% Graphite composites, the major elements are Al, C, and O [8]. A clear indication of graphite smearing was observed as about 30% volume percentage of the tribosurface is covered by the graphite film. With increasing graphite content, the thickness of the film on the tribosurface increased. The formation of the solid lubricant film between asperities reduces metal-metal contact and thus reduces friction.

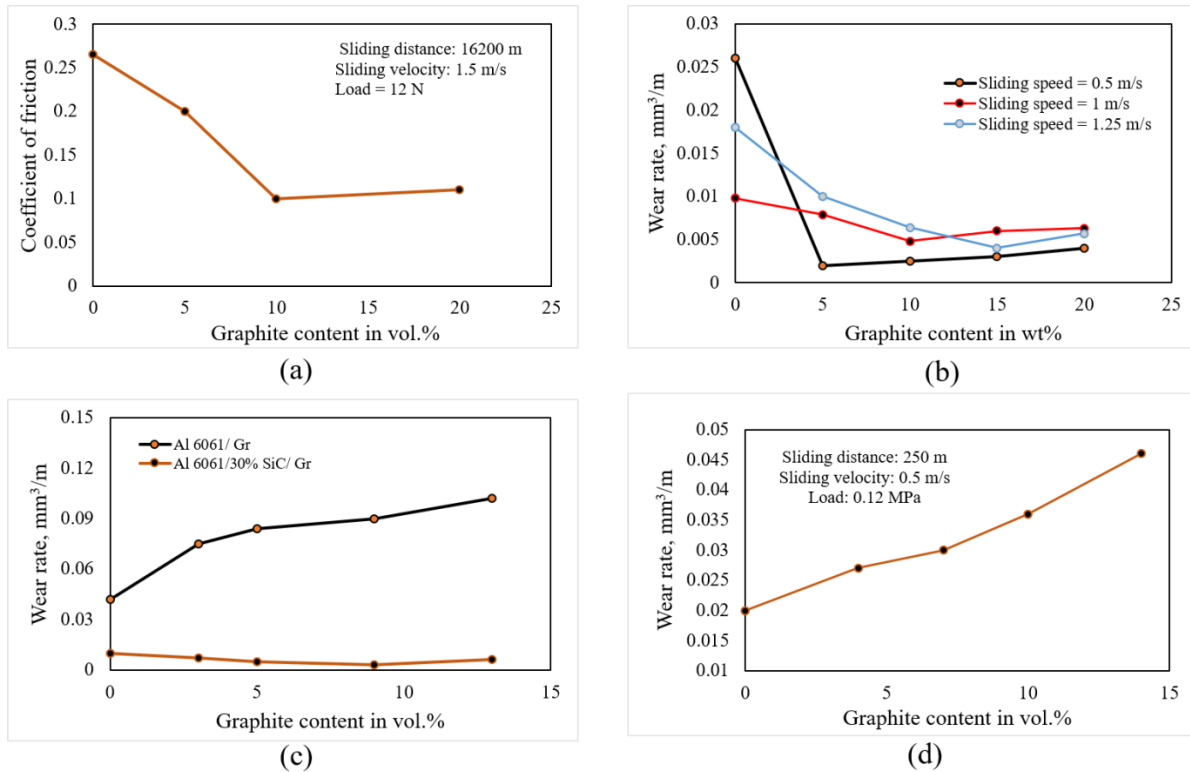


Figure 4.1. Dependencies on the graphite content of (a) the COF (Al 6061/ Gr) [10], and (b) wear rate, Al 6061/Gr [70], (c) Al 6061/Gr and Al 6061/30% SiC/Gr [22], (d) Al 6061/7% Gr composites [71] for sliding against steel.

Having these two countering effects, aluminum-graphite MMCs could have an optimum composition when both the wear rate and the COF are at minimum. Akhlaghi et al [20], Ravindran et al. [72], Baradeswaran et al. [23] reported that the wear rate decreases significantly with increasing graphite content and reaches the minimum value at 5% graphite content, which they described as the optimum composition from the wear standpoint. With a further increase in graphite content, the wear rate increases though it is significantly lower than the base aluminum alloys. Similar results were reported for COF (**Figure 4.1(a)**), where the COF reduced sharply with graphite content, reached a minimum value, and then again increased with further graphite addition [10, 15, 20, 23, 72]; the reason as to why the COF increases above a certain percentage

of graphite is not clear. In another study, Baradeswaran and co-worker reported that the optimum graphite content for minimum wear rate varies with tribological test parameters, including sliding velocity [70]. They observed the minimum wear rate at 5%, 10%, and 15% graphite content for sliding velocities of 0.5 m/s, 1 m/s, and 1.25 m/s respectively for Al 6061/Gr composites (**Figure 4.1(b)**). The optimum graphite content for COF was dependent on other parameters as well.

In another study, Mahdavi and co-workers reported that for Al 6061/ Graphite composites, the wear rate increased with increasing graphite addition (**Figure 4.1(c)**). A similar finding about wear rate was reported by Jha and co-workers (**Figure 4.1(d)**) [71]. Mechanical properties like ductility or fracture toughness and surface properties like porosity were reported as the possible reasons for this unusual wear behavior of Al 6061/Graphite composites. With increasing graphite content in the Al matrix, the tendency of crack propagation and delamination of the reinforcement phase increase. The increased amount of porosity with increasing graphite content can speed up the crack propagation process by decreasing the required linking length between two cracks.

4.4.1.2. Influence of graphene content

The incorporation of graphene in the matrix material causes a direct enhancement in the tribological performance of the composites. The single or multi-layer graphene embedded in the matrix serves as a solid lubricant that provides lubrication during sliding application. Additionally, the presence of graphene modifies mechanical properties including hardness and tensile strength that impact the tribological characteristics of these MMCs.

4.4.1.2.1. Graphene as a solid lubricant

The lowering of the COF and wear rate of aluminum-graphene MMCs due to graphene addition is achieved through two underlying mechanisms: increase of hardness and tribofilm formation [68].

The increase of hardness of the MMC due to graphene addition is achieved through Orowan strengthening, load transfer, grain refinement, and the mismatch of CTE between graphene and the aluminum matrix [68]. As the Archard equation correlates hardness to be inversely proportional to wear, an increase in hardness caused by graphene addition effectively lowers the wear rate. The wear rate vs. graphene content plots (**Figure 4.2(a)**) for aluminum-graphene MMCs show a consistent lowering in the wear rate with graphene addition. A sharp decrease is observed at a smaller graphene content and then a more gradual decrease is observed up to a critical graphene content where the wear rate is the minimum. Often a slight increase in the wear rate is observed after the optimum graphene content. It could be due to an increase in brittleness of aluminum-graphene above a certain level of graphene in the matrix. However, this slight increase is not as drastic as the increase in wear rate that would be achieved by lowering the graphene content.

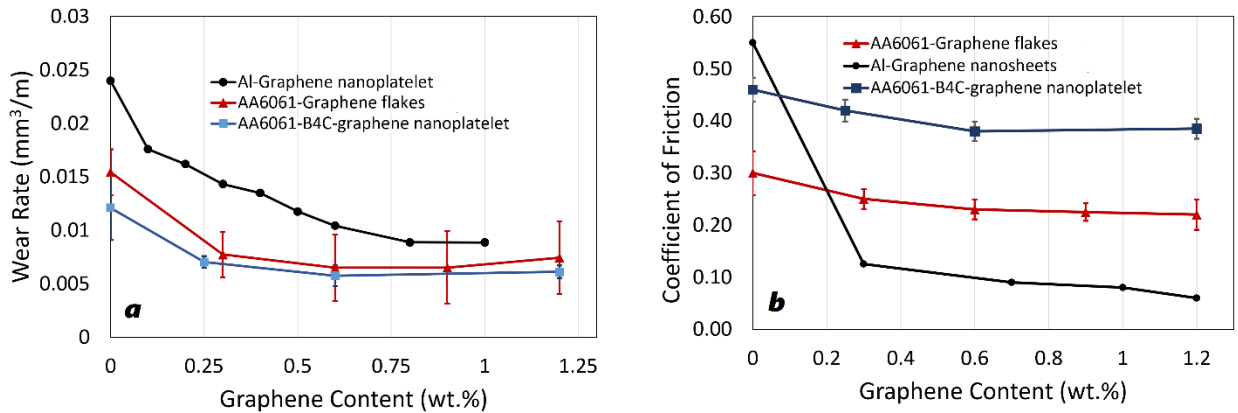


Figure 4.2. Effect of graphene content on (a) wear rate [41,44,48] (b) COF [38,41,44] of aluminum-graphene MMCs

The graphene-rich tribofilm formation depends on the graphene nanosheets in the bulk that smear on the tribosurface during sliding wear [69]. The successful formation of a stable micro tribofilm causes a diminution of the max peak (R_p) and max valley (R_v) of the surface profile and lowers the contact between asperities of the mating surfaces [44]. Consequently, the tribofilm effectively smoothens the tribosurface and minimizes direct metal-on-metal interaction and the frictional heat during the sliding interaction [41]. The COF vs graphene content plots (**Figure 4.2(b)**) for aluminum-graphene MMCs show a consistent decrease in the COF with graphene addition. After increasing graphene content slightly from 0 wt.%, the COF decreases significantly. Further increases in the graphene content above a critical value cause further smaller decreases in COF, but the decrease is not quite as sharp as the initial decrease.

The type of graphene (graphene nanoplatelets, graphene microplatelets, graphene flakes, monolayer graphene, graphene oxide, reduced graphene oxide, multilayer graphene, etc.) as the reinforcement phase and the number of graphene layers influences the extent to which the friction and wear are lowered. The frictional force has been reported to decrease with the number of graphene layers [73]. Interlayer sliding in multilayer graphene, graphene nanosheets, and even in graphene nanoparticles is responsible for the reduction of the frictional force [68]. Berman et al. [27] further experimentally demonstrated that the multilayer graphene (3-4 layers) has a longer lifespan than the monolayer graphene and is more durable against sliding wear. The interlayer sliding between nanolayers of graphene in aluminum-graphene MMCs is a major reason behind the superior friction performance of these MMCs compared to aluminum-graphite MMCs.

4.4.1.2.2. Graphene addition and mechanical properties

Mechanical properties including hardness, ductility, strength, and elastic modulus of aluminum MMCs are dependent on the size of the reinforcement particles. Large reinforcement particles or particle agglomeration in the aluminum matrix adversely affects mechanical properties by promoting defects such as pores and cracks. Material hardness and tensile strength of aluminum-graphene MMCs with respect to graphene content are presented in **Figure 4.3**. Almost similar trends are observed across studies where the tensile strength and hardness increase with graphene addition until a certain point, and then exhibit a downward trend with further increases.

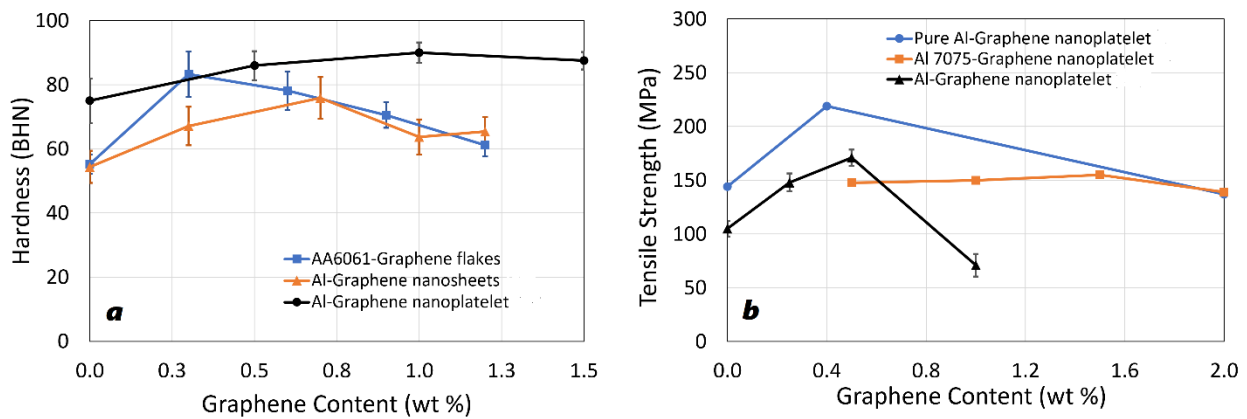


Figure 4.3. Effect of graphene content on (a) hardness [38,39,44] and (b) tensile strength [74,75,76] of aluminum-graphene MMCs

A uniform dispersion and orientation of graphene in the aluminum matrix promotes a better bonding between the matrix and the reinforcement phase and attain superior mechanical properties in aluminum-graphene MMCs. Shahzad et al. [41] reported that uniform dispersion of graphene nanoplatelets (GNPs) in aluminum matrix resulted in an efficient load transfer, citing this as the reason for the increase in strength of the composites. They also observed more graphene shearing at the tribosurface and deterioration of mechanical performance for 1.2 wt.% graphene compared to 0.6 wt.% graphene as the reinforcement. They attributed this to the weight fraction being too

high for the GNPs to uniformly disperse within the matrix. Kumar and co-workers [40] reported that graphene addition at and above 1.2 wt.% can cause agglomeration, which weakens the structure by increasing porosity and cracks. Furthermore, significant agglomeration of graphene causes serious defects in aluminum-graphene MMCs and promotes premature failure of the composites [68].

Several strengthening mechanisms including coefficient of thermal expansion (CTE) mismatch, load transfer, grain refinement strengthening, and Orowan strengthening have been reported for aluminum-graphene MMCs with graphene addition [68]. The CTE mismatch increases the strength of the composites through interfacial prismatic punching of dislocations. The load transfer depends on the matrix-reinforcement bonding and works especially well with types of graphene reinforcements that have high aspect ratios. In the case of GNPs, the 2D structure and crumpled surface increase the interfacial contact with the aluminum matrix [41]. The grain refinement strengthening is explainable by the Hall-Petch relationship [68]. In the Orowan bypass mechanism, inserting nanometer-scale particles such as GNPs forms residual dislocation loops, whose resulting back stress increases the strength by repelling the motion of the dislocation [41].

4.4.1.3. Effect of matrix material

Properties of the aluminum alloys used as the matrix phase in aluminum-graphene MMCs influence the mechanical and tribological behavior. The addition of different alloying elements with the pure aluminum alloys enhances mechanical properties like strengths, elastic modulus, and hardness. Dispersion of graphene in the aluminum matrix, bonding between the matrix and the reinforcement phase, and the possibility of any chemical reaction depend on the unique microstructural properties of different aluminum alloys. Consequently, different friction and wear

characteristics including wear resistance and critical load for the transition from mild to severe wear can be notably different in aluminum MMCs depending on the matrix alloy.

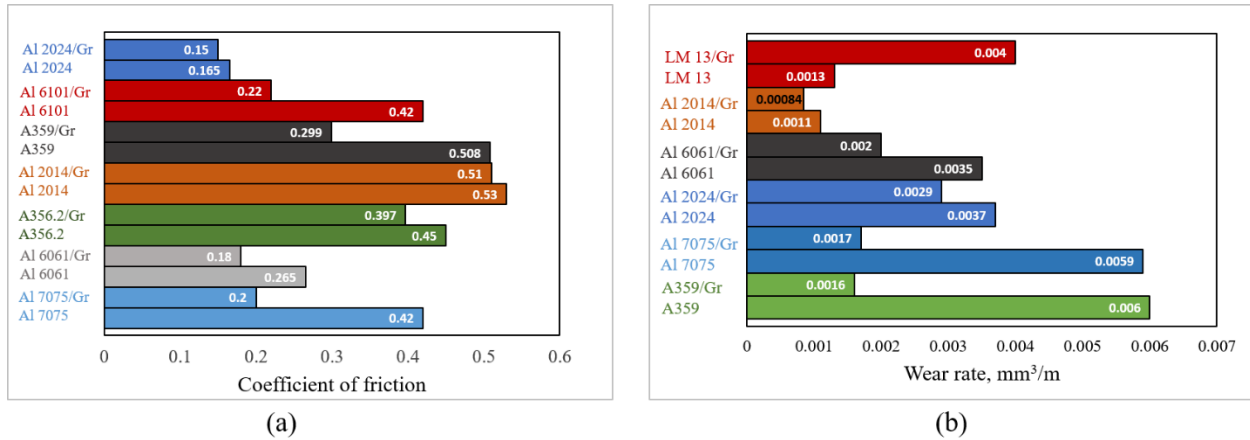


Figure 4.4. Comparison of (a) the COF [9,10,13,14,23,77-79] and (b) wear rate [9,10,12,14,23,78,79] between different Al base alloys and their graphite (Gr) MMCs (5 wt.% Gr).

Comparative representation of the COF and wear rates between different aluminum base alloys and their corresponding MMCs containing graphite (5 wt.%), are represented in **Figure 4.4(a)** and **Figure 4.4(b)**, respectively. The COF of the base alloys without any graphite significantly varied with alloy composition in the range 0.165 to 0.53. The same is true for wear rate that varies between 0.0011 mm³/m to 0.006 mm³/m. The tribological behavior improvement of the MMCs with graphite addition greatly depended on the matrix alloys. In all cases, for every aluminum alloy composition, the COF and wear rate decreased with the incorporation of graphite particles (5 wt.%) in their matrices (except LM 13). However, the amount of decrease in COF and wear rate is different for different base alloys. The COF for 5 wt.% graphite containing aluminum alloys ranges from 0.15 to 0.51. However, the minimum COF (0.08) and wear rate (0.00038 mm³/m) under dry condition were reported for Al 6061 alloy with 8.9 wt.% graphite, and A359

alloy with 8 wt.% graphite respectively [24, 78]. Among different alloys, a significant reduction of COF was observed in Al 7075, Al 6061, A359, and Al 6101 alloys while better wear performance was observed in A359, Al 6061, Al 2014, and Al 7075 alloys as a result of incorporation of graphite particles in the matrix. Composition of the base alloys, processing procedure, microstructure, and several other factors can be responsible for this.

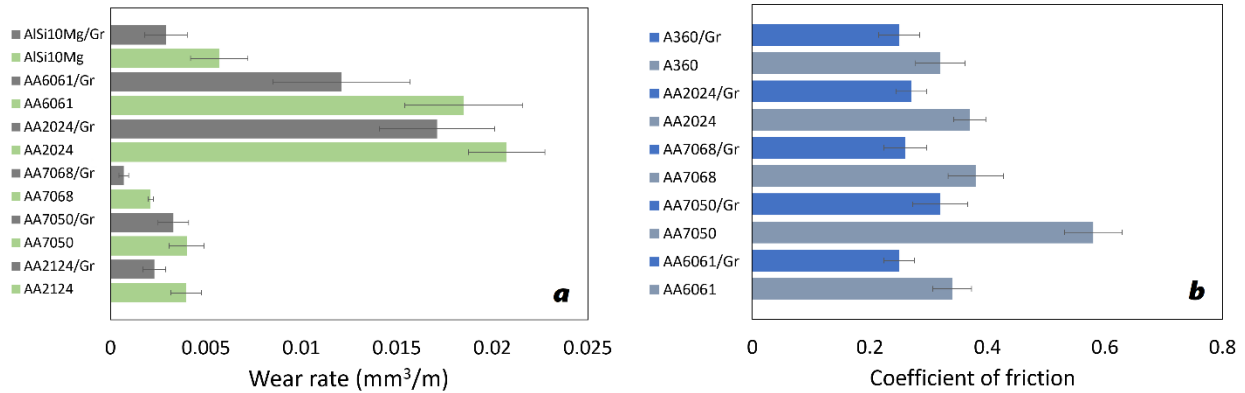


Figure 4.5. (a) wear rate and [32, 36, 37, 40, 44, 80] (b) coefficient of friction [32, 37, 40, 44, 45] of different aluminum base alloys and their corresponding aluminum-graphene (Gr) composites

The average wear rate and COF of different unreinforced aluminum alloys and their graphene-reinforced (0.25 wt.% - 0.5 wt.%) composites at comparable loading and testing conditions are presented in **Figure 4.5(a)**. The aluminum-graphene MMCs consistently showed reduced friction and reduced wear compared to the corresponding unreinforced alloys (**Figure 4.5(b)**). However, the difference in COF and wear rate is more pronounced for some alloys than others. Also, a significant decrease in wear rate does not necessarily occur with a significant decrease in COF, and vice versa. For example, AA7075 showed the most drastic decrease in COF for 0.3 wt.% of graphene addition, while the decrease in wear rate was comparatively small for the same composition [37].

4. 4.1.4. Effect of the manufacturing process and heat treatment

Powder metallurgy, casting, and spray deposition are the common processing techniques used for synthesis of aluminum-graphite MMCs. The synthesis of the composites using powder metallurgy (PM) involves the mixing of aluminum and graphite in the powder phase, compacting, and sintering [20]. The large size and regular shape (spherical) of the powder ensure better distribution and mixing of the particles [1]. Casting is another popular processing technique for Al/Graphite composites due to its ability to manufacture complex shapes at a relatively lower cost. Pressure infiltration and stir mixing followed by casting are the two major types of casting techniques used for the synthesis of Al/Graphite MMCs. Squeeze casting is a common example of an impregnation method where a pressure differential governs the liquid metals into a preform of particles to form the composite. Compcasting and stir casting are some of the examples of the dispersion method where graphite particles are stirred into aluminum alloys [81]. Then the slurry mixture is cast by a conventional casting process using gravity or external pressure. Spray deposition is another processing technique for Al/Graphite composites. Dispersed graphite powder in liquid aluminum is sprayed directly on the substrate using an atomizer in this technique. The bonding between the matrix and reinforcement phase, distribution of graphite particles in the Al matrix, and physical properties like density and porosity depend upon the processing procedure. As a result, material processing procedures have significant effects on the tribological behaviors of the MMCs.

Theoretically, graphene addition in the aluminum matrix should cause dramatic improvement in the mechanical and tribological properties [24]. However, uniform dispersion of graphene in the aluminum matrix and good interfacial bonding between them is required to achieve these improvements. Consequently, manufacturing processes and heat treatments are important for

aluminum-graphene MMCs. Nanoparticle agglomeration, formation of pores, weak interfacial bonding, carbide formation, and cracks in subsurface regions are some of the common defects associated with the manufacturing processes. Powder metallurgy, conventional casting, severe plastic deformation, and additive manufacturing are some of the common manufacturing processes for these MMCs [68].

Powder metallurgy has been the most popular manufacturing route for aluminum-graphene MMCs. Unclean aluminum-graphene interfaces and oxidation of the aluminum matrix often occur in this process due to improper selection of process parameters [68]. In addition, graphene is often present at grain and powder boundaries. These defects can notably impact the mechanical and tribological properties. Casting is less commonly used for aluminum-graphene MMCs, compared to powder metallurgy. This manufacturing route can be cost-effective, but it offers less control over the distribution of graphene in the aluminum matrix. High processing temperatures in casting processes promote interfacial reactions between aluminum and graphene. Moreover, the density mismatch between aluminum and graphene often causes segregation and agglomeration of graphene nanoparticles [68]. Porosity is another issue associated with the gravity casting process which can reduce the strength in these MMCs. All these casting issues can negatively affect mechanical and tribological properties. Cracks and fractures in the microstructure are often the issues associated with the severe plastic deformation technique of manufacturing aluminum-graphene MMCs. The main challenges with additive manufacturing like the selective laser melting of aluminum-graphene composites involve porosity and low plasticity, which can make it difficult to process them into complex parts.

Solution treatment and T6 heat treatment are some of the most common processes used for the heat treatment of aluminum alloys and their composites. Mechanical property enhancement

(e.g., increasing ductility, fatigue resistance), microstructural refinement (e.g., grain size refinement), and increasing strength and material hardness are some of the effects of heat treatment processes that can directly influence tribological behavior. However, in the traditional tribological studies, the effects of processing techniques and heat treatment are often ignored. Data-driven approaches are suitable for solving this problem. In this study, the effect of the material processing procedures and heat treatment on friction and wear of aluminum-graphite and aluminum-graphene MMCs will be analyzed.

4.4.1.5. Effect of hardness

The hardness of the Al matrix, and composite materials is an important parameter in predicting tribological behaviors. Molecules at the surface of materials possessing high hardness have strong molecular bonds which contribute to higher resistance to adhesion. As a result, the adhesion component of friction is low in sliding contact. Again, high hardness refers to low plastic deformability in a material. So, the deformation component of friction is also low. As both the adhesion and deformation components are small, generally a low COF is expected for harder materials. However, the relation between friction and hardness is not straightforward, and singling out hardness to predict COF can produce unreliable results. On the other hand, wear behaviors exhibit a more consistent trend with hardness than COF. As a harder material offers less plastic deformation and material removal during sliding contact, a lower wear rate is observed. Gore and Gates studied the effect of hardness on different forms of wear and reported that for single-phase materials, a general reduction in wear is observed with increasing hardness while for multi-phase materials, no such general trend is observed [82]. They opined that micro-facture wear mechanisms and other material variables can be the reasons for the unexpected wear behavior of the multi-phase materials. However, Gopi et al. reported the general trend of wear rate reduction with

increasing hardness in multi-phase materials and alloys as well [83]. Such differences in findings across studies imply that the effect of hardness on tribological behaviors can be better understood if analyzed together with other material and tribological variables.

4.4.2. Tribological variables

Normal load, tribological testing methods, counterface material, sliding distance, sliding speed, and the lubrication condition are some of the important tribological testing variables. In this section, the effect of tribological test variables on friction and wear behaviors of aluminum-graphite and aluminum-graphene MMCs will be discussed.

4.4.2.1. Effect of normal load

The normal load is often regarded as the most influential tribological parameter during sliding interactions. According to Archard and Hirst [67], wear is directly proportional to normal load, and the progression from mild to severe wear also depends on this parameter. **Figure 4.6** presents the effect of normal load on the wear rate and the COF of aluminum-graphene and aluminum-graphite MMCs. Increasing the load enhances the nano- and microscale asperity contact between the sliding surfaces. Moreover, larger plastic deformation of the tribosurface is expected with an increased asperity contact. All of these contribute to the increase of the overall friction force. However, for a two-phase self-lubricating material like aluminum-graphene MMCs, the load dependency of the friction and wear characteristics may be more complex since the increasing load can also lead to increased spreading of the softer phase on the tribosurface. Consequently, for aluminum-graphene MMCs, both increase and decrease in the COF with normal load are observed across studies (**Figure 4.6(b)**).

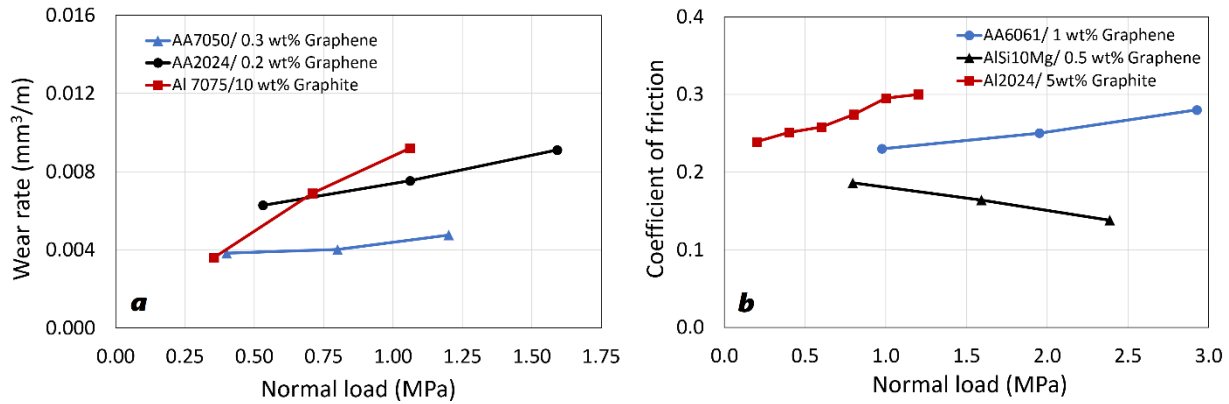


Figure 4.6. Effect of normal load on (a) wear rate [37, 44, 23], (b) coefficient of friction [36, 40, 72]

Also, the friction and wear of aluminum-graphite MMCs containing a higher wt.% of graphite were found higher compared to aluminum-graphene MMCs containing much smaller wt.% of graphene at similar loading conditions (**Figure 4.6**). Superior mechanical properties of aluminum-graphene MMCs and the formation and retention of the graphene-rich film play an important role in this. At the initial stage of sliding, the tribosurface is scratched and the graphene phase embedded in the metal matrix smeared on it [68]. Further sliding can cause more graphene smearing and eventually the formation of a stable graphene-rich film which can lower the friction and wear between the surfaces with load compared to the initial condition. However, once the stable graphene film has been formed, both the friction and wear are expected to increase with the normal load. In lower normal loads, mild wear is expected when the graphene film remains intact and contributes to limiting the friction and wear. The graphene-rich film is often destroyed or is no longer able to protect against the severe wear which is observed at higher loads. Wu et al. [36] reported that the wear mechanism in aluminum-graphene MMCs transitions from abrasive to delamination wear with increasing load. They also reported high surface roughness and shear strain at high normal loads. After ANOVA analysis, Venkatesan et al. [37] reported the normal load as

the most influential parameter for aluminum-graphene MMCs for the prediction of both the wear rate and COF.

4.4.2.2. Influence of sliding distance

For self-lubricating aluminum matrix composites, the influence of sliding distance on friction and wear is not straightforward. The solid-lubricating film formation, loading, and sliding conditions can make the relation complex. The effect of sliding distance on the wear rate and the COF of aluminum-graphene and aluminum-graphite MMCs are presented in **Figure 4.7**. For aluminum-graphite MMCs, both the COF and the wear rate increased with increasing sliding distance. Microthermal softening caused by interfacial heat and diminished graphite film on the tribosurface during extended sliding are considered to be responsible for these [59].

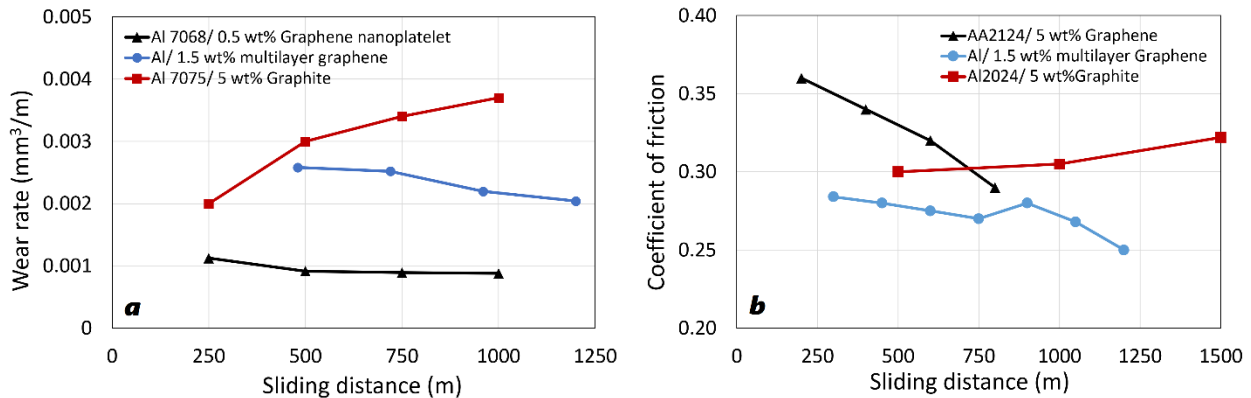


Figure 4.7. Effect of sliding distance on (a) wear rate [32, 47, 23], (b) coefficient of friction [31, 47, 72].

For aluminum-graphene MMCs, both the COF and the wear rate decrease with sliding distance. This inverse correlation linking the wear rate and sliding distance can be attributed to the hard graphene materials that protrude from the surface with extended sliding providing a mechanism through which the aluminum-graphene composites resist wear [37]. The presence of

stable graphene layers on the tribosurface also helps to reduce the COF with sliding distance. Furthermore, the ANOVA analysis performed by Venkatesan et al. [37] with tribological data of aluminum-graphene MMCs suggested that sliding distance has a greater influence on the wear rate than on the COF.

4.4.2.3. Influence of sliding speed

An increase in sliding speed generates frictional heat that raises the tribosurface temperature. This temperature rise promotes microthermal softening of the matrix. Moreover, it contributes to oxide formation, dissolution of precipitates in microstructure, and flow stress reduction [61]. All of these contribute to an elevated wear rate in aluminum MMCs. The effect of sliding speed on the wear rate and the COF of aluminum-graphene and aluminum-graphite MMCs are presented in **Figure 4.8**.

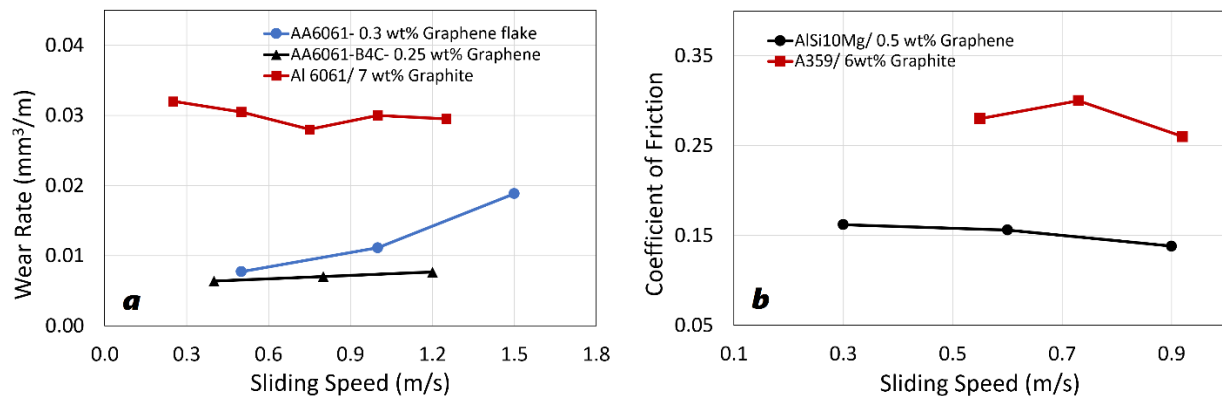


Figure 4.8. Effect of sliding speed on (a) wear rate [40, 41, 71], (b) coefficient of friction [36, 78].

The wear mechanism can be either mild or severe depending on the sliding speed. At a low sliding speed, mild wear is observed in aluminum-graphene MMCs when small wear rates are observed due to the fully functioning graphene lubrication films. In aluminum-graphite MMCs,

the wear rate is reported to decrease briefly with sliding speed in the mild wear regime [71]. As the sliding speed moves up towards a critical value, the wear rate increases both for aluminum-graphene and aluminum graphite MMCs. However, the wear rates observed in aluminum-graphene MMCs were notably lower than that of the aluminum-graphite MMCs even with a higher percentage of reinforcement.

On contrary, up to a critical value, the COF of aluminum-graphene and aluminum-graphite MMCs decreases with sliding speed. Besides the lubrication provided by the graphene or graphite-rich layers, an increase in sliding speed minimizes the real area of contact which reduces the adhesive component of friction between the sliding surfaces. Frictional heat generated with increasing sliding speed also helps to reduce the friction during sliding interactions. Also at low sliding speeds, the resulting increase in strain rate increases flow strength and hardness [41]. Consequently, the real area of contact is reduced between the mating surfaces and the COF and wear are reduced.

4.5. Friction and wear performance of aluminum-graphite and aluminum-graphene composites

Analysis of the tribological performances of different studies indicated that the required amount of graphene in weight percentage as the reinforcement phase is significantly lower than graphite to obtain similar COF and wear rate under comparable loading conditions [20,22,32,35,36,70,72]. The incorporation of larger graphite particles in aluminum matrix causes notable decrease in mechanical properties including hardness, ductility, and strength in aluminum-graphite MMCs. Also, large graphite particles have a higher tendency to agglomerate in the aluminum matrix [24]. All of these can adversely affect the tribological performance of these MMCs compared to aluminum-graphene MMCs. On the other hand, comparatively smaller

graphene nanoparticles are reported to disperse in the aluminum matrix more uniformly. The graphene nanoparticle addition significantly improves the mechanical properties and the corresponding tribological performance of aluminum-graphene MMCs. These could be probable reasons of a better friction and wear performance in nanoparticle reinforced aluminum-graphene MMCs compared to microparticle reinforced aluminum-graphite MMCs.

Through statistical analysis using the experimental data of the above studies, we intended to test the hypothesis if a notably lesser wt.% of graphene as the reinforcement in aluminum matrix can exhibit a similar friction performance to a much higher wt.% of graphite. We performed the Linear Contrast Analysis (LCA) with the COF data of aluminum-graphite (10 wt.% graphite) and aluminum-graphene (0.5 wt.% graphene) under similar loading conditions using the IBM SPSS Statistics software to find if the COF values of the paired combination are statistically similar. Datasets of 33 COF values were considered where the mean and the standard deviation (SD) of the COF of aluminum-graphite composites were 0.1968 and 0.0862 and those of aluminum-graphene composites were 0.2047 and 0.0603, respectively. The sample size of the test satisfied the requirement of the central limit theorem for the normal distribution approximation. The LCA test yielded a p-value of 0.77 for the linear term larger than α (0.05), indicating the failure of rejecting the null hypothesis. As a result, with a 95% confidence level, we could conclude that there is no statistical evidence that the mean COF values of the paired combination of aluminum-graphite (10 wt.% graphite) and aluminum-graphene (0.5 wt.% graphene) composites are different. So, the statistical analysis validated the claim that a much lesser amount of graphene in the aluminum matrix as the reinforcement phase can generate a similar tribological performance as a higher amount of graphite in the aluminum matrix in comparable tribological conditions.

4.6. Materials and methods

In this section, the development and performance enhancement of ML models in detail to predict the friction and wear behavior of aluminum-graphite and aluminum-graphene MMCs are discussed. This discussion includes data collection, data processing, model development, and optimization of parameters of different ML models.

4.6.1. Data collection and input-output parameters

The predictive capacity and robustness of ML models largely depend on the data collection process. Using a large relevant dataset from multiple sources covering a wide range of input-output relations for developing ML models ensures generalization capability and robustness. Using data from different sources is recommended as it prevents the passing of unsought trends from a particular source which can weaken the generalization capacity of the models. The resource and time required for developing multiple tribological testing set-ups and preparing samples with different material properties to generate the required data are formidable. For developing efficient ML models, we collected published tribological performance data for aluminum-graphite [2,9-17,20-23,70-72,77-79,81,84] and aluminum-graphene [24, 31, 32, 34-50, 80] MMCs separately.

For aluminum-graphite MMCs, eleven material and tribological variables namely graphite content, hardness, ductility, processing procedure, heat treatment, silicon carbide content, yield strength, tensile strength, normal load, sliding speed, and sliding distance were considered as the input parameters or features. Among these variables, processing procedure, and heat treatment were considered as categorical, while other variables were numerical. COF, and wear rate were the two output parameters. For modeling different ML algorithms to predict COF, and wear rate, 533 and 852 sample data points were used respectively.

For aluminum-graphene MMCs, datasets of 432 and 390 sample data points were considered to build ML models to predict the COF and the wear rate, respectively. 15 tribological and material variables were considered as the inputs of regression models. Graphene content, aluminum content, SiC content, hardness, tensile strength, type of graphene, manufacturing process, heat treatment, ductility, and density were the considered material variables. Sliding distance, normal load, speed, counterface, and tribo-testing method were the considered tribological variables. Among the input variables, type of graphene, manufacturing process, heat treatment, counterface, and tribo-testing method were categorical, and the rest were numerical.

4.6.2. Machine learning algorithms

Supervised machine learning regression models can predict the output from input variables. For this purpose, the models are required to be trained with training examples consisting of input-output relationships. 5 Machine Learning (ML) regression models: Artificial Neural Network (ANN), K-Nearest Neighbor (KNN), Random Forest (RF), Support Vector Machine (SVM), and Gradient Boosting Machine (GBM) were developed for predicting the wear rate and COF of aluminum-graphite and aluminum-graphene MMCs. Python programming language and the scikit-learn toolkit were used for developing the models and running the ML analysis. The details of the abovementioned ML models are discussed at length in **chapter 2** of this dissertation.

4.6.3. Data preprocessing and standardization

Data cleaning, handling of missing and unusual values, shuffling, data standardization, and splitting to the training and test sets are some important data preprocessing steps before developing the ML models. We performed the preprocessing steps on the data using manual techniques and using Python and its standard libraries. Through manual techniques, the missing and unusual

values in the datasets were dealt with accordingly. We shuffled the data to restrict unsolicited biases passing into the ML models.

Bringing the inputs in a comparable numeric range improves the responsiveness of the developed models. This process of data standardization/feature scaling was executed using the “RobustScaler” which is known for its effectiveness with outliers in the dataset. Splitting the dataset into mutually exclusive training and test sets is required for developing ML regression models. The standard 75%-25% splitting scheme was selected where 75% of the total data were used to train the ML models and the remaining 25% were used as the test set.

4.6.4. Optimization of the ML models

Careful optimization of the developed ML models ensures maximization of predictive performance. The parameters of different models that require optimization are discussed in **Chapter 2** of this dissertation. We used grid search and cross-validation techniques to find the optimized parameters for the prediction models. Under these optimization techniques, we selected different ranges of the parameters and run the prediction models numerous times. The optimization parameters generating the finest performance in wear rate and COF prediction models for aluminum-graphite MMCs were selected and are presented in **Table 4.1** and **Table 4.2**.

Table 4.1. Parameter optimization for COF of aluminum-graphite MMCs

ML model	Parameter optimization
ANN	Hidden layer sizes = (10,10,10), alpha = 0.01, activation function: logistic
KNN	n=3

RF	n_estimators= 100, max_features = 4
SVM	kernel = "rbf", C = 100, gamma = .01
GBM	n_estimator = 100, learning rate = 0.3

Table 4.2. Parameter optimization for wear rate of aluminum-graphite MMCs

ML model	Parameter optimization
ANN	Hidden layer sizes = (10,10,10), alpha = 0.06, activation function: tanh
KNN	n=7
RF	n_estimators=100, max_features = 4
SVM	kernel = "rbf", C = 100, gamma = .25
GBM	n_estimator = 100, learning rate = 0.1

Similarly, the optimization parameters of the ML models for aluminum-graphene MMCs were presented in **Table 4.3** and **Table 4.4**.

Table 4.3. Optimization of COF models for aluminum-graphene MMCs

Model name	Selected Parameters
ANN	alpha = 0.012, activation function: tanh, hidden layers = (10,10,10),
KNN	weights= 'uniform', n_neighbors=5
RF	max_features = 4, n_estimators= 80,
SVM	gamma = 0.08, C = 100, kernel = rbf

GBM learning rate = 0.8, n_estimator = 150,
max_depth = 2

Table 4.4. Optimization of wear rate models for aluminum-graphene MMCs

Model name	Selected parameters
ANN	alpha = 0.04, activation function: relu, hidden layers = (10,10,10)
KNN	weights= 'uniform', n_neighbors=3
RF	max_features = 5, n_estimators= 30
SVM	gamma = 0.3, C = 100, kernel = rbf
GBM	learning rate = 0.01, n_estimator = 150, max_depth = 7

4.7. Result and discussion

ML analysis results and the analysis of the efficiency of the developed results with standard performance evaluation metrics have been presented in this section. The findings of the data-driven analysis on how different input parameters influence the wear and friction of aluminum-graphite and aluminum-graphene MMCs have also been discussed.

4.7.1. Evaluation of model performance

For evaluating the performance of ML models, different performance metrics are used. These metrics provide a numerical estimation of how well an ML model fits the actual data. The coefficient of determination (R^2 value) is the most important among them and presents the

percentage of variation in data that can be explained by the model. R^2 Can be defined as $R^2 = 1 - \frac{SS_r}{SS_t}$, where SS_r is the residual sum of squares, and SS_t is the total sum of squares. R^2 value ranges from 0 to 1. $R^2 = 1$ means perfect fitting and the model can accurately predict the data which is unusual for any experimental dataset. R^2 value over 0.9 refers to a very satisfactory model execution while a value ranging between 0.7-0.9 indicates fairly satisfactory performance. R^2 values below 0.5 indicate that the model is inadequate to predict the output of a dataset.

Besides R^2 values, mean squared error (MSE), root mean squared error (RMSE), and mean absolute error (MAE) are other metrics that can be used to evaluate the performance of an ML model. MSE is the average of the squared differences between the observed and predicted values. RMSE is obtained by performing the square root of the MSE value. MAE is the average of the absolute difference between the observed and predicted value of each data point of the dataset. A value of 0 of these errors means a perfect fitting of the model with the data set. The smaller the value the better the predictive performance of the ML model.

4.7.2. Result for COF prediction

The performance metrics of the ML models for predicting COF are presented in **Table 4.5**. With R^2 values ranging from 0.7561 to 0.9636 and small error values, each model for COF prediction performed satisfactorily.

Table 4.5. Performance of the ML methods for COF

ML	Reinforcement	MSE	RMSE	MAE	R^2 value
Model					
ANN	Graphite	0.0037	0.0611	0.0403	0.8630

ANN	Graphene	0.0037	0.0613	0.0396	0.8936
KNN	Graphite	0.0066	0.0816	0.0460	0.7561
KNN	Graphene	0.0046	0.0682	0.0408	0.8683
RF	Graphite	0.0037	0.0612	0.0332	0.8626
RF	Graphene	0.0013	0.0362	0.0244	0.9628
SVM	Graphite	0.0064	0.0802	0.0547	0.7644
SVM	Graphene	0.0034	0.0583	0.0340	0.9037
GBM	Graphite	0.0028	0.0538	0.0360	0.8941
GBM	Graphene	0.0012	0.0358	0.0219	0.9636

For aluminum-graphite MMCs, the GBM model exhibited the highest prediction capacity ($R^2= 0.8941$) among the ML models and it could predict the COF of the test set with 89.41% accuracy. However, the ML models developed for aluminum-graphene MMCs consistently outperformed those for aluminum-graphite MMCs. The decision tree based RF ($R^2=0.9628$, RMSE=0.0362, MAE=0.0244, and MSE=0.0013) and GBM ($R^2=0.9636$, RMSE=0.0358, MAE=0.0219, and MSE=0.0012) models produced the best prediction performances for aluminum-graphene MMCs. The boosting and bagging mechanisms of the GBM and the RF models were found efficient in handling the friction data with categorical variables [58-61]. For the GBM model, 150 boosting stages (n_estimators) with a maximum depth of 2 for each individual regression unit yielded the best prediction performance in COF prediction. With the COF data, a higher learning rate of 0.8 along with other optimized parameters was found efficient. The comparison between the actual COF (experimentally measured) and the predicted COF by the

best-performing GBM model is presented in **Figure 4.9**. Impressive agreement between the predicted and actual experimental COF values was observed.

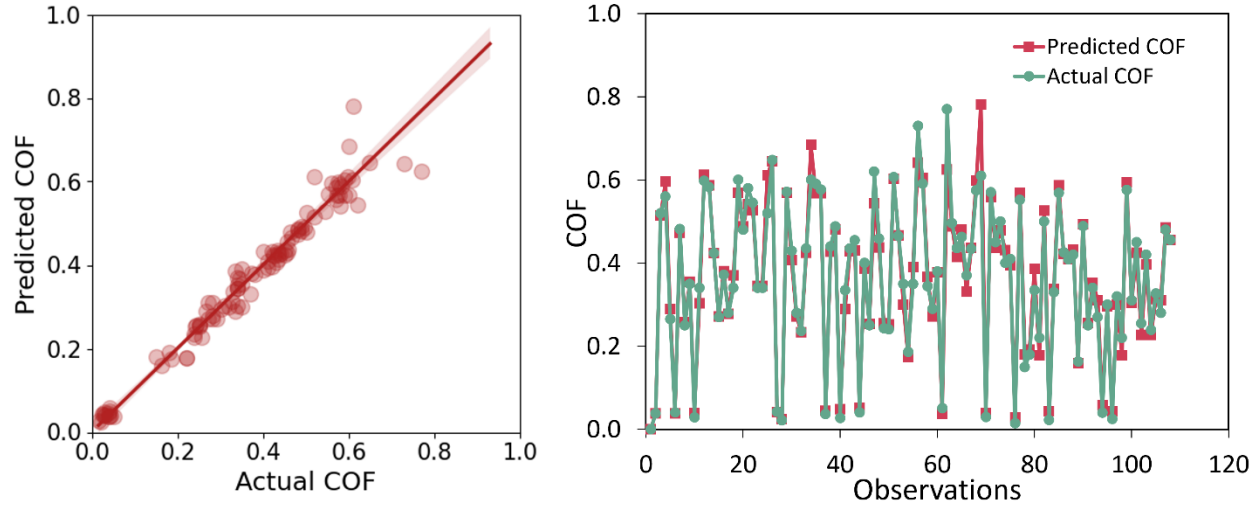


Figure 4.9. The comparison of the actual (experimentally measured) COF and the anticipated COF by GBM regression model for aluminum-graphene MMCs.

For the RF model, 80 decision trees with 4 considered features during the best split (`max_features`) produced the best prediction performance with an R^2 value of 0.9628. With the presence of categorical variables in the dataset, the decision tree based GBM, and RF models performed notably well compared to other models. Among the developed models, the distance function based KNN was the simplest and was outperformed by all other models. 5 neighboring datapoints to make a prediction for a new datapoint with a uniform weight to each datapoint produced the best prediction performance in the KNN model. However, the model still struggled to address the complex COF dataset compared to other ML models. With an R^2 value of 0.8936, the ANN model could predict the COF with an accuracy of about 89.36%. With small error terms, the prediction performance of the ANN model can be considered decent.

4.7.3. Influence of input variables in COF prediction

The effect of each independent variable on predicting the output can be summarized by the “feature importance” attribute of decision tree-based ML models. The sum of the scores of each variable of such a feature importance analysis chart equals 1. A high individual score suggests a significant contribution in output prediction while a zero score suggests no contribution at all. The feature importance chart from the RF algorithm for predicting the COF for aluminum-graphite MMCs is presented in **Figure 4.10**. A non-zero score for each input variable confirms that all the selected input variables impact the COF. All independent variables performed fairly and contributed to predicting the COF. The graphite content and the hardness of the Al alloy matrix had the highest score and had the maximum contribution in the COF prediction. Graphite content, which is often considered as the most important material variable in the traditional analysis had almost equal contribution as the hardness. The formation of the graphite lubricating film reduces friction of Al/Gr composites. The effect of hardness on the COF can be explained by stronger resistance of harder materials to the deformation of asperities during sliding. Processing procedure had a higher contribution than heat treatment in predicting the COF. Among the tribological test parameters, sliding speed scored higher and played an important role in the COF prediction.

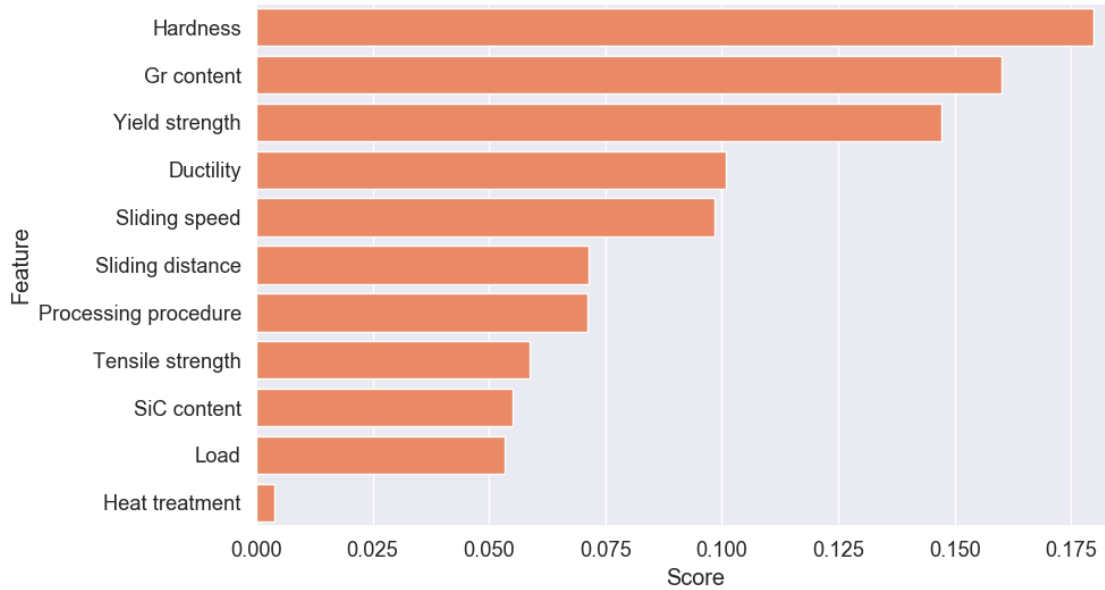


Figure 4.10. Relative significance of material and tribological test variables identified by the RF model for predicting the COF of aluminum-graphite MMCs

For aluminum-graphene MMCs, the influence of each input variable in anticipating the COF is identified by the feature importance attribute of the RF model (**Figure 4.11**). The analysis result showed that the load, graphene content, and hardness were the most important parameters in COF prediction. Normal load is directly related to the asperity contact of the sliding surfaces and the formation and retention of the lubrication film between them. The weight percentage of graphene is also important to promote the self-lubrication effect for reducing friction as we discussed in **section 3**. Material hardness had also significant influence in COF prediction. The analysis also suggest that the type of graphene used in the aluminum-graphene metal matrix composites had a comparatively lesser impact on COF prediction.

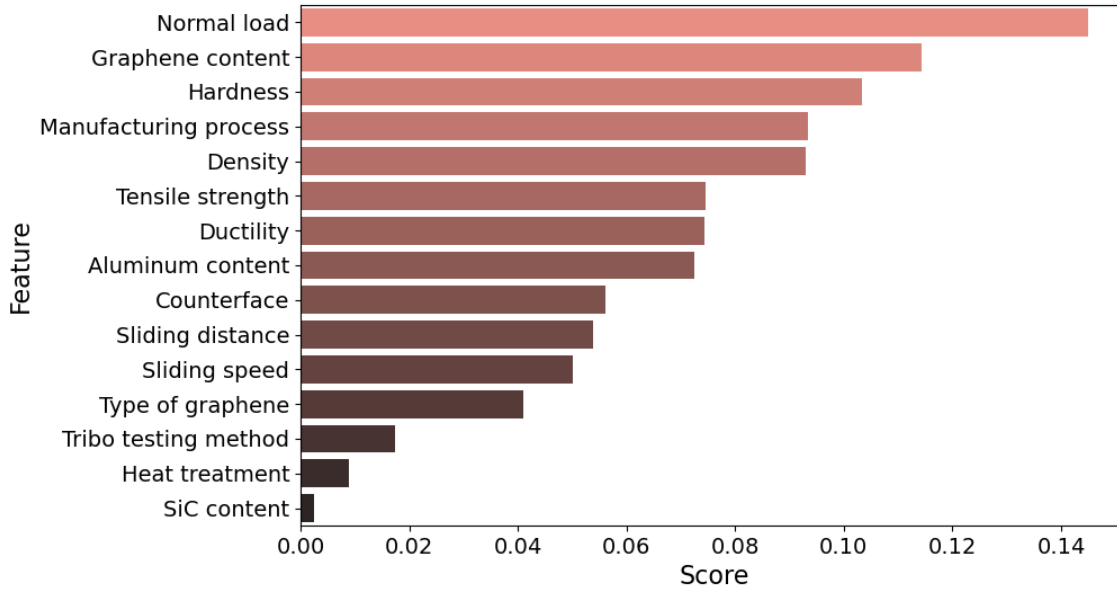


Figure 4.11. The relative importance of input variables for predicting the COF (feature importance).

4.7.4. Wear rate prediction

The performance metrics of the ML models for predicting wear rate are presented in **Table 4.6**. R^2 values on test sets of different ML models range between 0.7395 to 0.8832, and the MSE, RMSE, and MAE are reasonably small. These numbers indicate satisfactory execution of the ML models for predicting the wear behavior of aluminum-graphite and aluminum-graphene composites.

Table 4.6. Performance of the ML models for wear rate prediction

ML Model	Reinforcement	MSE	RMSE	MAE	R^2 value
ANN	Graphite	0.0031	0.0558	0.0181	0.7395
ANN	Graphene	0.0007	0.0259	0.0092	0.9325

KNN	Graphite	0.0017	0.0422	0.0114	0.8512
KNN	Graphene	0.0026	0.0515	0.0137	0.7349
RF	Graphite	0.0014	0.0374	0.0093	0.8832
RF	Graphene	0.0009	0.0312	0.0086	0.9039
SVM	Graphite	0.002	0.041	0.010	0.8581
SVM	Graphene	0.0011	0.0331	0.0122	0.8897
GBM	Graphite	0.0016	0.0408	0.0123	0.8607
GBM	Graphene	0.0005	0.0230	0.0097	0.9467

For aluminum-graphite MMCs, the RF model outperformed others in predicting the wear behavior. With an R^2 value of 0.8832, it could predict the wear rate of the test dataset with 88.32% accuracy. The results show that the performances of different ML models were different in predicting COF and wear rate of aluminum-graphite MMCs for the same data sets. RF and GBM are decision tree-based, ensemble algorithms where several decision trees are developed to map the input data to output. However, there are differences in the decision tree development and the result generation processes in these two algorithms. RF uses the bagging mechanism where each tree is built independently with random samples from the dataset and generate the final result by averaging the individual results of each tree at the end of the tree building process. In contrast, GBM uses the boosting mechanism where each tree is built once at a time (each tree depends on the previous tree) with weighted samples from the dataset and generate the final result by combining the individual results of each tree along the tree building process. With proper parameter optimization, the boosting mechanism is more effective than the bagging mechanism in handling complex problems, while the bagging mechanism is more effective when a large

fluctuation or variability is present in the dataset. The variability in the wear rate data set (0.00055 mm³/m to 0.37 mm³/m) was more prevalent than that of the COF dataset (0.1 to 0.93). Consequently, GBM exhibited the best performance in the COF prediction, and RF outperformed GBM in wear rate prediction.

For aluminum-graphene MMCs, the performance evaluation metrics of the ML models for wear rate anticipation are presented in **Table 4.6**. With R^2 values ranging from 0.8897 to 0.9467, ANN, SVM, RF, and GBM models performed excellently. However, the KNN model underperformed in wear rate prediction as the distance function-based model was too simple to explain the complex correlations in wear data. For the complex dataset of wear rate, ANN exhibited excellent performance ($R^2 = 0.9325$, RMSE = 0.0259, MAE = 0.0092, and MSE = 0.0007) and as expected. The decision tree based GBM model produced the best prediction performance ($R^2 = 0.9467$, RMSE = 0.0230, MAE = 0.0097, and MSE = 0.0005). The model could predict the wear rate with the maximum accuracy of 94.67%. The boosting mechanism of the GBM regression model produced consistent performance in presence of categorical variables in the wear rate data.

The comparison between the actual wear rate (experimentally measured) and the predicted counterpart by the best performing GBM regression model is presented in **Figure 4.12**. Excellent correlation between the predicted and actual experimental wear rate values was observed.

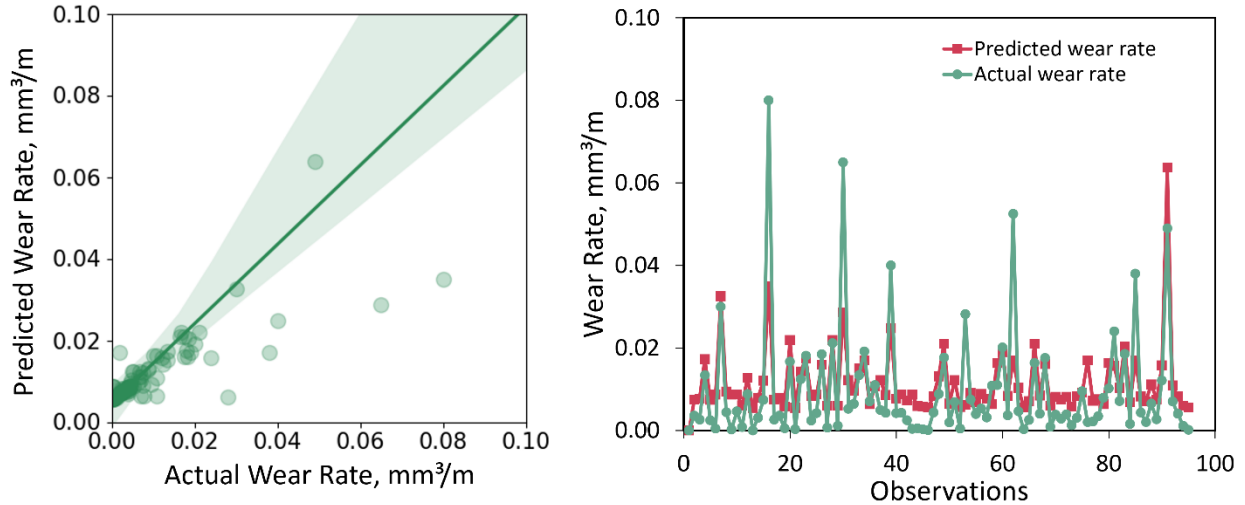


Figure 4.12. The comparison of the actual (experimentally measured) and the anticipated wear rate by GBM regression model.

RF, the other decision tree based model, also performed satisfactorily in wear prediction. An R^2 value above 0.9 and small error term values indicate satisfactory model execution. The ANN model exhibited excellent prediction performance for wear rate with an R^2 value of 0.9325 and extremely low values of MAE, RMSE, and MSE. With 3 hidden layers each having 10 neurons, “relu” activation function, and a small regularization term ($\alpha = 0.04$), the ANN model satisfactorily handled the complex wear rate data. The distance function based KNN model was once again notably outperformed by other models in handling complex wear data.

The selection of appropriate independent variables for ML analysis is important to get a better predictive performance (R^2 value) for the output. However, the selection of independent variables in predicting COF and wear rate is a complicated process as numerous material and tribological parameters affect them. In this study, we could not include more microstructural features (e.g., average grain size of microstructure, information about grain boundary, graphite particle size) due to the unavailability of those data which could potentially improve the R^2 value

of those models. Another, inconvenience with tribological data is that the tribological and material properties affecting the tribological behavior are often correlated. Correlation among the independent variables affects the R^2 value of prediction. Also increasing the number of data points might improve the R^2 value of the developed ML models.

4.7.5. Influence of the input variables on wear rate prediction

The feature importance chart from the RF algorithm for predicting the wear rate of Al/Gr composites is presented in **Figure 4.13**. Graphite content had the highest score and contributed the most in predicting wear rate. The strong dependence of the wear rate on graphite content can be attributed to two contrasting factors. First, the diminution of several mechanical properties including hardness, ductility, and fracture toughness of the MMCs with graphite addition. With increasing graphite content, crack propagation and delamination of the graphite phase increase due to a weaker bonding with the aluminum matrix. On the other hand, the formation of a thin graphite film over the tribosurface provides lubrication and eliminates metal-to-metal contact during sliding. Due to these diverse effects, graphite content has a greater influence on the wear rate of the Al/Gr MMCs than any other material or tribological variables.

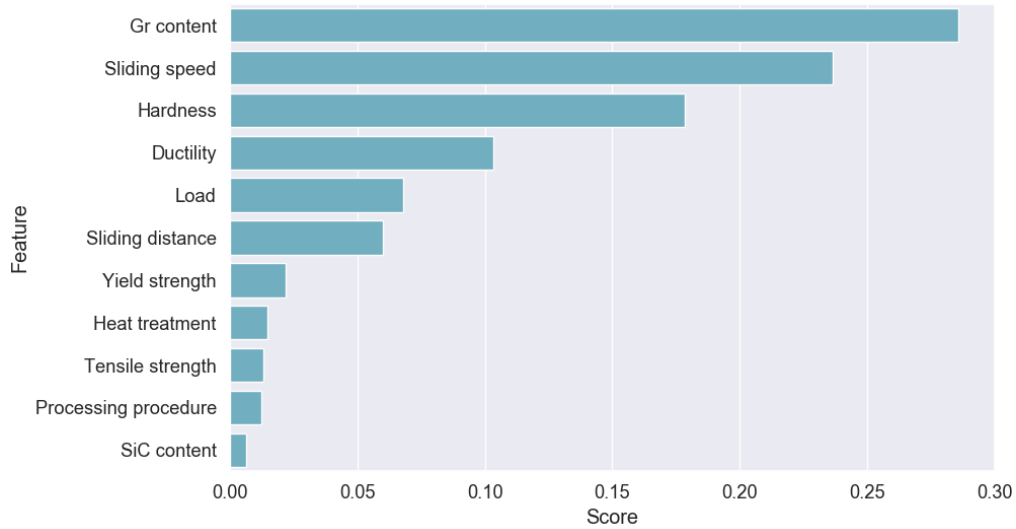


Figure 4.13. The relative importance of input variables for predicting the wear rate of aluminum-graphite MMCs

Among the tribological test variables, the effect of the sliding speed was the most significant. A brief initial decrease in wear rate was observed up to a critical sliding speed for Al/Gr MMCs. This initial dip in wear rate is due to the graphite film formation on the tribosurface. Once the sliding speed surpasses the critical speed, the effect of the graphite lubrication film is diminished, and more metal-metal contact occurs during sliding. This causes a drastic sudden increase in wear rate. Normal load also contributed fairly to wear rate prediction. An increase in the normal load deteriorates the graphite film and increases the frictional heat that softens the tribosurface. As a result, increased plastic deformation of the tribosurface is observed, and the COF and wear rate are increased.

For aluminum-graphene MMCs, the influence of each input variable in anticipating the wear rate is identified by the feature importance attribute of the RF model (**Figure 4.14.**). A non-zero score for each input variable confirms that all the selected input variables impact the wear rate. The feature importance analysis showed that graphene content, hardness, and normal load

were the most dominant variables in wear prediction. Graphene content is directly related to mechanical property enhancement and self-lubrication effect in aluminum-graphene MMCs and was identified as the most important parameter in the analysis. Hardness resisted material removal during tribological interactions and played an important role in wear prediction. Hardness was found having more influence on friction and wear than tensile strength probably because at the surface (unlike in the bulk material) hardness resist material removal more than the strength of the bulk material. Normal load was also important as it impacted the asperity contact between the surfaces, formation, and retention of the graphene film at the tribosurface and controlled the transition between mild and severe wear. The type of graphene used in the aluminum-graphene metal matrix composites had a larger impact on the wear rate unlike COF. Besides the incorporating self-lubricating effect, the type of graphene and the number of graphene layers modify the surface and mechanical properties including porosity, ductility, hardness, strength, and the bonding between aluminum and graphene. Different morphology of graphene can induce different levels of microcracking and brittle fracture during tribological interactions. All these aspects can significantly influence the wear rate in aluminum-graphene metal matrix composites.

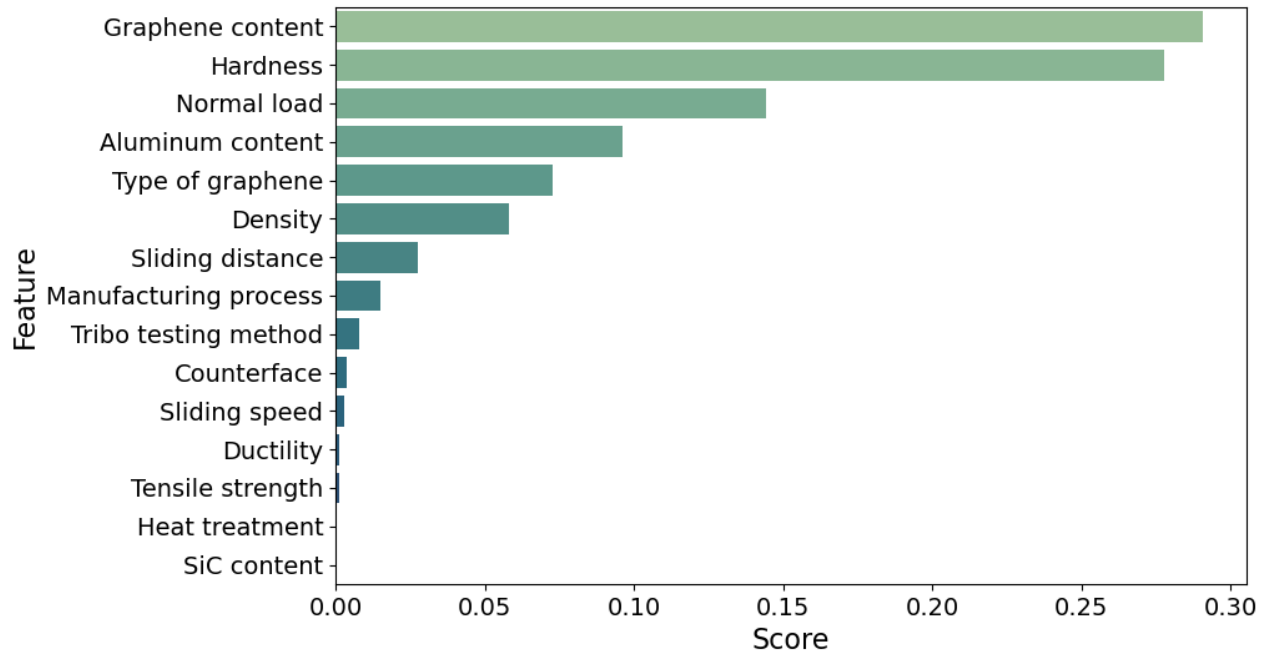


Figure 4.14. The relative importance of input variables for predicting the wear rate of aluminum-graphene MMCs.

4.7.6. Prediction performance comparison

We performed a comparative analysis of ML models for COF and wear rate anticipation of aluminum alloys, aluminum-graphite, and aluminum-graphene composites in dry conditions [58-61]. With categorical variables in input, the decision tree based ML models: GBM and RF consistently generated excellent prediction performance for friction and wear rate. Statistical performance metrics suggested that the ML models for aluminum-graphene and aluminum-graphite composites notably outperformed those for aluminum base alloys. For aluminum-graphene and aluminum-graphite composites, the friction and wear characteristics significantly depend on the self-lubricating effect caused by graphite and graphene incorporation in the aluminum matrix. Graphene content and graphite content were identified as the most influential variables in friction and wear prediction for these two composites, respectively. Consequently, the

prediction models performed excellently. For aluminum base alloys, without any liquid and solid lubricant, the COF and the wear rate heavily depended on material hardness and different tribological variables. The dataset represented a certain degree of randomness and a more complicated correlation among the input-output variables. Consequently, the ML models underperformed than those for aluminum-graphene and aluminum-graphite composites.

The ML models we have developed are capable of predicting the COF and wear rate of aluminum-graphene MMCs with an accuracy up to 96%. We can predict the COF and wear for a wide range of loading conditions and material variables without running any experiments. Moreover, these models can identify the most crucial parameters affecting the friction and wear of aluminum-graphene MMCs analyzing a large data from more than 20 experimental studies. This information can be effectively utilized for improving the synthesizing process of aluminum-graphene MMCs and finding optimum operating conditions for practical applications.

4.8. Conclusion

The effect of graphite and graphene addition on the material properties of self-lubricating aluminum-graphite and aluminum-graphene MMCs was investigated. The friction and wear mechanisms of these MMCs were analyzed and a phenomenological study of their dry friction and wear behavior in sliding interactions was presented. Additionally, the tribological characteristics of aluminum-graphene MMCs were compared with those of aluminum-graphite MMCs.

- We observed an increase in hardness and tensile strength with graphene addition in aluminum-graphene MMCs due to several strengthening mechanisms.

- A notable reduction in the COF and wear rate was observed with increasing graphene content in the aluminum-graphene MMCs which was attributed to the formation of graphene-rich film at the tribosurface.
- Linear contrast analysis showed that a much lower wt.% of graphene in the aluminum matrix as the reinforcement phase can lead to similar decrease in COF which are obtained with a much higher amount of graphite in the aluminum MMCs under comparable tribological conditions. A similar trend was observed for wear rate as well for these MMCs.
- The models to predict wear and friction of aluminum-graphite and aluminum-graphene MMCs performed extremely well. Also, the ML models for aluminum-graphene MMCs outperformed those for aluminum-graphite MMCs in COF and wear rate prediction. However, the decision tree based RF ($R^2=0.9628$, RMSE=0.0362, MAE=0.0244, and MSE=0.0013) and GBM ($R^2=0.9636$, RMSE=0.0358, MAE=0.0219, and MSE=0.0012) models exhibited superior predictive performance in COF prediction, while the GBM ($R^2= 0.9467$, RMSE = 0.0230, MAE = 0.0097, and MSE = 0.0005) and ANN ($R^2= 0.9325$, RMSE = 0.0259, MAE = 0.0092, and MSE = 0.0007) models provided the best prediction for wear.
- ML analysis revealed that for predicting both the COF and wear rate of aluminum-graphite MMCs, the graphite content was the most significant parameter. For friction, the hardness of the Al matrix and played a role, while the sliding speed was a significant parameter for predicting wear rate.
- For aluminum-graphene MMCs, ML study suggested that load, graphene content, and hardness were the most influential parameters in COF prediction. However, the graphene content, normal load, and hardness had the greatest influence on the wear behavior of aluminum-graphene MMCs.

4.9. References

1. Rohatgi, P. K., S. Ray, and Yun Liu. "Tribological properties of metal matrix-graphite particle composites." *International materials reviews* 37, no. 1 (1992): 129-152.
2. Omrani, Emad, Afsaneh Dorri Moghadam, Pradeep L. Menezes, and Pradeep K. Rohatgi. "Influences of graphite reinforcement on the tribological properties of self-lubricating aluminum matrix composites for green tribology, sustainability, and energy efficiency—a review." *The International Journal of Advanced Manufacturing Technology* 83, no. 1 (2016): 325-346.
3. Liu, Y., R. Asthana, and P. Rohatgi. "A map for wear mechanisms in aluminium alloys." *Journal of materials science* 26, no. 1 (1991): 99-102.
4. Zhang, J., and A. T. Alpas. "Transition between mild and severe wear in aluminium alloys." *Acta materialia* 45, no. 2 (1997): 513-528.
5. Umanath, K. P. S. S. K., K. Palanikumar, and S. T. Selvamani. "Analysis of dry sliding wear behaviour of Al6061/SiC/Al₂O₃ hybrid metal matrix composites." *Composites Part B: Engineering* 53 (2013): 159-168.
6. Ames, W., and A. T. Alpas. "Wear mechanisms in hybrid composites of graphite-20 Pct SiC in A356 aluminum alloy (Al-7 Pct Si-0.3 Pct Mg)." *Metallurgical and Materials Transactions A* 26, no. 1 (1995): 85-98.
7. Bragg, W.H., 1928, An introduction to crystal analysis, G. Bell and sons, Limited, London.
8. Rohatgi, P. K., Y. Liu, M. Yin, and T. L. Barr. "A surface-analytical study of tribodeformed aluminum alloy 319-10 vol.% graphite particle composite." *Materials Science and Engineering: A* 123, no. 2 (1990): 213-218.

9. Liu, Y. B., S. C. Lim, S. Ray, and P. K. Rohatgi. "Friction and wear of aluminium-graphite composites: the smearing process of graphite during sliding." *Wear* 159, no. 2 (1992): 201-205.
10. Chu, Hsu-Shen, Kuo-Shung Liu, and Jien-Wei Yeh. "An in situ composite of Al (graphite, Al₄C₃) produced by reciprocating extrusion." *Materials Science and Engineering: A* 277, no. 1-2 (2000): 25-32.
11. Gibson, P. R., A. J. Clegg, and A. A. Das. "Wear of cast Al-Si alloys containing graphite." *Wear* 95, no. 2 (1984): 193-198.
12. Biswas, S. K., and BN Pramila Bai. "Dry wear of Al-graphite particle composites." *Wear* 68, no. 3 (1981): 347-358.
13. Sharma, Pardeep, Krishan Paliwal, Ramesh Kumar Garg, Satpal Sharma, and Dinesh Khanduja. "A study on wear behaviour of Al/6101/graphite composites." *Journal of Asian ceramic societies* 5, no. 1 (2017): 42-48.
14. Deaquino-Lara, R., N. Soltani, A. Bahrami, E. Gutiérrez-Castañeda, E. García-Sánchez, and M. A. L. Hernandez-Rodríguez. "Tribological characterization of Al7075-graphite composites fabricated by mechanical alloying and hot extrusion." *Materials & Design* 67 (2015): 224-231.
15. Guo, ML Ted, and C-YA Tsao. "Tribological behavior of self-lubricating aluminium/SiC/graphite hybrid composites synthesized by the semi-solid powder-densification method." *Composites science and technology* 60, no. 1 (2000): 65-74.
16. Rohatgi, P. K., and B. C. Pai. "Seizure resistance of cast aluminium alloys containing dispersed graphite particles of various sizes." *Wear* 59, no. 2 (1980): 323-332.

17. Guo, ML Ted, and Chi-YA Tsao. "Tribological behavior of aluminum/SiC/nickel-coated graphite hybrid composites." *Materials Science and Engineering: A* 333, no. 1-2 (2002): 134-145.
18. Zhang, J., R. J. Perez, and E. J. Lavernia. "Effect of SiC and graphite particulates on the damping behavior of metal matrix composites." *Acta Metallurgica et Materialia* 42, no. 2 (1994): 395-409.
19. Rohatgi, P. K., R. Asthana, and Solidification Das. "Solidification, structures, and properties of cast metal-ceramic particle composites." *International metals reviews* 31, no. 1 (1986): 115-139.
20. Akhlaghi, F., and A. Zare-Bidaki. "Influence of graphite content on the dry sliding and oil impregnated sliding wear behavior of Al 2024–graphite composites produced by in situ powder metallurgy method." *Wear* 266, no. 1-2 (2009): 37-45.
21. Singh, Jaswinder. "Fabrication characteristics and tribological behavior of Al/SiC/Gr hybrid aluminum matrix composites: A review." *Friction* 4, no. 3 (2016): 191-207.
22. Mahdavi, S., and F. Akhlaghi. "Effect of the graphite content on the tribological behavior of Al/Gr and Al/30SiC/Gr composites processed by in situ powder metallurgy (IPM) method." *Tribology Letters* 44, no. 1 (2011): 1-12.
23. Baradeswaran, A., and A. Elaya Perumal. "Wear and mechanical characteristics of Al 7075/graphite composites." *Composites Part B: Engineering* 56 (2014): 472-476.
24. Moghadam, Afsaneh Dorri, Emad Omrani, Pradeep L. Menezes, and Pradeep K. Rohatgi. "Mechanical and tribological properties of self-lubricating metal matrix nanocomposites reinforced by carbon nanotubes (CNTs) and graphene—a review." *Composites Part B: Engineering* 77 (2015): 402-420.

25. Omrani, Emad, Afsaneh Dorri Moghadam, Pradeep L. Menezes, and Pradeep K. Rohatgi. "New emerging self-lubricating metal matrix composites for tribological applications." In *Ecotribology*, pp. 63-103. Springer, Cham, 2016.
26. Choi, H. J., S. M. Lee, and D. H. Bae. "Wear characteristic of aluminum-based composites containing multi-walled carbon nanotubes." *Wear* 270, no. 1-2 (2010): 12-18.
27. Berman, Diana, Ali Erdemir, and Anirudha V. Sumant. "Graphene: a new emerging lubricant." *Materials Today* 17, no. 1 (2014): 31-42.
28. Lee, Changgu, Xiaoding Wei, Jeffrey W. Kysar, and James Hone. "Measurement of the elastic properties and intrinsic strength of monolayer graphene." *science* 321, no. 5887 (2008): 385-388.
29. Lee, Changgu, Xiaoding Wei, Qunyang Li, Robert Carpick, Jeffrey W. Kysar, and James Hone. "Elastic and frictional properties of graphene." *physica status solidi (b)* 246, no. 11-12 (2009): 2562-2567.
30. Wang, Jingyue, Zhiqiang Li, Genlian Fan, Huanhuan Pan, Zhixin Chen, and Di Zhang. "Reinforcement with graphene nanosheets in aluminum matrix composites." *Scripta Materialia* 66, no. 8 (2012): 594-597.
31. El-Ghazaly, A., Geraldine Anis, and Hanadi G. Salem. "Effect of graphene addition on the mechanical and tribological behavior of nanostructured AA2124 self-lubricating metal matrix composite." *Composites Part A: Applied Science and Manufacturing* 95 (2017): 325-336.
32. Alipour, Mohammad, and Reza Eslami-Farsani. "Synthesis and characterization of graphene nanoplatelets reinforced AA7068 matrix nanocomposites produced by liquid metallurgy route." *Materials Science and Engineering: A* 706 (2017): 71-82.

33. Bartolucci, Stephen F., Joseph Paras, Mohammad A. Rafiee, Javad Rafiee, Sabrina Lee, Deepak Kapoor, and Nikhil Koratkar. "Graphene–aluminum nanocomposites." *Materials Science and Engineering: A* 528, no. 27 (2011): 7933-7937.
34. Dorri Moghadam, Afsaneh, Benjamin F. Schultz, J. B. Ferguson, Emad Omrani, Pradeep K. Rohatgi, and Nikhil Gupta. "Functional metal matrix composites: self-lubricating, self-healing, and nanocomposites-an outlook." *Jom* 66, no. 6 (2014): 872-881.
35. Islam, Mohammad, Yasir Khalid, Iftikhar Ahmad, Abdulhakim A. Almajid, Amine Achour, Theresa J. Dunn, Aftab Akram, and Saqib Anwar. "Microstructural evaluation of inductively sintered aluminum matrix nanocomposites reinforced with silicon carbide and/or graphene nanoplatelets for tribological applications." *Metallurgical and Materials Transactions A* 49, no. 7 (2018): 2963-2976.
36. Wu, Liyun, Zhanyong Zhao, Peikang Bai, Wenjie Zhao, Yuxin Li, Minjie Liang, Haihong Liao, Pengcheng Huo, and Jing Li. "Wear resistance of graphene nano-platelets (GNPs) reinforced AlSi10Mg matrix composite prepared by SLM." *Applied Surface Science* 503 (2020): 144156.
37. Venkatesan, S., and M. Anthony Xavier. "Wear property evaluation of aluminum alloy (AA7050) metal matrix composite reinforced with graphene fabricated by stir and squeeze cast processes." *Materials Today: Proceedings* 22 (2020): 3330-3339.
38. Du, X., R. Chen, and F. Liu. "Investigation of graphene nanosheets reinforced aluminum matrix composites." *Dig. J. Nanomater. Biostruct.(DJNB)* 12 (2017): 37-45.
39. Omrani, Emad, Afsaneh Dorri Moghadam, Ashish K. Kasar, Pradeep Rohatgi, and Pradeep L. Menezes. "Tribological performance of Graphite nanoplatelets reinforced Al and Al/Al₂O₃ self-lubricating composites." *Materials* 14, no. 5 (2021): 1183.

40. HG, Prashantha Kumar, and Anthony Xavier. "Tribological aspects of graphene-aluminum nanocomposites." In *Graphene Materials-Structure, Properties and Modifications*. IntechOpen, 2017.
41. Shahzad, Muhammad, Mahmood Khan, Sultan Mehmood, Waqar Adil Syed, Abdul Basit, Nasir Mehboob, and Tahir Ali. "Mechanical, tribological, and electrochemical behavior of hybrid aluminum matrix composite containing boron carbide (B₄C) and graphene nanoplatelets." *Journal of Materials Research* 34, no. 18 (2019): 3116-3129.
42. Tabandeh-Khorshid, Meysam, Emad Omrani, Pradeep L. Menezes, and Pradeep K. Rohatgi. "Tribological performance of self-lubricating aluminum matrix nanocomposites: role of graphene nanoplatelets." *Engineering science and technology, an international journal* 19, no. 1 (2016): 463-469.
43. Kostecki, Marek, Jarosław Woźniak, Tomasz Cygan, Mateusz Petrus, and Andrzej Olszyna. "Tribological properties of aluminium alloy composites reinforced with multi-layer graphene—the influence of spark plasma texturing process." *Materials* 10, no. 8 (2017): 928.
44. Kumar, HG Prashantha, and M. Anthony Xavier. "Assessment of mechanical and tribological properties of Al 2024-SiC-graphene hybrid composites." *Procedia engineering* 174 (2017): 992-999.
45. Martin, Seçkin, Sinan Kandemir, and Maksim Antonov. "Investigation of the high temperature dry sliding wear behavior of graphene nanoplatelets reinforced aluminum matrix composites." *Journal of Composite Materials* 55, no. 13 (2021): 1769-1782.
46. Xavier, M. Anthony, HG Prashantha Kumar, and K. Ajith Kumar. "Tribological studies on AA 2024–Graphene/CNT Nanocomposites processed through Powder Metallurgy." *Materials Today: Proceedings* 5, no. 2 (2018): 6588-6596.

47. Zou, Jia-Liang, Xiao-Liang Shi, Qiao Shen, Kang Yang, Yu-Chun Huang, Ao Zhang, Yu-Fu Wang, and Qiao-Xin Zhang. "Tribological Behavior of TiAl–Multilayer Graphene–Ag Composites at Different Temperatures and Sliding Speeds." *Acta Metallurgica Sinica (English Letters)* 30, no. 3 (2017): 193-200.
48. Çavdar, U., and O. Akkurt. "The Effect of Sintering on the Microstructure, Hardness, and Tribological Behavior of Aluminum–Graphene Nanoplatelet Powder Composites." *Powder Metallurgy and Metal Ceramics* 57, no. 5 (2018): 265-271.
49. Xu, Zengshi, Xiaoliang Shi, Wenzheng Zhai, Jie Yao, Siyuan Song, and Qiaoxin Zhang. "Preparation and tribological properties of TiAl matrix composites reinforced by multilayer graphene." *Carbon* 67 (2014): 168-177.
50. Rengifo, Sara, Cheng Zhang, Sandip Harimkar, Benjamin Boesl, and Arvind Agarwal. "Tribological behavior of spark plasma sintered aluminum-graphene composites at room and elevated temperatures." *Technologies* 5, no. 1 (2017): 4.
51. Jeon, Chi-Hoon, Yong-Ha Jeong, Jeong-Jin Seo, Huynh Ngoc Tien, Sung-Tae Hong, Young-Jin Yum, Seung-Hyun Hur, and Kwang-Jin Lee. "Material properties of graphene/aluminum metal matrix composites fabricated by friction stir processing." *International Journal of Precision Engineering and Manufacturing* 15, no. 6 (2014): 1235-1239.
52. Khodabakhshi, Farzad, Martin Nosko, and Adrian P. Gerlich. "Effects of graphene nanoplatelets (GNPs) on the microstructural characteristics and textural development of an Al-Mg alloy during friction-stir processing." *Surface and Coatings Technology* 335 (2018): 288-305.
53. Zhang, Huijie, Baoxin Zhang, Qiuzhi Gao, Jianling Song, and Guoliang Han. "A review on microstructures and properties of graphene-reinforced aluminum matrix composites fabricated by friction stir processing." *Journal of Manufacturing Processes* 68 (2021): 126-135.

54. Bai, Peikang, Yang Jin, Zhanyong Zhao, Liang Li, Minjie Liang, Haihong Liao, Wenjie Zhao, Yanbin Hu, and Wenbo Du. "Microstructure and tribological behavior of graphene/Al composites produced by selective laser melting." *Materials Research Express* 6, no. 10 (2019): 1065c1.
55. Sharma, Abhishek, Vyas Mani Sharma, Agam Gugaliya, Pragya Rai, Surjya Kanta Pal, and Jinu Paul. "Friction stir lap welding of AA6061 aluminium alloy with a graphene interlayer." *Materials and Manufacturing Processes* 35, no. 3 (2020): 258-269.
56. Liu, Jun, Yingyan Zhang, Yihe Zhang, Sritawat Kitipornchai, and Jie Yang. "Machine learning assisted prediction of mechanical properties of graphene/aluminium nanocomposite based on molecular dynamics simulation." *Materials & Design* 213 (2022): 110334.
57. Hasan, Md Syam, and Michael Nosonovsky. "Topological data analysis for friction modeling." *EPL (Europhysics Letters)* 135, no. 5 (2021): 56001.
58. Hasan, Md Syam, Amir Kordijazi, Pradeep K. Rohatgi, and Michael Nosonovsky. "Triboinformatic modeling of dry friction and wear of aluminum base alloys using machine learning algorithms." *Tribology International* 161 (2021): 107065.
59. Hasan, Md Syam, Amir Kordijazi, Pradeep K. Rohatgi, and Michael Nosonovsky. "Triboinformatics Approach for friction and wear prediction of al-graphite composites using machine learning methods." *Journal of Tribology* 144, no. 1 (2022).
60. Hasan, Md Syam, Amir Kordijazi, Pradeep K. Rohatgi, and Michael Nosonovsky. "Application of Triboinformatics Approach in Tribological Studies of Aluminum Alloys and Aluminum-Graphite Metal Matrix Composites." In *Metal-Matrix Composites*, pp. 41-51. Springer, Cham, 2022.

61. Hasan, Md Syam, Amir Kordijazi, Pradeep K. Rohatgi, and Michael Nosonovsky. "Machine learning models of the transition from solid to liquid lubricated friction and wear in aluminum-graphite composites." *Tribology International* 165 (2022): 107326.
62. Lanka, Sridhar, Evgeniya Alexandrova, Marina Kozhukhova, Md Syam Hasan, Michael Nosonovsky, and Konstantin Sobolev. "Tribological and wetting properties of TiO₂ based hydrophobic coatings for ceramics." *Journal of Tribology* 141, no. 10 (2019).
63. Hasan, Md Syam, Filip Zemajtis, Michael Nosonovsky, and Konstantin Sobolev. "Synthesis of ZnO/TiO₂-Based Hydrophobic Antimicrobial Coatings for Steel and Their Roughness, Wetting, and Tribological Characterization." *Journal of Tribology* 144, no. 8 (2022): 081402.
64. Hasan, Md Syam, and Michael Nosonovsky. "Lotus effect and friction: does nonsticky mean slippery?." *Biomimetics* 5, no. 2 (2020): 28.
65. Wilson, S., and A. T. Alpas. "Wear mechanism maps for metal matrix composites." *Wear* 212, no. 1 (1997): 41-49.
66. Bowden, Frank Philip, Frank Philip Bowden, and David Tabor. *The friction and lubrication of solids*. Vol. 1. Oxford university press, 2001.
67. Archard, John Frederick, and Wallace Hirst. "The wear of metals under unlubricated conditions." *Proceedings of the Royal Society of London. Series A. Mathematical and Physical Sciences* 236, no. 1206 (1956): 397-410.
68. Su, Jinlong, and Jie Teng. "Recent progress in graphene-reinforced aluminum matrix composites." *Frontiers of Materials Science* 15, no. 1 (2021): 79-97.
69. Zhang, Jiangshan, Shufeng Yang, Zhixin Chen, Hui Wu, Jingwei Zhao, and Zhengyi Jiang. "Graphene encapsulated SiC nanoparticles as tribology-favoured nanofillers in aluminium composite." *Composites Part B: Engineering* 162 (2019): 445-453.

70. Baradeswaran, A., and A. Elayaperumal. "Effect of graphite content on tribological behaviour of aluminium alloy-graphite composite." *European Journal of Scientific Research* 53, no. 2 (2011): 163-170.
71. Jha, A. K., S. V. Prasad, and G. S. Upadhyaya. "Dry sliding wear of sintered 6061 aluminium alloy—graphite particle composites." *Tribology international* 22, no. 5 (1989): 321-327.
72. Ravindran, P., K. Manisekar, R. Narayanasamy, and P. Narayanasamy. "Tribological behaviour of powder metallurgy-processed aluminium hybrid composites with the addition of graphite solid lubricant." *Ceramics International* 39, no. 2 (2013): 1169-1182.
73. Penkov, Oleksiy, Hae-Jin Kim, Hyun-Joon Kim, and Dae-Eun Kim. "Tribology of graphene: a review." *International journal of precision engineering and manufacturing* 15, no. 3 (2014): 577-585.
74. Bhadauria, Alok, Lavish K. Singh, and Tapas Laha. "Effect of physio-chemically functionalized graphene nanoplatelet reinforcement on tensile properties of aluminum nanocomposite synthesized via spark plasma sintering." *Journal of Alloys and Compounds* 748 (2018): 783-793.
75. Prakash, P. Bhanu, K. Brahma Raju, K. Venkatasubbaiah, and N. Manikandan. "Microstructure Analysis and Evaluation of Mechanical Properties of Al 7075 GNP's Composites." *Materials Today: Proceedings* 5, no. 6 (2018): 14281-14291.
76. Li, Jianchao, Xuexi Zhang, and Lin Geng. "Improving graphene distribution and mechanical properties of GNP/Al composites by cold drawing." *Materials & Design* 144 (2018): 159-168.
77. Yang, J. B., C. B. Lin, T. C. Wang, and H. Y. Chu. "The tribological characteristics of A356. 2Al alloy/Gr (p) composites." *Wear* 257, no. 9-10 (2004): 941-952.

78. Lin, C. B., T. C. Wang, Z. C. Chang, and H. Y. Chu. "Tribological analysis of copper-coated graphite particle-reinforced A359 Al/5 wt.% SiC composites." *Journal of materials engineering and performance* 22, no. 1 (2013): 94-103.
79. Ravindran, P., K. Manisekar, P. Rathika, and P. Narayanasamy. "Tribological properties of powder metallurgy–Processed aluminium self lubricating hybrid composites with SiC additions." *Materials & design* 45 (2013): 561-570.
80. Ghazaly, A., B. Seif, and H. G. Salem. "Mechanical and tribological properties of AA2124-graphene self lubricating nanocomposite." In *Light Metals 2013*, pp. 411-415. Springer, Cham, 2016.
81. Vencl, Aleksandar, Filip Vučetić, Biljana Bobić, Ján Pitel, and Ilija Bobić. "Tribological characterisation in dry sliding conditions of compocasted hybrid A356/SiCp/Grp composites with graphite macroparticles." *The International Journal of Advanced Manufacturing Technology* 100, no. 9 (2019): 2135-2146.
82. Gore, G. J., and J. D. Gates. "Effect of hardness on three very different forms of wear." *Wear* 203 (1997): 544-563.
83. Gopi, Vivek, R. Sellamuthu, and Sanjivi Arul. "Measurement of hardness, wear rate and coefficient of friction of surface refined Al-Cu alloy." *Procedia Engineering* 97 (2014): 1355-1360.
84. Basavarajappa, S., G. Chandramohan, K. Mukund, M. Ashwin, and M. Prabu. "Dry sliding wear behavior of Al 2219/SiCp-Gr hybrid metal matrix composites." *Journal of Materials Engineering and Performance* 15, no. 6 (2006): 668-674.

CHAPTER 5: TRIBOINFORMATICS MODELING OF THE TRANSITION FROM SOLID TO LIQUID LUBRICATED FRICTION AND WEAR IN ALUMINUM-GRAPHITE COMPOSITES

In previous chapters, Triboinformatics modelling of dry friction and wear of aluminum alloys and aluminum-based MMCs had been presented. The friction and wear mechanisms in these alloys and MMCs change notably in liquid lubricated conditions. In this chapter, besides, the study of wear and friction of aluminum-graphite composites in different lubrication conditions, the effect of the transition between lubrication regimes will be studied using supervised and unsupervised ML models.

5.1. Introduction

Aluminum (Al) based alloys are prevailing engineering materials for low density combined with corrosion resistance, high stiffness, strength, and thermal conductivity [1]. However, Al alloys exhibit high friction and wear rates along with a tendency to seize under dry sliding or poor lubricating conditions [2,3]. Consequently, liquid or solid lubrication is required. Liquid lubrication is the process of controlling the wear and friction between sliding surfaces through films of oil-based liquids: petroleum-based mineral oil, synthetic oil, and other additives. SAE 5W-30, SAE 10W-30, and SAE 20W-50 are some commercially available liquid lubricant grades for industrial applications. Reducing friction and wear by keeping the moving parts apart, controlling the temperature and contaminants, heat dissipation, and corrosion resistance are some desirable consequences of using liquid lubricants. Self-lubrication by solid graphite can be achieved using Al metal matrix composites (MMCs) with graphite particles incorporated into the Al alloy matrix [4]. The atoms in the layer share strong covalent bonds, while weak van der Waals

forces act between the layers, so they shear easily relative to each other. Consequently, graphite is strong in compression but weak in shear, making it a good solid lubricant [5].

In graphite reinforced aluminum aluminum-graphite MMCs, graphite is continuously released at the sliding surface, acting as a self-replenishing solid lubricant, reducing friction and wear. Graphite forms a thin film on the surface of the composite material, in some cases possibly a monolayer. Note that while graphene (monolayer graphite) was discovered only in 2004, carbon monolayers on metallic surfaces were observed already in 1962 [6] and possibly, in tribological applications of aluminum-graphite MMCs where a thin graphite tribolayer is formed [7]. The graphite-on-graphite contact can also lead to the so-called superlubricity or significantly reduced friction [8,9] due to the incommensurate character of atomic-scale asperities. From the physics, the transition to superlubricity is an example of the commensurate-to-incommensurate phase transition.

Tribological behaviors of self-lubricating aluminum-graphite MMCs have been studied actively since low-cost cast aluminum-graphite composites were first synthesized around 1965. Low friction and wear were reported, and graphite content was optimized along with other variables for best mechanical and tribological performance [10, 11]. The friction and wear of aluminum-graphite MMCs are influenced by material variables such as matrix characteristics, graphite content, size and shape of the graphite particles, and material processing procedure [12,13]. Tribological test variables like the sliding distance, speed, and load are also important factors. However, since such a large number of variables influence the mechanical and tribological properties of these composites, the effects of multiple-parameter variations have not been quantified, despite considerable investigation of two-parameter relationships. The multi-parameter study requires data-driven approaches, a common feature of materials tribology, with plentifully

available data on surface properties, friction, wear, and material behavior. Tribology remains a data-driven scientific discipline, especially for complex materials such as two-phase composites, whose surface characteristics change with time. Due to the emergence and rapid development of new methods of Machine Learning (ML) and Artificial Intelligence (AI), it became possible to obtain and study new correlations in data-driven areas of science. In particular, recently, the area of so-called Triboinformatics has been suggested [14,15] and applied to the study of Al base alloy and unlubricated aluminum-graphite composites [16,17]. Complex high-order correlations of the tribological properties of aluminum based materials with material and mechanical properties, manufacturing and processing procedure, and tribological test conditions were successfully modeled using data-driven ML approaches [16,17].

The tribological behavior of aluminum-graphite composites in unlubricated conditions has been studied in recent years to analyze the self-lubricating behavior. Analyzing their tribological and self-lubricating behavior in the presence of liquid lubrication and the transition from lubricated to unlubricated state as a result of drainage in lubricating liquid are of importance in situations where such sudden loss of lubricant can lead to instant seizures and catastrophic failures. For example, a liquid lubricating film separates the piston ring and the cylinder liner during the operation of an internal combustion engine. A sudden draining out of the lubricant causes extensive metal-to-metal contact that gives rise to heavy wear and an abrupt temperature increase. Consequently, piston elements undergo seizure, and an instant system failure occurs. The work in this paper shows that the presence of graphite particles in the matrix enables the aluminum alloys even after the lubricant is accidentally drained.

In this study, a systematic analysis will be performed to understand the underlying mechanisms of wear and friction for liquid lubricated aluminum-graphite composites and the wear

behavior during the transition of different lubrication conditions. Different supervised and unsupervised ML models will be developed for tribological behavior prediction and finding wear and friction patterns in the presence of liquid lubrication.

5.2. Liquid and solid lubricated wear and friction of aluminum-graphite

In this section, the wear and friction mechanisms of aluminum-graphite composites in dry and lubricated conditions will be discussed. Also, different parameters used to characterize lubricated friction and wear regimes will be presented and their relations to the data parameters will be discussed.

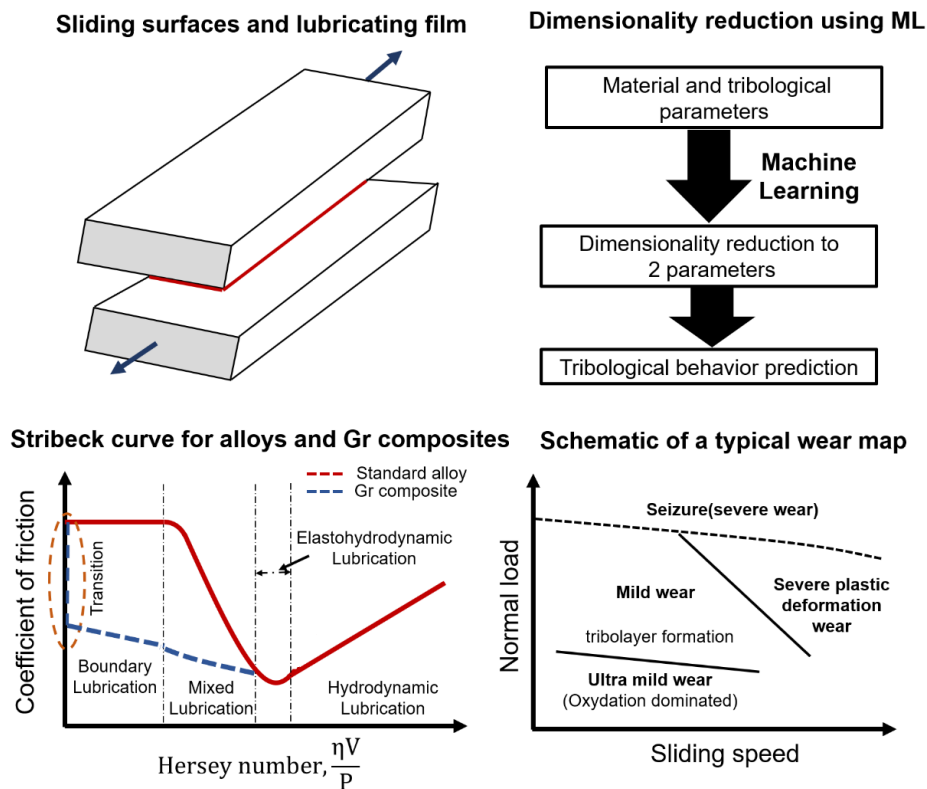


Figure 5.1. Schematic of sliding surfaces and lubricating film, lubrication regimes in Stribeck curve for standard alloys and graphite MMCs, dimensionality reduction technique in ML, and the schematic of a typical wear map

5.2.1. Friction behavior of Al/Gr MMCs in dry condition

According to the classical theory of friction by Bowden and Tabor, the friction force (F_f) has two independent components: adhesion (F_a) and deformation (F_d) [18]. The coefficient of friction (COF) [19] or μ quantifies the friction between interacting surfaces, which is presented as

$$\mu = \frac{F_f}{N} = \frac{F_a + F_d}{N} = \frac{F_a}{N} + \frac{F_d}{N} = \mu_a + \mu_d \quad (1)$$

where the COF for the adhesion and deformation is presented by μ_a and μ_d , respectively.

The adhesion component, F_a depends on the real area of contact at the asperity level between interacting surfaces. During extend sliding under a normal load, the graphite particles are squeezed out from the embedded state from the metal matrix. The smearing of these particles occurs on the tribosurface and forms a lubricating film that reduces the surface-to-surface real area of contact. Wear of the MMC exposes new graphite particles which cause continual replenishment of the graphite film.

If the graphite content in the aluminum-graphite composite is sufficient, a uniform and durable graphite-rich film is established on the tribosurface. It causes a significant reduction of the real area of contact and corresponding adhesion component.

The COF of aluminum-graphite metal matrix composites can be presented by the following equation using the rule of mixture [20].

$$\mu = (1 - A_g)\mu_m + A_g\mu_g \quad (2)$$

where μ_m is the COF of the Al matrix, while μ_g and A_g are the COF and area fraction of the tribosurface enveloped by the graphite film, respectively. The deformation component, F_d

depends on material and mechanical properties such as yield strength, hardness, elasticity, etc., which are subject to the graphite content in the Al matrix of the aluminum-graphite composites.

In a word, the friction behavior of aluminum-graphite MMCs in dry conditions largely depends on the presence of the secondary graphite phase in the aluminum matrix and the extent of the solid lubricating film formation on the tribosurface.

5.2.2. Friction behavior of Al/Gr MMCs in liquid lubrication

The effect of liquid lubrication on friction is usually analyzed with the so-called Stribeck curve, which summarizes different fluid lubrication regimes: the hydrodynamic (HDL), elastohydrodynamic (EDL), mixed, and boundary lubrication (**Figure 5.1**). The COF is plotted against the Hersey number = $\frac{\eta V}{P}$ [21], a dimensionless product of the dynamic viscosity (η) of the fluid and sliding speed (V) divided by the normal load (P). Large Hersey numbers correspond to the hydrodynamic lubrication regime when liquid viscosity is the main factor supporting the load. Small Hersey numbers correspond to the boundary lubrication with nanoscale or molecular layer of the lubricant exists. Hersey number equal to zero corresponds to dry friction.

In the hydrodynamic lubrication regime, the lubricating films between sliding surfaces are stable and thicker than the height of the asperities or irregularities. The elastohydrodynamic lubrication regime is found for heavily loaded contacts where elastic deformation of the mating surfaces shapes the HDL process with a comparatively thinner film thickness [22]. No direct contact among the asperities of the mating surfaces occurs in these regimes, which are often considered ideal in sliding applications. Since the lubricating film supports almost the entire load, the wear and friction are low, and the graphite content does not affect the friction behavior of the Al/Gr MMCs much. In Al/Gr MMCs, the hydrodynamic effects become dominant at a lower

sliding velocity than aluminum base alloys. However, significant differences in the Stribeck curves are observed in aluminum alloys and Al/Gr MMCs during the transition from the EDL regime to the mixed and the boundary lubrication regime [7].

In the mixed lubrication regime, low sliding speed, high load, and increased lubricant temperature are observed with a notable reduction in the lubricant viscosity. Due to a high load, graphite particles are squeezed out of the Al matrix, but the liquid lubricant hinders the self-lubricating graphite film formation and its retention on the tribosurface [10]. Consequently, the graphite content cannot influence the friction characteristics of the aluminum-graphite composites notably in the mixed lubrication regime. A low COF is observed mainly due to the presence of the liquid lubrication film on the tribosurface.

With further increased normal load combined with lower sliding speed and reduced lubricant viscosity, boundary lubrication is observed. Due to the absence of a steady liquid lubrication film, the normal load is entirely supported by extensive asperity contact. Clean surfaces with no lubrication correspond to high surface energy and high friction. However, in aluminum-graphite composites, graphite particles are freed from the matrix material at extensive sliding and form a solid-lubricating graphite film on the tribosurface. Consequently, the friction behavior of aluminum-graphite composites in this lubrication regime depends on the graphite content and the graphite film formation.

In summary, for self-lubricating materials, such as the Al/Gr MMC, the Stribeck curve would be significantly different from the standard one because, in the limit of moderate and absent lubrication, the solid lubrication prevails over other mechanisms.

5.2.3. Friction behavior of Al/Gr MMCs in the transition from liquid to dry condition

In the dry condition, the graphite content and the solid-lubricating graphite film formation are critical factors for the friction behavior of Al/Gr MMCs. However, in the fully lubricated condition, when a stable liquid lubrication film is present between the mating surfaces, the graphite content has little impact on the friction behavior. The COF of Al 6061 alloy and Al 6061/Gr MMCs with varied graphite content in the fully lubricated condition is compared with the COF of Al 6061 alloy in the dry condition against the same counterface in **Figure 5.2(a)** [23]. A significant decrease in COF is observed in the Al 6061 alloy in the fully lubricated condition.

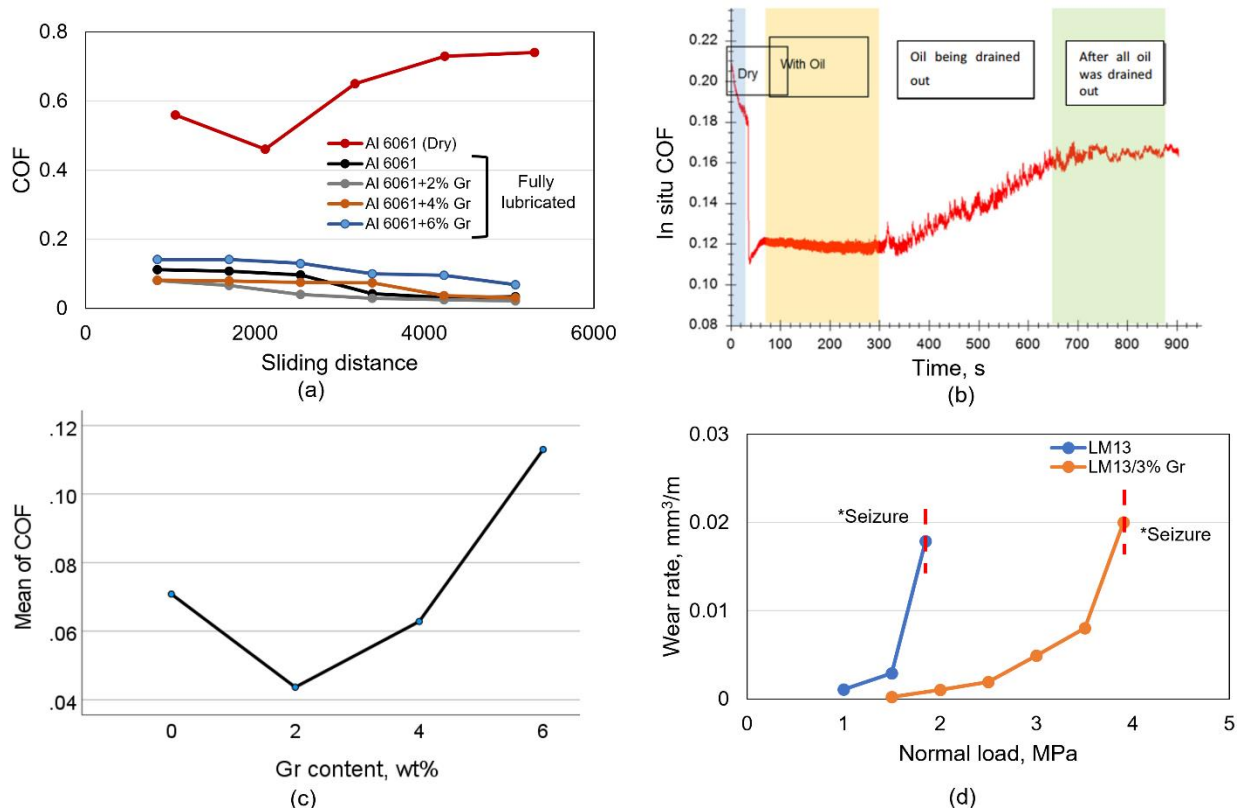


Figure 5.2. (a) COF vs sliding distance in dry and fully lubricated conditions, (b) in situ COF data with time for Al-16Si-5Ni-5Graphite MMC in different lubrication conditions (Reprinted by permission from Springer, Ref. [24], Copyright (2016)), (c) Mean of COF vs Gr content plot from the Linear Contrast Analysis, (d) wear and seizure behavior of LM13 alloy and LM13/3%

Gr MMC under different normal load at the same sling speed

In the fully lubricated condition, the alloy and MMCs with different graphite content exhibited similar COF values. We performed statistical analysis to find any statistically significant differences between the COF of Al 6061 alloys and the Al 6061/Gr MMCs with 2%, 4%, and 6% Gr in the fully lubricated condition. First, we performed the normality test to check if the COF data is normally distributed using the IBM SPSS Statistics software. During hypothesis testing in statistical analysis, the significance level (presented as α) denotes the possibility of the “Type 1” error (the probability of rejecting the null hypothesis when it is true). The probability value (p-value) in the normality test was $0.092 > \alpha$ (0.05). With a 95% confidence level, we failed to reject the null hypothesis that the data is normally distributed. Then, we performed the Linear Contrast Analysis (LCA) to find if there are statistically significant differences between the mean COF of Al 6061 alloys and Al 6061/Gr MMCs with 2%, 4%, and 6% Gr. The p-value in the LCA test was 0.13, which is larger than α (0.05). Consequently, with a 95% confidence level, we failed to reject the null hypothesis, which states that there is no statistical difference between the paired combinations of the mean COF values (**Figure 5.2(c)**). The statistical analysis indicates that for Al 6061 and Al 6061/Gr MMCs in the fully lubricated condition and under similar tribological conditions, a variation in graphite content causes little variation in the friction behavior.

Omrani et al. studied the friction behavior of Al-16Si-5Ni-5Gr MMC against a steel counterface where the lubrication condition is changed in four stages in an experiment [24]. The first stage was dry friction when the COF was reduced from 0.21 to 0.18 because of the graphite film formation (**Figure 5.2(b)**). The second stage was in a fully lubricated condition when a reduced constant value of COF (0.12) was observed. During the third stage, when the lubricant was gradually being drained out, a gradual increase in COF was observed. The final stage began in the absence of lubricant and continued till the end of the test when a stable COF (0.165) was

observed, which is less than the COF (0.18) of the first stage of dry friction just before the introduction of the lubrication. Besides the graphite self-lubricating film, nanoscale or molecular layer of the lubricant retention on the microporous surface can cause this transition in friction behavior of aluminum-graphite composites.

In summary, the incorporation of the liquid lubrication causes a transition in friction behavior in aluminum-graphite composites by forming the liquid lubrication film, nanoscale, or molecular layer of lubricant retention on the microporous surface and influencing the graphite film formation process on the tribosurface.

5.2.4. Wear behavior of Al/Gr MMCs in dry

Wear regimes of various materials are often characterized by so-called wear maps, where the transition among different wear mechanisms is typically presented as a function of two variables: the normal load and sliding speed (**Figure 5.1**). Due to the extensive effect of normal load and sliding speed on wear mechanisms, wear maps provide an instantaneous and convenient approximation of general wear patterns in a wide range of tribological interactions.

A transient process followed by the steady-state condition characterizes the wear behavior of aluminum-graphite composites in dry conditions [13,25]. The wear behavior depends on the formation and the retention of the solid lubricant graphite film over the tribo-interface and its physical properties [16]. The wear of the aluminum matrix phase and the graphite reinforcement phase both contribute to the overall wear. Adhesive, abrasive, and delamination are reported as the most dominant wear mechanisms in aluminum-graphite composites [25,26]. At the early stages of sliding or with a low graphite content, there are not enough graphite particles available at the tribosurface to form a stable graphite film. Consequently, extensive metal-to-metal contact is

observed between the sliding surfaces, and adhesive junctions are formed at the spots of the real area of contact. These adhesive junctions are sheared during sliding and cause adhesive wear. Due to the fracture and plastic deformation during extensive shearing, material transfer from the softer to the harder surface takes place.

Once a stable graphite film is formed, and a critical thickness is exceeded, delamination becomes the dominant wear mechanism in aluminum-graphite composites. In delamination wear, the accumulation of dislocations causes subsurface cracking at a certain depth under the tribosurface as the soft graphite film is deformed [27]. Frictional and material properties and tribological parameters govern the crack initiation and propagation at the subsurface region. Under repeated loading, an unstable propagation of cracks occurs once it exceeds a critical length, and a thin laminate of the softer material is generated as wear debris. Besides these two forms of wear, abrasive wear is observed for aluminum-graphite composites while sliding against a harder counterface. Several forms of plastic deformation: cutting, plowing, and wedge formation of the asperities of the softer surface take place in abrasive wear.

Wear mechanisms and wear behavior of aluminum-graphite composites are greatly dependent on the operating condition. Archard and Hirst suggested two distinct wear regimes: mild wear and severe wear in sliding contact depending upon the normal load [28]. The transition from mild to severe wear in aluminum-graphite composites occurs at the critical load beyond which the protective oxide and graphite layers are destroyed, and considerable metal-to-metal contact occurs. This wear regime is known as severe, which is characterized by a rough wear surface and a high wear rate. Significant material removal through adhesive and delamination wear is observed. For aluminum-graphite composites, wear regimes are also dependent on the sliding speed. Up to a critical sliding speed, the film on the tribosurface remains intact with little metal-to-metal contact.

Mild wear is observed at this stage with a low wear rate. Once the sliding speed surpasses the critical value, the effect of the lubricating film is diminished, and a sudden drastic increase of wear rate is observed.

Das et al. compared the wear and seizure behavior of LM13 alloy and LM13/Gr MMC in different loading conditions at the same sliding speed [29]. They reported significant improvement in wear performance and seizure resistance with graphite addition (**Figure 5.2(d)**). The aluminum alloy exhibited high wear rates and seized at a low load and sliding distance. On the contrary, the aluminum-graphite composite exhibited low wear rates for an extended sliding distance and increased load before the seizure. Rohatgi and co-workers also reported similar findings where the seizure resistance of aluminum-graphite composites increased with the weight percentage of graphite in the aluminum matrix [30].

5.2.5. Wear mechanism of aluminum-graphite composites in liquid lubrication

The lubrication regime, the nature of the liquid lubrication film, graphite film formation, and the mixing of graphite particles with the liquid lubricant dictate the wear mechanism and behavior of the aluminum-graphite composites. The reduction of surface-to-surface contact in liquid lubrication causes reduced wear. In the HDL regime, the liquid lubricating film is stable and thick enough to support almost the entire normal load. No direct contact between the sliding surfaces is observed, and the wear behavior is practically unaffected by the graphite content. However, adhesive wear at the beginning and the ending of sliding, corrosion, and fatigue are common forms of wear mechanism noticed in the EDL regime.

For aluminum-graphite composites, adhesive, delamination, and abrasive wear mechanisms are dominant in the mixed lubrication regime. In this regime, graphite particles are freed from the

Al matrix at extended sliding but fail to form a stable graphite film on the tribosurface due to the presence of the liquid lubricant. Instead of forming a stable graphite film, graphite particles mix with the liquid lubricant. Prasad analyzed the influence of graphite particles in the lubricant mixture and the corresponding effect on the wear performance of composites. He reported the existence of an optimum graphite particle concentration in the liquid lubricant that leads to superior wear performance [31]. Higher graphite content and the disproportionate mixing with the liquid lubricant may cause protruding out of graphite particles from the tribosurface and an increased weight loss [10].

In the boundary or starved lubrication condition, the graphite content and the solid-lubricating film formation on the tribosurface become dominant factors for the wear behavior. Adhesive, abrasive, and delamination are the governing wear mechanisms in boundary lubrication.

In Machine Learning, presenting the friction and wear maps, which are dependent on a small number of parameters using the multi-parameter data (such as material properties and tribological test variables), is a typical problem of dimensionality reduction. Such problems are handled by the principal component analysis (PCA), topological data analysis, and similar. In the next section, we will develop unsupervised and supervised ML models to present and predict the tribological performance of aluminum-graphite composites in the presence of liquid lubrication.

5.3. Materials and methods

This section covers the collection and processing of data, measures for optimizing and improving the prediction capacity of the developed supervised and unsupervised ML models to predict and analyze the tribological behavior of aluminum-graphite composites.

5.3.1. Collection of data

Relevant and representative data are a prerequisite for developing efficient ML models. The development of ML models requires a significant amount of data that can be highly time and resource-intensive to generate through experimentation. Additionally, experimental data from multiple sources are preferred in developing ML models from the data science’s point of view to avoid passing unsolicited trends from a particular source and improving generalization capacity. For these, we collected data of aluminum-graphite composites in lubricated and dry conditions from selected sources reported in the literature [10,22,24,29,30,32-38]. A total of 325 and 330 data points were considered in friction and wear modeling, respectively.

A total of 14 material and tribological variables: graphite content, hardness, ductility, processing procedure, heat treatment, silicon carbide content, yield strength, normal load, sliding distance, sliding speed, counterface, tribo-test method, lubrication condition, and lubricant viscosity were considered as the input parameters for the ML analysis. Heat treatment, processing procedure, counterface, tribo-test method, and lubrication conditions were defined as categorical data, while the rest of the input variables were numerical. For the developed ML regression models, the output parameters were the COF and the wear rate. Lubricants used in different studies and their corresponding dynamic viscosities at room temperature are presented in **Table 5.1**.

Table 5.1. Lubricant types, grades, and dynamic viscosities at room temperature

Lubricant type	Lubricant grade	Dynamic viscosity, Ns/m²
Engine oil	SAE 10	0.079
Synthetic motor oil	SAE 5W-30	0.207
Synthetic motor oil	SAE 10W30	0.170

Mineral engine oil	SAE 20W-50	0.521
Crankcase oil	SAE 15W	0.110
Engine oil	SAE 30	0.310
Engine oil	SAE 40	0.430
Gear oil	VG 46 (ISO 3848)	0.461

5.3.2. Machine Learning models

Unsupervised and Supervised data-driven ML models were developed for dimensionality reduction and tribological behavior prediction of Al/Gr MMCs. Unsupervised Principal Component Analysis (PCA) was used for dimensionality reduction and data visualization. Supervised standalone ML regression models: Gradient Boosting Machine (GBM), Random Forest (RF), Artificial Neural Network (ANN), Support Vector Machine (SVM), K Nearest Neighbor (KNN), and hybrid ensemble regression model: RF-GBM (hybrid model combining RF and GBM) were developed for this. Python, its standard libraries, and toolkits were used to perform the ML analysis. The ML models used in this study have been discussed at length in **Chapter 2** of this dissertation.

5.3.3. Data preprocessing

Data preprocessing techniques for the ML models included data cleaning, correcting unusual and missing values, data normalization or feature scaling, data shuffling, and data splitting for the training and testing. We used the Python programming language and its standard libraries for this purpose. Any unusual and missing values in the dataset were handled accordingly. Data normalization or feature scaling was performed, which brought the input variables in the same

numerical range and improved the sensitivity of the ML models for different variables. To scale the features, we used the “RobustScaler” due to its effectiveness in handling outliers. We considered the classical data splitting scheme for ML regression models: 75% data for training and 25% for testing. 25% of the total training data were used to validate and improve the model performance. Data shuffling was done before data splitting to avoid undesired biases passing to the training and test sets.

5.3.4. Optimization of parameters for regression models

The optimization of parameters of regression models is required to maximize the predictive performance for different data types. We found the parameter values for the optimized performance of different ML models through grid search and five-fold cross-validation methods. These are optimization techniques additive to the developed ML models. In these techniques, ML models are executed numerous times with different ranges of parameters, and the best parameters are recommended through performance evaluation. The optimized parameters for different ML regression models are documented in **Table 5.2** and **Table 5.3**.

Table 5.2. Optimized parameters for COF prediction

ML model	Optimized parameters
GBM	n_estimators = 300, learning rate = 0.4
RF	n_estimators= 80, max_features = 4
ANN	activation function: tanh, alpha = 0.012, hidden layer sizes = (10,10,10)
SVM	C = 100, gamma = 0.08, kernel = rbf
KNN	n_neighbors=3, weights = distance

RF-GBM	n_estimators= 50, max_features = 4, learning
hybrid	rate = 0.4, max_depth = 3

Table 5.3. Optimized parameters for wear rate prediction

ML model	Optimized parameters
RF	n_estimators= 100, max_features = 4
GBM	n_estimators = 100, learning rate = 0.015
KNN	n_neighbors=3, weights = uniform
ANN	Activation function: tanh, alpha = 0.07, hidden layer sizes = (10,10,10)
SVM	C = 100, gamma = 0.25, kernel = rbf,
RF-GBM	n_estimators= 100, max_features = 3, learning
hybrid	rate = 0.015, max_depth = 2

5.4. Result and discussion

Here we document the results of the unsupervised and supervised ML models to analyze the tribological performance of aluminum-graphite composites in the presence of liquid lubrication. Model performance evaluation with standard performance evaluation metrics and insights on friction and wear behavior from the ML analysis are also presented.

5.4.1. Friction and wear patterns through dimensionality reduction using PCA

The wear rate of Al/Gr MMCs is plotted in a 2-dimensional PCA plot against the first two principal components in **Figure 5.3**. The principal components are mutually uncorrelated new

variables derived from the linear combinations of the actual input variables. The cumulative variance plot (**Figure 5.3**) shows that for wear rate data, the first two principal components can explain about 60% variance of the actual data represented by the total 14 input variables. Increasing the number of principal components improves the cumulative explained variance in the dataset but makes the presentation of the dataset impossible in a plot. In the PCA plot for wear rate, 5 clusters of data with differential wear rates are observed. This indicates the possibility of having five distinct wear zones in a traditional wear map.

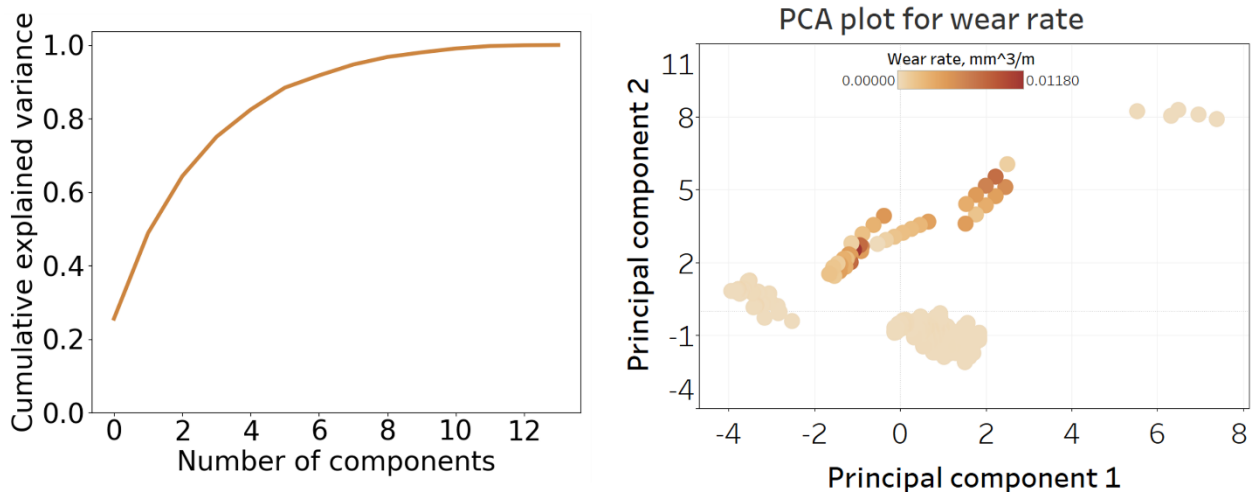


Figure 5.3. Cumulative explained variance and PCA plot for wear rate

Figure 5.4 presents the cumulative explained variance plot and the 2-dimensional PCA plot for COF. The first two principal components can explain about 65% variance of the actual COF data represented by 14 input variables. Though the PCA plot for COF cannot present clear segregation of data like the wear rate data with just two principal components, it exhibits several clusters of data for COF, which might be due to different lubrication regimes and applied loading conditions.

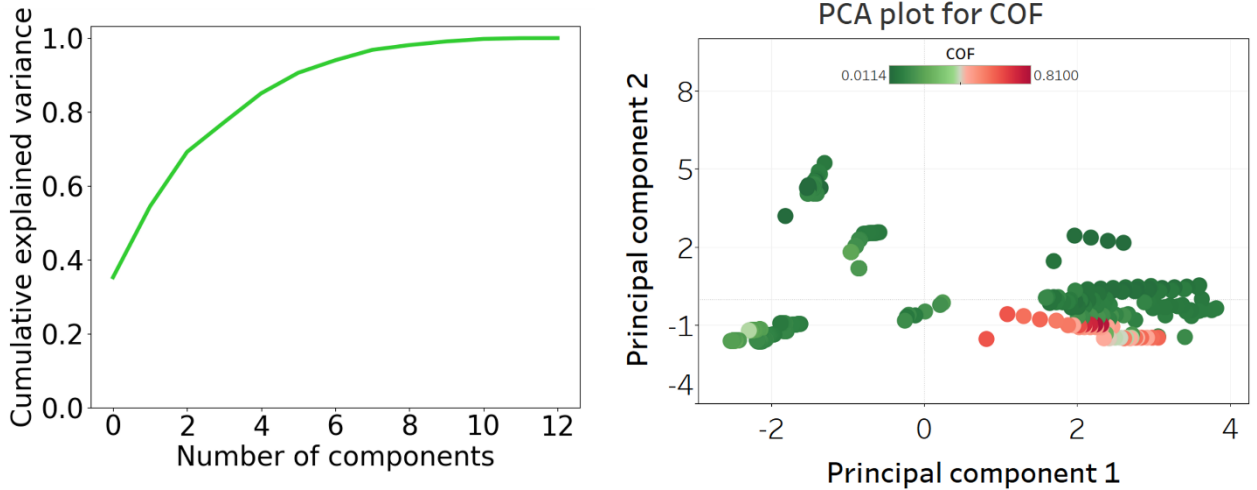


Figure 5.4. Cumulative explained variance and PCA plot for COF

Finally, we used PCA for feature extraction to develop ML regression models in wear and friction prediction. The cumulative explained variance plot of both wear rate and COF indicates that the first five principal components preserve more than 90% variance in the data. To find the presence of redundant input variables for ML models, we extracted the first five principal components (PCA descriptors) for wear rate and COF and used them as input variables for the best performing ML regression models. The regression model performance with PCA descriptors comparing with the performance with all 14 input variables will provide an idea about the soundness of the feature selection process for the ML study.

5.4.2. ML regression model performance analysis

The performance of ML regression models is studied with standard measures: the coefficient of determination (R^2), mean squared error (MSE), root mean squared error (RMSE), and mean absolute error (MAE). Values of $0.7 < R^2 < 0.9$ are viewed as a satisfactory fit, while $R^2 > 0.9$ is excellent ML regression model execution [16]. Small values of MSE, RMSE, and MAE are sought for a good fit.

5.4.2.1. Model performance for COF prediction

The prediction performance of the developed regression models for COF is presented in **Table 5.4**. For the five standalone ML models, the R^2 value ranged between 0.8777 – 0.9546 with significantly low values of MSE, RMSE, and MAE. Statistically, the ML models performed “very satisfactorily” in COF prediction using the 14 material and tribological variables. With $R^2 = 0.9546$, MAE = 0.0226, MSE = 0.0015, and RMSE = 0.0391, decision tree based GBM displayed the best prediction model execution among the standalone ML models by explaining about 95.5% variation in the dataset.

Table 5.4. Prediction performance metrics for COF

Model name	MSE	RMSE	MAE	R^2 value
GBM	0.0015	0.0391	0.0226	0.9546
RF	0.0016	0.0410	0.0216	0.9503
ANN	0.0018	0.0431	0.0252	0.9450
SVM	0.0023	0.0483	0.0216	0.9311
KNN	0.0041	0.0643	0.0286	0.8777
RF-GBM hybrid	0.0012	0.0356	0.0201	0.9626
RF-GBM hybrid with PCA descriptors	0.0057	0.0755	0.0356	0.8315

The actual vs. predicted COF using GBM presented in **Figure 5.5** demonstrates an excellent agreement between observed and predicted outputs. RF, the other decision tree-based ML model also performed very satisfactorily with $R^2 = 0.9503$, MAE = 0.0216, MSE = 0.0016,

and RMSE = 0.0410. The hybrid RF-GBM model was developed by integrating the two best standalone models. The performance metrics: $R^2 = 0.9626$, MAE = 0.0201, MSE = 0.0012, and RMSE = 0.0356, indicate that the hybrid model has improved prediction capacity as it could explain about 96.26% variation in the data. **Figure 5.6** shows an excellent agreement between the actual and the predicted data using the hybrid RF-GBM model. Again, the RF-GBM hybrid model with PCA descriptors performed “satisfactorily” with $R^2 = 0.8315$, MSE = 0.0057, RMSE = 0.0755, and MAE = 0.0356. However, the predictive performance is weaker compared with other hybrid and standalone ML models. This indicates that the actual 14 variables considered in the study are significant in COF prediction and the 5 PCA descriptors (preserves about 90% variance of the actual variable set) derived through dimensionality reduction from the actual 14 variables has suffered information loss which is directly related to the COF prediction.

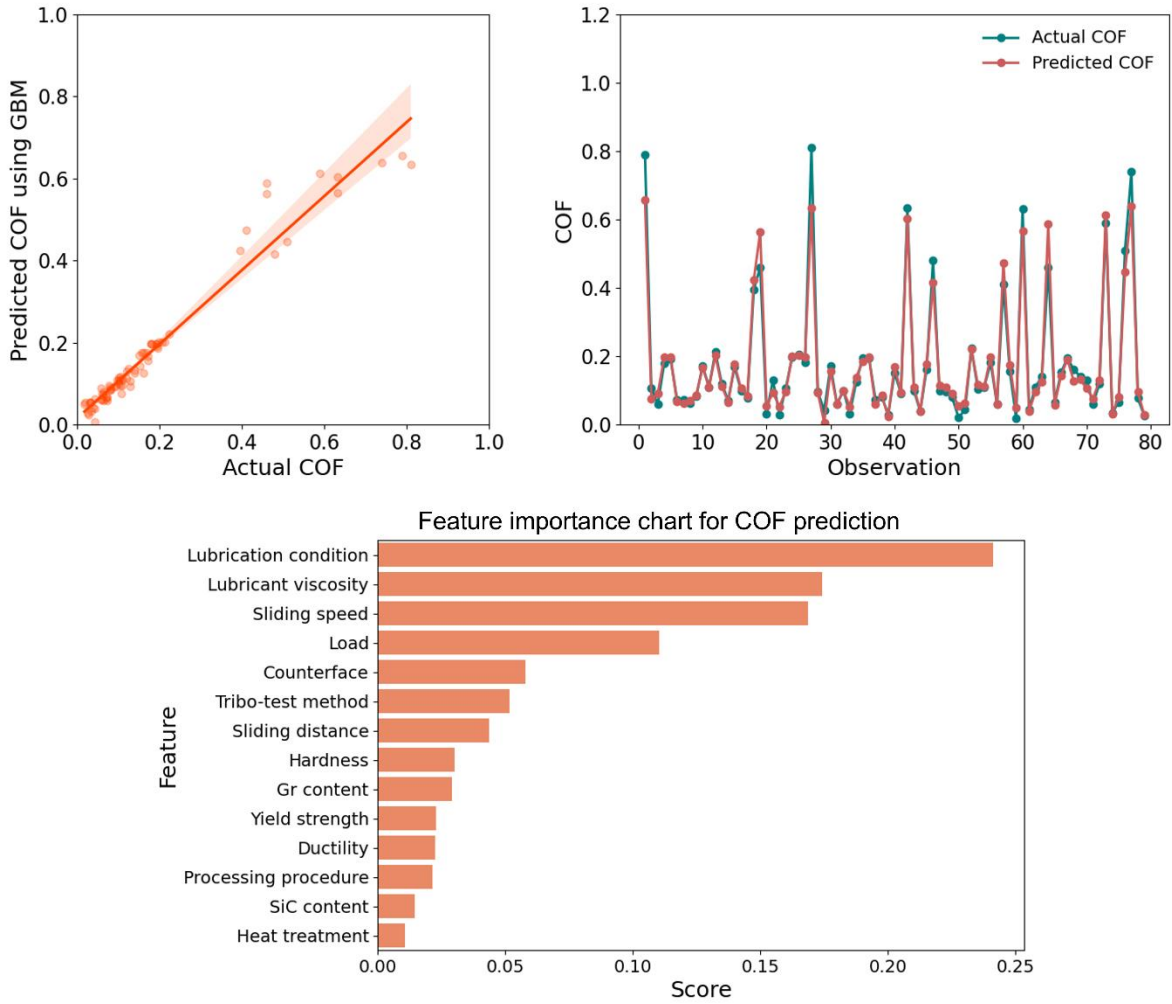


Figure 5.5. Plot of predicted vs. actual COF using GBM, feature importance chart for predicting COF

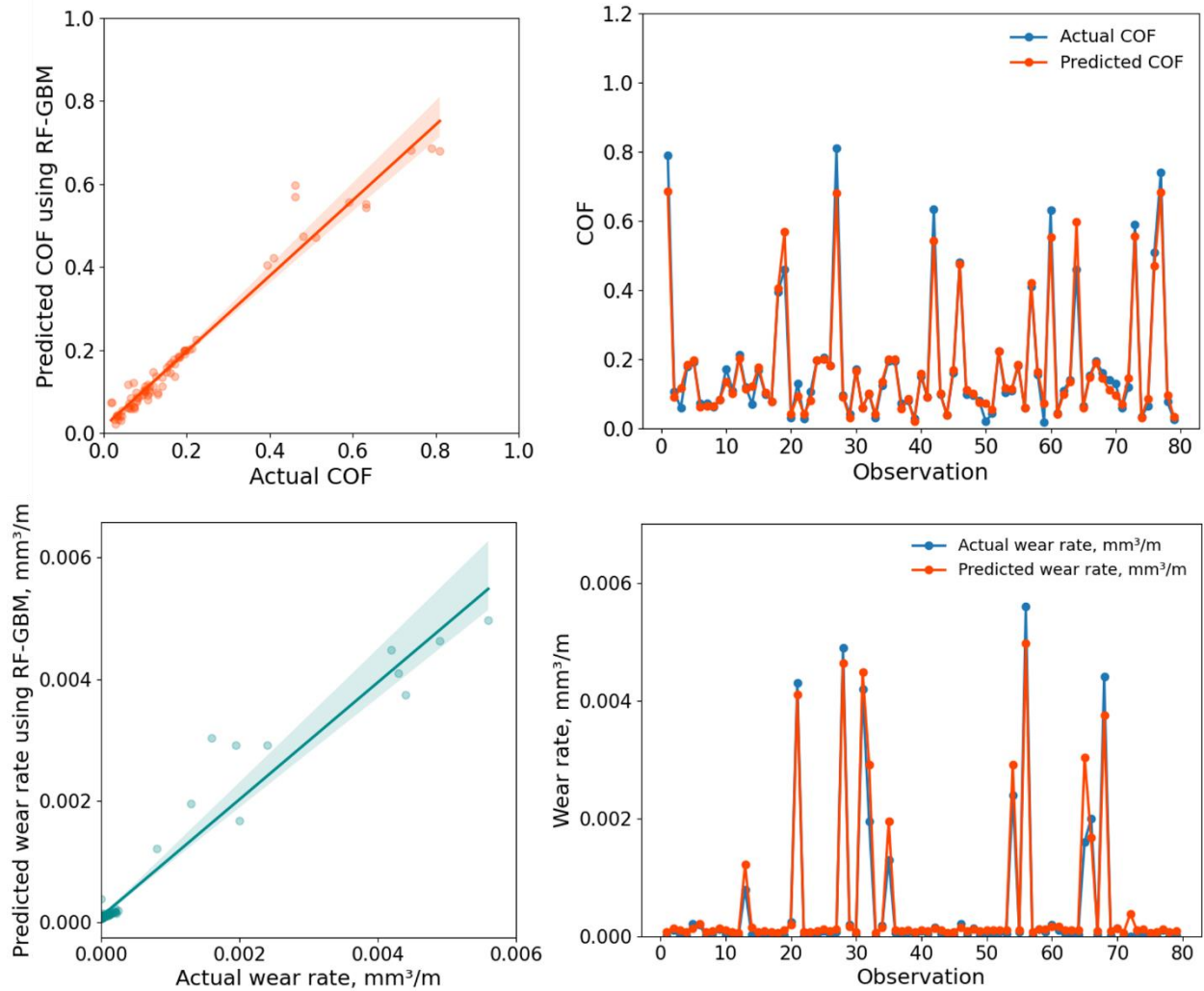


Figure 5.6. Plot of actual vs. predicted COF and wear rate using RF-GBM hybrid model

5.4.2.2. Feature importance for COF prediction

The relative importance of each of the 14 independent material and tribological variables for COF prediction is presented in the feature importance chart of **Figure 5.5**. Lubrication condition and lubricant viscosity have the highest contribution in COF prediction of the Al/Gr MMCs. Sliding speed and load also have significant contributions in COF prediction. In the presence of liquid lubrication, stable graphite films that provide the self-lubrication effect cannot form on the tribosurface as effectively as the dry condition [10]. Consequently, the effect of

graphite content is no longer significant comparing to the result of the previous study of Al/Gr MMCs in the dry condition [16]. A non-zero contribution of the independent variables indicates that none of the selected variables is redundant for the regression models and contributes to COF prediction. For this reason, the developed RF-GBM hybrid model with 5 PCA descriptors exhibited lower predictive performance compared to other ML models.

5.4.2.3. Model performance in wear rate prediction

The prediction performance of the developed machine learning regression models for wear rate is presented in **Table 5.5**. For the 5 standalone ML models, the R^2 value ranged between 0.7924 – 0.9283 with significantly low values of MSE, RMSE, and MAE. Statistically, the ML models performed “satisfactorily” and “very satisfactorily” in wear rate prediction with the 14 material and tribological variables. Among the standalone models, the decision tree-based RF outperformed others with $R^2=0.9283$, $MSE = 1.02 \times 10^{-7}$, $RMSE = 0.0003$, and $MAE = 0.0001$ by accounting for about 93% variation in the dataset.

Table 5.5. Prediction performance metrics for wear rate

Model name	MSE	RMSE	MAE	R^2 value
RF	1.02×10^{-7}	0.0003	0.0001	0.9283
GBM	1.59×10^{-7}	0.0004	0.0002	0.8879
KNN	2.03×10^{-7}	0.0005	0.0002	0.8566
ANN	2.10×10^{-7}	0.0004	0.0003	0.8518
SVM	2.94×10^{-7}	0.0005	0.0003	0.7924
RF-GBM hybrid	6.79×10^{-8}	0.0002	0.0001	0.9521

RF-GBM hybrid with	1.76×10^{-7}	0.0004	0.0002	0.8755
PCA descriptors				

An excellent agreement between the actual and predicted wear rate for the RF model is observed in **Figure 5.7**. Decision tree based GBM displayed the second-best prediction model execution for wear rate with $R^2 = 0.8879$, MAE = 0.0002, MSE = 1.59×10^{-7} , and RMSE = 0.0004. A hybrid RF-GBM model for wear rate prediction was developed through the hybridization process of the two best standalone models. The performance metrics ($R^2 = 0.9521$, MSE = 6.79×10^{-8} , RMSE = 0.0002, and MAE = 0.0001) indicate that the hybrid RF-GBM model improved the prediction capacity and could explain about 95.21% variation in the wear rate data. **Figure 5.6** shows an excellent agreement between the actual and the predicted wear rate for the hybrid RF-GBM model. The RF-GBM hybrid model with 5 PCA descriptors performed “satisfactorily” with $R^2 = 0.8755$, MSE = 1.76×10^{-7} , RMSE = 0.0004, and MAE = 0.0002. Also, the predictive performance with dimensionality reduction (5 PCA descriptors) is better than the 3 standalone ML models (ANN, KNN, AND SVM) with the complete set of 14 variables. These results indicate that one or more variables considered in this study for wear rate prediction may be weakly related to the wear rate, and the dimensionality reduction did not cause too much information loss for a satisfactory prediction of the wear rate of Al/Gr MMCs.

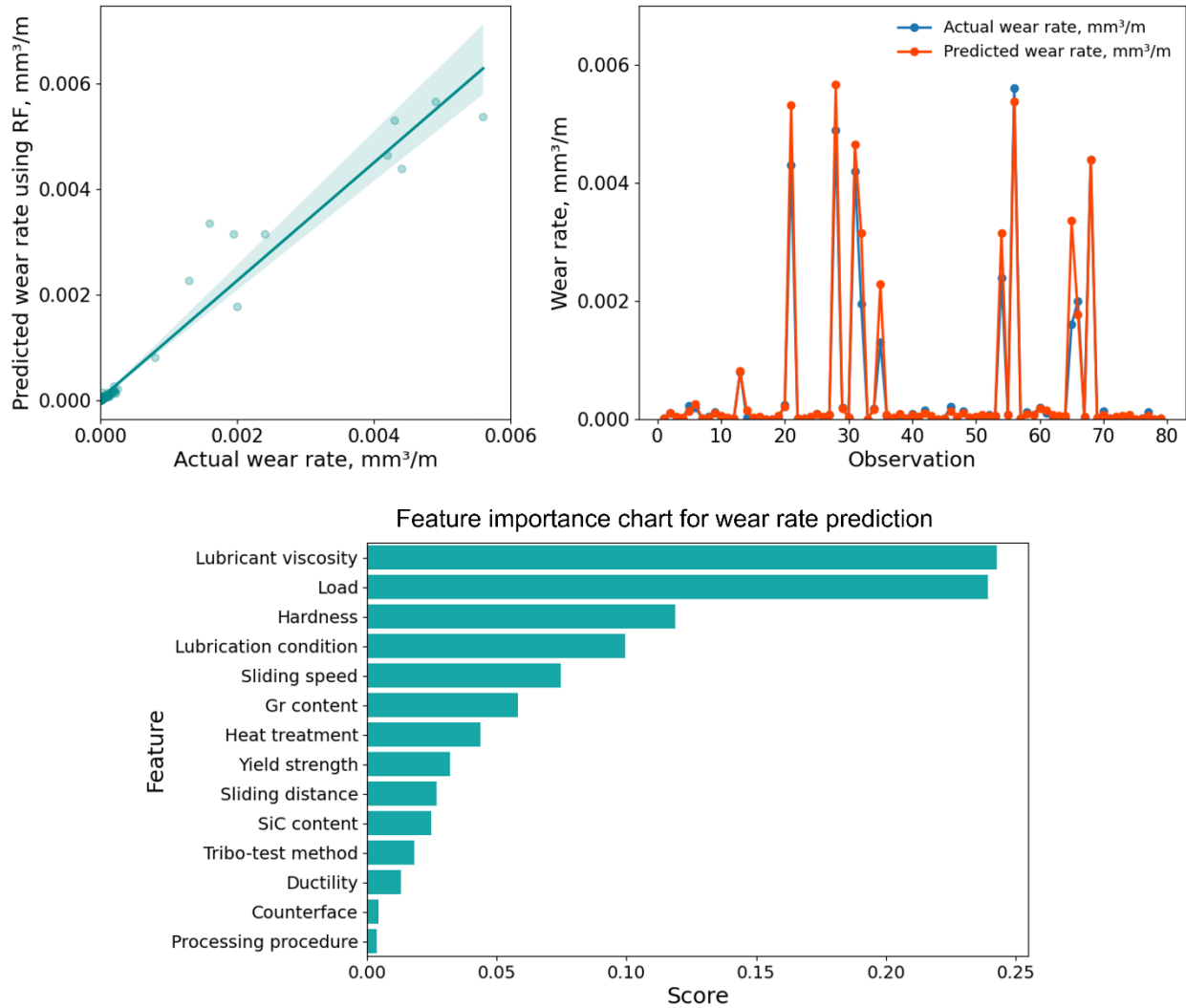


Figure 5.7. Plot of predicted vs. actual wear rate using RF, feature importance chart for predicting wear rate

5.4.2.4. Feature importance for predicting wear rate

The importance comparison of each of the 14 independent material and tribological variables for wear rate prediction is presented in the feature importance chart of **Figure 5.7**. Among the considered variables, lubricant viscosity, load, hardness, lubricating condition, and sliding speed have the biggest contribution. ML analysis suggests that, unlike the COF, the wear rate of the aluminum-graphite composites has a notable dependency on graphite content in the

presence of liquid lubrication. A disproportionate mixing of loose graphite particles with the lubricant and protruding out of graphite particles from the tribosurface directly impact the wear rate. Among the considered variables in the wear rate prediction, the counterface and the processing procedure have negligible contributions. The presence of the liquid lubricating film separates the two sliding materials and carries almost the entire load, especially in the hydrodynamic lubrication regime. This could be a probable reason that the variation in the collected wear rate data for these two variables was not significant. Due to this, the RF-GBM hybrid model with 5 PCA descriptors exhibited better predictive performance than some of the standalone ML models.

5.4.3. Selection of ML models in tribological behavior prediction

In this section, insights into the tribological performance of aluminum-graphite MMCs in the presence of liquid lubrication will be presented from the ML analysis. Also, ML models will be recommended for different aluminum alloys, aluminum-graphite, and aluminum-graphene MMCs in different lubrication conditions.

The statistical performance metrics of the developed standalone and hybrid machine learning models for wear and friction prediction of aluminum-graphite composites in the lubricated condition were compared with those in our previous study at the dry condition [16]. The statistical evidence indicates that the ML models performed significantly better in tribological behavior prediction in the presence of liquid lubrication despite having a smaller dataset than in the dry condition. In other words, the wear and friction behavior of aluminum-graphite composites are more predictable in the presence of liquid lubrication than in the dry condition. In the dry condition, graphite content was the key parameter in tribological behavior prediction. The complexity

associated with the formation of a stable graphite film on the tribosurface was one of the primary reasons for the low predictive performance of the ML models in dry conditions.

In presence of the liquid lubrication, the lubrication condition and the lubricant viscosity were identified as the most influential parameter. In a fully lubricated hydrodynamic lubrication condition, the stable and thick lubricating film separates the sliding surfaces, and there is no or minimal contact between the Al/Gr samples and the counterface materials during the tribological test. In the wear rate study with ML, the influence of counterface was negligible in the feature importance chart. The effect of graphite content is also found less important than the dry condition for both COF and wear rate prediction. Consequently, the tribological behavior of aluminum-graphite composites was more predictable for liquid lubrication conditions.

Finally, we tried to find and recommend the best ML regression models for the tribological behavior prediction of aluminum alloys and aluminum-graphite and aluminum-graphene composites from the findings of different studies [16,17,41]. The decision tree-based models (RF and GBM) outperformed other standalone machine learning models consistently in the presence of categorical variables and fluctuations in the dataset. Both models use ensemble algorithms that involve developing decision trees with the data for mapping the output. However, there are significant differences in the decision tree-building processes of these two models. RF uses the bagging mechanism where trees are built independently using random samples from the dataset, and once the tree-building process is completed, the average of the individual results of each tree yields the final result. The bagging mechanism makes RF efficient in solving overfitting problems and handling large fluctuations and outliers in the dataset. GBM uses the boosting mechanism, which may be affected by fluctuations and outliers but is effective for handling complex datasets. As variations and outliers are less prevalent in the friction data than wear, RF often displays the

best prediction model execution for wear rate, while GBM excels in COF prediction [16,17,41]. In this study, it was found that hybrid ensemble models integrating the standalone RF and GBM model can maximize the predictive performance.

5.5. Conclusion

A systematic analysis was performed to understand the mechanisms of friction and wear of aluminum-graphite composites in dry, partially lubricated, and lubricated conditions and investigated the transition of different lubricating regimes. Supervised and unsupervised ML models were developed to predict the wear and friction behavior and patterns of aluminum-graphite composites in the presence of liquid lubrication. Using PCA, dimensionality reduction was performed, the higher dimensional data in 2-D plots were presented, and possible clusters in the tribological data were identified. Five standalone regression models, one hybrid regression model combining the best two standalone models, and one hybrid regression model with the PCA descriptors for both COF and wear rate prediction were developed. Decision tree based machine learning models displayed the best predictive model execution with tribological data, which is consistent with previous studies [16,17]. The decision tree based GBM ($R^2 = 0.9546$, MAE = 0.0226, MSE = 0.0015, and RMSE = 0.0391,) and RF ($R^2 = 0.9283$, MAE = 0.0001, MSE = 1.02×10^{-7} , and RMSE = 0.0003) models outperformed others in predicting COF and wear rate, respectively among the standalone ML models. The hybrid RF-GBM models developed by integrating the best two standalone models displayed the best predictive model execution for COF ($R^2 = 0.9626$, MAE = 0.0201, MSE = 0.0012, and RMSE = 0.0356) and wear rate ($R^2 = 0.9521$, MAE = 0.0001, MSE = 6.79×10^{-8} , and RMSE = 0.0002).

ML analysis revealed that the lubrication condition and lubricant viscosity are the most important variables, along with applied load and sliding speed in predicting wear rate and COF. Graphite content, which was the most crucial parameter in the dry condition [16], has reduced impact in the presence of liquid lubricants. Variations and outliers in wear and friction data were less prevalent in liquid lubricated conditions. Consequently, the ML models exhibited better predictive performance in the presence of liquid lubrication than in the dry condition. Overall, the tribological characteristics of aluminum-graphite composites are more consistent and predictable in the liquid lubricated condition than the dry. The presence of graphite particles in the matrix of aluminum alloys enables them to run longer at lower friction even after the lubricant is drained out.

5.6. References

1. Macke, Anthony, B. F. Schultz, and Pradeep Rohatgi. "Metal matrix composites." *Adv. Mater. Processes* 170, no. 3 (2012): 19-23.
2. Liu, Y., R. Asthana, and P. Rohatgi. "A map for wear mechanisms in aluminium alloys." *Journal of materials science* 26, no. 1 (1991): 99-102.
3. Zhang, J., and A. T. Alpas. "Transition between mild and severe wear in aluminium alloys." *Acta materialia* 45, no. 2 (1997): 513-528.
4. Das, Sarit K., Stephen U. Choi, Wenhua Yu, and T. Pradeep. *Nanofluids: science and technology*. John Wiley & Sons, 2007.
5. Bragg, W.H., 1928, An introduction to crystal analysis, G. Bell and sons, Limited, London.
6. Boehm, Hans-Peter, A. Clauss, G. O. Fischer, and U. Hofmann. "Das adsorptionsverhalten sehr dünner kohlenstoff-folien." *Zeitschrift für anorganische und allgemeine Chemie* 316, no. 3-4 (1962): 119-127.

7. Badia, F. A., and Rohatgi, P.K. "Gall Resistance of Cast Graphitic Aluminum Alloys," SAE Transactions **78**, no. 2 (1969): 1200–1207,
8. Erdemir, Ali, and Jean-Michel Martin, eds. *Superlubricity*. Elsevier, 2007.
9. Dienwiebel, Martin, Gertjan S. Verhoeven, Namboodiri Pradeep, Joost WM Frenken, Jennifer A. Heimberg, and Henny W. Zandbergen. "Superlubricity of graphite." *Physical review letters* 92, no. 12 (2004): 126101.
10. Akhlaghi, F., and A. Zare-Bidaki. "Influence of graphite content on the dry sliding and oil impregnated sliding wear behavior of Al 2024–graphite composites produced by in situ powder metallurgy method." *Wear* 266, no. 1-2 (2009): 37-45.
11. Baradeswaran, A., and A. Elaya Perumal. "Wear and mechanical characteristics of Al 7075/graphite composites." *Composites Part B: Engineering* 56 (2014): 472-476.
12. Moghadam, Afsaneh Dorri, Emad Omrani, Pradeep L. Menezes, and Pradeep K. Rohatgi. "Mechanical and tribological properties of self-lubricating metal matrix nanocomposites reinforced by carbon nanotubes (CNTs) and graphene—a review." *Composites Part B: Engineering* 77 (2015): 402-420.
13. Omrani, Emad, Afsaneh Dorri Moghadam, Pradeep L. Menezes, and Pradeep K. Rohatgi. "New emerging self-lubricating metal matrix composites for tribological applications." In *Ecotribology*, pp. 63-103. Springer, Cham, 2016.
14. Kordijazi, Amir, Hathibelagal M. Roshan, Arushi Dhingra, Marco Povolo, Pradeep K. Rohatgi, and Michael Nosonovsky. "Machine-learning methods to predict the wetting properties of iron-based composites." *Surface Innovations* 9, no. 2–3 (2020): 111-119.
15. Hasan, Md Syam, and Michael Nosonovsky. "Topological data analysis for friction modeling." *EPL (Europhysics Letters)* 135, no. 5 (2021): 56001.

16. Hasan, Md Syam, Amir Kordijazi, Pradeep K. Rohatgi, and Michael Nosonovsky. "Triboinformatics Approach for friction and wear prediction of al-graphite composites using machine learning methods." *Journal of Tribology* 144, no. 1 (2022).
17. Hasan, Md Syam, Amir Kordijazi, Pradeep K. Rohatgi, and Michael Nosonovsky. "Triboinformatic modeling of dry friction and wear of aluminum base alloys using machine learning algorithms." *Tribology International* 161 (2021): 107065.
18. Bowden, Frank Philip, Frank Philip Bowden, and David Tabor. *The friction and lubrication of solids*. Vol. 1. Oxford university press, 2001.
19. Lanka, Sridhar, Evgeniya Alexandrova, Marina Kozhukhova, Md Syam Hasan, Michael Nosonovsky, and Konstantin Sobolev. "Tribological and wetting properties of TiO₂ based hydrophobic coatings for ceramics." *Journal of Tribology* 141, no. 10 (2019).
20. Rohatgi, P. K., S. Ray, and Yun Liu. "Tribological properties of metal matrix-graphite particle composites." *International materials reviews* 37, no. 1 (1992): 129-152.
21. Hasan, Md Syam, and Michael Nosonovsky. "Lotus effect and friction: does nonsticky mean slippery?." *Biomimetics* 5, no. 2 (2020): 28.
22. Bhushan, Bharat. *Introduction to tribology*. John Wiley & Sons, 2013.
23. Lin, Jen Fin, Ying Chong Yung, and Chi Yuan Tsao. "Tribological performance of 6061 aluminum alloy/graphite materials under oil-lubricated and dry sliding conditions." *Tribology transactions* 41, no. 2 (1998): 251-261.
24. Omrani, Emad, Afsaneh Dorri Moghadam, Mahmoud Algazzar, Pradeep L. Menezes, and Pradeep K. Rohatgi. "Effect of graphite particles on improving tribological properties Al-16Si-5Ni-5Graphite self-lubricating composite under fully flooded and starved lubrication

- conditions for transportation applications." *The International Journal of Advanced Manufacturing Technology* 87, no. 1 (2016): 929-939.
25. Wilson, S., and A. T. Alpas. "Wear mechanism maps for metal matrix composites." *Wear* 212, no. 1 (1997): 41-49.
26. Basavarajappa, S., G. Chandramohan, K. Mukund, M. Ashwin, and M. Prabu. "Dry sliding wear behavior of Al 2219/SiCp-Gr hybrid metal matrix composites." *Journal of Materials Engineering and Performance* 15, no. 6 (2006): 668-674.
27. Suh, Nam P. "The delamination theory of wear." *Wear* 25, no. 1 (1973): 111-124.
28. Archard, John Frederick, and Wallace Hirst. "The wear of metals under unlubricated conditions." *Proceedings of the Royal Society of London. Series A. Mathematical and Physical Sciences* 236, no. 1206 (1956): 397-410.
29. Das, S., S. V. Prasad, and T. R. Ramachandran. "Microstructure and wear of cast (Al-Si alloy)-graphite composites." *Wear* 133, no. 1 (1989): 173-187.
30. Rohatgi, P. K., and B. C. Pai. "Seizure resistance of cast aluminium alloys containing dispersed graphite particles of various sizes." *Wear* 59, no. 2 (1980): 323-332.
31. Prasad, B. K. "Investigation into sliding wear performance of zinc-based alloy reinforced with SiC particles in dry and lubricated conditions." *Wear* 262, no. 3-4 (2007): 262-273.
32. Biswas, S., A. Shantharam, N. A. P. Rao, K. Narayana Swamy, P. K. Rohatgi, and S. K. Biswas. "Performance of graphic aluminium particulate composite materials." *TRIBOLOGY international* 13, no. 4 (1980): 171-176.
33. Biswas, S., and P. K. Rohatgi. "Tribological properties of cast graphitic-aluminium composites." *Tribology international* 16, no. 2 (1983): 89-102.

34. Chu, Hsiao Yeh, and Jen Fin Lin. "Experimental analysis of the tribological behavior of electroless nickel-coated graphite particles in aluminum matrix composites under reciprocating motion." *Wear* 239, no. 1 (2000): 126-142.
35. Lin, Jen Fin, Ming Guu Shih, and Yih Wei Chen. "The tribological performance of 6061 aluminum alloy/graphite composite materials in oil lubrications with EP additives." *Wear* 198, no. 1-2 (1996): 58-70.
36. Pai, B. C., P. K. Rohatgi, and S. Venkatesh. "Wear resistance of cast graphitic aluminium alloys." *Wear* 30, no. 1 (1974): 117-125.
37. Miloradović, Nenad, Rodoljub Vujanac, and Ana Pavlović. "Wear behaviour of ZA27/SiC/graphite composites under lubricated sliding conditions." *Materials* 13, no. 17 (2020): 3752.
38. Babić, M., B. Stojanović, S. Mitrović, I. Bobić, and N. Miloradović. "Wear properties of A356/10SiC/1Gr hybrid composites in lubricated sliding conditions." *Tribology in industry* 35, no. 2 (2013): 148.
39. Jolliffe, Ian T., and Jorge Cadima. "Principal component analysis: a review and recent developments." *Philosophical Transactions of the Royal Society A: Mathematical, Physical and Engineering Sciences* 374, no. 2065 (2016): 20150202.
40. Ardabili, Sina, Amir Mosavi, and Annamária R. Várkonyi-Kóczy. "Advances in machine learning modeling reviewing hybrid and ensemble methods." In *International Conference on Global Research and Ed.*
41. Hasan, Md Syam, Tien Wong, Pradeep K. Rohatgi, and Michael Nosonovsky. "Analysis of the friction and wear of graphene reinforced aluminum metal matrix composites using machine learning models." *Tribology International* 170, (2022): 107527.

CHAPTER 6: DATA TOPOLOGY APPROACHES FOR ROUGHNESS CHARACTERIZATION AND FRICTION MODELING

Rough surfaces possess complex topography, which cannot be characterized by a single parameter. Similarly, proper identification of relevant degrees of freedom is crucial for the development of adequate frictional models, such as the state-and-rate models. Topological data analysis (TDA) is a data-driven mathematical method that can generate novel insights in dimensionality reduction for datasets characterizing surface roughness, contact of rough surfaces, and frictional sliding. In this chapter, data topology approaches in roughness characterization and friction modeling will be discussed.

6.1. Introduction

Surface roughness affects various properties of materials including adhesion of solids and liquids to rough surfaces, wetting, friction, wear, as well as bio-adhesion and biocide properties of some surfaces. While it is common to evaluate surface roughness and characterize it quantitatively, there is no one single parameter, which could thoroughly describe the roughness [1-4]. Most nominally flat surfaces are not absolutely smooth because they have asperities. The height of asperities is usually measured above the center-line, which is defined for a 2D roughness profile $z(x)$ as the mean $m = \frac{1}{L} \int_0^L z dx$, where L is the length of the profile or the sampling interval for a particular measurement. Surface roughness is then defined by averaging the absolute value of the vertical deviation from the mean line

$$R_a = \frac{1}{L} \int_0^L |z - m| dx \quad (1)$$

While R_a provides a general insight on the height of the asperities, this parameter is insufficient for many purposes. This is because very different rough surfaces can have the same value of R_a . Moreover, it does not contain any information about horizontal size of typical asperities [5-7]. Note that the definition of asperity is tricky. This is because roughness is often multiscale, and there are smaller asperities imposed over larger ones, which makes it difficult to define which element of the rough profile constitutes the true asperity. One approach is that the concept of asperity is only relevant to the mechanical contact, so that “an asperity is what makes a contact” [8]. An alternative description of roughness is based on treating it as a random signal. Many rough surfaces possess the Gaussian or normal distribution of roughness height

$$p(z) = \frac{1}{\sqrt{2\pi}} e^{-\frac{(z-m)^2}{2\sigma^2}} \quad (2)$$

where $p(z)$ is the probability density function and $\sigma^2 = \frac{1}{L} \int_0^L (z - m)^2 dx$ is the squared standard deviation of profile height. The latter is related to the surface roughness as $\sigma = R_a \sqrt{\pi/2}$.

The autocorrelation function (ACF) is often used for characterizing the horizontal size of roughness details by averaging correlation between two profile points separated by the distance τ

$$C(\tau) = \lim_{L \rightarrow \infty} \frac{1}{L\sigma^2} \int_0^L (z(x) - m)(z(x + \tau) - m) dx \quad (3)$$

In the absence of statistical correlation, $C(\tau)$ approaches zero. Many real surfaces have an exponentially decaying ACF

$$C(\tau) = e^{-\frac{\tau}{\beta}} \quad (4)$$

where β is the correlation length [7]. An alternative value $\beta^* = 2.3\beta$ is often used to characterize the drop of the ACF by ten times from its original value. For the Gaussian roughness distribution and exponential ACF, σ and β^* characterize typical height and length of roughness.

More sophisticated parameters can be used to characterize surface roughness for different advanced purposes [1]. Modern Artificial Intelligence (AI) methods allow obtaining correlations in large databases built of tensors, a multidimensional generalization of the spreadsheet table. One method to obtain correlations in these large datasets is the topological data analysis (TDA). The TDA reduces the dimension of datasets in order to find low-dimensional structures with reproducible topology. Such structures may be low-dimensional surfaces in spaces of higher dimension. The topological data analysis includes such concepts as the persistent homology, barcodes and topological invariants [10-12]. While topological methods are used in surface science to characterize the complexity of 2D patterns with the Voronoi entropy [9] and with the continuous measures of symmetry [13], and to study of faceted liquid droplets [14-15], topological data analysis is still rarely used in surface science and tribology. The new area of *triboinformatics* has been proposed to include AI methods of study of surface effects [10, 16-18].

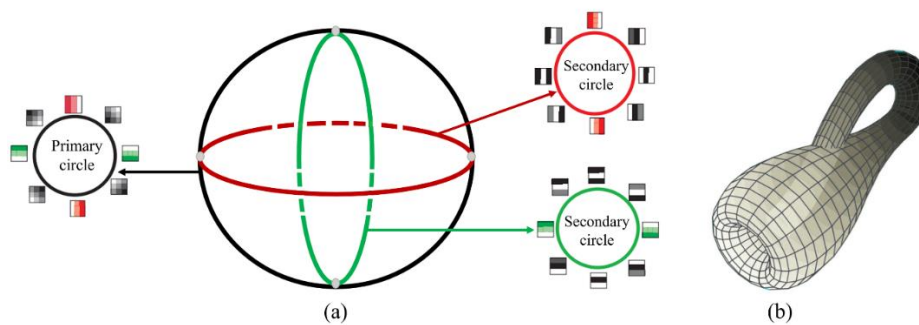


Figure 6.1 (a) Statistics of 3×3 pixel patches from natural images involves the primary circle (due to isotropic brightness gradients) and two secondary circles due to the prevalence of vertical and

horizontal over inclined features in the images. Each secondary circle intersects twice with the primary circle. **(b)** Such configuration topologically fits the Klein bottle surface [19-20].

A well-known TDA result in the image processing is related to 3×3 black-and-white pixel patches of regular black-and-white photo images [19-20]. Each pixel is characterized by one value of brightness, and thus any 3×3 patch can be viewed as a point A_{ij} ($i, j = 1, 2, 3$) in a 9D dataspace. The data is normalized so that in any patch the brightest pixel has value “1” and the darkest has value “-1”. Many patches represent gradual changes of brightness with isotropic probability distribution of the direction of the gradient, θ . In the 9D dataspace this corresponds to a parametrically specified circle referred to as the “primary circle”:

$$A_{i,j} = \frac{1}{|\cos \theta| + |\sin \theta|} \begin{pmatrix} -\cos \theta + \sin \theta & \sin \theta & \cos \theta + \sin \theta \\ -\cos \theta & 0 & \cos \theta \\ -\cos \theta - \sin \theta & -\sin \theta & \cos \theta - \sin \theta \end{pmatrix} \quad (5)$$

In addition, there are patches corresponding to the vertical and horizontal features forming a secondary circle in the parametric form

$$A_{i,j} = \begin{pmatrix} -1 & \sin \alpha & 1 \\ -1 & \sin \alpha & 1 \\ -1 & \sin \alpha & 1 \end{pmatrix}, A_{i,j} = \begin{pmatrix} 1 & \sin \alpha & -1 \\ 1 & \sin \alpha & -1 \\ 1 & \sin \alpha & -1 \end{pmatrix} \quad (6)$$

$$A_{i,j} = \begin{pmatrix} 1 & 1 & 1 \\ \cos \alpha & \cos \alpha & \cos \alpha \\ -1 & -1 & -1 \end{pmatrix}, A_{i,j} = \begin{pmatrix} -1 & -1 & -1 \\ \cos \alpha & \cos \alpha & \cos \alpha \\ 1 & 1 & 1 \end{pmatrix} \quad (7)$$

Eq. 5 describes the primary circles, while Eqs 6-7 describe two secondary circles. The primary and secondary circles intersect at $\alpha = \theta = 0$ and at $\alpha = \theta = \pi$ (Eq. 6) and at $\alpha = \theta = \pm\pi/2$ (Eq. 6). The secondary circles do not intersect with each other. Since isotropic gradients, vertical, and horizontal features are common in images, data points tend to attain these three circles (one primary and two secondary circles) in the 9D dataspace. It has been shown by Carlsson and

co-workers [19-20] that such a construction with three circles involves one primary circle and two non-intersecting secondary circles (**Figure 6.1a**) is topologically equivalent to the Klein bottle (**Figure 6.1b**).

The persistence barcode diagrams study of datasets such as $A_{i,j}$, implies that a sphere of a certain proximity radius r is formed around any data point (**Figure 6.2**). When spheres connect, they form an n -dimensional void, and the number of voids constitute the feature H_n , which is present within a certain range of values of the proximity radius r . The TDA methods have been applied successfully in materials science for various purposes including the analysis of soft materials. However, their application in surface science and tribology has not been wide so far. Since visual black-and-white images have a structure very similar to the surface roughness topography map $z(x,y)$, it is anticipated that the TDA methods would be beneficial for surface roughness characterization. Roughness parameters tend out to be scale-dependent, with nanoscale roughness values being different from that measured at the micro- and macroscale. It is therefore important to understand how roughness parameters behave at the nanoscale. It is believed that the reduction of the number of degrees of freedom from the nanoscale to the macroscale is the central inherent characteristic of friction [1, 21-23].

Novel metallic materials including alloys and composites are particularly challenging due to the difficulty of predicting their tribological properties [24]. We study brass surfaces in particular due to their relevance to bactericide and anti-viral action [25-27]. While it is believed that Cu^+ and Zn^+ ions are responsible for the bactericide action, there are indication that surface roughness may be involved as well [28-29]. The objective of the present paper is to seek similar persistent data structures in roughness data obtained with Atomic Force Microscopy (AFM) and to compare them with relevant more traditional microscale and nanoscale roughness parameters.

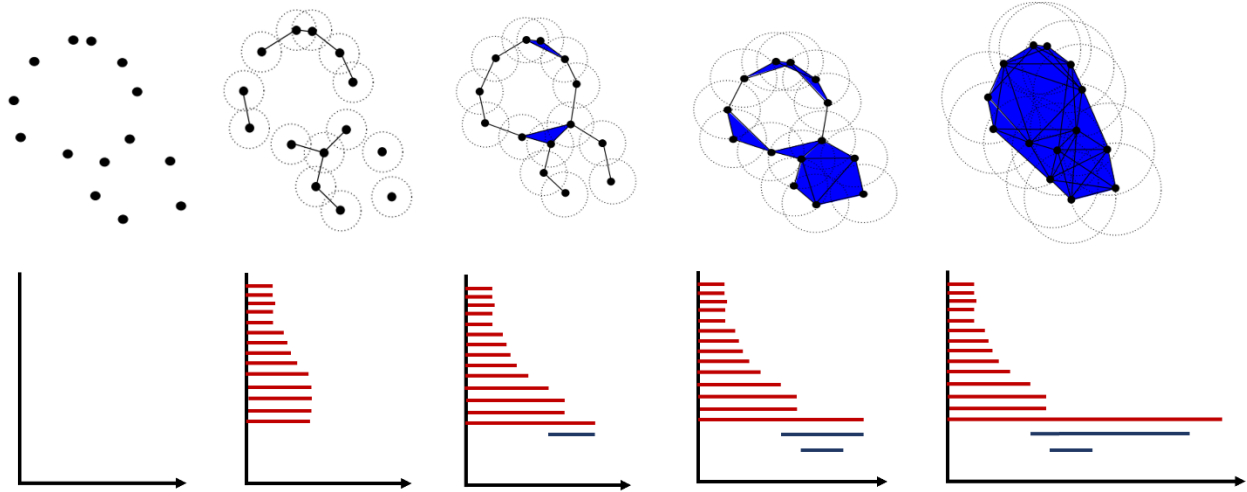


Figure 6.2. Schematics of the persistence barcodes concept. With increasing the proximity radius (horizontal axis), connected structures (red bars) are formed and disappear, as well as 1D voids (holes, blue).

Dry sliding friction is a complex phenomenon, which involves several mechanisms acting simultaneously, such as adhesion (including covalent, electrostatic, van der Waals, and capillary forces) and surface roughness-dominated effects (including elastic and plastic deformation of asperities, and their fracture). Due to this complexity of friction, it is extremely difficult to predict frictional properties from the first principles of molecular or microscopic interactions [30,31].

At the molecular scale, intermolecular and interatomic bonds are dominant leading to atomic and molecular motion. The effects of molecular motion are usually observed in the form of temperature and other averaged thermodynamic parameters. At the mesoscale, material non-idealities and defects, as well as roughness asperities, are dominant. Their motion contributes to the macroscale dissipation of energy. A typical mesoscale description would model every asperity contact as an elastic deformable spring so that the number of degrees of freedom is related to the number of asperity contacts. Macroscale parameters can be viewed as a result of neglecting many

unessential degrees of freedom in the frictional system. Computationally, different methods of modeling frictional processes are used at different scale lengths, from the Molecular Dynamics (MD) simulation at the atomic scale to Monte Carlo, Cellular Automata, and other similar methods at the mesoscale, whereas standard macroscale methods involve Finite Element Analysis (FEA) and computational fluid dynamics.

Conventional methods of statistical and thermodynamic analysis and averaging do not always capture the complex frictional interactions, because thermodynamically friction is a non-equilibrium process, while at the same time it is a multi-scale phenomenon [7, 31-32]. Besides being a non-equilibrium and multi-scale phenomenon, friction is a non-linear phenomenon. According to the Coulomb-Amontons law, the frictional force is always collinear with the sliding velocity [30]

$$\vec{F} = \mu W \frac{\vec{v}}{|\vec{v}|} \quad (8)$$

where W is the normal load and μ is the coefficient of friction (COF). The discontinuity of the function $\text{sign}(V) = \frac{v}{|v|}$ (or $\frac{\vec{v}}{|\vec{v}|}$) at $V=0$ makes the Coulomb-Amontons law non-linear. Friction leads to a number of non-linear and hysteretic effects, such as the memory of the past states of the system in the static “stick” states. The sliding velocity is zero in these states; however, the friction force can have any value in the range $F < \mu|W|$ depending on the past history of the system. Transitions between the stick and slip states are associated with dynamic sliding instabilities, and stick-slip is a common frictional phenomenon.

While friction is often viewed as a non-linear phenomenon related to the reduction of the degrees of freedom, there is no simple way of reducing a molecular-scale model with many degrees of freedom to the minimalistic models involving internal state variables with only a small number

of most relevant degrees of freedom characterizing motion [31]. Since traditional statistical mechanics and thermodynamics methods do not always work well for this task (thus, there are difficulties in deriving the dry friction laws from the Second Law of thermodynamics, [33]), more advanced computational methods, such as the topological data analysis, Machine Learning (ML) and Artificial Neural Networks (ANN) could provide new insights on establishing correlations leading to the reduction of degrees of freedom [34].

Multidimensional data analysis methods represent data as cubes or “tensors,” a multidimensional generalization of the spreadsheet table. To obtain correlations in these large datasets, the topological data analysis is often employed to reduce the dimension of datasets by using the so-called persistent homology in order to find low-dimensional structures with reproducible topology. Such structures may be low-dimensional surfaces in spaces of higher dimensions. The topological data analysis includes such concepts as the persistent homology, barcodes, and Betti numbers, which will be discussed later. While topological methods are used in surface science to characterize the complexity of 2D patterns with the Voronoi entropy [9] and with the continuous measures of symmetry [13], for clustering analysis [35] and to study of faceted liquid droplets [14-15], topological data analysis is still rarely used in surface science and tribology.

In this study, nanoscale surface roughness of brass (Cu Zn alloy) samples roughened by a sonochemical treatment will be analyzed using 3×3 , 4×4 , and 5×5 -pixel patches obtained from AFM images. Roughness parameters, correlation length will be calculated, and extremum point distribution, persistence diagrams, and barcodes will be discussed and compared. Additionally, TDA and data-driven approaches will be applied to seek patterns and persistence in friction-related datasets.

6.2. Persistence analysis of data topology

Data points in the data space often tend to attain certain surfaces. These surfaces may form topological features such as holes and voids. Persistence analysis shows how these topological features depend on the spatial resolution.

For the analysis of surface roughness data, persistence diagrams and barcodes can be used. Both represent the same data: how topological invariants depend on the resolution over varying length scales. Topological invariants are connected components (H_0), 1D holes (H_1), and higher dimensional voids (H_2 , H_3 , etc). The intervals of the feature appearance and disappearance are plotted as bars in the barcode diagram or as a point characterizing their appearance and disappearance in the persistence diagram. The longer bars present more persistent invariants relative to noise (**Figure 6.2**).

In order to analyze the proximity of data point to each other, a certain proximity radius can be chosen, and connection of circles (or spheres) with the center at the data points is observed. The proximity radius is gradually increased from zero. This causes the appearance and disappearance of the topological invariants which is shown at the barcode diagram as a function of the proximity radius. At the persistence diagram each barcode line is presented as a function of the point of its appearance and disappearance. Different colors at the diagram usually represent different features or invariants. Thus, the topological invariant H_0 represents the entire structure without holes. The topological invariant H_1 represents a 1D hole (i.e., a cylindrical type of structure). The topological invariant H_2 represents a 2D empty void (enclosed by a surface) and higher order topological invariants, H_n , represent n -dimensional voids. Long lines at barcode diagrams or points away from the diagonal at persistence diagrams represent stable features with exists at a significant range of the proximity radii, so that presumable they more objectively characterize the data set. As opposed

to that, short barcode lines or points close to the diagonal at the persistence diagram represent features with only exist for a short range of the proximity radii and they are likely caused by noise.

Barcodes and persistence diagrams for roughness data are generated using the Python interface with the required TDA and other standard libraries. Surface profile data as a square matrix (256×256) is used as the input for generating the barcodes. The original matrix is divided into 3×3 patches which were used to generate the filtered simplicial complex. We used the Vietoris-Rips filtration to generate the simplicial complex. In Rips complex, the filtration value is the proximity parameter (radius) that we varied over the sampling length for different samples. In a simplicial complex, a topological space is formed with the data points. The topological space can be characterized by the topological invariants. The optimization of the Euclidian distance matrix was performed with a maximum dimension of 3 in calculation of the persistent homology of the simplicial complex. So, our developed persistence diagram and barcodes can present up to three distinct topological invariants that we can compare for different surface profile data. The barcodes diagram presents the topological invariants in a single homology dimension. The horizontal axis presents the homology dimension in terms of the proximity radius which is the main output from a barcode diagram and the vertical axis just presents an arbitrary ordering of topological invariants. It is expected that anisotropic surfaces would form secondary circles in the data space.

6.3. Experimental Procedure

Surface roughness profiles of brass (Cu-Zn alloy) surfaces obtained by atomic force microscopy (AFM) were used in this study (**Figure 6.3**). Two untreated samples were used with different scanning sizes of $5 \times 5 \mu\text{m}$ and $10 \times 10 \mu\text{m}$ in order to isolate the effect of scan size on the roughness parameters.

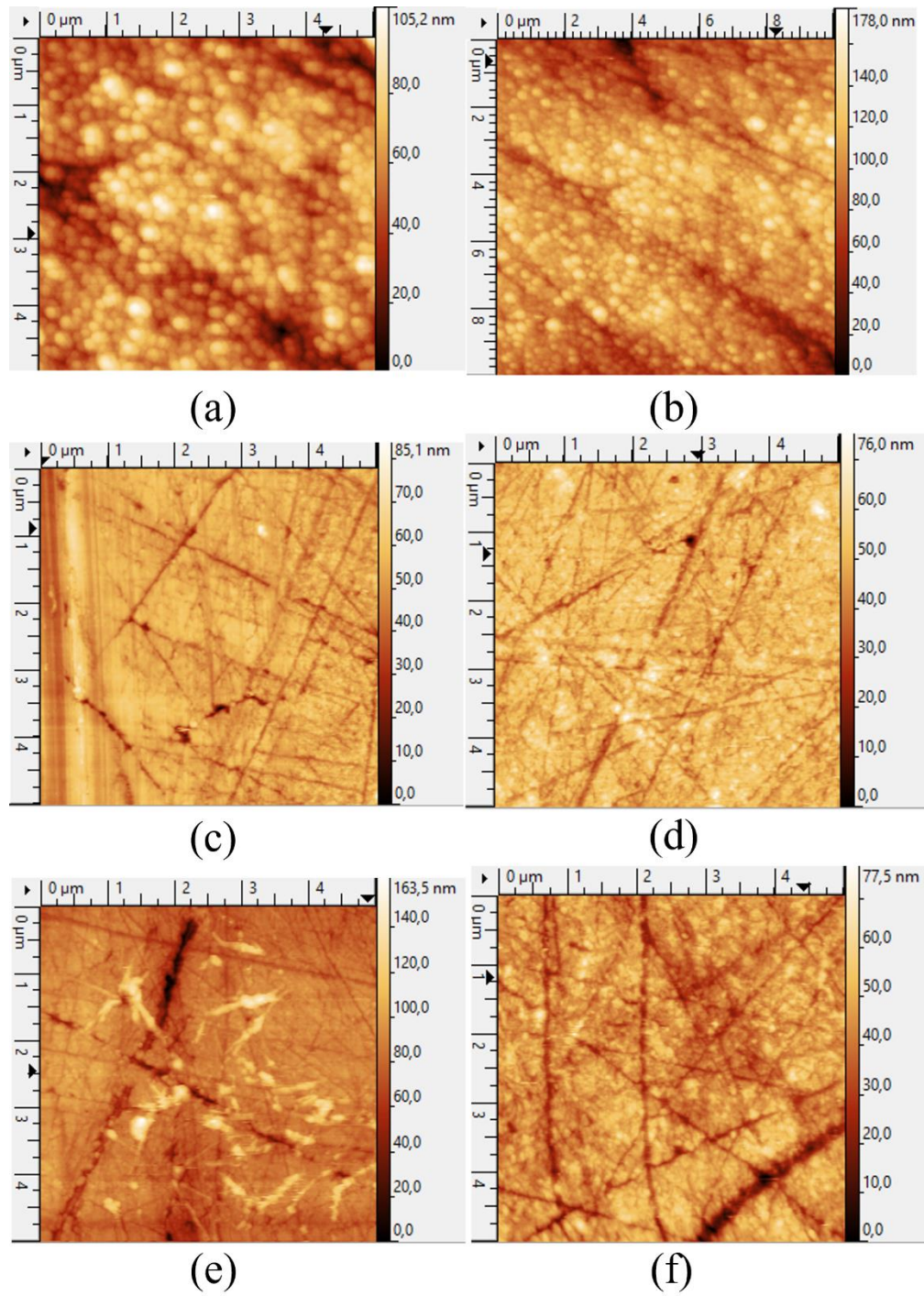


Figure. 6.3. AFM surface roughness profiles of the (a) 5×5 μm and (b) 10×10 μm untreated brass samples and roughened samples sonicated at amplitudes of (c) 30%, (d) 50%, (e) 70%, and (f) 90% of the maximum power.

Following that, four $5 \times 5 \mu\text{m}$ surfaces treated sonochemically in 100 mL 5M NaOH solution and sonicated at various amplitudes (30%, 50%, 70%, and 90% of the maximum power) of the acoustic ultrasound source were studied. Note that the treated surfaces were also ground manually by sandpaper and polished, which led to some oriented roughness features (scratches) at the surface making them anisotropic. Moreover, the sample treated at 70% showed some features (white spots in **Figure 6.3e**) possibly caused by oxidation, oxidation and fraction separation is not uncommon effect of the sonochemical treatment of brass [29].

Advances in sonochemical treatment of the surface allow for “surface” capsules [36] which are interesting for biomedical applications, membrane materials, lab-on-chip, organ-on-chip, and for template synthesis. Moreover, the treatment provide attractive self-healing anticorrosion [37] and antifouling prospects [38,39]. Previously, analysis of atomic force microscopy (AFM) allow to find the effect of oscillation of crystal size vs. time of treatment for medical implant materials. Here, we aim for the analysis of biocide brass [29].

A scanning probe microscope Ntagra Aura (NT-MDT, Russia) and HA_NC series cantilever probes (NT-MDT, Russia) with the tip diameter of 20 nm were used to study the surface of the samples. The topography of the sample surface was studied using the semi-contact and contact scanning modes by means of AFM. The semi-contact mode was chosen as the primary mode to reduce the invasive impact of the probe on the structures. The frequency was at about 140 kHz and the average probe spring force constant was about 3.5 N/m. The resolution of the images was 256×256 points, which corresponded to a step between the points of about 19.5 nm for a scanning area of $5 \times 5 \mu\text{m}^2$ and about 39.1 nm for a scanning area of $10 \times 10 \mu\text{m}^2$. The scanning speed was about 8 $\mu\text{m/s}$ for the scanning area of $5 \times 5 \mu\text{m}^2$ and about 16 $\mu\text{m/s}$ for the scanning area of $10 \times 10 \mu\text{m}^2$. The samples were studied in the air at an average temperature of 21-23°C and

relative humidity within 30-40%. Both passive and active vibration isolation methods were used for the measurements to reduce the vibrational noise. The Optem optical registration system with a camera and zoom was used for aligning the probe and select the area for AFM measurements.

For untreated samples, the following values of surface roughness were obtained by the AFM software (Gwyddion): $R_a=10.30$ nm (5×5 μm sample) and $R_a=12.05$ nm (10×10 μm sample), average height above the reference plane $m=56.4$ nm (5×5 μm sample) and $m=73.2$ nm (10×10 μm sample), $\sigma=13.31$ nm (5×5 μm sample) and $\sigma=15.77$ nm (10×10 μm sample). To modify surface roughness, a plate of Cu-Zn alloy was mixed with 100 mL of (0.5, 0.1, 5, M) NaOH. The 5M NaOH concentration was selected for consequent measurements. The solution was sonicated by the ultrasonic processor UIP1000hd (Hielscher Ultrasonics, Germany) for 30 min at different amplitudes (30%, 50%, 70%, 80%, 90% of the maximum power). The apparatus was equipped with the sonotrode BS2d18 with a head area of 2.5 cm^2 . After the treatment, the Cu-Zn alloy was washed up with distilled water and dried at $120\text{ }^\circ\text{C}$ for 24 h. Plates were cut from a single sheet, ground by sandpaper, and polished by progressively smaller diamond powders with the ending step of $0.5\text{ }\mu\text{m}$.

6.4. Data analysis for roughness characterization

The focus of the present study is data topology parameters (persistence barcodes. However, for comparison purposes, several surface roughness-related parameters were calculated using the AFM roughness profile data. First, the ACF was obtained and the value of the correlation length β^* was calculated. These values represent the surface roughness at the *microscale* with the characteristic length of roughness features of several microns. The ACF was calculated separately in the x - and the y -direction. For that end, a square submatrix of 256×256 dimension from the

AFM dataset was obtained. Using Python programming language and its standard statistical libraries, we plotted the values of the ACF vs. the sampling length along the x - and the y -direction (**Figure 6.4**) for the $5 \times 5 \mu\text{m}$ and $10 \times 10 \mu\text{m}$ samples. In the AFC plots, we observe both positive and negative correlations before the ACF eventually decays to zero.

The following values of the correlation length were found for Dataset 1, the value of $\beta^* = 0.31 \mu\text{m}$ and $\beta^* = 0.55 \mu\text{m}$ in the x - and y -directions (untreated $5 \times 5 \mu\text{m}$ sample) and $\beta^* = 0.96 \mu\text{m}$ and $\beta^* = 1.25 \mu\text{m}$ in the x - and y -directions (untreated $10 \times 10 \mu\text{m}$ sample). For all samples, the values of β^* , which is a horizontal roughness parameter, exceed the values of σ , which is a vertical roughness parameter, by almost two orders of magnitude. As expected, for the sample with larger scan region, the values of the correlation length are larger. One can estimate the slope of the profile as σ/β^* in the range between $13.3/310=0.043$ and $13.3/550=0.024$ ($5 \times 5 \mu\text{m}$ sample) and $15.77/960=0.016$ and $15.77/1250=0.013$ ($10 \times 10 \mu\text{m}$ sample).

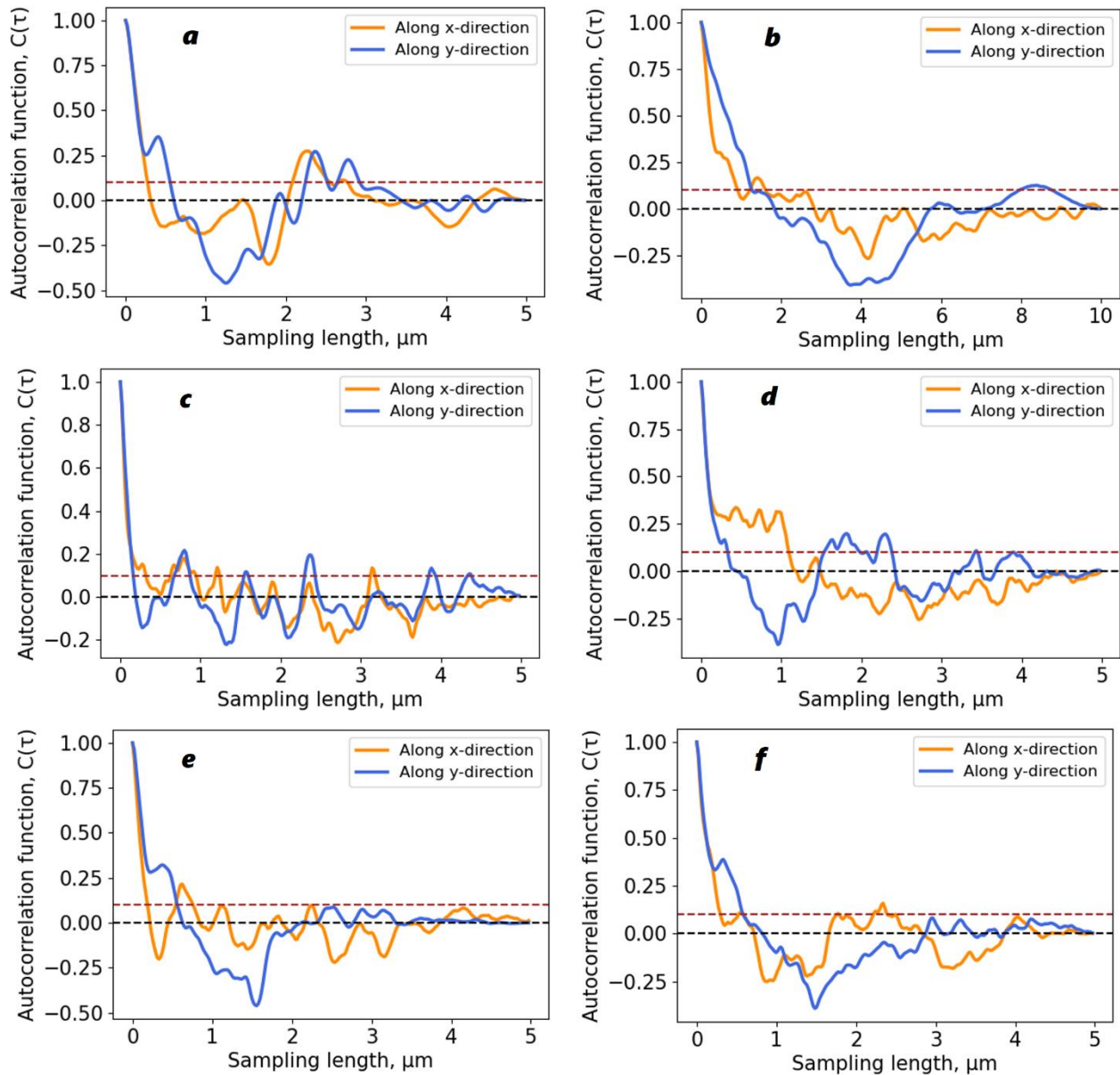


Figure 6.4. ACFs for the roughness profile extracted from the AFM images (a) untreated 5×5 μm surface, (b) untreated 10×10 μm surface, and treated surfaces sonicated at amplitudes (c) 30%, (d) 50%, (e) 70% and (f) 90% of the maximum power.

The surface roughness properties of all samples are presented in **Table 6.1**. For untreated samples, the surface roughness is larger for the larger sample due to increased scan size. The roughness parameters of treated samples were smaller than for untreated ones likely due to

polishing. Higher power of the sonochemical treatment resulted in higher roughness. The difference of values on the *x*- and *y*-directions as well as different ACF, suggest that the samples were anisotropic, and the anisotropy was much more pronounced for the treated samples with scratches.

Table 6.1. Surface roughness properties of the samples

Sample	Average roughness, R_a (nm)	Vertical roughness parameter, σ (nm)	Correlation length, β^*		Slope of the profile, σ/β^*	
			Along <i>x</i> -direction, nm	Along <i>y</i> -direction, nm	Along <i>x</i> -direction	Along <i>y</i> -direction
Cu-Zn (5×5 μm)	10.03	13.31	310.00	550.00	0.043	0.024
Cu-Zn (10×10 μm)	12.05	15.77	960.00	1250.00	0.016	0.013
Cu-Zn-5M NaOH-30%	4.44±0.86	5.97±1.22	290±80	160±20	0.021±0.010	0.037±0.012
Cu-Zn-5M NaOH-50%	4.02±0.26	5.03±0.36	1007±150	320±40	0.005±0.001	0.016±0.003
Cu-Zn-5M NaOH-70%	5.15±0.17	6.7±0.47	230±105	580±165	0.029±0.015	0.012±0.004
Cu-Zn-5M NaOH-90%	5.82±0.21	7.63±1.64	265±55	570±90	0.029±0.011	0.013±0.005

For the study of the anisotropy, 3×3, 4×4, and 5×5 sub-matrices or patches of the roughness profiles for untreated Cu-Zn samples were obtained, and statistics of the location of the minimum and maximum values were studied (**Figure 6.5**). The larger patches (4×4 and 5×5) were studied in order to validate the results obtained from the 3×3 patches. The size of the patches was between 58 nm× 58 nm for the 3×3 submatrices of small (5×5 μm) samples to (432 nm× 432 nm) for the 5×5 submatrices of small (10×10 μm) samples. Therefore, this data provides information about the surface roughness at the *nanoscale*; however, its resolution scale is in dozens of nanometers by the order of magnitude.

In general, when the resolution is smaller than a typical roughness detail, it is expected that the extreme (maximum and minimum) values of profile height are located at the border layer of the pixels rather than at the central pixels, with most extreme values at the corners. The statistical data shows that indeed, only a small number of extreme values were located at the inside pixels, ranging from 3%-5% for the 3×3 patches to 9%-18% for the 5×5 patches. The majority of extreme values are indeed located at the corners, ranging from 63%-67% for the 3×3 patches to 33%-43% for the 5×5 patches. However, some extreme values are located at the border layers but not at the corners, indicating anisotropic behavior in the *x*- and *y*-direction. Thus, for the 3×3 patches 16%-18% for the *x*-direction vs. 12%-15% for the *y*-direction, for the 4×4 patches 23% for the *x*-direction vs. 16%-21% for the *y*-direction, and for the 5×5 patches 24%-26% for the *x*-direction vs. 19%-24% for the *y*-direction.

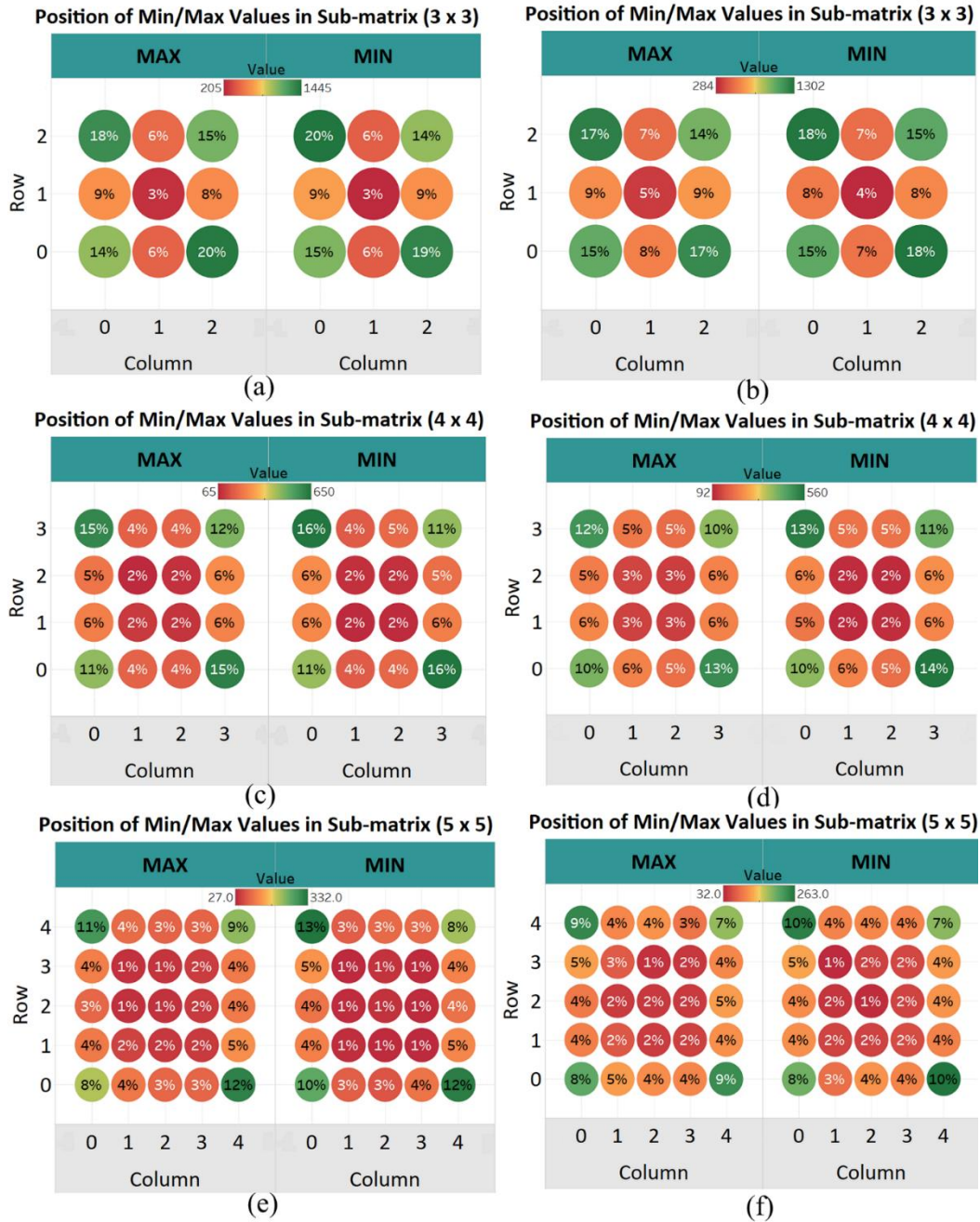


Figure 6.5. Position of the min and max values for 3x3, 4x4, and 5x5 pixel sub-matrices for (a, c, e) Dataset 1 (5x5 μm), (b, d, f) Dataset 2 (10x10 μm)

Similar patterns were observed for NaOH and ultrasound-treated Cu-Zn alloy surfaces sonicated at amplitudes corresponding to 30%, 50%, 70% and 90% of the maximum power for 3x3 submatrices (**Figure 6.6**).



Figure 6.6. Position of the min and max values in 3x3 pixel sub matrices subject to NaOH sonicated at amplitudes (a) 30%, (b) 50%, (c) 70% and (d) 90% of the maximum power

Persistence analysis of data topology has been conducted as well. The original 256x256 matrices were divided into 3x3 submatrices or patches (58 nm x 58 nm and 116 nm x 116 nm) and persistence diagrams and barcodes were generated (**Figure 6.7**). Barcodes with varying proximity radius are presented in **Figure 6.7(a)** and **Figure 6.7(c)**, respectively. For both datasets, the first topological invariant, H_0 is persistent over the entire proximity radius range indicating to the connected component.

The second topological invariant, H_1 , corresponds to 2D holes in data and in can be interpreted as corresponding to the primary circle parametrically given in a generic form by Eq. 5. This invariant is significant at the resolution length corresponding to the size scale of the profile approximately in the range of 5 nm – 15 nm.

The third topological invariant, H_2 , corresponds to 3D voids in the datasets and can be interpreted as the trace of the anisotropy of the profile. Its typical size is above 10 nm. This is consistent with the data from **Figure 6.5**, which showed anisotropy at the scale of dozens of nanometers.

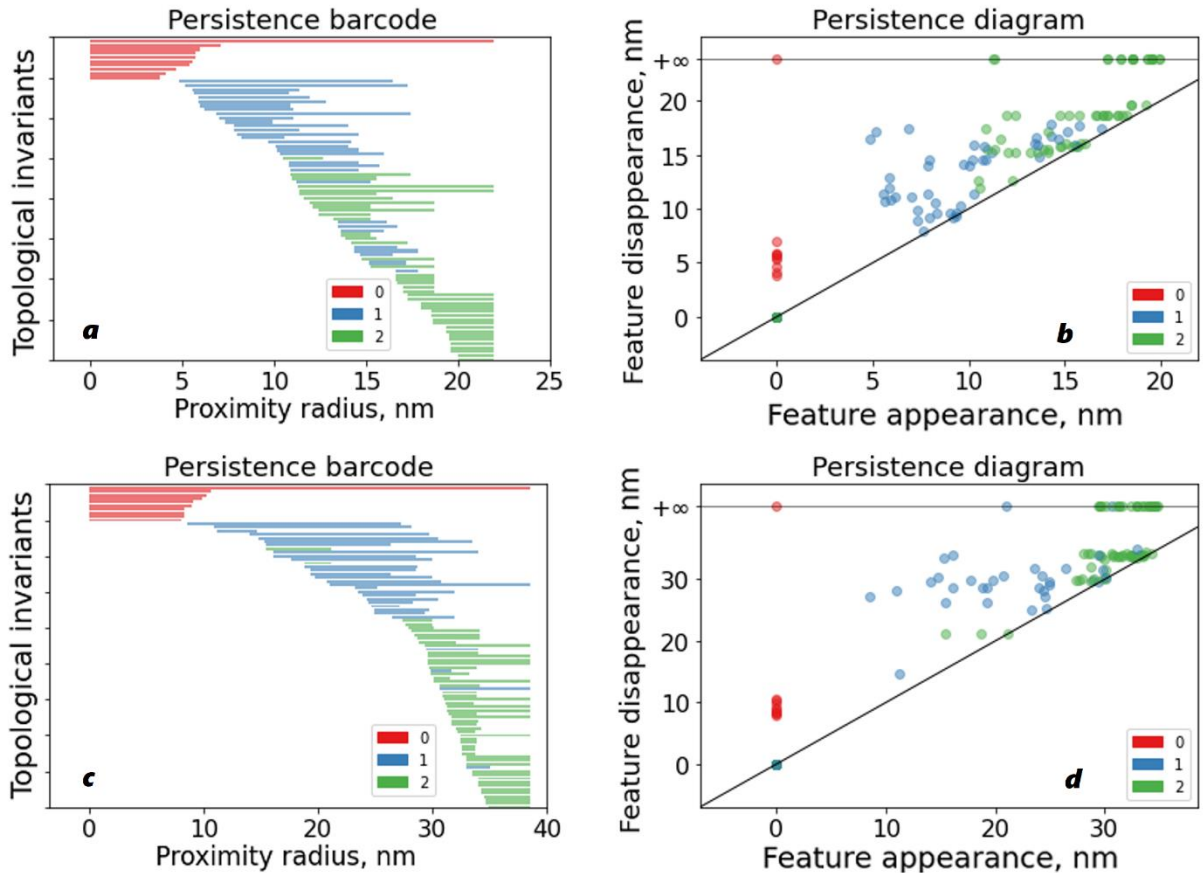


Figure 6.7. Persistence diagram and barcodes showing topological invariants for untreated sample (a-b) 5×5 μm surface, (c-d) 10×10 μm surface.

Barcodes with the varying proximity radius for 3×3 patches (58 nm× 58 nm) of Cu-Zn alloys mixed with 100 mL 5M NaOH sonicated at different amplitudes are presented in **Figure 6.8**. The persistence presence of the first, second and third topological invariants suggest anisotropic nature of the surface profile at the nanoscale, which is consistent with the results in **Figure 6.6** and **Table 6.1**. Note that the 70%-amplitude treated sample (**Figure 6.8c**) has more pronounced H_I roughness features. This is likely due to the inhomogeneous spots observed in **Figure 6.3(e)**. This feature characterizing this sample is not captured by other roughness measures.

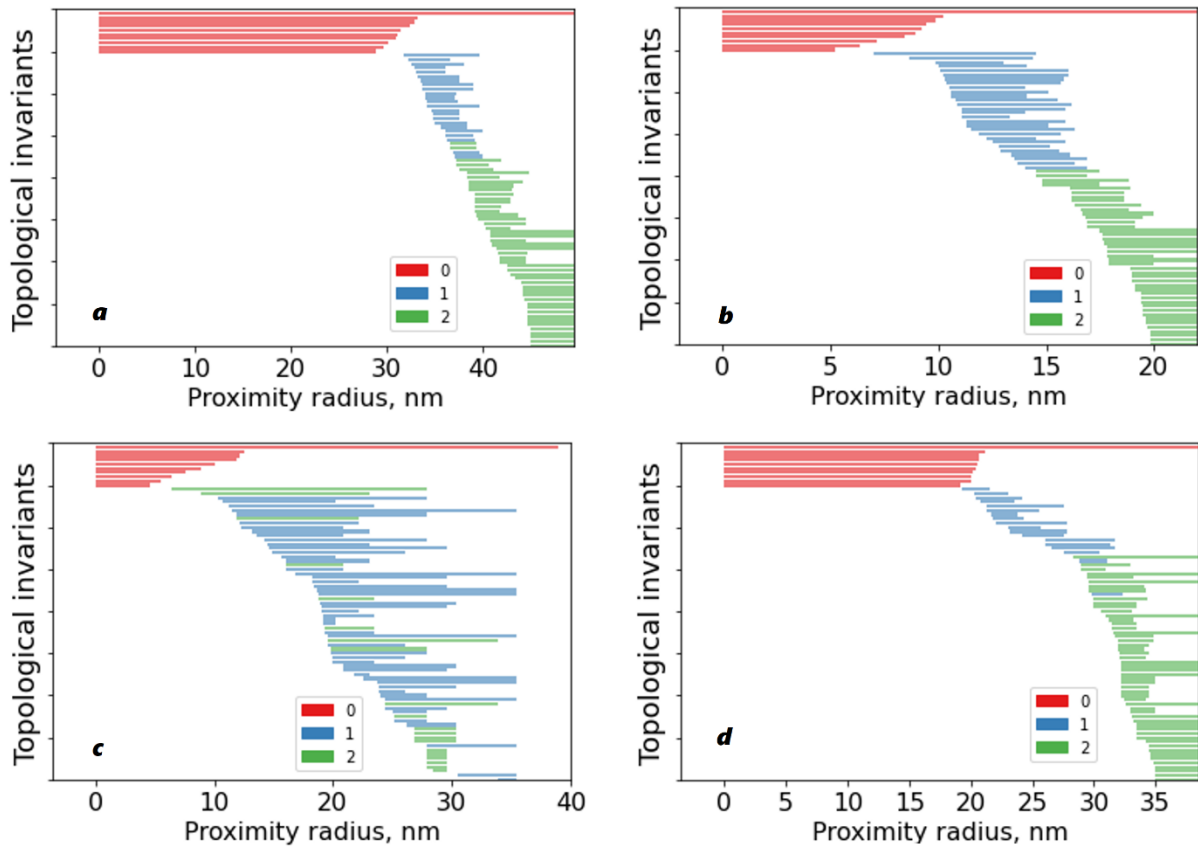


Figure 6.8. Persistence barcodes showing topological invariants for 3×3 patches subject to NaOH solution sonicated at amplitudes corresponding to (a) 30%, (b) 50%, (c) 70% and (d) 90% of the maximum power

6.5. Contact parameters for friction

Both statistical and fractal models of rough surfaces, for elastic and plastic contacts, result in an almost linear dependency of the friction force upon the normal load. The classical model of Bowden and Tabor [30] suggested that the friction force F is directly proportional to the real area of contact A_r and adhesive shear strength at the interface τ_f

$$F = \tau_f A_r \quad (9)$$

Statistical models of rough surfaces contact show that for small and moderate loads, A_r is almost directly proportional to the applied normal load W . This applies to both elastic and plastic surfaces and it explains the empirically observed linear proportionality of F and W (i. e., the Coulomb-Amontons law) with the assumption of constant τ_f being a material constant for a given combination of two materials in contact.

For elastic contact, in most cases, only the highest asperities participate in the contact yielding a linear dependency of the real area of contact on the normal load

$$A_r \propto \frac{W\beta^*}{\sigma E} \quad (10)$$

where W is the normal load force and E is the composite elastic modulus. For plastic contacts, the contact area is related to the normal load through the material hardness.

The kinetic friction may involve more complex dependencies of the real area of contact on the normal load. Tolstoi was the first who paid attention to the importance of the normal degree of freedom (the vertical coordinate) during dry sliding [40]. The separation distance between the sliding bodies decreases with decreasing velocity. More time for the asperity contact means more time for asperities to deform, so the separation distance decreases. This results in an increase of

the real area of contact and of the friction force (**Figure 6.9(a)-(c)**). Recent models emphasize the importance of the coupling of the normal and tangential motion during friction [41-42]. Dynamic models based on such physical effects as time-dependent creep-like relaxation and viscosity predict that increasing velocity would typically result in a decrease of friction.

While the linear Coulomb-Amontons law is widely applied, there are numerous problems with characterizing a bi-material interface with only one parameter, such as the COF. Experiments demonstrate that for the same combination of materials, the COF may vary significantly [43]. Moreover, for dynamic friction, the COF is also not constant as a function of time. To overcome these difficulties, phenomenological rate-and-state models of friction introduce internal degrees of freedom to model the dependency of friction on the age of contact [44,45]. The coefficient of friction be a sum of a reference value μ_0 and the terms dependent on the sliding velocity V (the “rate” parameter) and on an internal “state” parameter θ with the dimension of time (thus often interpreted as an averaged age of contact)

$$\mu(V, \theta) = \mu_0 + a \ln\left(\frac{V}{V_0}\right) + b \ln\left(\frac{\theta V_0}{D_c}\right) \quad (11)$$

$$\frac{d\theta}{dt} = 1 - \frac{\theta V}{D_c} \quad (12)$$

where a and b are non-dimensional constants, V_0 is a reference velocity and D_c is a constant with the dimension of length. Note that the second term is often omitted (by setting $a=0$) to avoid infinities in the static limit of $V \rightarrow 0$.

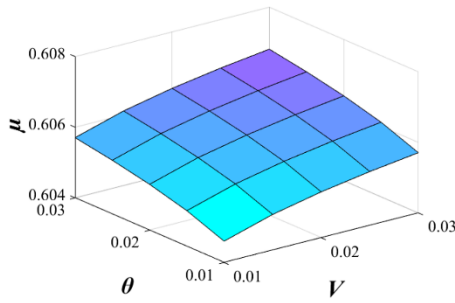
Following a change in the sliding velocity, friction decreases, due to creep relaxation, to a velocity-dependent steady-state value

$$\mu(V) = \mu_0 + (a - b) \ln \frac{V}{V_0} \quad (13)$$

For constant sliding velocity, θ is inverse proportional to the sliding velocity yielding the dependency of the real area of contact on the sliding velocity

$$A_r = A_{r0} \left(1 - C \ln \frac{V}{V_0}\right) \quad (14)$$

where C and V_0 are parameters of the model (**Figure 6.9(a-c)**).



$$\mu(\theta, V) = \mu_0 + a \ln\left(\frac{V}{V_0}\right) + b \ln\left(\frac{V_0 \theta}{D_c}\right)$$

$$\frac{d\theta}{dt} = 1 - \frac{V\theta}{D_c} \quad (\text{Dieterich, aging law})$$

μ_0 = Reference base friction
 θ = State parameter
 D_c = Critical slip distance
 V_0 = Reference velocity
 a, b = Constants

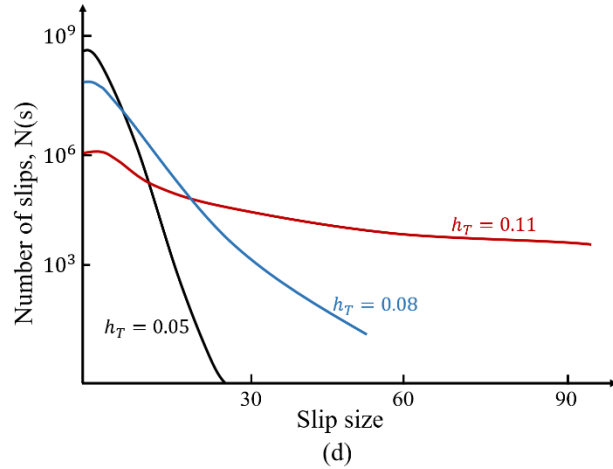
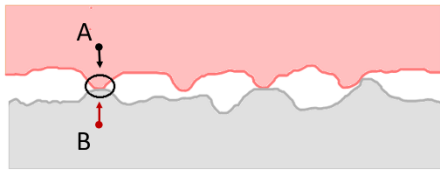
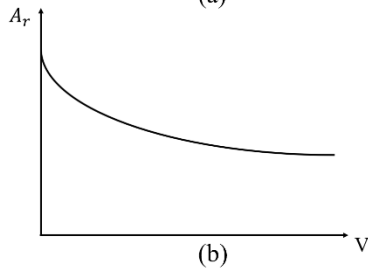


Figure 6.9. (a) 3D plot for state-and-rate model, (b) the dependency of the real area of contact with sliding velocity, (c) the increase of the real area of contact with the age of contact, (d) the plots of the number of slips vs. slip size for different threshold heights, h_T

While rate-and-state models of dynamic friction are common in geophysics, similar models gained popularity in the areas of control engineering and robotics [46-47]. Note that the models with internal variables are pure phenomenological since their parameters are not deduced from

atomic-scale models or from the contact of individual asperities. In the next section, the data topology approaches which may be used to reduce the number of degrees of freedom in the models will be discussed.

6.6. Contact of rough surfaces

6.6.1. Static contact

The contact between two rough surfaces may be characterized in a similar manner. A Boolean variable is introduced with the value $b(x, y) = 0$ when there is no contact between the two surfaces at the point (x, y) , and $b(x, y) = 1$ when there is a contact. The total number of 3×3 combinations defining the following matrix is $2^9=512$.

$$\begin{pmatrix} b(x-d, y-d) & b(x-d, y) & b(x-d, y+d) \\ b(x, y-d) & b(x, y) & b(x, y+d) \\ b(x+d, y-d) & b(x+d, y) & b(x+d, y+d) \end{pmatrix} \quad (15)$$

However, not all of these combinations will appear with equal probability. It is likely that many will represent the complete separation or complete contact states. Many others will likely represent the transition between the contact and separation zones. On the other hand, patterns representing vertical, horizontal, or random features, would be rare. The approach could be easily generalized for 5×5 patterns leading to $2^{25}=33,554,432$ combinations.

Asperity is often defined as a feature that makes a contact, so the persistent homology barcode approach is very significant in defining asperity.

6.6.2. Stick-slip

The contact analysis can be generalized for the stick-slip motion by introducing a variable with three values value $b(x, y) = 0$ when there is no contact between the two surfaces at the point

(x, y) , $b(x, y) = 1$ when there is a static stick contact, and $b(x, y) = 2$ when there is slip. Now the space of possible combinations is $3^9=19,683$ for the 3×3 patterns and $3^{25}=847,288,609,443$ for the 5×5 patterns.

Fleurquin and co-workers [48] analyzed the distribution of slip of the tip of an atomic force microscope scanning over the Robin Hood landscape and reported three different types of distributions of the number of slips depending on the slip size. **Figure 6.9(d)** presents the plots of the number of slips vs slip size for different threshold heights, h_T . The histograms of the number of slips vs size approximate the Gaussian distribution for small values of h_T ($h_T = 0.05$), the exponential distribution for $0.08 < h_T < 0.1$, and the lognormal distribution for $h_T > 0.1$.

Correlations between the size of stick and slip and the spatial resolution revealed by the barcode persistence analysis are expected to indicate meaningful data regarding the physical mechanisms generating the statistics of the distribution of the stick and slip zones. For example, it has been suggested that so-called self-organized criticality is responsible for the one-over-frequency statistical distributions [7].

For the analysis of the stick-slip motion, the contact analysis can be generalized by introducing a variable with three values value $b(x, t) = 0$ when there is no contact between the two surfaces at the point (x, t) , $b(x, t) = 1$ when there is a static stick contact, and $b(x, t) = 2$ when there is slip.

Correlations should be sought between the age of contact and the size of contact. It is expected that these correlations would lead to dependencies similar to the empirical state-and-rate laws such as Eqs. 11-14. It has been also suggested that the Poincaré–Brouwer theorem [49] may be applicable to the stick-slip situations.

6.7. Conclusions

Microscale and nanoscale roughness of metallic sample surfaces made of brass were studied applying different approaches to the evaluation of roughness parameters including the standard deviation of the rough profile height, correlation length, analyzing the extreme point location and persistence diagrams in the data space. These parameters provided valuable insights on roughness properties beyond the traditional quantitative characteristics of surface roughness. The autocorrelation function provides information about the horizontal (tangential) size of roughness details at the microscale. The analysis of the 3×3 , 4×4 , and 5×5 sub-matrices or patches provides information about the anisotropic features of the profile at the nanoscale, which are not captured by more traditional surface roughness parameters. The persistence diagrams provide more detailed information about the scale dependency of the roughness features.

Proper reduction of the number of degrees of freedom is the key to the development of adequate models of friction. Methods of topological data analyses provide a mathematical tool for dimensionality reduction for datasets characterizing surface roughness, contact of rough surfaces, and frictional sliding. It is anticipated that the development and application of software for automated tribological data analysis may provide new insights on the models of dynamic friction with internal parameters.

6.8. References

1. Nosonovsky, Michael, and Bharat Bhushan. "Biologically inspired surfaces: broadening the scope of roughness." *Advanced Functional Materials* 18, no. 6 (2008): 843-855.

2. Tadmor, Rafael, Ratul Das, Semih Gulec, Jie Liu, Hartmann E. N'guessan, Meet Shah, Priyanka S. Wasnik, and Sakshi B. Yadav. "Solid-liquid work of adhesion." *Langmuir* 33, no. 15 (2017): 3594-3600.
3. Jiang, Youhua, Yujin Sun, Jaroslaw W. Drelich, and Chang-Hwan Choi. "Topography-dependent effective contact line in droplet depinning." *Physical Review Letters* 125, no. 18 (2020): 184502.
4. Tadmor, Rafael. "Open problems in wetting phenomena: pinning retention forces." *Langmuir* 37, no. 21 (2021): 6357-6372.
5. Menezes, Pradeep L., Michael Nosonovsky, Sudeep Prabhakar Ingole, Satish Vasu Kailas, and Michael R. Lovell, eds. *Tribology for scientists and engineers*. New York: Springer, 2013.
6. Bormashenko, Edward Yu. *Wetting of real surfaces*. de Gruyter, 2018.
7. Nosonovsky, Michael, and Vahid Mortazavi. *Friction-induced vibrations and self-organization: mechanics and non-equilibrium thermodynamics of sliding contact*. CRC Press, 2013.
8. Greenwood, J. A., and J. J. Wu. "Surface roughness and contact: an apology." *Meccanica* 36, no. 6 (2001): 617-630.
9. Bormashenko, Edward, Mark Frenkel, Alla Vilks, Irina Legchenkova, Alexander A. Fedorets, Nurken E. Aktaev, Leonid A. Dombrovsky, and Michael Nosonovsky. "Characterization of self-assembled 2D patterns with Voronoi Entropy." *Entropy* 20, no. 12 (2018): 956.
10. Hasan, Md Syam, and Michael Nosonovsky. "Topological data analysis for friction modeling." *EPL (Europhysics Letters)* 135, no. 5 (2021): 56001.
11. Duman, Ali Nabi. "Grain analysis of atomic force microscopy images via persistent homology." *Ultramicroscopy* 220 (2021): 113176.

12. Solis, Ingrid Membrillo, Tetiana Orlova, Karolina Bednarska, Piotr Lesiak, Tomasz R. Woliński, Giampaolo D'Alessandro, Jacek Brodzki, and Malgosia Kaczmarek. "Structural heterogeneity: a topological characteristic to track the time evolution of soft matter systems." arXiv preprint arXiv:2106.13169 (2021).
13. Frenkel, Mark, Alexander A. Fedorets, Leonid A. Dombrovsky, Michael Nosonovsky, Irina Legchenkova, and Edward Bormashenko. "Continuous symmetry measure vs Voronoi entropy of droplet clusters." *The Journal of Physical Chemistry C* 125, no. 4 (2021): 2431-2436.
14. Janai, Erez, Andrew B. Schofield, and Eli Sloutskin. "Non-crystalline colloidal clusters in two dimensions: size distributions and shapes." *Soft Matter* 8, no. 10 (2012): 2924-2929.
15. Guttman, Shani, Zvi Sapir, Moty Schultz, Alexander V. Butenko, Benjamin M. Ocko, Moshe Deutsch, and Eli Sloutskin. "How faceted liquid droplets grow tails." *Proceedings of the National Academy of Sciences* 113, no. 3 (2016): 493-496.
16. Hasan, Md Syam, Amir Kordijazi, Pradeep K. Rohatgi, and Michael Nosonovsky. "Triboinformatic modeling of dry friction and wear of aluminum base alloys using machine learning algorithms." *Tribology International* 161 (2021): 107065.
17. Hasan, Md Syam, Amir Kordijazi, Pradeep K. Rohatgi, and Michael Nosonovsky. "Triboinformatics Approach for friction and wear prediction of al-graphite composites using machine learning methods." *Journal of Tribology* 144, no. 1 (2022).
18. Hasan, Md Syam, Tien Wong, Pradeep K. Rohatgi, and Michael Nosonovsky. "Analysis of the friction and wear of graphene reinforced aluminum metal matrix composites using machine learning models." *Tribology International* (2022): 107527.
19. Carlsson, Gunnar. "Topology and data." *Bulletin of the American Mathematical Society* 46, no. 2 (2009): 255-308.

20. Carlsson, Gunnar, Tigran Ishkhanov, Vin De Silva, and Afra Zomorodian. "On the local behavior of spaces of natural images." *International journal of computer vision* 76, no. 1 (2008): 1-12.
21. Urbakh, Michael, Joseph Klafter, Delphine Gourdon, and Jacob Israelachvili. "The nonlinear nature of friction." *Nature* 430, no. 6999 (2004): 525-528.
22. Muser, Martin H., Michael Urbakh, and Mark O. Robbins. "Statistical mechanics of static and low-velocity kinetic friction." *Advances in Chemical Physics* 126 (2003): 187-272.
23. Nosonovsky, Michael, and Bharat Bhushan. "Multiscale friction mechanisms and hierarchical surfaces in nano-and bio-tribology." *Materials Science and Engineering: R: Reports* 58, no. 3-5 (2007): 162-193.
24. Omrani, Emad, Afsaneh Dorri Moghadam, Pradeep L. Menezes, and Pradeep K. Rohatgi. "New emerging self-lubricating metal matrix composites for tribological applications." In *Ecotribology*, pp. 63-103. Springer, Cham, 2016.
25. Dulle, Jana, Silke Nemeth, Ekaterina V. Skorb, and Daria V. Andreeva. "Sononanostructuring of zinc-based materials." *RSC advances* 2, no. 32 (2012): 12460-12465.
26. Skorb, Ekaterina V., and Daria V. Andreeva. "Bio-inspired ultrasound assisted construction of synthetic sponges." *Journal of Materials Chemistry A* 1, no. 26 (2013): 7547-7557.
27. Ulasevich, Sviatlana A., Elena I. Koshel, Ilya S. Kassirov, Nadzeya Brezhneva, Liubov Shkodenko, and Ekaterina V. Skorb. "Oscillating of physicochemical and biological properties of metal particles on their sonochemical treatment." *Materials Science and Engineering: C* 109 (2020): 110458.

28. Rosenberg, Merilin, Heiki Vija, Anne Kahru, C. William Keevil, and Angela Ivask. "Rapid in situ assessment of Cu-ion mediated effects and antibacterial efficacy of copper surfaces." *Scientific reports* 8, no. 1 (2018): 1-12.
29. Ma, Yaqin, Xingqian Ye, Yunbin Hao, Guoneng Xu, Guihua Xu, and Donghong Liu. "Ultrasound-assisted extraction of hesperidin from Peggan (*Citrus reticulata*) peel." *Ultrasonics Sonochemistry* 15, no. 3 (2008): 227-232.
30. Bowden, Frank Philip, Frank Philip Bowden, and David Tabor. *The friction and lubrication of solids*. Vol. 1. Oxford university press, 2001.
31. Urbakh, Michael, Joseph Klafter, Delphine Gourdon, and Jacob Israelachvili. "The nonlinear nature of friction." *Nature* 430, no. 6999 (2004): 525-528.
32. Muser, Martin H., Michael Urbakh, and Mark O. Robbins. "Statistical mechanics of static and low-velocity kinetic friction." *Advances in Chemical Physics* 126 (2003): 187-272.
33. Nosonovsky, Michael. "Entropy in tribology: in the search for applications." *Entropy* 12, no. 6 (2010): 1345-1390.
34. Hasan, Md Syam, Amir Kordijazi, Pradeep K. Rohatgi, and Michael Nosonovsky. "Machine learning models of the transition from solid to liquid lubricated friction and wear in aluminum-graphite composites." *Tribology International* 165 (2022): 107326.
35. Bormashenko, Edward, Alexander A. Fedorets, Mark Frenkel, Leonid A. Dombrovsky, and Michael Nosonovsky. "Clustering and self-organization in small-scale natural and artificial systems." *Philosophical Transactions of the Royal Society A* 378, no. 2167 (2020): 20190443.
36. Skorb, Ekaterina V., and Helmuth Möhwald. "'Smart' surface capsules for delivery devices." *Advanced Materials Interfaces* 1, no. 6 (2014): 1400237.

37. Skorb, Ekaterina V., Dmitry G. Shchukin, Helmuth Möhwald, and Daria V. Andreeva. "Ultrasound-driven design of metal surface nanofoams." *Nanoscale* 2, no. 5 (2010): 722-727.
38. Andreeva, Daria V., Dmitry V. Sviridov, Admir Masic, Helmuth Möhwald, and Ekaterina V. Skorb. "Nanoengineered Metal Surface Capsules: Construction of a Metal-Protection System." *Small* 8, no. 6 (2012): 820-825.
39. Andreeva, D. V., A. Kollath, N. Brezhneva, D. V. Sviridov, B. J. Cafferty, Helmuth Möhwald, and E. V. Skorb. "Using a chitosan nanolayer as an efficient pH buffer to protect pH-sensitive supramolecular assemblies." *Physical Chemistry Chemical Physics* 19, no. 35 (2017): 23843-23848.
40. Tolstoi, D. M. "Significance of the normal degree of freedom and natural normal vibrations in contact friction." *Wear* 10, no. 3 (1967): 199-213.
41. Heuberger, Manfred, Carlos Drummond, and Jacob Israelachvili. "Coupling of normal and transverse motions during frictional sliding." *The Journal of Physical Chemistry B* 102, no. 26 (1998): 5038-5041.
42. Zaloj, V., M. Urbakh, and J. Klafter. "Modifying friction by manipulating normal response to lateral motion." *Physical review letters* 82, no. 24 (1999): 4823.
43. Hasan, Md Syam, and Michael Nosonovsky. "Lotus effect and friction: does nonsticky mean slippery?." *Biomimetics* 5, no. 2 (2020): 28.
44. Dieterich, James H. "Modeling of rock friction: 1. Experimental results and constitutive equations." *Journal of Geophysical Research: Solid Earth* 84, no. B5 (1979): 2161-2168.
45. Dieterich, James H., and Brian D. Kilgore. "Direct observation of frictional contacts: New insights for state-dependent properties." *Pure and Applied Geophysics* 143, no. 1 (1994): 283-302.

46. Armstrong-Hélouvry, Brian, Pierre Dupont, and Carlos Canudas De Wit. "A survey of models, analysis tools and compensation methods for the control of machines with friction." *Automatica* 30, no. 7 (1994): 1083-1138.
47. Olsson, Henrik, Karl Johan Åström, Carlos Canudas De Wit, Magnus Gäfvert, and Pablo Lischinsky. "Friction models and friction compensation." *Eur. J. Control* 4, no. 3 (1998): 176-195.
48. Fleurquin, Pablo, Hugo Fort, Mordechai Kornbluth, Roman Sandler, Mordecai Segall, and Fredy Zypman. "Negentropy generation and fractality in the dry friction of polished surfaces." *Entropy* 12, no. 3 (2010): 480-489.
49. Bormashenko, Edward, and Alexander Kazachkov. "Rotating and rolling rigid bodies and the "hairy ball" theorem." *American Journal of Physics* 85, no. 6 (2017): 447-453.

CHAPTER 7: ROUGHNESS, WETTING, AND TRIBOLOGICAL ANALYSIS OF ANTIMICROBIAL AND ANTICORROSIVE COATINGS USING TRADITIONAL AND DATA TOPOLOGY APPROACHES

TiO₂/ZnO based multilayer hydrophobic coatings have been developed to confer self-cleaning, water repellence, anticorrosive, photocatalytic, and antimicrobial properties to different substrates. Due to the diverse applications of the coated substrates, characterization of the roughness, wetting, and tribological behavior and understanding their interrelation are important. For example, to combat water and ice-induced damage of roadways and pavements, the coated surface should be water-repellant and anti-corrosive while retaining enough friction for the tires. Similarly, for many application, water-repellant and antimicrobial properties of the substrate materials are desired without a notable change in the friction behavior. In this chapter, data topology approaches have been applied besides traditional analysis to understand the roughness, wetting, and tribological behavior and their interrelation.

7.1. Introduction

Like many other infections, Covid-19 caused by the SARS-CoV-2 coronavirus primarily spreads through airborne respiratory micro-droplets and aerosols [1-3]. Due to the prolonged survival period of the SARS-CoV-2 and its new strains, contaminated surfaces holding virus bearing droplets are common sources of infection [4]. Available evidence suggests that a direct contact with such contaminated surfaces and subsequent touching of mouth, nose, and eye causes the risk of Covid-19 infection [5]. The World Health Organization (WHO), Centers for Disease Control and Prevention (CDC), and other regulatory bodies in healthcare recommend regular cleaning and disinfecting of commonly touched surfaces to limit the transmission [6,7].

Consequently, the synthesis of surface nanocoatings with effective antimicrobial properties can limit the surface-to-human transmission of the SARS-CoV-2. Antibacterial [8-11] and antiviral [12-14] coatings for surfaces have been explored over the years for different applications. Most of the commercially available antimicrobial coatings, for example, silver-based coatings used in medical applications, incorporate complex synthesis and application processes, which make them expensive. Toxic chemicals and poor durability in applications involving surface interactions are other constraints often limiting the application of the existing antimicrobial coatings.

An ideal antimicrobial coating should possess effective photocatalytic properties to deactivate harmful pathogens through catalytic decomposition, sustainable hydrophobic properties to repel the respiratory droplets, and durability to withstand a wide range of surface interactions without exhibiting toxicity. Antimicrobial treatment based on the photocatalytic property of TiO_2 has been studied for different applications including sanitation and sterilization [15-18]. TiO_2 nanoparticles embedded on a surface can oxidize and deactivate organic matters and pollutants deposited on it in presence of sunlight [15]. The antimicrobial and photocatalytic properties of ZnO nanoparticles are also well-studied [19-21]. The TiO_2/ZnO -phosphate (TP/ZP) based surface coatings developed in this study incorporate hydrophobic and photocatalytic properties to limit the transmission of pathogens. Hydrophobic properties resist the sustenance of respiratory droplets on the surface and the TiO_2 and ZnO nanoparticles work in pathogen deactivation through the release of hydroxyl radicals during photocatalytic reactions.

To combat water and ice-induced damage of roadways and pavements, novel ideas and approaches are coming forward for developing superhydrophobic pavements required for modern transportation system. However, it is a challenging task to synthesize the superhydrophobic concrete or asphalt surface. Concrete is a composite material similar to ceramics, which is also

typically porous and hydrophilic. Despite that, a certain progress has been made recently in this area [22-24] of producing hydrophobic, “overhydrophobic” (i.e., with the contact angle $> 120^\circ$ but less than 150°), and, in some cases, superhydrophobic concrete using polyethyl hydrogen siloxane (PESHO) or polymethyl hydrogen siloxane (PMHS) admixture, combined with sub-micron or nanosized particles [23, 25].

Tire traction and the coefficient of friction (COF) are highly dependent on rubber friction and applied load [26]. It has been observed that the presence of water can affect the rubber friction and tire traction with paved surfaces significantly. Tire hydroplaning on wet pavement surfaces is the most common reason for vehicle and aircraft skidding, which is often a reason for the accident [26-28]. In countries with snowfall, the effect of the presence of water on roads and pavements is even a more critical issue. The deposition of ice can reduce the COF between the tire and the surface and make the roads accident-prone. As a result, billions of dollars are spent for snow and ice removal as well as on the maintenance of the roadways and pavements [29].

When water solidifies into ice, its volume increases by about 9%. Consequently, the ice transformation of water in the small pores of concrete causes the formation of cracks, severe damage, and significant reduction of service life [30]. To avoid unwanted consequences, it is highly desirable that the pavement surface itself is water repulsing. There are two wetting states which can exist when a liquid droplet is placed on a rough solid surface: the Wenzel state (complete or homogeneous wetting) and the Cassie state, when tiny air pockets are trapped under the water droplets, which eventually reduce the solid-liquid contact area and make the surface superhydrophobic [31]. As water cannot wet the surface, water droplets can easily be rolled off by a small mechanical work or by tilting the surface. It is difficult to realize a durable superhydrophobic surface on a conventional concrete; however, engineered concrete and fiber

reinforced composites were reported to reach ($120^\circ - 150^\circ$) and superhydrophobic ($>150^\circ$) states [23].

Multi-layer TiO_2 based coatings have been explored for synthesizing hydrophobic and superhydrophobic concrete for transportation applications. The porous and hydrophilic nature of concrete makes the synthesis of superhydrophobic asphalt or concrete surface a challenging task. However, the combination of micro- or nanosized particles with PESH0 or PMHS admixture has been used to successfully synthesize hydrophobic, overhydrophobic, and superhydrophobic concrete and ceramic tile surfaces [22,23,25]. However, it is commonly expected that the application of “non-sticky” coatings, such as PTFE, PESCO, PMHS, and similar, would reduce the coefficient of friction (COF) between the tire and the concrete surface because friction tends to depend on adhesive forces between the coating surfaces. This makes it questionable, whether the hydrophobic and superhydrophobic coatings can be used for applications, where strong traction is needed, such as roads or runway pavements. Friction also depends on the presence of a liquid at the interface, so wetting properties affect the friction. Therefore, the correlation between the wetting and frictional properties of superhydrophobic concrete pavements is needed.

Tribological characterization is required to understand the behavior of the surface coatings during interactions with external stimuli in relative motion. The coefficient of friction (COF) between interacting surfaces [32] is the ratio of friction force (F_f) to the normal load (N) that presses the surfaces together, $\mu = \frac{F_f}{N}$. The tribological characterization reveals how the developed coatings are altering the friction behavior of the surfaces. It also provides important information about the durability of the coatings in tribological applications.

The sample preparation for the antimicrobial coatings has been discussed at length in the study of Hasan et al. [33]. Two grades of steel, 1018 grade cold finished carbon steel (CS) and 304 grade and annealed stainless steel (SS) were supplied from Speedy Metals were used as substrates further referred to as the base material (BM) for the coatings. The BM samples were machined to 1”×1” size coupons, sandblasted and ultrasonically cleaned in an acetone bath. Some of the carbon steel BM samples were then phosphated in a room temperature bath (composed of ZnO 5g/L; 85% H₃PO₄ 11.3mL/L; NaNO₂ 1g/L dissolved in H₂O_{di} – all these precursors were purchased from MilliporeSigma) and referred to as RTP CS. After immersing in the bath for 30 minutes, the RTP CS samples were rinsed thoroughly with water and dried in air. All three substrates: CS, SS, and RTP CS were further used for coating application and performance analysis. The TiO₂/ZnO-phosphate based first layer was hydrophilic in nature which is followed by a second layer of PMHS based hydrophobic layer [33]. The combination of these two layers induced the desired water-repellence and antimicrobial properties to the substrates. The PMHS based hydrophobic layer was also applied on the BM samples directly (without the 1st layer) to synthesize 1-layer hydrophobic samples. The schematic diagram of the coating layers on the base material surface is presented in **Figure 7.1**.

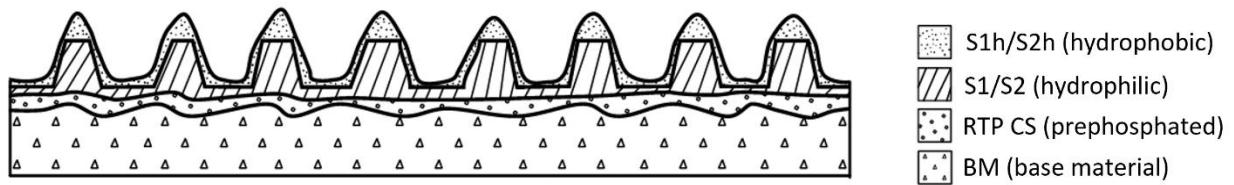


Figure 7.1. Schematic diagram of different coating layers on the base material surface [33]

Sample preparation for the anticorrosive coatings has been discussed in the study of Lanka et al. [34]. Unglazed clay ceramic tile (supplied by Blick) flat samples were cut to 50 mm x 30

mm size and tested for friction against a nitrile rubber pin. Three types of ceramic tile samples were prepared and tested in this study: (i) uncoated, (ii) coated with TiO₂-phosphate (hydrophilic), and (iii) coated using TiO₂-phosphate + PMHS two-stage process (+PMHS, hydrophobic).

In this chapter, the roughness, wetting, and friction behavior of the developed coatings will be analyzed using the traditional and data topology approaches. The durability of the developed coatings for tribological applications will also be investigated. Finally, correlations between surface roughness, wetting, and friction properties will be investigated.

7.2. Materials and procedures

7.2.1. Surface roughness characterization

Surface characterization of the antimicrobial and anticorrosive coatings was performed using a scanning electron microscope (SEM) and confocal laser scanning microscope (CLSM). To characterize surface roughness and patterns of the sample surfaces, an Olympus LEXT OSL model-4100 CLSM was used. The samples were placed on the sample stage of the microscope and using the joystick eight spots on different locations of each sample were selected randomly for characterization. The average roughness, R_a of each sample was reported by averaging the R_a of each measurement for a sample surface. Using the LEXT software, 3D images of the surface at 20× magnification were captured by laser scanning. With the resolution of 0.625 μm, the sampling profile length of 80 μm was selected in both the x- and y-direction. For the antimicrobial coated samples, besides the image profiles, the surface roughness profiles were recorded in numeric datasets as 128×128 matrices and stored in csv files. From each scan, 16384 data points of the roughness height were received.

To characterize the overall surface appearance, JEOL JSM-6460L Scanning Electron Microscope was used. Prior to characterization, the specimens coated with antimicrobial coatings

were gold/palladium sputtered to improve sample conductivity, reduce surface charging, and increase the overall micrographs quality using Denton Desk II Sputter Coater. Secondary electrons accelerated to 15 kV were used as a source. Every image was taken on a 45 mm spot size and a working distance of 12 mm.

7.2.2. Tribological test procedure

For tribological characterization, the COF between the samples and the pins of carefully selected materials was measured using the universal mechanical tester (CETR UMT 2) under dry conditions. The pin-on-flat regime of the tribometer with the reciprocating (oscillatory) motion of the flat substrate was used for the measurement of the COF between the samples and the pins.

For the samples coated with the antimicrobial coatings, high-density polyethylene (HDPE) pins having a diameter of 6.35mm were used. Using a metallic pin caused significant removal of materials from the uncoated and coated samples and no longer presented the friction behavior of the surfaces (rather presented that of the bulk material). On the other hand, the HDPE pin helped to characterize the friction behavior of the uncoated and coated surfaces consistently as no notable material removal was involved. The sample was placed in a sample holder specially designed for holding the 1”×1” samples. Then it was mounted on the reciprocating base of the tribometer which is designed to move along the x-axis (horizontally) with the help of a DC motor. The HDPE pin was attached to the upper frame of the suspension of the tribometer which is connected to the sensor (DFH-50-0767). Using the UMT software, the motion of the sample holder and the suspension was controlled. During the experiment, a constant normal load was maintained by the control unit through a continuous adjustment of the Z carriage movement in the vertical direction. The command script of the tribological test included a preload sequence: 15 N normal load with a slider velocity of 2 mm/s for 30 seconds and a reciprocating sequence: 15 N normal load with a

slider velocity of 0.2 m/s for 120 seconds. The normal load of 15 N was selected (which is in the recommended range of the DFH-50-0767 sensor) after running the friction tests of the tribo-pairs for different normal loads (5N, 15N, 20N, 25N, and 30N) and visually observing the scratch marks on the surface. A stroke length of 10 mm and the corresponding 0.2 m/s sliding velocity which is in the recommended range were used in the pin-on-flat reciprocating test. The run-time of the tests was selected fulfilling the requirement of the pin-on-flat reciprocating test.

To study the effect of tire-concrete friction in the laboratory setup, the “model” nitrile rubber, and ceramic tiles (uncoated and coated with anticorrosive coatings) as material model were used, the properties of which are similar to those of tires and concrete pavements, respectively. The rubber pin holder was clamped to the suspension while the tile sample was attached to the reciprocating stage. The tile sample was attached to the sample holder, which included a mold, an L-shaped supporting base, and clamps. The sample holder was then affixed to the fixture of the reciprocating base. The preload step was set for a duration of 30 s and had input velocity of 0 Hz in a counterclockwise direction and slider velocity of 2 mm/s, while the reciprocating step set for 90 s and had input velocity of 5 Hz also in a counterclockwise direction with slider velocity at 1000 mm/s. During the entire experiment, a normal load was maintained at 25 N, which corresponded to the actual field loading.

7.2.3. Wetting test procedure

To characterize wetting, we measured the water contact angles of the samples using the Rame-Hart 250 goniometer. The device is comprised of several components: micro-syringe assembly, sample holder base, a high-speed camera, and a light source (**Figure 7.2**).

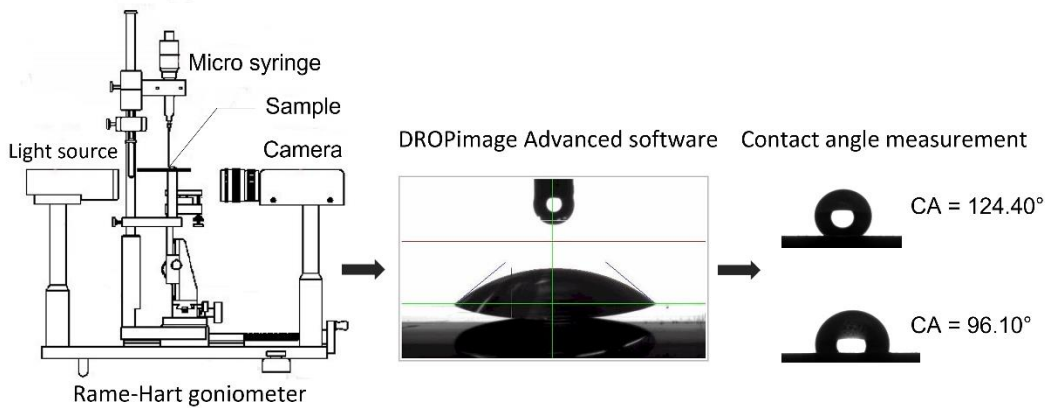


Figure 7.2. Measurement of contact angles in Rame-Hart goniometer

Using the micro-syringe assembly, we placed 4 μl distilled water (DI) droplets at five different locations on the samples. The images of the droplets were captured by the high-speed camera and were then analyzed by the “DROPIimage” software for the CA characterization. “DROPIimage” software provided the CA values at each location which were then averaged and reported as the CA of the samples.

7.3. Result and discussion

7.3.1. Surface roughness characterization

For the antimicrobial coatings, the average roughness, R_a of the base substrate materials, and the coated samples were presented in **Table 7.1** and **Table 7.2**. The R_a values of the BM samples of CS, RTP CS, and SS were 3.705 μm , 2.805 μm , and 2.907 μm , respectively. In the microstructure of the BM surfaces, both the CS and the SS surfaces were observed to be similarly roughened as a similar surface treatment was used. In the micrograph of the prephosphated carbon steel (RTP CS), due to the phosphating reaction, structures composed of fine zinc and iron phosphate crystals were developed that emerge from the surface.

Table 7.1 shows that the application of the single layer of PMHS on the BM decreased the R_a . In contrast, the single layer of TP/ZP coatings on the BM increased the R_a notably. A further increase in R_a was observed when an additional layer of PMHS was applied over the TP/ZP layer. The R_a values observed for the 2-layer coating on the CS, RTP CS, and SS BM samples were 8.805 μm , 5.016 μm , and 6.161 μm , respectively. Among the BM samples, the carbon steel exhibited the maximum R_a of 8.805 μm when the 2-layer coatings were applied on the sample.

In the X-ray diffraction analysis (XRD), for all three substrates coated with the S1 coating material, the presence of crystalline zinc phosphate on the surfaces was confirmed. In case of the coated carbon steel (S1 CS) and prephosphated carbon steel (S1 RTP CS) samples, the crystal structures were dense and highly developed. In contrast, the coated stainless steel (S1 SS) sample demonstrated lesser attachment of crystals to the surface, thus forming microstructure of lower density compared to S1 CS and S1 RTP CS products. The micrograph of the CS BM coated with the S2 coating material exhibited a distinct surface morphology. Crystal structures of zinc phosphate (platelets) protruding through a nano-titania layer were observed.

The confocal 3D microscopic view for the uncoated ceramic tile and TiO_2 – phosphate coated samples (anticorrosive coatings) R2, R5, R7, R9, O2 were done to understand the tendencies related to the roughness on the sample surface and to understand the length of crack and depth of cracks on coated samples after the thermal treatment.

7.3.2. Topological data analysis and surface characterization

Surface roughness data involves many parameters which are usually organized in multidimensional space [35]. The reduction of the dimensionality of the data (i.e., the organization of data in subspaces along the surface) is achieved through topological analysis. Topological data

analysis helps to identify persistent features over different resolution scales which represents the true features of the underlying space, unlike random noise and artifacts. Persistent homology involves the computation of topological features: topological invariants, n-dimensional simplicial complex, Betti numbers, etc. at different spatial resolutions. Connected components (H_0), 1-D holes (H_1), and higher dimensional voids (H_2 , H_3 , etc.) are the major topological invariants observed over varying length scales. The appearance and disappearance of homological invariants or features in different sampling lengths are presented in the persistence diagram. The most persistent topological features are presented by the data points that are located far away from the diagonal. In barcodes, each horizontal bar presents the interval of the feature appearance and disappearance. While shorter bars are representative of random noises, the longer bars present the more persistent topological invariants.

To analyze the surface topology, we considered the surface profile (roughness height) data of the CS BM, CS BM-PMHS, S1 CS, and the 2-layer S1 CS-PMHS coated samples. We presented the persistence homology with persistence diagrams and barcodes in **Figure 7.3** where the homological invariants were expressed as a function of the resolution length. A sampling length of 80 μm with a resolution of 0.625 μm in both x- and y- directions was considered. For generating the diagrams for surface profile data, we used the standard libraries of Python. The datasets in the form of 128 \times 128 matrices were subdivided into 3 \times 3 submatrices for generating the barcodes [35,36]. First, we generated a filtered simplicial complex from the data points. We considered Vietoris-Rips filtration in the analysis and the maximum dimension of 4 to calculate the persistent homology for the Euclidean distance matrix.

Each of the samples exhibited a distinct topology for the surface profile data at different length scales in **Figure 7.3**. For the uncoated CS BM sample, H_0 , H_1 , and H_2 were the major

persistent topological invariants. The first topological invariant, H_0 , which indicated the connected components in topological space was found persistent over the entire sampling length range. The other persistent invariant, H_1 corresponding to 1-D holes was significant at the resolution length corresponding to the size scale of the profile, approximately in the range of 35–45 μm . Application of the hydrophobic PMHS layer on the CS BM caused a decrease in average roughness (**Table 7.1**). From the persistence diagram and barcodes, it was seen that the higher dimensional void (H_2) is no longer persistent for the CS BM-PMHS sample as the surface is smoothed. For the S1 CS sample, well-developed crystalline structures of ZP were observed on the surface and the average roughness increased notably (**Table 7.2**). Due to more complex surface morphology, an additional higher dimensional void (H_3) invariant was found persistent besides H_0 , H_1 , and H_2 from the persistence diagram and barcodes. Longer bars for H_3 in the barcode diagram for the S1 CS sample (**Figure 7.3(e-f)**) indicated that higher dimensional voids were more prevalent than those observed in the BM sample. Moreover, this invariant was significant at the resolution length corresponding to the size scale of the profile, approximately in the range of 45–52 μm . For the 2-layer S1 CS-PMHS samples, the average roughness increased further. However, the second layer of PMHS covered the ZnO-phosphate crystal structures and made the surface profile more uniform. Consequently, in the persistence diagram and barcodes, the 1-D holes (H_1) and the higher dimensional voids (H_2, H_3) were found less persistent than those of the CS BM and the S1 CS samples.

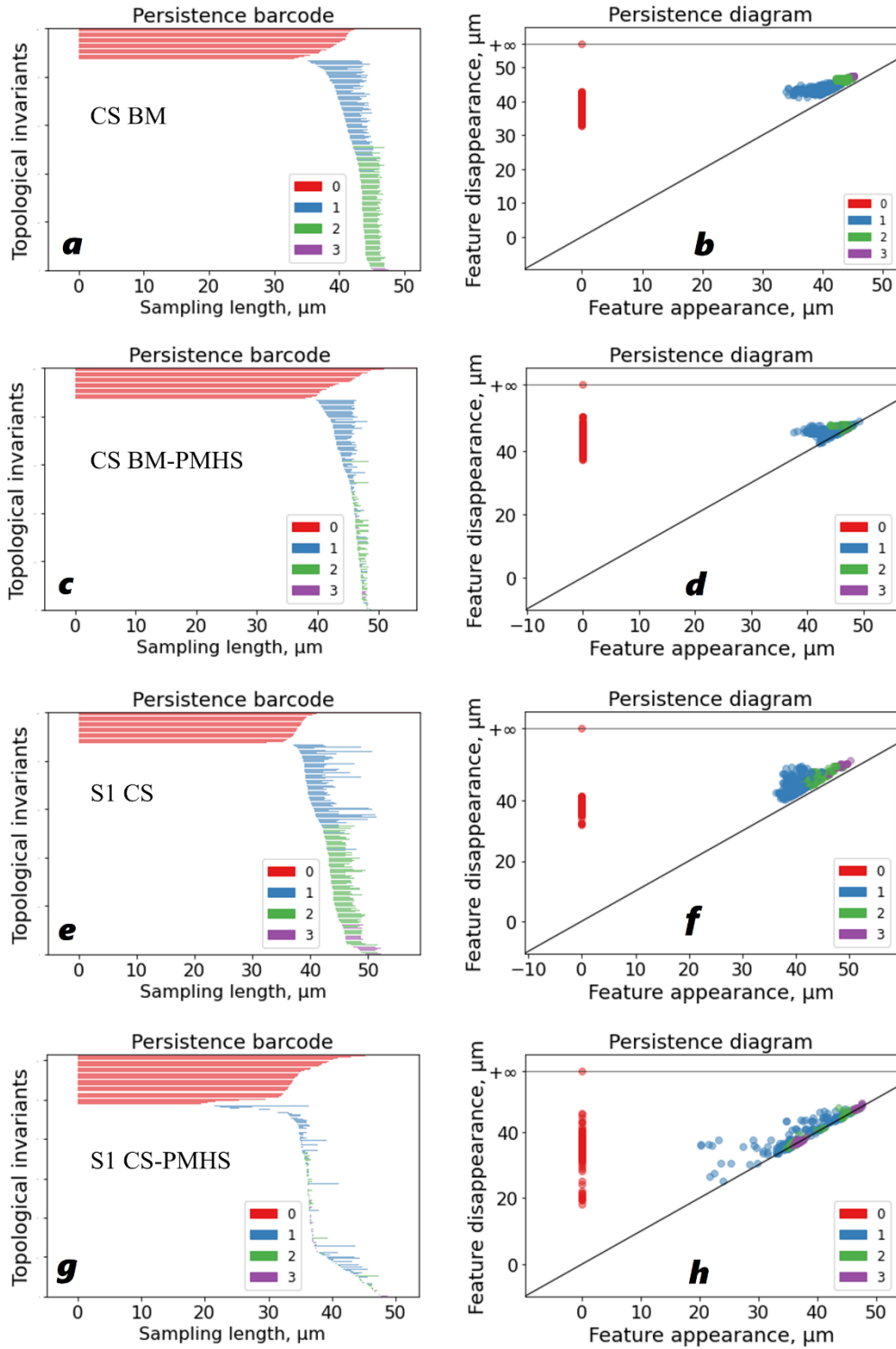
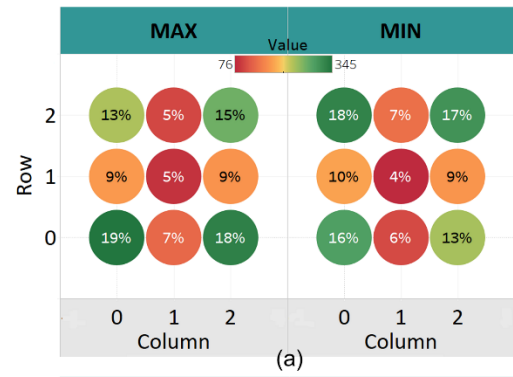


Figure 7.3. Persistence diagram and persistence barcodes for the surface roughness of (a-b) CS BM, (c-d) CS BM-PMHS, (e-f) S1 CS, and (g-h) 2-layer S1 CS-PMHS samples.

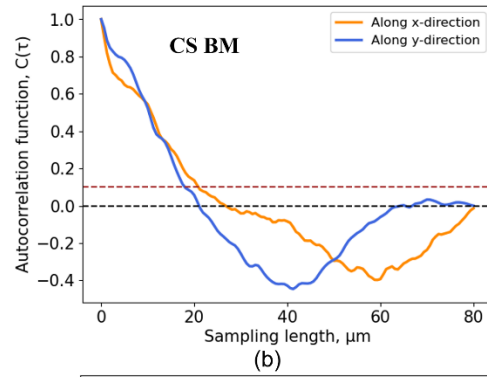
To analyze the roughness data and visualize the patterns in roughness profiles for CS BM, CS BM-PMHS, S1 CS, and the 2-layer S1 CS-PMHS hydrophobic samples, we divided the 128×128 matrix of each representative sample's roughness profile into 3×3 square sub-matrices (3698 units) using a Python program. The average roughness values of these samples were 3.705 μm, 2.611 μm, 6.473 μm, and 8.805 μm, respectively. To compare the roughness profiles, we considered the sampling length of 80 μm with the resolution of 0.625 μm in both the horizontal and vertical direction (x- and y-direction) for each sample. The autocorrelation function (ACF) and the distribution of the maximum and minimum roughness heights in cell positions for the sub-matrices for the abovementioned samples are presented in **Figure 7.4**. Among the samples, the CS BM had the largest correlation length, β^* (the smallest sampling length at which the ACF dropped to 10% of its original value) along the x (20.9 μm) and the y (17.5 μm) direction. The minimum value of β^* was found for the hydrophobic CS BM-PMHS sample (8.5 μm along the x direction and 15.4 μm along the y direction). The β^* values for the S1 CS (11.9 μm and 11.0 μm along the x and y direction), and the 2-layer S1 CS-PMHS sample (18.1 μm and 12.5 μm along the x and y direction) were also notably smaller than the those of the CS BM. These β^* values indicated that surface profile and patterns in the coated samples were changing more rapidly along the sampling length than observed for the uncoated BM.

For the 2-layer S1 CS-PMHS hydrophobic sample, the diagonal cell positions of the 4×4 sub-matrix: (0,0), (0,2), (2,0), and (2,2) held the most maximum and minimum values of the roughness heights, **Figure 7.4(g)**. The correlation length for the roughness profile was notably greater than the size of the patch of 1.875 μm, and the greatest number of maxima and minima were observed at the diagonal positions. Moreover, the total percentage of the number of maxima and minima in the positions (0,1), (2,1) was 12% (for maxima) and 12% (for minima), while the

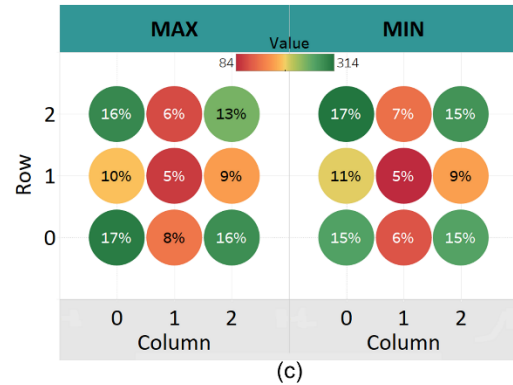
total percentage in the positions (1,0), (1,2) was 20% (for maxima) and 20% (for minima). This suggested that the distribution was anisotropic, **Figure 7.4(g)** where the surface gradients for surface roughness in the x-direction were more prevalent than in the y-direction. The distribution of the maxima and minima varied among the other samples. However, we observed the anisotropic distribution of roughness in each case in vertical and horizontal directions.



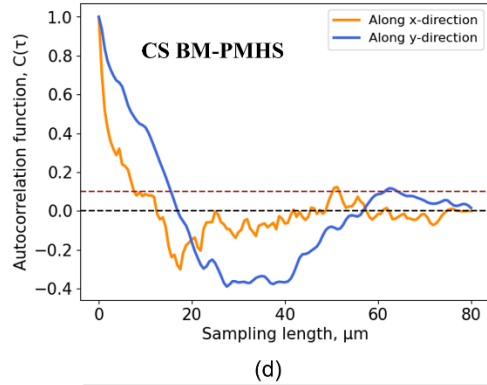
(a)



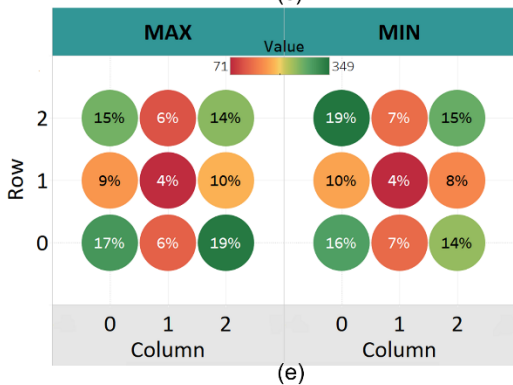
(b)



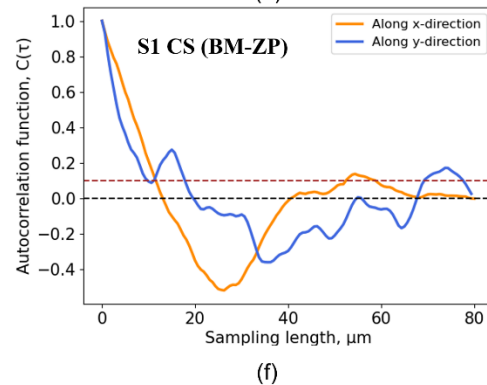
(c)



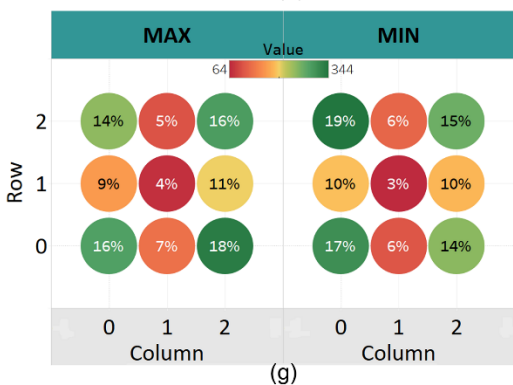
(d)



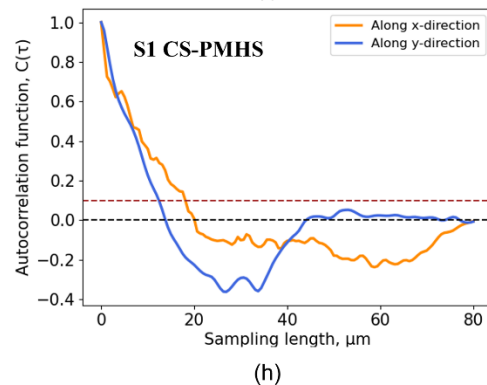
(e)



(f)



(g)



(h)

Figure 7.4. Position of the maximum and minimum values in 3×3 sub-matrices and corresponding autocorrelation function for surface profile data for (a-b) CS BM, (c-d) CS BM-PMHS, (e-f) S1 CS (BM-ZP), (g-h) S1 CS-PMHS

Besides characterizing the surface roughness of the samples using traditional measurement techniques, we studied correlation lengths, analysis of the extreme point location, and persistence diagrams in the data space. Novel insights into the roughness properties were generated by these parameters which were beyond the scope of the traditional quantitative surface roughness characterizations. From the autocorrelation functions, information of the horizontal size of the microscale roughness details was received. Details about anisotropic microscale features that are not identified by the more traditional roughness parameters were presented by the analysis of the 3×3 submatrices. The persistence diagrams and barcodes presented the details of the scale-dependency of the roughness features.

7.3. Wetting test

The wetting test results of the samples coated with the antimicrobial coatings are presented in **Table 7.1** and **Table 7.2**. The uncoated BM samples after sandblasting and the BM samples coated with S1 and S2 coating materials were hydrophilic in nature without a stable wetting profile. We didn't report the CA of those hydrophilic samples. BM samples with the single layer of the PMHS coating exhibited stable wetting profiles with average CAs between 95.65° -98.37°. In contrast, the samples coated with the 2-layer coatings (S1 or S2 coating material + PMHS) exhibited impressive hydrophobic behavior where the average CA varied between 111.93° - 124.33°. We plotted CAs of the hydrophobic samples against average roughness in **Figure 7.5**.

The wetting test results of the samples coated with the anticorrosive coatings are presented in **Table 7.3**. The resulting CA of the samples before the tribological test ranges from 96.2° to 112.6°. We also presented the CAs of ceramic tiles coated with TP and PMHS layers against the average roughness in **Figure 7.5**. In each case, the CA increased with an increasing average roughness of the samples, which is consistent with other studies [33,34,37].

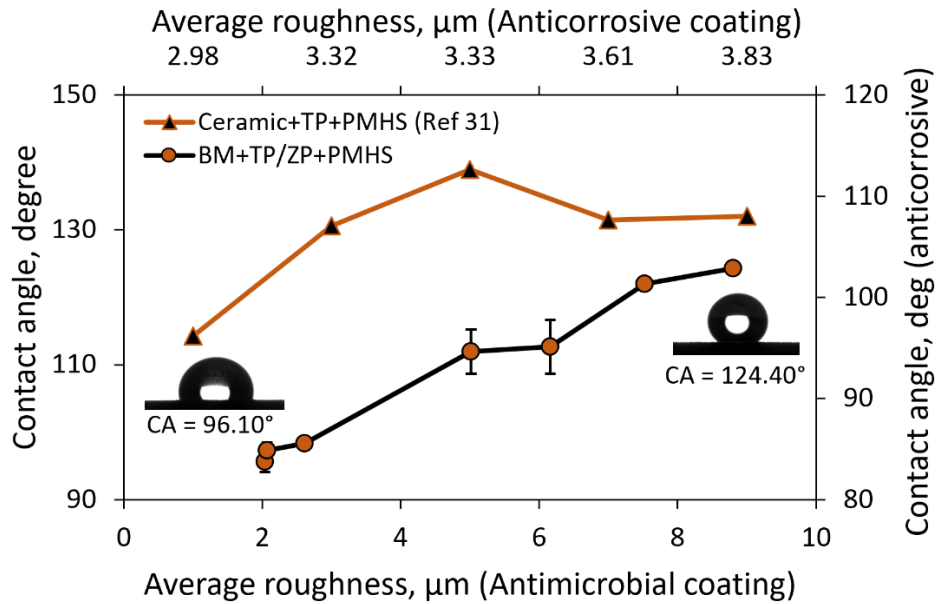


Figure 7.5. Contact angle vs. average roughness plot of hydrophobic samples coated with antimicrobial and anticorrosive coatings

BMs coated with a single layer of PMHS had smaller average roughness values among the hydrophobic samples and exhibited smaller CAs. Samples coated with the S1 and S2 coating materials (TP/ZP layer) followed by the PMHS layer had larger average roughness and exhibited larger CAs. The 2-layer coating of TP/ZP and the PMHS layers induced the maximum average roughness on the carbon steel BMs. The maximum CA (124.40°) was observed for the CS sample coated with the 2-layer coating. The micrographs demonstrated that the crystal structures were well-covered by the PMHS layer which made their appearance more blurred in the micrographs.

Among the samples, the surface of the S1h CS sample was less blurred by the PMHS layer which was distributed more evenly as the crystal structures on this substrate were more developed.

7.3.4. Tribological tests

We present the tribological test results for the base materials and the coated samples with the antimicrobial coatings in **Table 7.1** and **Table 7.2**. We used the COF of the BM samples as references to compare the friction performance of the developed coatings. For the BM samples, the COF ranged between 0.221 ± 0.063 to 0.269 ± 0.081 . For BM samples coated with the single layer of PMHS, a notable reduction in COF was observed (ranging between 0.155 ± 0.041 to 0.178 ± 0.045). As the BM surfaces were modified with the low surface energy coating, the surfaces were smoothed, and the average roughness was reduced. Consequently, lower COF values were observed for the samples.

Table 7.1. Properties of base materials before and after hydrophobic treatment (antimicrobial coatings)

BM	Average roughness (μm)		Coefficient of friction		Contact angle (Degree)	
	BM	+ PMHS coating	BM	+ PMHS coating	BM	+ PMHS coating
	CS	3.705	2.611	0.256 ± 0.077	0.174 ± 0.055	-
RTP CS	2.805	2.039	0.269 ± 0.081	0.155 ± 0.041	-	$95.65^\circ \pm 1.55^\circ$
SS	2.907	2.071	0.221 ± 0.063	0.178 ± 0.045	-	$97.30^\circ \pm 1.21^\circ$

BM samples coated with the single layer S1 (ZP) and S2 (TP-ZP) coating materials also exhibited lower COF than the uncoated BM samples. Ceramic debris generated in a powder form during the tribological testing provided a lubrication effect which caused the reduction in COF. However, the COF was slightly higher than the PMHS coated samples. BM samples coated with the 2-layer hydrophobic coatings (first layer of the S1 or the S2 coating material followed by a second layer of PMHS) exhibited COF values ranging from 0.234 to 0.273, which were similar to the reference uncoated base materials.

Table 7.2. Properties of the coated hydrophilic and hydrophobic samples (antimicrobial)

Coating material	BM	Average roughness (μm)		Coefficient of friction		Contact angle (Degree)	
		Phosphate coating	+ PMHS	Phosphate coating	+ PMHS	Phosphate coating	+ PMHS
		CS	6.473	8.805	0.193 \pm 0.074	0.273 \pm 0.081	-
S1	RTP CS	4.96	5.016	0.207 \pm 0.055	0.245 \pm 0.069	-	111.93 $^{\circ}$ \pm 3.26 $^{\circ}$
	SS	5.722	6.161	0.194 \pm 0.076	0.263 \pm 0.075	-	112.68 $^{\circ}$ \pm 4.01 $^{\circ}$
S2	CS	4.004	7.522	0.233 \pm 0.072	0.234 \pm 0.076	-	121.97 $^{\circ}$ \pm 0.86 $^{\circ}$

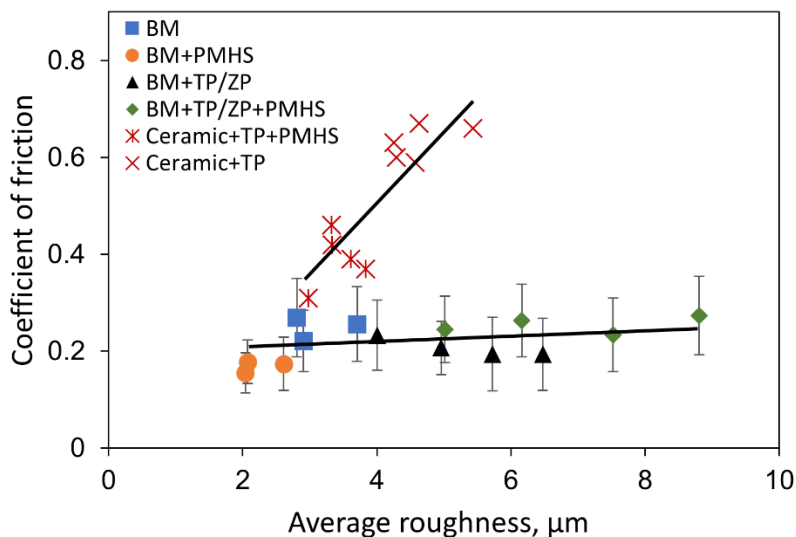


Figure 7.6. COF vs. average roughness plot for uncoated steel BMs and BMs coated with TP/ZP+PMHS and comparison with COF vs average roughness for ceramic tile samples coated with TP and TP+PMHS.

The friction between the uncoated ceramic tile vs. rubber was measured as a reference, and the value of the coefficient of friction (COF) was found to be 0.45 ± 0.24 . **Table 7.3** summarizes the roughness, COF and contact angle for TiO₂-phosphate coated hydrophilic samples R2, R5, R7, R9 and O2 and R2, R5, R7, R9 and O2 (TiO₂-phosphate + PMHS coated hydrophobic samples). According to the American National Standards Institute (ANSI), tiles appropriate for ramp applications require a dynamic coefficient of friction (DCOF) greater than 0.42. Our tribological tests provided the average coefficient of friction (F_x/F_z) which is the ratio of frictional force (F_x) to normal load (F_z) as 0.45 for uncoated reference ceramic tiles, which is close to the standard value. The COF for the TiO₂-phosphate coated samples varied from 0.59 to 0.67, which is higher than that of the standard value due to the strong bond and induced roughness. The application of the developed hydrophobic coatings on R2, R5, R7, R9, and O2 samples resulted in COF from 0.31 to 0.45. For optimal composition R2, even though the reduction of COF due to hydrophobic

coating and reduced roughness, a slight enhancement of COF was observed (0.46 vs 0.45 of the reference). This suggests that developed hydrophobic coatings do not necessarily reduce the dry frictional traction. As the properties of the tile samples used in the experiments were similar to concrete, it can be concluded that the hydrophobic coating developed in this study would not make the concrete surface slippery.

Table 7.3. The properties of anticorrosive TiO₂-phosphate coated (hydrophilic) and TiO₂-phosphate + PMHS coated (hydrophobic) samples

Type of sample	Roughness (μm)		Coefficient of friction		Contact angle (Degrees)	
	TiO ₂ -phosphate coating	TiO ₂ -phosphate + PMHS coating	TiO ₂ -phosphate coating	TiO ₂ -phosphate + PMHS coating	TiO ₂ -phosphate coating	TiO ₂ -phosphate + PMHS coating
R2	5.43	3.32	0.66±0.28	0.46±0.32	0°	107.15°
R5	4.29	3.83	0.60±0.31	0.37±0.29	0°	107.49°
R7	4.63	2.98	0.67±0.26	0.31±0.15	0°	96.18°
R9	4.25	3.33	0.63±0.31	0.42±0.32	0°	112.62°
O2	4.57	3.61	0.59±0.32	0.39±0.24	0°	107.66°

We plotted the COF values of the uncoated and coated BM with the developed coatings against the average roughness in **Figure 7.6**. Besides visualizing the COF of different types of samples, we observed a linear increasing trend of COF with increasing average roughness. This increasing trend was consistent with ceramic substrates coated the anticorrosive coatings with TP

and PMHS though the relationship between average roughness (which is a surface property) and the COF (which is a tribological response) can be more complex [38]. The tribological characterization indicated that the 2-layer hydrophobic coatings can be tuned to retain the friction behavior of the base materials while imparting desired hydrophobic properties to the substrate materials.

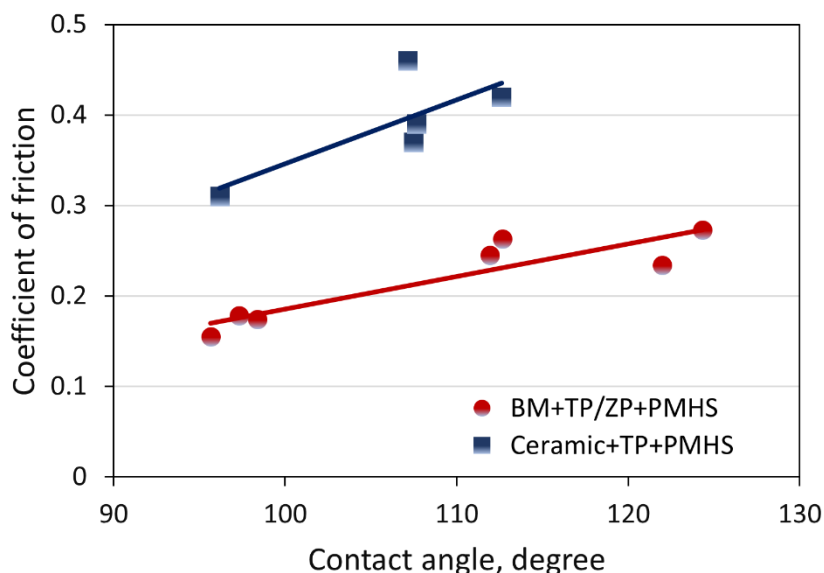


Figure 7.7. COF vs CA plot for the coated hydrophobic samples

The COF values of PMHS coated BM samples and 2-layer coated samples are plotted against the corresponding CAs in **Figure 7.7**. We observed a linear trend where the COF increased with an increasing CA. This observation was consistent with the ceramic tile samples coated with TP and PMHS.

We analyzed the SEM micrographs of the scratched 2-layer coated surfaces with antimicrobial coatings during the tribological tests. The intensive sliding of the tribometer pin on the coated samples caused visible detaching of the crystalline structures of TP/ZP from the substrates. However, the presence of a thin coating layer on the scratched substrate was clearly

visible unlike observed for the base metals. In a preliminary observation, the presence of microcracks on the micrographs also suggested the retention of the coating layer and abrasion resistance despite the severe sliding.

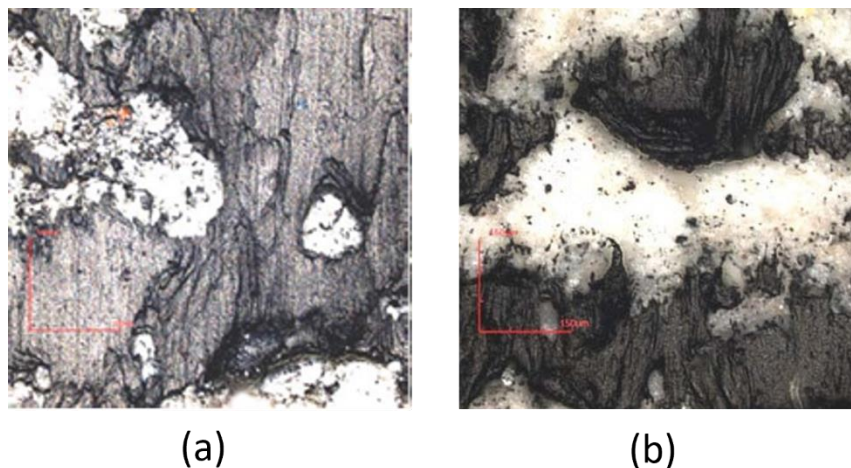


Figure 7.8. Confocal microscope images of the coated tile surfaces with the (a) R2 and (b) optimal (O2) anticorrosive hydrophobic coatings observed after the tribological test.

In order to evaluate the mechanical durability of the anticorrosive hydrophobic TiO₂-phosphate + PMHS coating, after the tribological tests, the tile samples were examined under the confocal microscope under 20X magnification. **Figure 7.8.** is an image of the surface of the O2 sample with hydrophobic coating observed under 20X magnification after the tribological test. From the magnified view, it is evident that rubber residue remained on the surface (black particles in the image) after the tribological test. The hydrophobic coating component (white particles in the image) remained intact on the tile surface. This image proved that like TiO₂-phosphate coated hydrophilic samples, the TiO₂-phosphate + PMHS coated hydrophobic samples had a high adhesion with the surface and good abrasion resistance. The results of the conducted tribological tests demonstrated that the anticorrosive coatings have the adequate abrasion resistance and

adhesion to the substrate, and, therefore, will potentially demonstrate an excellent wear resistance and overall durability in the field condition. A detailed study involving the wear rate can reveal more about the durability and abrasion resistance of the coatings.

7.4. Conclusions

In this study, the wetting, frictional, and roughness properties of hydrophobic antimicrobial and anticorrosive coatings were analyzed. The average roughness of the uncoated BM samples ranged between 2.805 μm to 3.705 μm . The single antimicrobial coating layer (S1 and S2) notably increased the roughness of the BM samples to the values ranging from 4.004 μm to 6.473 μm . The samples coated with the 2-layer hydrophobic coatings (ZnO/TiO₂-phosphate layer followed by PMHS) exhibited the maximum average roughness values (ranging between 5.016 μm to 8.805 μm). Here PMHS effectively amplified the roughness of single-coated substrates. The topological data analysis indicated anisotropic roughness distribution in the coated samples.

The BM samples coated with the 2-layer coatings had excellent and stable hydrophobic behavior with CA ranging between 111.93° to 124.33°. The 2-layer S1 CS-PMHS sample had the maximum average roughness and the highest CA. From the tribological characterization, the average COF of the BM samples was found between 0.221-0.256. The application of a single layer of hydrophobic PMHS or hydrophilic S1 or S2 coating material reduced the average COF. However, the COF values ranging between 0.234 to 0.273 for the 2-layer coated hydrophobic samples reached the levels of the uncoated BM samples. This observation indicated that the developed 2-layer hydrophobic coating did not alter the friction behavior of the base materials.

In the study of the anticorrosive coatings, the uncoated reference tile has a roughness value of 7.69 μm , the hydrophilic coated tiles roughness values lying in the range between 4.25 μm to 5.43 μm having a best roughness measurement as 5.43 μm and the hydrophobic coated tiles

roughness values lying in the range between 2.98 μm to 3.83 μm having a best roughness measurement as 3.83 μm with respect to reference tile. It is also observed that the coating material remains unharmed on the tile samples after rubber-tile friction of the tribological test. Moreover, rubber traces were observed in the CLSM images of the coated surfaces. While a detailed quantitative study of wear rates is required, it can be preliminary concluded that the coated surfaces have good wear and abrasion resistance, which is highly desirable for application on a pavement surface.

The reference tile has a COF of 0.45 compared to hydrophilic TiO_2 -phosphate coated tiles having COF lying in the range between 0.59 to 0.67 and the COF of hydrophobic TiO_2 -phosphate + PMHS coated tiles having COF in the range between 0.31 to 0.46. The results prove that the values of the COF between the rubber and ceramic tile samples having hydrophilic coating properties were enhanced and for some hydrophobic coatings, a reduction in COF in comparison to the uncoated tiles was observed. However, optimized hydrophobic coating R2 produced at TiO_2 to Phosphoric acid ratio of 4 and enhanced by PMHS had a COF of 0.46 which was better than that of reference.

7.5. References

1. Bourouiba, Lydia. "Turbulent gas clouds and respiratory pathogen emissions: potential implications for reducing transmission of COVID-19." *Jama* 323, no. 18 (2020): 1837-1838.
2. Lewis, Dyani. "Is the coronavirus airborne? Experts can't agree." *Nature* 580, no. 7802 (2020): 175.
3. Shiu, Eunice YC, Nancy HL Leung, and Benjamin J. Cowling. "Controversy around airborne versus droplet transmission of respiratory viruses: implication for infection prevention." *Current opinion in infectious diseases* 32, no. 4 (2019): 372-379.

4. Hasan, Md Syam, Konstantin Sobolev, and Michael Nosonovsky. "Evaporation of droplets capable of bearing viruses airborne and on hydrophobic surfaces." *Journal of Applied Physics* 129, no. 2 (2021): 024703.
5. Zhang, Sheng, MengYuan Diao, Wenbo Yu, Lei Pei, Zhaofen Lin, and Dechang Chen. "Estimation of the reproductive number of novel coronavirus (COVID-19) and the probable outbreak size on the Diamond Princess cruise ship: A data-driven analysis." *International journal of infectious diseases* 93 (2020): 201-204.
6. for Immunization, National Center. "Science Brief: SARS-CoV-2 and Surface (Fomite) Transmission for Indoor Community Environments." In *CDC COVID-19 Science Briefs [Internet]*. Centers for Disease Control and Prevention (US), 2021.
7. World Health Organization. (2020). Coronavirus disease (COVID-19): Cleaning and disinfecting surfaces in non-health care settings. Available: <https://www.who.int/news-room/q-a-detail/coronavirus-disease-covid-19-cleaning-and-disinfecting-surfaces-in-non-health-care-settings>. [Accessed: 24-March-2022].
8. Cloutier, Maxime, Diego Mantovani, and Federico Rosei. "Antibacterial coatings: challenges, perspectives, and opportunities." *Trends in biotechnology* 33, no. 11 (2015): 637-652.
9. Kaur, Rajbir, and Song Liu. "Antibacterial surface design—Contact kill." *Progress in Surface Science* 91, no. 3 (2016): 136-153.
10. Sabbouh, Mirna, Anna Nikitina, Elizaveta Rogacheva, Lyudmila Kraeva, Sviatlana A. Ulasevich, Ekaterina V. Skorb, and Michael Nosonovsky. "Separation of motions and vibrational separation of fractions for biocide brass." *Ultrasonics Sonochemistry* 80 (2021): 105817.

11. Heidenau, F., W. Mittelmeier, R. Detsch, M. Haenle, F. Stenzel, G. Ziegler, and H. Gollwitzer. "A novel antibacterial titania coating: metal ion toxicity and in vitro surface colonization." *Journal of Materials Science: Materials in Medicine* 16, no. 10 (2005): 883-888.
12. Botequim, D., J. Maia, M. M. F. Lino, L. M. F. Lopes, P. N. Simões, L. M. Ilharco, and L. Ferreira. "Nanoparticles and surfaces presenting antifungal, antibacterial and antiviral properties." *Langmuir* 28, no. 20 (2012): 7646-7656.
13. Haldar, Jayanta, Alisha K. Weight, and Alexander M. Klivanov. "Preparation, application and testing of permanent antibacterial and antiviral coatings." *Nature Protocols* 2, no. 10 (2007): 2412-2417.
14. Basak, Soumyadeep, and Gopinath Packirisamy. "Nano-based antiviral coatings to combat viral infections." *Nano-Structures & Nano-Objects* 24 (2020): 100620.
15. Faraldos, M., R. Kropp, M. A. Anderson, and K. Sobolev. "Photocatalytic hydrophobic concrete coatings to combat air pollution." *Catalysis Today* 259 (2016): 228-236.
16. Binas, Vassilios, Danae Venieri, Dimitrios Kotzias, and George Kiriakidis. "Modified TiO₂ based photocatalysts for improved air and health quality." *Journal of Materiomics* 3, no. 1 (2017): 3-16.
17. Sano, Taizo, Nobuaki Negishi, Kazuhide Koike, Koji Takeuchi, and Sadao Matsuzawa. "Preparation of a visible light-responsive photocatalyst from a complex of Ti⁴⁺ with a nitrogen-containing ligand." *Journal of Materials Chemistry* 14, no. 3 (2004): 380-384.
18. Ishibai, Yoichi, Junya Sato, Shoichi Akita, Takashi Nishikawa, and Shigeyoshi Miyagishi. "Photocatalytic oxidation of NO_x by Pt-modified TiO₂ under visible light irradiation." *Journal of Photochemistry and Photobiology A: Chemistry* 188, no. 1 (2007): 106-111.

19. Guo, Mu Yao, Alan Man Ching Ng, Fangzhou Liu, Aleksandra B. Djuricic, Wai Kin Chan, Huimin Su, and Kam Sing Wong. "Effect of native defects on photocatalytic properties of ZnO." *The Journal of Physical Chemistry C* 115, no. 22 (2011): 11095-11101.
20. Jongnavakit, Patcharee, Pongsaton Amornpitoksuk, Sumetha Suwanboon, and Tanakorn Ratana. "Surface and photocatalytic properties of ZnO thin film prepared by sol-gel method." *Thin Solid Films* 520, no. 17 (2012): 5561-5567.
21. Liu, Junli, Yuhan Wang, Jianzhong Ma, Yi Peng, and Aiqin Wang. "A review on bidirectional analogies between the photocatalysis and antibacterial properties of ZnO." *Journal of Alloys and Compounds* 783 (2019): 898-918.
22. Arabzadeh, Ali, Halil Ceylan, Sunghwan Kim, Kasthurirangan Gopalakrishnan, and Alireza Sassani. "Superhydrophobic coatings on asphalt concrete surfaces: Toward smart solutions for winter pavement maintenance." *Transportation Research Record* 2551, no. 1 (2016): 10-17.
23. Flores-Vivian, Ismael, Vahid Hejazi, Marina I. Kozhukhova, Michael Nosonovsky, and Konstantin Sobolev. "Self-assembling particle-siloxane coatings for superhydrophobic concrete." *ACS applied materials & interfaces* 5, no. 24 (2013): 13284-13294.
24. Ramachandran, Rahul, Konstantin Sobolev, and Michael Nosonovsky. "Dynamics of droplet impact on hydrophobic/icephobic concrete with the potential for superhydrophobicity." *Langmuir* 31, no. 4 (2015): 1437-1444.
25. Sobolev, Konstantin G., and Vladimir G. Batrakov. "Effect of a polyethylhydrosiloxane admixture on the durability of concrete with supplementary cementitious materials." *Journal of Materials in Civil Engineering* 19, no. 10 (2007): 809-819.
26. Heinrich, Gert, and Manfred Klüppel. "Rubber friction, tread deformation and tire traction." *Wear* 265, no. 7-8 (2008): 1052-1060.

27. Chu, Longjia, Tien F. Fwa, and Ghim P. Ong. "Evaluating hydroplaning potential of rutted highway pavements." *Journal of the Eastern Asia Society for Transportation Studies* 11 (2015): 1613-1622.
28. Tomita, Hisao. *Tire-Pavement Friction Coefficients*. NAVAL CIVIL ENGINEERING LAB PORT HUENEME CA, 1970.
29. Slone, Sean. *High costs of winter road maintenance, 2013-14*. Council of State Governments, 2014.
30. Kaufmann, Josef P. "Experimental identification of ice formation in small concrete pores." *Cement and Concrete Research* 34, no. 8 (2004): 1421-1427.
31. Feng, X. J., and Lei Jiang. "Design and creation of superwetting/antiwetting surfaces." *Advanced Materials* 18, no. 23 (2006): 3063-3078.
32. Hasan, Md Syam, Tien Wong, Pradeep K. Rohatgi, and Michael Nosonovsky. "Analysis of the friction and wear of graphene reinforced aluminum metal matrix composites using machine learning models." *Tribology International* 170, (2022): 107527.
33. Hasan, Md Syam, Filip Zemajtis, Michael Nosonovsky, and Konstantin Sobolev. "Synthesis of ZnO/TiO₂-Based Hydrophobic Antimicrobial Coatings for Steel and Their Roughness, Wetting, and Tribological Characterization." *Journal of Tribology* 144, no. 8 (2022): 081402.
34. Lanka, Sridhar, Evgeniya Alexandrova, Marina Kozhukhova, Md Syam Hasan, Michael Nosonovsky, and Konstantin Sobolev. "Tribological and wetting properties of TiO₂ based hydrophobic coatings for ceramics." *Journal of Tribology* 141, no. 10 (2019).
35. Hasan, Md Syam, and Michael Nosonovsky. "Topological data analysis for friction modeling." *EPL (Europhysics Letters)* 135, no. 5 (2021): 56001.

36. Zhukov, Mikhail, Md Syam Hasan, Pavel Nesterov, Mirna Sabbouh, Olga Burdulenko, Ekaterina V. Skorb, and Michael Nosonovsky. "Topological Data Analysis of Nanoscale Roughness in Brass Samples." *ACS Applied Materials & Interfaces* 14, no. 1 (2022): 2351–2359.
37. Wang, Xianchen, and Qin Zhang. "Insight into the Influence of Surface Roughness on the Wettability of Apatite and Dolomite." *Minerals* 10, no. 2 (2020): 114.
38. Menezes, P. L., and S. V. Kailas. "Role of surface texture and roughness parameters on friction and transfer film formation when UHMWPE sliding against steel." *Biosurface and Biotribology* 2, no. 1 (2016): 1-10.

CHAPTER 8: CONCLUSIONS

First, artificial neural network, *k*-nearest neighbor, support vector machine, gradient boosting machine, and random forest algorithm-based ML regression models geared towards establishing correlations in structure and tribological properties of aluminum alloys and particle reinforced aluminum MMCs (aluminum-graphite and aluminum-graphene) in dry conditions were developed by employing a Python language-based computational procedure have been developed. Statistical performance metrics suggested that the ML models could satisfactorily predict the friction and wear of these alloys and MMCs. ML models for aluminum-graphene and aluminum-graphite MMCs notably outperformed those for aluminum alloys in COF and wear rate prediction. In the presence of categorical variables as inputs, and the prevalent variability in the friction and wear data sets, the decision tree based standalone GBM and RF regression models and their hybrid ensemble models provided the best performance for the friction and wear prediction of aluminum alloys, aluminum-graphite, and aluminum-graphene MMCs.

Second, structure-property relationships between the material properties, composition of the alloys and MMCs, test conditions, and tribological properties of aluminum alloys and aluminum-based MMCs were analyzed. Traditional analysis showed that the presence of reinforcement particles (graphite/graphene) and the loading conditions notably affected the tribological properties. Additionally, the linear contrast analysis suggested that a much lower wt.% of graphene in the aluminum matrix as the reinforcement phase can lead to similar decrease in COF which are obtained with a much higher amount of graphite in the aluminum MMCs under comparable tribological conditions. This finding can be useful in choosing between these two aluminum MMCs for specific tribological applications. The most influential material properties

and tribological parameters in predicting the friction and wear behavior of these alloys and MMCs were identified using feature importance attribute of the decision tree-based RF models. The hardness, sliding distance, and tensile strength of the alloys influenced the COF most significantly. On the other hand, normal load, sliding speed, and hardness were the most influential parameters in predicting wear rate. Graphite content was identified as the most significant parameter in friction and wear prediction in Al-graphite MMCs. For aluminum-graphene MMCs, load, graphene content, and hardness have been identified as the most influential parameters in COF prediction while graphene content, load, and hardness have the greatest influence in the wear rate prediction. These findings suggested that the optimization of these small number of parameters can generate desired friction and wear performance in these aluminum alloys and MMCs.

Third, principal component analysis based unsupervised ML models and random forest and gradient boosting machine algorithm-based hybrid ensemble ML models for dimensionality reduction in structure-property relationships data and predicting the friction and wear behavior of aluminum-graphite MMCs in during the transition of lubrication regimes by employing a Python language-based computational method have been developed. The hybrid ensemble RF-GBM models performed the best than the other models for COF and wear rate prediction in aluminum-graphite MMCs in lubricated conditions. However, the predictive performance of the hybrid RF-GBM model with 5 PCA descriptors (variables derived through dimensionality reduction from the actual 14 input variables) was weaker compared to other hybrid and standalone ML models in COF prediction. This indicated that the actual 14 variables considered in the study are significant in COF prediction and the dimensionality reduction using PCA caused significant information loss. Lubrication condition, lubricant viscosity, and applied load have been identified as the most important variables in predicting wear rate and COF. Graphite content, which was the most crucial

parameter in the dry condition had reduced impact in friction and wear prediction of aluminum-graphite MMCs in the presence of liquid lubricants. The Linear Contrast analysis suggested that for the fully lubricated conditions, graphite content had little effect on the friction behavior of aluminum-graphite MMCs. In another word, the self-lubrication property of these MMCs in liquid-lubricated conditions are not as effective as those in the dry condition. This finding can be helpful in selecting the material between aluminum alloys and aluminum-graphite MMCs for applications in fully lubricated conditions.

Fourth, a new methodology of data-driven surface roughness analysis consisting of the calculation of roughness parameters, correlation lengths, extremum point distribution, persistence diagrams, and barcodes was developed and used for studying the roughness patterns, functional designs, and anisotropic distributions inherent in steel substrates coated with TiO_2/ZnO phosphate and PMHS based 2-layer antimicrobial and anticorrosive coatings, and sonochemically treated brass (Cu Zn alloy) samples. The autocorrelation function provided information about the horizontal (tangential) size of roughness details at the microscale. The analysis of the 3×3 , 4×4 , and 5×5 sub-matrices or patches provided information about the anisotropic features of the profile at the nanoscale, which are not captured by more traditional surface roughness parameters. In the anisotropic distribution of surface roughness in steel samples coated with antimicrobial coatings, the surface gradients in the horizontal direction were more prevalent than in the vertical direction. Additionally, the scale dependency of the roughness features was explained by the persistence diagrams and barcodes. These results can be helpful in optimizing the surface coatings for desired surface properties.

Fifth, comprehensive correlations between surface roughness, COF, and water contact angle were established for steel substrates coated with TiO_2/ZnO phosphate and PMHS based

antimicrobial and ceramic substrates coated with TiO₂ phosphate and PMHS based anticorrosive coating materials. The CA and COF of samples coated with both antimicrobial and anticorrosive coatings increased with increasing surface roughness. An overall linear increasing trend of COF with increasing average roughness was observed. A positive linear correlation between the COF and CA of the coated surface was also observed. The combined wetting and tribological characterization also revealed that the hydrophobic modification didn't make the coated surfaces slippery and retained adequate friction for transportation application. This refuted the general conception that non-sticky means slippery. Moreover, the results of the tribological tests demonstrated adequate abrasion resistance and adhesion to the substrate, and, therefore, potentially, excellent wear resistance and overall durability of the anticorrosive coatings in the field condition.

This dissertation demonstrates that data-driven Triboinformatics approaches can be successfully implemented in surface science, wetting, and tribology. These approaches can not only add value to the existing traditional characterizations but also can generate novel insights which are beyond the scope of the traditional quantitative analysis.

CURRICULUM VITAE

Education

- **Ph.D. in Engineering, University of Wisconsin-Milwaukee, WI, USA**

Spring 2022, Mechanical Engineering, CGPA: 4.00/4.00

Thesis: Triboinformatics approaches for surface characterization: tribological and wetting properties

- **MS Engineering, University of Wisconsin-Milwaukee, WI, USA**

Summer 2021, Mechanical Engineering, CGPA: 4.00/4.00

- **B.Sc., Bangladesh University of Engineering & Technology, Bangladesh**

March 2016, Mechanical Engineering

Publications

Journal Papers

1. **Hasan, M.S.** and Nosonovsky, M., Triboinformatics: machine Learning algorithms and data Topology methods for tribology, *Surface Innovations* **2022**, pp.1-11. Doi: <https://doi.org/10.1680/jsuin.22.00027>.
2. **Hasan, M.S.**, Wong, T., Rohatgi, P.K. and Nosonovsky, M., Analysis of the friction and wear of graphene reinforced aluminum metal matrix composites using machine learning models. *Tribology International* **2022**, 170, 107527.
3. **Hasan, M. S.**, Zemajtis, F., Nosonovsky, M., & Sobolev, K., Synthesis of ZnO/TiO₂-based hydrophobic antimicrobial coatings for steel and their roughness, wetting, and tribological characterization, *Journal of Tribology* **2022**, 144(8), 081402.

4. Zhukov, M., **Hasan, M.S.**, Nexterov, P., Sabboukh, M., Burdulenko, O., Skorb, E., and Nosonovsky, M., Topological data analysis of nanoscale roughness in brass samples, *ACS Applied Materials & Interfaces* **2021**, 14 (1), 2351–2359.
5. **Hasan, M.S.**, Kordijazi, A., Rohatgi, P.K., Nosonovsky, M., Machine learning models of the transition from solid to liquid lubricated friction and wear in aluminum-graphite composites, *Tribology International* **2022**, 165(2022), 107326.
6. **Hasan, M.S.**, Nosonovsky, M., Topological data analysis for friction modeling, *Europhysics Letters* **2021**, 135 (2021), 56001.
7. **Hasan, M.S.**, Kordijazi, A., Rohatgi, P.K., Nosonovsky, M., Triboinformatic modeling of dry friction and wear of aluminum base alloys using machine learning algorithms, *Tribology International* **2021**, 161(2021), 107065.
8. **Hasan, M.S.**, Kordijazi, A., Rohatgi, P.K., Nosonovsky, M., Triboinformatics approach for friction and wear prediction of Al-Graphite composites using machine learning methods, *ASME. J. Tribol* **2021**, 144(1), 011701.
9. **Hasan, M.S.**, Sobolev, K., and Nosonovsky, M., Evaporation of droplets capable of bearing viruses airborne and on hydrophobic surfaces, *J. Appl. Phys.* **2021**, 129(2), 024703.
10. **Hasan, M.S.** and Nosonovsky, M., Lotus Effect and Friction: Does Nonsticky Mean Slippery? *Biomimetics* **2020**, 5(2), 28.
11. **Hasan, M. S.**; Nosonovsky, M., Method of separation of vibrational motions for applications involving wetting, superhydrophobicity, and microparticle extraction, *Phys. Rev. Fluids* **2020**, 5(5), 054201.

12. Lanka, S., Alexandrova, E., Kozhukhova, M., **Hasan, M. S.**, Nosonovsky, M., Sobolev, K. Tribological and Wetting Properties of TiO₂ Based Hydrophobic Coatings for Ceramics. *ASME. J. Tribol* **2019**, 141(10), 101301.
13. Khan, A.H., **Hasan, M.S.**, Sarkar, M. A. R., Analysis of Possible Causes of Fukushima Disaster, *International Journal of Nuclear and Quantum Engineering* **2018**, 12(2), 53-58.

Book Chapter

- **Hasan, M. S.**, Kordijazi, A., Rohatgi, P. K., & Nosonovsky, M. (2022). Application of Triboinformatics Approach in Tribological Studies of Aluminum Alloys and AluminumGraphite Metal Matrix Composites. In *Metal-Matrix Composites* (pp. 41-51). Springer, Cham.

Conference presentation

- Hasan, M.S., Kordijazi, A., Rohatgi, P.K., Nosonovsky, M., Application of Triboinformatics Approach in Tribological Studies of Aluminum Alloys and Aluminum-Graphite Metal Matrix Composites, In *2022 TMS Annual Meeting & Exhibition 2022: Proceedings of the Metal-Matrix Composites: Advances in Processing, Characterization, Performance and Analysis*, CA, USA.
- Hasan, M.S., Kordijazi, A., Rohatgi, P.K., Nosonovsky, M., Machine learning approaches for predicting dry friction and wear behavior of aluminum alloys, *7th World Tribology Congress (WTC 2022)*, Lyon, France. (accepted)
- Hasan, M.S., Kordijazi, A., Rohatgi, P.K., Nosonovsky, M., Tribological behavior prediction of Al/Gr composites under dry condition using machine learning methods, *7th World Tribology Congress (WTC 2022)*, Lyon, France. (accepted)

Poster presentation

- Hasan, M.S., Kordijazi, A., Rohatgi, P.K., Nosonovsky, M., Triboinformatics: combining machine learning with studies of friction and wear of Al/Gr MMCs, UWM CEAS student research poster competition 2021.
- Hasan, M.S., Nunez, A, Nosonovsky, M., Silva M., Prediction of Escherichia coli concentration from physiochemical and wetting properties of beach sand using machine learning models, UWM CEAS student research poster competition 2022.

Award and Scholarship

- “Chancellor’s award (2020-2022) from University of Wisconsin-Milwaukee for outstanding research productivity as a graduate student.
- Graduate Student Travel Award, University of Wisconsin-Milwaukee (Spring 2022)
- Technical scholarship (2011-2015) from Bangladesh University of Engineering and Technology.